Comprehensive analysis of underground H2 storage with CO2 as a cushion gas in aquifers : Capacity assessments, thermodynamic approaches, and realistic reservoir simulations

Sabrine Ben Rhouma

Université de Pau et des Pays de L'Adour

École doctorale Sciences Exactes et leurs Applications – ED211

Laboratory: LFC-R

PhD thesis for Earth and Planetary Sciences

Comprehensive analysis of underground H_2 storage with CO_2 as a cushion gas in aquifers: Capacity assessments, thermodynamic approaches, and realistic reservoir simulations

---

Doctoral Dissertation of: **Sabrine Ben Rhouma**

Supervised by Daniel Broseta

and Rolland Masson

Presented and defended on December 14, 2023

In front of a jury composed of:

Adrian Cerepi, Prof. HDR	Director, ENSEGID	Reviewer
Curtis M. Oldenburg, DR	Geological Senior Scientist, LBNL	Reviewer
Laurent Jeannin, PhD-HDR	Senior Engineer, Storengy	Reviewer
Serge Van Gessel	Senior advisor economic affairs / TNO	Examiner
Pascal Audigane, PhD-HDR	Scientist / BRGM	Examiner
Sabine Delahaye	Engineer / TOTAL	Guest
Marelys Mujica Chacin, PhD	Scientist / RepSol	Guest
Daniel Broseta, Prof. HDR	Université de Pau	Advisor
Roland Masson, Prof. HDR	Université de Nice	Advisor

Co-supervised by:

Fernanda D.M.L.Veloso, PhD	Scientist / BRGM
Farid Smaï, PhD	Scientist / BRGM
Pierre Chiquet, PhD	Scientist / TEREGA
Alexandre DOS SANTOS	Scientist / TEREGA

"Oui, mes amis, je crois que l'eau sera un jour employée comme combustible, que l'hydrogène et l'oxygène, qui la constituent, utilisés isolément ou simultanément, fourniront une source de chaleur et de lumière inépuisables et d'une intensité que la houille ne saurait avoir."

L'Île Mystérieuse, Jules Verne, 1874

"Yes, my friends, I believe that water will one day be used as a fuel, that hydrogen and oxygen, which constitute it, used separately or simultaneously, will provide an inexhaustible source of heat and light, and of an intensity that coal cannot possess."

The Mysterious Island, Jules Verne, 1874

.....

Abstract

The global transition to sustainable energy sources, with a focus on hydrogen (H_2) as an energy carrier, presents a critical and urgent challenge. As H_2 production is intermittent, much like renewable electricity, storing significant quantities of H_2 is essential. Large-scale underground hydrogen storage (UHS) in porous reservoirs emerges as a promising solution. This thesis investigates the feasibility of UHS employing carbon dioxide (CO_2) as a cushion gas (CG), addressing concerns related to storage integrity, gas mixing, CG impact, storage capacities, and operational efficiency.

The initial phase of this research involves analytical calculations to assess storage height capacities using different CGs. Compared to conventional storage, where the entire gas column consists of H_2, employing denser CGs such as CO_2, CH_4, or N_2 significantly enhances both the safety and capacity of H_2 storage. This emphasizes the potential of CO_2 as a suitable CG. Additionally, a simple criterion is provided for the maximum H_2 injection velocity to avoid the fingering instability of the mixing front with the CG and H_2 and thus limit contamination of the stored H_2. This criterion is based on the viscosity vs. density behavior of the H_2-CG mixtures under storage conditions. This maximum velocity is rarely surpassed in practical applications, even in scenarios involving inclined mixing fronts.

To delve deeper into the complexities of UHS, the thermodynamic behavior of the H_2-CO_2 system is studied in detail, and numerical simulations are considered. A comprehensive exploration of thermodynamic models (GERG2008, cubic PR, and SRK) to assess their suitability for describing H_2-CO_2 mixtures under UHS storage conditions showed some difficulties with the cubic equations describing experimental densities under storage conditions, with an error up to 15%. However, a cubic equation model was integrated into the open-source reservoir simulation tool, ComPASS, and applied to simple case studies in the context of UHS. Such tools can offer more control and freedom in adjusting thermodynamic model parameters.

The study expands its scope by considering various reservoir pressure and temperature conditions, analyzing the thermodynamic behavior of the H_2-CO_2 system under these conditions, and characterizing the resulting static behavior of the reservoir. The investigation reveals the potential for two-phase separation into a dense CO_2-rich and H_2-rich phase under some specific conditions, which could influence the fluid-mixing zone due to gravity segregation. Notably, these conditions are particularly relevant to offshore reservoirs (or cold reservoirs). This supports the use of offshore reservoirs for storing both H_2 and CO_2, with the latter being permanently stored and the former being supplied by wind farms in close proximity.

Furthermore, a realistic reservoir case study with conditions in which CO_2- H_2 coexist as a single gas-phase system was modeled. Through reservoir simulations, various scenarios are explored to identify conditions that optimize H_2 recovery efficiency and purity. Geological and operational parameters influencing storage efficiency are examined. The findings indicate that the amount and purity of H_2 withdrawn progressively increases across successive cycles, and geological heterogeneities might play a role in mitigating up-coning effects. Short-period cycles are found to improve the hydrogen productivity index, while the production rate

significantly affects gas quality and mixing zone characteristics.

Overall, this research demonstrates that achieving H_2 storage with reasonable gas recovery parameters is feasible, and CO_2 as a CG emerges as a promising solution for the sustainable energy transition.

Key words: UHS, CO_2 cushion gas, Thermodynamic, Multiphase flow, Mixing zone, Realistic reservoir modeling.

Résumé

La transition vers des sources d'énergie durables, notamment en utilisant l'hydrogène (H_2) en tant que vecteur énergétique, est un défi critique et urgent. Étant donné que la production de H_2 est intermittente, un stockage efficace du H_2 est essentiel. Dans ce contexte, le stockage souterrain d'hydrogène (UHS) dans des aquifères émerge comme une solution prometteuse. Cette thèse se penche sur la faisabilité de l'UHS en utilisant le dioxyde de carbone (CO_2) comme gaz coussin (GC) et explore divers enjeux liés à l'intégrité du stockage, au mélange des gaz, à l'impact du GC, aux capacités de stockage et à l'efficacité opérationnelle.

Tout d'abord, nous avons effectué des calculs analytiques visant à évaluer les capacités de stockage en utilisant différents types de GC. Par rapport au stockage conventionnel où l'ensemble de la colonne de gaz est composé de H_2, l'utilisation de GC plus denses tels que le CO_2, le CH_4 ou le N_2 améliore la sécurité et la capacité de stockage du H_2. Cela met en évidence le potentiel du CO_2 en tant que GC adapté. En outre, un critère simple est fourni pour la vitesse d'injection maximale de H_2 afin d'éviter l'instabilité de la zone de mélange avec le gaz coussin et le H_2 (fingering), limitant ainsi la contamination du H_2 stocké. Il est à noter que cette vitesse maximale est rarement dépassée dans les applications pratiques, même dans les scénarios impliquant des zones de mélange inclinées.

Par la suite, pour approfondir notre compréhension des complexités de l'UHS, une exploration des modèles thermodynamiques (tels que GERG2008, les équations cubiques : PR et SRK) a été mené afin d'évaluer leur aptitude à décrire le mélange H_2-CO_2. Cette évaluation a révélé des difficultés avec les équations cubiques pour décrire les densités expérimentales, avec une marge d'erreur d'environ 15 %. Cependant, un module thermodynamique basé sur l'équation cubique a été intégré à l'outil de simulation open-source, ComPASS. Cet outil a été employé dans des études de cas simples liées à l'UHS, offrant ainsi une plus grande liberté pour ajuster les paramètres du modèle.

L'étude étend son domaine d'investigation en prenant en compte diverses conditions de pression et de température du réservoir. Le comportement du système H_2-CO_2 dans ces conditions a été analysé afin de caractériser le comportement statique résultant du réservoir. Cette analyse met en évidence la possibilité d'une séparation en deux phases (une phase dense riche en CO_2 et une phase riche en H_2) dans certaines conditions spécifiques, ce qui pourrait influencer la zone de mélange des fluides en raison de la ségrégation gravitationnelle. Ces conditions sont pertinentes pour les réservoirs offshores (ou les réservoirs froids). Cela encourage la conception de réservoirs offshore où l'H_2 peut être stocké efficacement à proximité des parcs éoliens.

Ensuite, une étude d'un réservoir réaliste dans des conditions où le CO_2-H_2 coexistent en tant que système monophasé a été modélisée. À travers des simulations de réservoir exhaustives, différents scénarios sont explorés pour optimiser l'efficacité et la pureté de la récupération de H_2. Les paramètres géologiques et opérationnels ayant un impact significatif sur l'efficacité du stockage sont examinés. Les résultats mettent en évidence une augmentation progressive du taux de récupération de l'H_2 au fur et à mesure des cycles successifs. D'autre part, il est observé que les hétérogénéités géologiques du site jouent un rôle dans la réduction des effets de coning. Les cycles de courte durée s'avèrent améliorer l'indice de productivité de

l'hydrogène, tandis que le débit de production influe considérablement sur la qualité du gaz et les caractéristiques de la zone de mélange.

En conclusion, cette recherche démontre la faisabilité du stockage du H_2 avec des taux de récupération de gaz raisonnables. De plus, elle souligne le rôle prépondérant du CO_2 en tant que GC dans la transition vers des solutions énergétiques durables.

Mots clés : UHS, CO_2 gaz coussin, Thermodynamique, Flux multiphasique, Zone de mélange, Modélisation réservoir réaliste.

Acknowledgements

Completing this section of my manuscript was the last assignment, and unlike my expectations, it turned out to be a reflective task. While summarizing my scientific work in a single page was achievable, to sum up three years of experience proved to be quite the challenge. So, I ask for your patience as I try to be concise.

This work has been made possible through the generous funding of TEREGA and BRGM, conducted under the guidance of the University of Pau and the University of Nice. Therefore, my foremost gratitude extends to these institutions for providing the resources and the environment necessary to conduct this PhD.

Naturally, this leads me to acknowledge my supervision board, starting with my PhD directors, Daniel Broseta and Roland Masson, whose guidance navigated me through this academic path. Working full-time at BRGM under the DRP/SPU unit, I must acknowledge the dedication of my supervisors, Fernanda De Mesquita L.Veloso and Farid Smai, whose daily interactions and unwavering support, both scientifically and personally, were invaluable—thank you! I also express gratitude to colleagues at TEREGA for their collaboration, data sharing, and insightful exchanges, namely Pierre Chiquet and Alexandre Dos Santos.

Special recognition is extended to the members of the follow-up committee, Salaheddine Chabab and Georgios Kontogeorgis, as well as the panel of experts who evaluated my thesis during the defense. Their time, expertise, and constructive feedback have been instrumental in shaping this work.

The interdisciplinary nature of my research presented the first identified difficulty and challenge, but it also provided the opportunity to collaborate closely with multiple colleagues. In this context, I extend my thanks to Laurence Beaude, and Simon Lopez, who worked closely with me, particularly in the development of tools. Special mention goes to Ben Gilbert and Curtis Oldenburg, who graciously welcomed me into their lab at Berkeley and introduced me to their research.
I extend my gratitude to CMG for providing the GEM tool license, which helped achieving a significant part of this research.

Special thanks are due to my colleagues with whom I shared countless coffee breaks—perhaps one of the reasons this manuscript is not perfect. Special thanks also to BRGM for assigning me a mentor, Angélie Portal, whose guidance proved invaluable throughout this journey, including our shared bike rides to work.

Speaking of biking, I extend my thanks to all the other activities I practiced (like tennis, body sculpting, and swing) and to my partners who shared these experiences with me, especially Isaline Gravaud and Danièle Rossi. Note that these activities did not spare me from gaining weight by the end of the PhD, but they certainly helped me deal with the challenging moments.

Furthermore, I am deeply grateful for my circle of friends (Batran, Chames, Ghada, Ghassen, Ichraf, Maurizio, Nour, and many others that I didn't list– sorry, I promised to keep it short!), for their belief in me and their consistent support, even across distances. I also want to thank the other PhDs and postdocs whom I had the pleasure of meeting on various occasions. Whether sharing a beer, a laugh, or simply experiences, their encounter has enriched my journey.
Lastly, my heartfelt thanks goes to my partner, Simon, who supported me through this journey. I extend my deepest appreciation to both his family and mine, whose encouragement has been the endless source of strength and inspiration.

شكرا جزيلا ! (Shukran jazeelan)

Contents

List of Figures

List of Tables

List of Acronyms

BHP Bottom Hole Pressure 99

CapEx Capital Expenditures 13

CCS Carbon Capture and Storage 2

CCUS Carbon Capture, Use, and Storage 1

CG Cushion Gas 6

ECS Extended Corresponding State 21

EoS Equation of State 14

FWL Free Water Level 26

IFT Interfacial Tension 23

LCOHS Levelized Cost of Hydrogen Storage 7

OpEx Operational Expenditures 13

PR Peng–Robinson 41

SRK Soave-Redlich-Kwong 41

UHS Underground Hydrogen Storage 4

VdW Van der Waals 41

VLE Vapor-Liquid Equilibrium 41

WG Working Gas 7

WGC Water-Gas Contact 25

List of Symbols

α_L	The longitudinal dispersivity in (m)
Λ	Permeability tensor : resistance of the medium to the flow (m^2)
λ	Bulk thermal conductivity of the fluid and rock mixture ($W.m^{-1}.K^{-1}$)
$\mathbf{g}$	Gravity ($m.s^{-2}$)
$\mathbf{q}$	Generalized Darcy velocity ($m.s^{-1}$)
$\mathbf{q}^\alpha$	The velocity of each phase α ($m.s^{-1}$)
$\mathcal{F}_i$	The volumetric source of component i
μ^α	Dynamic viscosity of the phase α (Pa.s)
N_{tot}	The total number of moles
ϕ	Porosity
ρ^α	Volumetric mass in the phase α ($kg.m^{-3}$)
τ	Tortuosity of the rock
φ_i^α	The fugacity coefficient of the component i in the phase α
$\boldsymbol{\mu}$	Chemical potential
ζ	Molar density ($mol.m^{-3}$)
D'_L	The longitudinal hydrodynamic dispersion
D'_T	The transverse hydrodynamic dispersion
D_{diff}	The molecular diffusion coefficient (cm^2/s)
D_m	Effective gas-gas diffusion coefficients (cm^2/s)
$D_{\text{disp},L}$	Mechanical dispersion coefficient longitudinal
$D_{\text{disp},T}$	Transverse mechanical dispersion coefficient
E_f	Fluid energy per unit pore volume ($J.m^{-3}$)

E_r Rock energy per unit rock volume ($J.m^{-3}$)

f_i^α The fugacity of the component i in the phase α (Pa)

G^E Excess Gibbs free energy

h^α Molar enthalpy of the phase α ($J.mol^{-1}$)

h_i^α Partial molar enthalpy of the component i in the phase α ($J.mol^{-1}$)

k_r Relative permeability

M_r Mobility ratio of one fluid displacing another fluid

N_i The number of moles for each component i

n_i The number of moles per unit pore volume of each component i ($mol.m^{-3}$)

P^α Pressure of the phase α (Pa)

P_{ce} Capillary entry (or displacement) pressure

R The universal gas constant

T Temperature (Kelvin)

U^α Molar internal energy in the phase α ($J.mol^{-1}$)

x_i^α Molar fractions of the component i in the phase α

CHAPTER 1

General Introduction

1.1 Scope

In the pursuit of reducing the emission of Carbon dioxide (CO_2) into the atmosphere, a transition strategy to replace fossil fuel-based energy with more convenient renewable sources has became inevitable. However, despite efforts to reduce fossil fuel consumption, it remains constant since 2019, with higher gas production (2.7 EJ) and coal consumption (10.6 EJ) compensating for the decline in oil demand (Fig.1.1 left). This phenomenon was triggered by a rebound in economic growth, which in turn, led to an increase in CO_2 emissions with 0.8% increase in 2022 over 2021 (Fig.1.1 right).

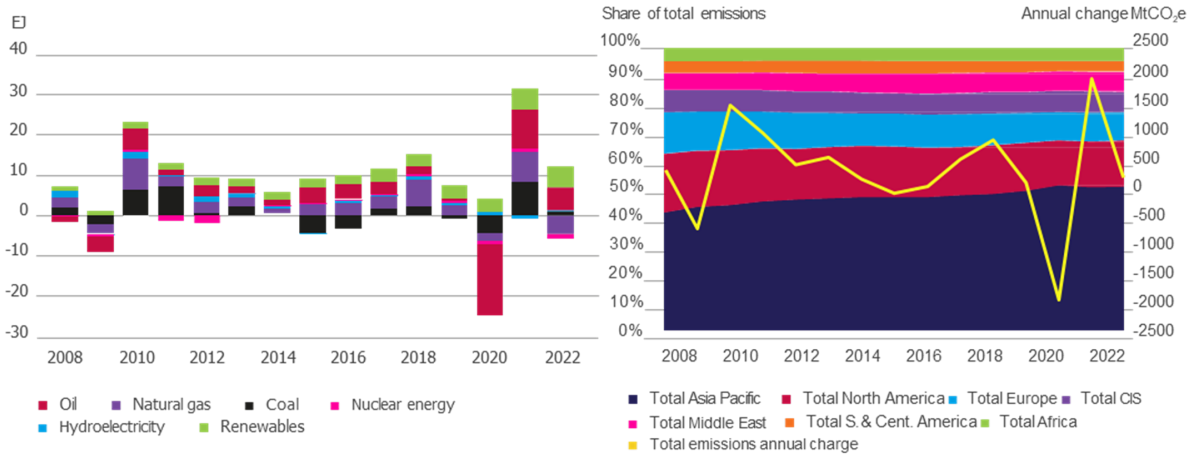

FIGURE 1.1: Left: The variations in primary energy consumption from different sources over time. Right: The fluctuation in carbon emissions during the same period [1].

To achieve the decarbonization plan, low-carbon energy sources and technologies already exist today, including wind and solar power, biofuels, blue and green Hydrogen (H_2), *Carbon Capture, Use, and Storage* (CCUS), and CO_2 removal techniques. The implementation of renewable energies to meet the rising energy demand becomes imperative. According to the statistical

report of the Energy Institute from 2023, renewable energy has experienced significant growth, contributing to 14% of the total power generation in 2022 (40.9 EJ), with a remarkable growth rate of nearly 16% [1]. However, renewable energy sources, such as wind, solar, and tidal power, face challenges due to their seasonal production fluctuations. The supply rates depend on factors such as wind force, sunlight intensity, and geographic location, which are influenced by natural environmental factors, leading to an imbalance between production and demand. To address this variation and ensure a continuous and reliable energy supply throughout the year, H_2 emerges as a promising solution. By storing a substantial volume of H_2, it can serve as a buffer to prevent energy losses or deficits, effectively mitigating the drawbacks of renewable energy sources. Thus, H_2 holds the potential to play a significant role in complementing and enhancing the transition to renewable energy, facilitating the journey towards a carbon-neutral future.

1.2 Hydrogen origin and storage

H_2 is an energy carrier that promotes the carbon-free transition, provided that the origin, production process, and energy sources required for the processes have net-zero carbon emissions or at least minimal emissions. In this section, we will first discuss the potential sources of H_2 and the resulting H_2 labels. In the second part, we will delve into related large-scale storage solutions, with particular emphasis on aquifers, as they constitute the primary focus of this research.

1.2.1 Origin

H_2 gained visibility and significant attention due to its potential to harness renewable energy sources profitability and decarbonize processes in industries with high carbon emissions. However, as of 2021, H_2 produced through electrolysis represents only 0.1% of the total 94Mt of H_2 generated [2]. As an initial step toward the transition to a H_2 economy, 83% of the H_2 produced in 2021 was sourced from hydrocarbon processes. At this stage, H_2 results from gasification technologies using lignite coal or biomass, or it is extracted from natural gas via steam methane reforming. These forms of H_2 are referred to as *gray* and *brown* H_2, respectively. When *gray* H_2 is associated with *Carbon Capture and Storage* (CCS) strategies, H_2 production is deemed possible with minimal CO_2 emissions (knowing that the H_2 production generates ten times its amount CO_2), despite being derived from fossil fuels. This type of H_2 is noted as *blue* H_2.

More recently, to support the H_2 economy, the concept of blending green H_2 has come to light [3]. This has paved the way for various other options and has made it essential to color-code H_2 based on its source (water, biomass, natural gas, and different types of coal) and the production process (electrolysis, steam methane reforming, gasification, thermochemical, photochemical, biochemical, and biological processes) [4], as depicted in Table 1.1. However, beyond the commonly employed labels of *gray*, *green*, and *blue*, ongoing debates persist about color definitions like *pink/purple*, *orange/yellow*, *gold*, and *red*. In this study, we refer to *orange* H_2 as H_2 produced using an energy source derived from a mix of electricity grid power. Yet, in other research papers, such as the work by Osselin et al. [5], *orange* H_2 is considered to be natural H_2 resulting from the alteration of metamorphic rocks. This natural H_2 is generated through

the reduction of water, and its distinctive orange color is associated with the transformation of ferrous iron to ferric iron in an anoxic and abiotic process. Although, the International Energy Agency avoids ambiguity by designating H_2 as originating either from electrolysis powered by renewable energy or via biomass [2]. Ultimately, the environmental impact of H_2 can have varying levels of low or high, direct or indirect CO_2 emissions, depending on the source of energy and the method of H_2 production, as clarified in Fig.1.2.

Table 1.1: Definitions of color categories for hydrogen, encompassing the corresponding technologies employed, and the sources of Hydrogen.

Terminology	Technology	Source of Hydrogen
Gray	Steam methane reforming	Natural Gas
Blue	Steam methane reforming + CCUS	Natural Gas
	coal | Gasification + CCUS	
Turquoise	Pyrolysis + solid CO_2 storage	Natural gas
Brown	Gasification	Lignite coal | biomass
Black	Gasification	Bituminous coal
Green	Electrolysis powered by Renewable energy	Water
Pink	Electrolysis powered by nuclear	Water
Red	Thermolysis|Thermochemical by nuclear	Water
Orange	Electrolysis powered by mixed-origin grid energy	Water
Yellow	Electrolysis powered by solar energy	Water
White	Naturally occurring hydrogen	-

The gray shading indicates processes for hydrogen production based on electricity from fossil fuels.

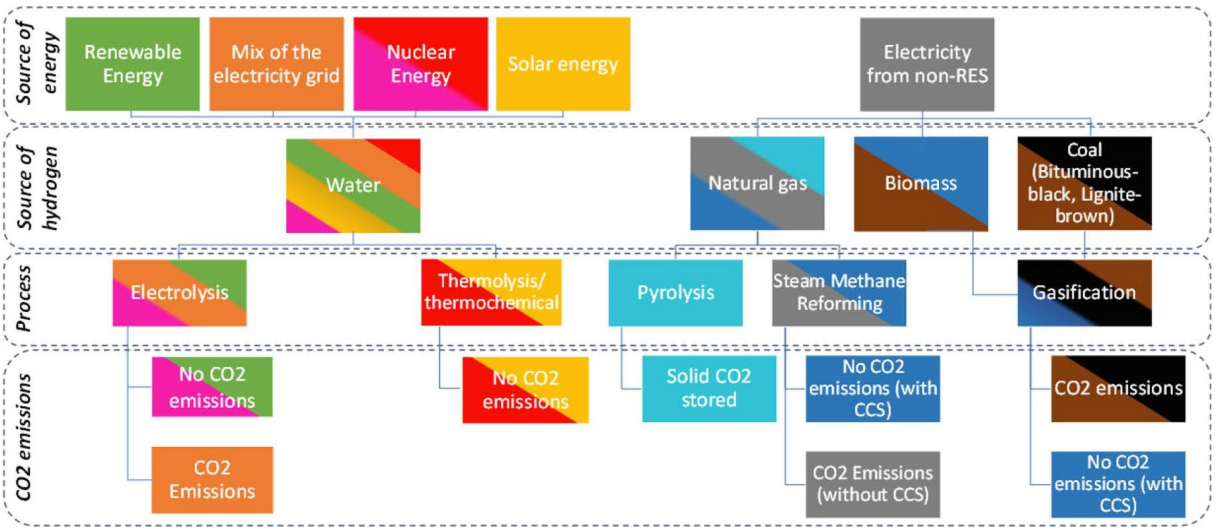

FIGURE 1.2: Overview of energy source origins, hydrogen origins, production processes, and associated emissions corresponding to the diverse color classifications assigned to hydrogen [6].

A recent review analyzed the environmental footprint of the distinct colors of H_2 (Fig.1.3) [6]. For instance, biomass-based sources of energy have the highest environmental impact, followed by *orange* H_2, which is dependent on the type of energy source mixed. The impact of *blue* H_2 also relies on the technology used and storage percentage. *Yellow* H_2's CO_2 emissions are attributed to the construction of solar farms. In contrast, *red* and *pink* H_2 are associated with minimal

direct CO_2 emissions, though other concerns may arise (radiation, security, etc.). While this representation underscores the benefits of using H_2 produced through water electrolysis powered by renewable energy, it is important to consider water source availability, disposal of waste, and the impact of desalination. Additionally, it is crucial to take into account factors like that H_2 has a relatively low energy density ($3\,kWh/Nm^3$ or $33\,kWh/kg\,H_2$) and that electrolysis efficiency is about 60%. To illustrate, the process of producing $1\,m^3$ of H_2 through electrolysis (at atmospheric pressure and 0°C) requires 1 liter of water and 5 kWh of electricity. The resulting H_2 contains 3 kWh of energy. If this H_2 is subsequently converted back into electricity using a turbine with a 50% efficiency, the final output is 1.5 kWh of electricity. Therefore, the overall efficiency in this case is 30% compared to the 5 kWh required upstream [7].

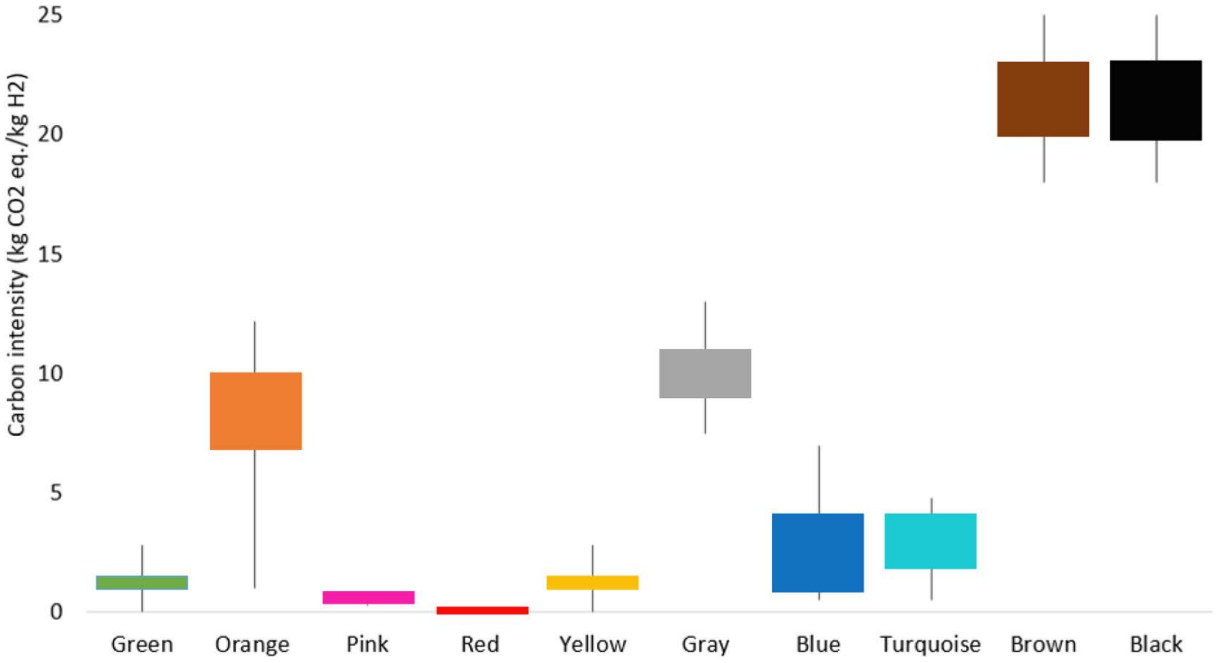

FIGURE 1.3: Comparative Carbon Intensity Across Hydrogen Color Categories [6].

Ongoing economic studies are delving into this topic with a growing interest in applying H_2 production. One certainty is that in order to produce H_2 from renewable energies, it should ideally occur during periods of excess electricity when renewable energy supply is abundant, likely during periods of low demand. This sets the stage for the following section, where the concept of storage necessity will be elaborated upon.

1.2.2 Storage

The variability in energy production and consumption due to the seasonal nature of renewable energies necessitates efficient storage solutions. H_2, in either liquid or gaseous state, offers different means of energy storage. Well-established surface-based H_2 storage technologies include compressed gas cylinders, liquid tanks, metal hydrides, and carbon structures [8]. However, to effectively address the intermittent nature of renewable energy sources, our focus shifts to *Underground Hydrogen Storage* (UHS). UHS helps balance energy fluctuations by providing substantial storage capacities for surplus energy production, releasing it when demand peaks.

This technology has already demonstrated technically its capability to offer large-scale storage capacities [9].

The field of underground storage, whether permanent or seasonal, has undergone decades of study and practical implementation. With accumulated experience and research, this technology has matured and demonstrated its adaptability to various types of fluids. In most instances, geological storage serves as a reversible storage solution, offering a second life and economic value to stored products, a practice widely adopted by petroleum companies for natural gas storage. Yet, it can function as a permanent solution for storing products that can no longer be retrieved, as seen in applications like CCS or CCUS. Geological structures for UHS should be chosen based on a detailed geological study that considers both geological and engineering criteria. The geological storage of gases is generally categorized into two concepts: storage in porous media (encompassing depleted natural gas and oil reservoirs and aquifers) and storage in artificial underground spaces (such as salt caverns and disused mine workings).
Four primary subsurface storage structures (salt cavers, mines, depleted reservoirs and aquifers) are commonly utilized and detailed below.

1.2.2.1 Artificial underground space

Salt caverns are artificially created by injecting water from the surface into deep salt domes or shallower bedded formation deposits, causing them to dissolve and form caverns through solution mining. The feasibility and capacity of creating salt caverns depend on factors such as the depth and thickness of the salt deposit and the homogeneity of the lithologies, including the amount of insoluble rock components [10]. The salt formation could be unevenly distributed geographically and not located in regions that offers the highest storage need and potential, as shown in the Fig.1.4. UHS in salt caverns shares similarities with natural gas storage in caverns. However, due to the smaller size of H_2 molecules, the storage pressure should be lowered compared with that used for natural gas. Maintaining storage pressures in caverns within the range of 5-10 MPa is feasible [11]. Nevertheless, the transfer capacity of the surface installation is limited. While salt caverns offer operational flexibility and a lower contamination risk, their main drawback is the disposal of freshwater for cavern leaching, which can have ecological and environmental impacts.

Abandoned salt mines and rock caverns present in regions lacking salt caverns, hard rock caverns, created by excavating hard rocks (such as igneous or metamorphic rocks) and encasing them with impermeable liners (typically made of steel or plastic), can serve as UHS options. These liners serve as an effective barrier, isolating the stored gas from the surrounding rock and ensuring containment. To reduce hydrostatic pressure on the lining, groundwater is drained from these caverns. However, it is important to note that hard rock caverns have pressure limitations; most types of rocks tend to deform under pressures exceeding 4 MPa. To mitigate this concern, concrete layers are often injected to absorb the excess pressure.

1.2.2.2 Storage in porous media

Geological aspects and conditions play a crucial role in UHS selection. Porous media offer greater geographic flexibility, with abundant and large-capacity geological reservoirs, making them an attractive choice.

Depleted gas/oil reservoirs are the most common underground storage reservoirs worldwide. Their geology is usually well understood, and the existing infrastructure, although requiring conversion, can reduce the budget for adapting them into UHS [12]. Consequently, utilizing these reservoirs for H_2 storage can prove to be an economically efficient option. Depleted gas/oil reservoirs typically exhibit characteristics such as high permeability, significant depth (often exceeding 1000 meters), and a minimal presence of hydrogen sulfide (H_2S) [13]. However, this type of storage presents challenges, including the risk of gas contamination with pre-existing hydrocarbons and the need for purification equipment. *Cushion Gas* (CG) is necessary to prevent reservoir rock fracturation and maintain reservoir pressure. In most cases, the volume of CG comprises approximately half of the reservoir's total volume. it is worth noting that any abandoned gas or oil remaining in these reservoirs can also be repurposed as part of the CG. Notably, a case study in the Netherlands showcased the potential of depleted gas reservoirs for future H_2 infrastructure. A techno-economic study involving subsurface modeling and surface

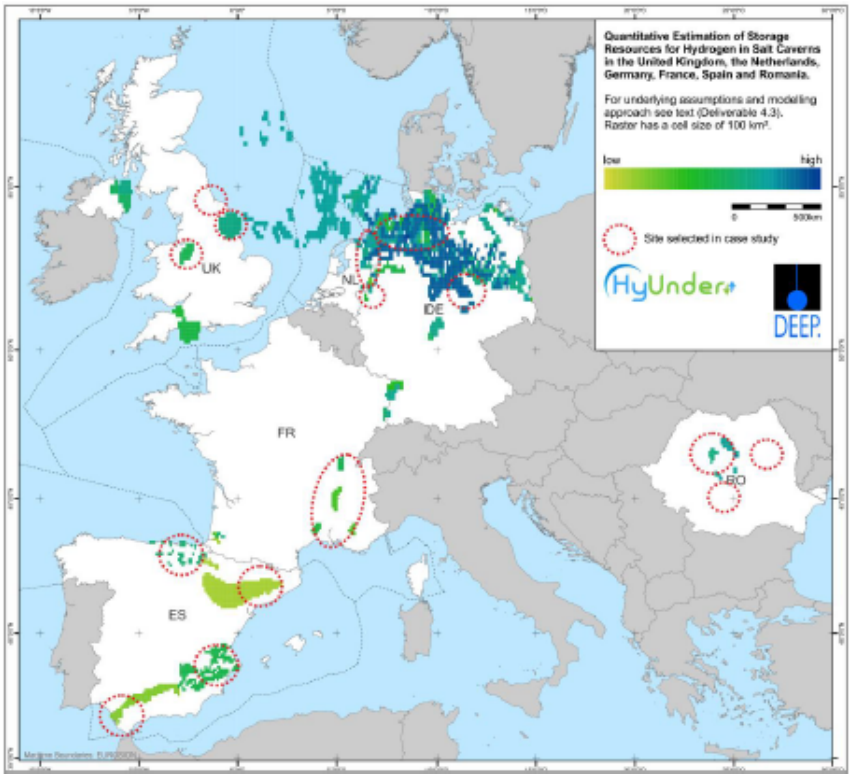

FIGURE 1.4: The geographic distribution of salt deposits for potential storage in six countries. The color code reference to the UHS capacity and the circled zones represent the sites selected for the study [10].

facility design concepts calculated the *Levelized Cost of Hydrogen Storage* (LCOHS). In a base case scenario with H_2 as the CG, the LCOHS was estimated at 0.79€ per kilogram, with the investment cost of the CG accounting for 76% of the total cost [14]. Replacing the CG with nitrogen (N_2) reduced the LCOHS to 0.49€ per kilogram. Furthermore, increasing the number of cycles had a substantial impact, reducing the LCOHS to 0.25€ per kilogram.

Another study identified the Sekihara gas field in Niigata prefecture, Japan, as a suitable candidate for UHS due to its storage capacity of approximately $2.06 \cdot 10^8$ cubic meters and a depth of 1000 meters. Critical parameters, including formation depth, rock-brine- H_2 interactions, caprock integrity, and well performance, were assessed [15]. The recovery factor of 82.7% in the sixth cycle of production indicates the site as prospective site for UHS. Additionally, the study simulated UHS in a depleted oil reservoir, using CO_2, N_2, and CH_4 as CG. The results demonstrated maximum H_2 recovery (89.7%) when CH_4 was used as the CG, and an estimated maximum of 84.5% in the absence of CG. Pressure buildup prior to water breakthrough improved H_2 recovery in annual cycles, but negatively affected UHS performance after water breakthrough [16]. The study also compared H_2 storage capacities and deliverabilities to natural gas in a seasonal storage facility. The H_2 facility exhibited the capability to store and supply 42% of the energy capacity of natural gas, delivering power at an average rate of approximately 100 GWh per day, equivalent to 40% of natural gas's energy deliverability. Importantly, the study identified minimal technical barriers to H_2 storage [17].

Aquifers have recently gained attention in the context of potential CCS plans, although they have already been successfully used for natural gas purposes. These porous and permeable rock formations are initially filled with fresh or saline water, making them an attractive option due to their wide geographic distribution and large storage capacity (see Fig.1.5). Given their substantial pore space, aquifers offer the potential to store significant volumes of gas underground, making UHS in aquifers a promising solution to align with the transition strategy for balancing energy production and demand. To be effective, aquifers must possess geological features similar to depleted hydrocarbon reservoirs, including high porosity, permeability, and reservoir capacity. However, their use is often more expensive than depleted reservoirs due to a lack of infrastructure and geological information. Creating effective gas traps in aquifers requires geological structures like anticlines with impermeable caprock and appropriate surrounding hydrostatic and threshold pressures. In addition to subsurface installations like wells and pipelines, CG is required to provide pressure support for the *Working Gas* (WG), i.e., H_2 [19]. This permanently stored CG contributes to the reservoir's structural integrity. Unlike in depleted reservoirs, aquifer storage may demand a larger volume fraction of CG. In aquifer gas storage, CG typically comprises approximately 30-60% of the total gas in the storage system [20]. The ratio CG/ WG in UHS in aquifers is important information [21]. The loss of H_2 and the CG is inevitable. It is worth noting that a considerable fraction of the CG remains trapped by heterogeneities within the reservoir and cannot be recovered. When a different gas is used instead of H_2 as a CG, there is a potential for gas loss resulting from the mixing process.

UHS in saline aquifers, the focus of this study, presents several challenges, including water

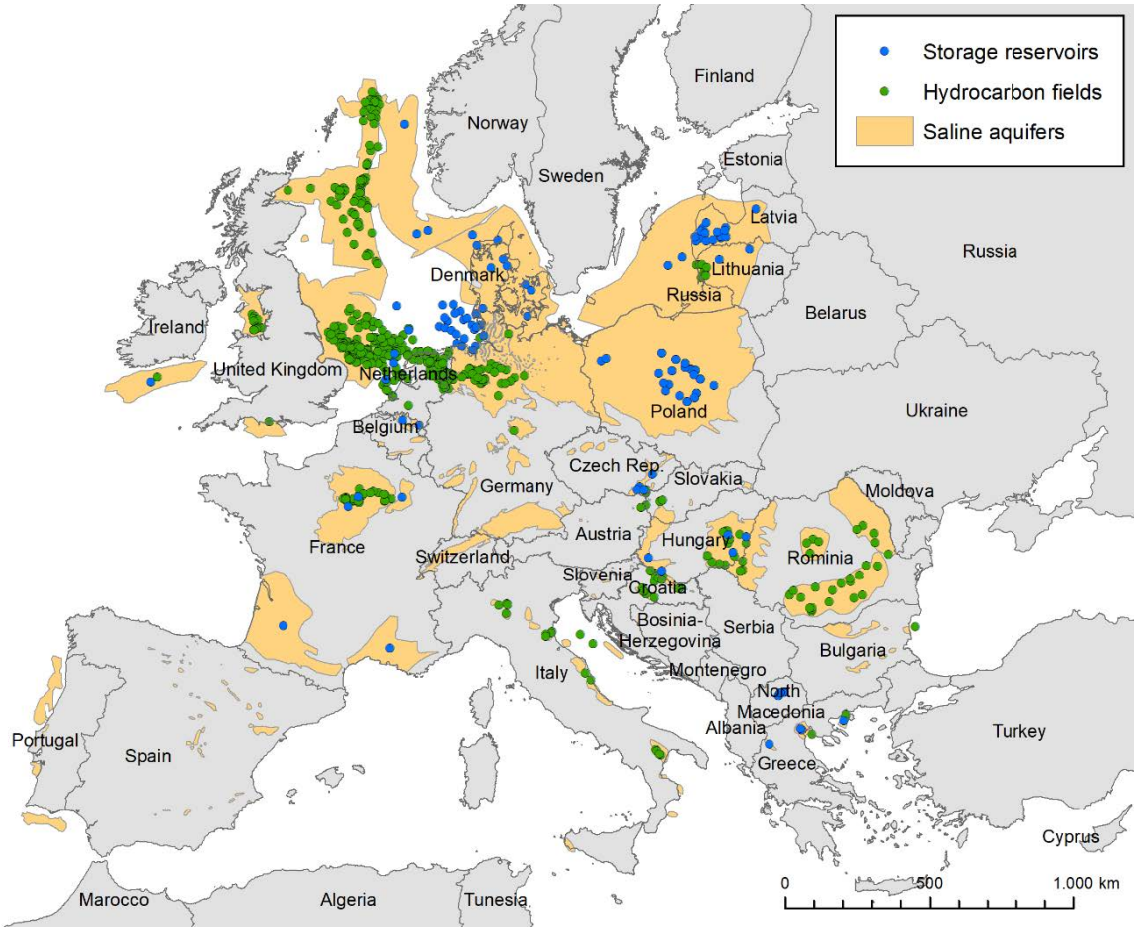

FIGURE 1.5: Geographic distribution of saline aquifers (highlighted in yellow), alongside the locations of hydrocarbon fields and storage reservoirs (depicted as marked points) across Europe [18].

production and achieving sufficient production pressure. Additionally, there is the challenge of identifying various geologic and operational parameters that impact the mixing of CG and H_2, thereby influencing the cost-effectiveness of the project [22, 23]. These challenges will be thoroughly examined in a dedicated section.

In summary, storing fluids underground and altering the natural properties of the originally in-place fluids can lead to changes in pressure and, consequently, affecting the geomechanical distribution of stress and posing a risk of capillary failure of the caprock. These changes may result in fluid migration and potential leakage, a risk common to all types of underground storage. Additionally, the presence of potable water in the vicinity can pose a contamination risk. A thorough geological characterization and comprehensive assessment of storage capacities are crucial in the selection of UHS sites. This is essential for mitigating the risks associated with fluid migration and the probability of migration through the surrounding area and overlying formations, necessitating careful planning and mitigation strategies. Furthermore, as mentioned earlier, when advocating for the use of green H_2 storage through electrolysis, it is crucial to consider the overall efficiency of this process, which is already affected by both the electrolysis

and the subsequent conversion of H_2 back into electricity. If, in addition to these steps, there is a need to convert H_2 to facilitate its transportation to the storage site, an additional energy cost is incurred (for example, 1 kWh for H_2 liquefaction). For instance, if the energy source is far from the storage or usage location, the transportation energy losses become more significant. Consequently, for an efficient and sustainable operation, the storage site must be located in close proximity to the primary energy source.

1.3 Challenges for UHS in aquifers

The UHS presents various challenges and is currently considered as a conceptual study. It requires further exploration, pilot projects, and actual implementations to mature for commercial operations.

The storage in porous media represents geological challenges such as **geochemical and microbial risks**. H_2 is a highly reactive molecule that can initiate geochemical reactions with the surrounding rock and microbial reactions. When H_2 dissolves in water, it can interact with minerals sensitive to redox reactions, leading to dissolution and precipitation that can alter the reservoir properties. However, the low solubility of H_2 may limit its reactivity, and most abiotic reactions remain limited. Geochemical reactions are temperature-dependent, with cold reservoirs ($T < 80°C$) presenting limited geochemical risks. Yet, there is high uncertainty in porous media due to the mineral heterogeneity of the reservoir and variations in fluid composition. Recent experimental studies have expanded our knowledge of the process, but they are often conducted under conditions different from actual storage. Additionally, when H_2 is preceded by CG (N_2, CO_2, CH_4, H_2) injection, H_2 is less likely to come into contact with the gas-water interface.

Additional difficulties involve the H_2 migration through the caprock, which raises questions about the **sealing and integrity of the reservoir** to prevent H_2 leakage to the surface.

Other challenges include optimizing **reservoir performance and site selection**, choosing the CG, comparing the influence of CG types on H_2 recovery rates in saline aquifers, and considering the associated costs, which can be substantial. The impact of cyclic periods on fluid migration and mixing is also noteworthy. Relative permeability can change over time due to multiple cycles of H_2 injection and production, and the loss of CG can become irretrievable in the reservoir. Additional data collected under varying conditions and in different formations are essential for making accurate predictions about the development of the H_2 plume and for defining optimal production strategies. These data should be integrated into hydrodynamic and multiphase flow models.

At the surface, H_2, being a corrosive molecule, raises concerns about **wells, pipelines, and surface facilities**, especially in terms of potential gas separation requirements. The risk of H_2 leakage through improperly completed or abandoned wells or unmapped boreholes can impact the environment, project economics, and safety due to the risk of explosions and fires.

UHS must align with market dynamics, including supply and demand chains, and consider the **economic aspects** of the project. It is important to note that one of the significant challenges already encountered in actual CO_2 storage projects is the **societal embedding** of the method. The social dimension of UHS has not been thoroughly explored yet.

1.4 Previous experiences in UHS

It is worth noting that there are currently no dedicated pilot sites for UHS. Therefore, to gain insights into this innovative concept, we turn to analogous experiences from town gas storage, where the gas mixture can contain up to 60% H_2. These historical town gas storage sites provide valuable lessons and comparisons for the development of UHS technology. These experiences can provide answers and assistance in addressing some of the issues raised in the preceding section.

It is important to note that H_2 primarily induces biotic redox reactions, including iron reduction, sulfate reduction, methanogenesis, and acetogenesis, ranked from most energetically favorable to least favorable [24]. The sulfate reduction reaction leads to the formation of H_2S, a toxic and corrosive gas that requires gas treatment. CH_4 is formed during methanogenesis, which alters the gas mixture's composition (see Fig.1.6). However, abiotic redox reactions between H_2 and rock minerals can also take place and has to be considered [25, 26]

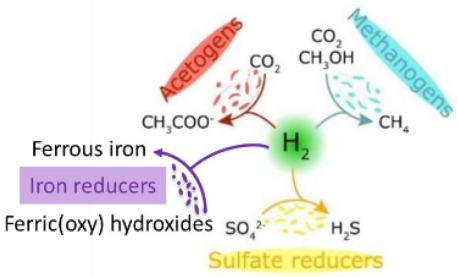

FIGURE 1.6: Main microbial processes in UHS [27].

The history of experiences with town gas storage sites (gas mixture containing 25 to 60% H_2, 10 to 33% CH_4, 12 to 20% CO ,CO_2, and $<$ 30% N_2) includes:

- **Ketzin (Germany, 1964-1985):** The gas composition changed over time, causing gas losses. This change observed is considered too significant to be only attributed to microbial reactions.
- **Beynes (France, 1956-1972):** It was reported that H_2S was produced, likely originating from the abiotic reduction of pyrite by bacteria [28]. The low reservoir temperature suggests a suitable environment for microbial activity.
- **Lobodice (Czech Republic, 1965-1995):** The initial gas reported into the reservoir is a mixture of 54% H_2, 22% CH_4, 12% CO_2, 9% CO, and 2.5% N_2. During the injection and withdrawal cycles, the gas composition changed, and the reservoir pressure decreased. The changes included a decrease in acidic gases (CO_2 and CO) compensated by an increase in CH_4 production. The new gas composition was the following : 40% CH_4, 37% H_2, 9% CO_2, 9% N_2, and 3% CO), over one cycle of 7 months [29, 30]. A portion of the gas volume (10 to 20%) was lost, and the formation of CH_4 was associated with the growth of methanogenic bacteria (change in the isotopic signature of CH_4 typical of bacterial activity) [30].

- **Engelborstel, Bad Lauchstaedt, Kiel (Germany, 1955-1998):** One of the initial sites, and throughout many years of operation, has had no reported cases of containment failures at these town gas storage facilities. Nevertheless, there is a belief that some changes in the composition of the stored gas may have occurred [31].

These experiences from natural gas storage sites have similarities to UHS in terms of geochemical reactivity, providing valuable insights [32]. However, it is important to note that town gas is a mixture of molecules, making it more reactive than pure H_2 and possibly more reactive than H_2 and CO_2. Numerous research projects on UHS have been initiated in the last decade, including:

- **Hychico (Argentina, 2010)**: A pilot site in a **depleted gas reservoir** focused CH_4 production from H_2 and CO_2 using controlled methanogenesis. The project also addressed the adaptation of surface facilities to accommodate H_2. Notably, the injection process involved pure H_2 along with a "Poor" gas mixture (comprising 35% CO_2, CH_4, etc.). The project was supported by experimental studies involving methanogens. Despite the presence of Archean microorganisms, H_2, and CO_2, methanogenesis did not consistently occur, and it was found to be highly influenced by specific experimental conditions [33].

- **HyUnder (Europe, 2012):** Project that stood as a significant initiative that comprehensively examined the primary obstacles to full-scale adoption of UHS [34].

- **H2STORE (Germany, 2012):** This project investigated the feasibility of large scale UHS in porous reservoirs, along with in-situ CH_4 generation processes. The project covered various aspects, including geo-hydraulic, mineralogical, geochemical, and biological processes, gas mixing mechanisms, caprock integrity, and fluid transport properties of reservoir rocks in converted gas fields [35].

- **ANGUS+ (UK, 2013):** A project that explored the pre-feasibility of UHS and methanation in **depleted gas reservoirs**. The project examined the spatial interactions among various subsurface applications. The main goal was to establish the geological foundations for these storage methods, while also taking into account economic, political, and legal factors [36].

- **HyInteger (Germany, 2016):** A follow-up project of H2STORE, focused on microbial metabolism's effects on well integrity and material behavior under corrosive conditions. This project included laboratory experiments and a modelling part.

- **Underground Sun Storage and Sun Conversion projects (Austria, 2016, 2030):** Projects that examined microbial consumption of H_2 during combined storage of natural gas with added H_2 (from green sources) and CO_2 in **depleted gas fields**. If the production of CH_4 in the reservoir is favorable in the context of underground storage of town gas, the loss of H_2 induced by microbial consumption in the presence of CO_2 should be considered not only as a vector of net H_2 loss (partly due to microbial activity) but also as a factor contributing to the decline in H_2 quality in the reservoir (H_2-CO_2 mixture) in the context

of UHS. Interestingly, these projects observed a slight change in effective permeability, which may have been influenced by a concurrent decrease in water saturation.

- **Hystories (Europe, 2020):** Project that investigated H_2 technologies for storage of pure H_2 **in depleted fields or aquifers**.

- **HyUSPRe (Europe, 2021):** This project shares the findings of an evaluation of storage capacity, including an estimate of the potential UHS capabilities in European underground gas storage sites located in **porous geological formations** (mainly Ukraine, Italy, and the Netherlands) .

Currently, H_2 storage is operated in salt caverns. However, aquifers offer very large storage capacities, which will become increasingly essential to meet future demand. The analysis of previous projects underscores that most of these studies have focused on depleted reservoirs rather than aquifers. The concept of UHS in aquifers is still emerging and has not yet been commercially deployed, presenting several technical challenges that require further investigation.

To embark on this exploration, it is crucial to begin by defining the demand profile and the required storage volumes. Once these volumes are established, a valuable next step is to conduct a comparative assessment of various CGs from both technical and economic standpoints. Determining the optimal H_2-CG ratio for each scenario is essential, as aquifer storage necessitates a CG different from pure H_2 itself. Commonly suggested CGs include CH_4, CO_2, and N_2. The volume and viability of the chosen CG play a pivotal role in determining project profitability and overall cost. Furthermore, evaluating the storage integrity of each configuration is imperative.

The impact of geochemical and microbial activity needs to be further investigated, especially in light of the unique molecules and conditions present in the reservoir. The physical and chemical characteristics of UHS differ significantly from natural gas storage, making it essential to understand how these phenomena may affect the safety and economics of the project.

Another critical aspect that requires exploration is storage performance, with injection and production rates considered key parameters to meet demand, closely tied to the purity of the produced gas. The storage of H_2 in aquifers introduces the possibility of loss, irrecoverability, or contamination due to various processes linked to reservoir characteristics and fluid properties. Therefore, a deep understanding of fluid behavior within the reservoir and the mixing processes involved is essential. Achieving this necessitates accurate reservoir modeling that must be both validated and further developed. However, it is worth noting that a lack of in-situ observations, experimental measurements, and the underdevelopment of modeling tools contribute to uncertainties in the outcomes of these models, posing potential risks to safety and project profitability. Additionally, the surface facilities and well infrastructure are integral components to consider in the equation.

The assessment of risks in UHS is currently inadequate, and reliable models for risk assessment and qualification have not yet been established. Some progress has been made, with a few projects investigating risks (such as caprock integrity and H_2 migration) in different geological scenarios and their impact on H_2 storage security. A database employing a Features Events Process (FEP) derived from common risks with other subsurface operations (Nuclear Waste Storage and

CO_2 storage), was created to identify key factors contributing to H_2 leakage. This database offered a comprehensive overview of risks associated with H_2 storage operations [37]. Another study focused on establishing selection criteria for risk assessment methods and aimed to assess the suitability of various risk assessment techniques commonly employed in petroleum and CCS projects for assessing the risks associated with UHS [38]. Consequently, creating a thorough risk assessment technique developed especially for UHS in aquifers remains an ongoing challenge.

Societal acceptance and embeddedness can introduce delays in projects, constituting a challenge that must be addressed proactively. Furthermore, the immaturity of the field, including the lack of cost data, market frameworks, and regulations, can impact project evaluations and increase uncertainties in both *Capital Expenditures* (CapEx) and *Operational Expenditures* (OpEx). Note that CapEx represents the initial investment outlays, including those associated with CG, while OpEx accounts for continuous operational costs from the project's inception.

While identifying lower-risk sites that consider reservoir characteristics, environmental factors, technical feasibility, economic viability, and societal acceptance is still a challenging task, we can work towards validating the concept technically and demonstrating its feasibility. Detailed site selection criteria and evaluation methods were previously explored in the Hystories project for porous rock storage, and these need to be further adapted and developed for aquifer-based storage. This task also brings to the forefront the competition for subsurface and surface space between UHS and other activities and functions.

In summary, this section has reviewed the current state of research in the field and highlighted several research gaps. These gaps lay the foundation for the research undertaken during this PhD, focusing on UHS in aquifers with CO_2 as a CG.

1.5 The thesis aim

In this research, we explore an approach to aquifer-based H_2 storage. In this setup, the aquifer comprises a CG that remains permanently stored, while the WG, which, in this case, is H_2, is injected and recovered during operational cycles. Due to both economic and technical considerations, H_2 storage by itself may not be the most efficient option in aquifers. Therefore, we propose considering H_2 as a WG supported by a different CG.

The idea is to utilize a substantial volume of CO_2 as the CG. CO_2 would play a dual role, acting as a barrier to prevent the migration of H_2 and safeguarding the integrity of the storage. Additionally, the CG would provide essential operational pressure support within the reservoir during the withdrawal of the WG. The use of CO_2 as a CG is essential to enhancing the profitability of UHS by reducing operational costs. The choice of CO_2 as a CG is rooted in the fact that we can use sites already designated for carbon sequestration, where CO_2 is permanently stored to mitigate greenhouse gas emissions. CO_2, in its dense phase, represents favorable physical properties compared to H_2, including differences in density and viscosity. This presents an opportunity to repurpose CO_2 as a CG, not only serving the storage function but also contributing to underground carbon sequestration, aligning with emissions reduction goals. The

concept of using CO_2 as a CG has been previously suggested in compressed air energy storage [39].

Nonetheless, a lingering concern with utilizing an alternative gas like CO_2 as a CG is the potential for mixing with the WG, which could necessitate costly purification processes. Understanding the spreading of the H_2-CO_2 mixing zone is crucial, as this is where methanogenic and/or acetogenic microorganisms may consume H_2 and CO_2 to produce CH_4 and acetate, respectively [8, 40, 41, 42, 43]. However, it is essential to clarify that our study focuses on comprehensively examining the behavior of this system, including the conditions affecting mixing. The microbial aspects mentioned are beyond the scope of this work.

To conduct this study, we employ two simulation tools: a commercial simulator (GEM from Computer Modelling Group CMG) and an open-source code (ComPASS). One of our primary objectives is to develop a thermodynamic model and integrate it into the open-source code, which offers greater flexibility. In reservoir simulations, compositional multiphase flow coupled with detailed physical laws based on equations of state remains an important and challenging problem. Although the *Equation of State* (EoS) of pure gas phase is well documented, the EoS for the gas mixtures is less understood in the reservoir conditions. Moreover, CO_2 may exist in a supercritical state, possessing properties such as liquid-like densities, gas-like viscosities, and diffusivities intermediate between those of liquids and gases. This complexity adds an additional challenge for EoS to accurately predict its behavior. As a result, we devoted a portion of our research to evaluating various viscosity models and density predictions, recognizing the importance of these thermophysical properties in achieving reliable UHS processes.

The key control parameters for evaluating the UHS concept's efficiency include reservoir pressure and temperature conditions, caprock characteristics, well numbers and locations for pumping and withdrawals, recovery cycles, and pressure management to avoid excessive overpressure within the reservoir. We provide a comprehensive overview of potential reservoir conditions, enabling us to assess the state and behavior of the CO_2 - H_2 system. This analysis informs our understanding of static reservoir behavior.

Another critical aspect of this PhD research involves assessing the performance of the storage concept. This assessment depends on both the storage capacity and the ability to recover gas within the reservoir-caprock system. To tackle this task, we utilize the more advanced CMG simulator, enabling us to study the performance of various storage scenarios within a realistic geological model. We also perform a stability analysis of key parameters to identify the optimal operational scenario.

These research's plan will be elaborated upon in the subsequent sections of this thesis.

1.6 The structure of the thesis

In this section, we outline the structural framework of the thesis, providing an overview of the chapters and their respective objectives:

In chapter 2, we employ analytical methods to compare storage capacities in porous reservoirs using H_2 as a CG, as well as denser gases like CO_2, natural gas (CH_4), N_2, or mixtures. We assess caprock capacity, governed by low permeability and entry pressure, and address gas mixing between the CG and H_2. We calculate a practical limit for H_2 injection rates based on reservoir permeability and fluid properties, ensuring operational feasibility.

The following chapters exclude the idea of having other gases than CO_2 and focus only on the main concept of CO_2 as a CG:

Chapter 3 represents the different possible thermodynamic models and selects the cubic EoS and GERG-2008 equations to evaluate their suitability for describing the density behavior of the H_2-CO_2 system. This chapter will also argue the choice of the thermodynamic model to be developed in the open source code ComPASS.

Chapter 4 extends our discussion on ComPASS, the formulation used to solve the thermodynamic equilibrium and phase context. Then we explain the implementation, providing further insights into the development and adaptation of the code to resolve the phase's existence. We finish up with testing the integrated thermodynamic model.

The chapter 5 is a general evaluation of the system's behavior under a spectrum of reservoir temperature and pressure conditions. This chapter introduces different concept of static scenarios, offering predictions for diverse reservoir layering scenarios contingent upon the phases present.

Chapter 6 employs the advanced CMG simulator to conduct comprehensive simulations on a realistic reservoir. These simulations encompass a thorough sensitivity analysis, considering operational, geological, and reservoir-related variables (e.g., injection and production rates, heterogeneity, gas solubility, etc.). Our objective is to evaluate the influence of these factors on the performance of the H_2 storage system, ultimately identifying optimal storage scenarios.

The concluding chapter, chapter 7, synthesizes the key findings and insights from each preceding chapter. Additionally, it provides a forward-looking perspective, offering an outlook on potential applications and developments.

CHAPTER 2

Analytical approaches to UHS capacity assessments, caprock integrity, and front mixing [1]

The implementation of UHS in porous reservoirs requires the use of a CG, whether H_2 itself or a different gas such as CO_2, CH_4, N_2. In the latter case,H_2 mixing with the CG should be minimized to avoid expensive treatment of the back-produced gas. In this chapter, we employ analytical approaches to conduct a comparative assessment of storage capacities within porous reservoirs. We begin by considering a scenario where H_2 is in fact used as its own CG. Subsequently, we extend our analysis to include denser gases, such as CO_2, natural gas (CH_4), and N_2. The equations used in this study can potentially be extended to various gas mixtures. This investigation involves the examination of caprock capacity, which depends on factors such as low permeability and entry pressure.

Additionally, we delve into the critical issue of gas mixing between the CG and hydrogen, exploring basic strategies to minimize this phenomenon. Our analysis provides a simple criterion for calculating the practical limit for H_2 injection rates. This criterion takes into account reservoir permeability and the distinct properties of hydrogen-CG mixtures, including viscosity and density behavior. This limit serves as a benchmark for ensuring the operational feasibility of H_2 storage systems in various types of reservoirs.

2.1 Introduction

Advances in seasonal storage of natural gas and permanent CO_2 storage have paved the way for current research efforts in this area. In the case of storage in porous rocks, the CG, which is the gas that is permanently stored, plays a crucial role in maintaining sufficient pressure for adequate injection and withdrawal rates of the WG, in this study H_2, and preventing brine

[1] This chapter is derived from an article entitled "Mutual benefits of storing H_2 at the crest of CO_2 or other gas storages" submitted to the "Greenhouse Gases: Science and Technology"

production in aquifers [44, 21, 45]. CG is often identical to the WG and represents a significant fraction of the total gas stored, thus impacting the overall investment costs [46]. This is one of the reasons why the use of inert CG different from the valuable WG has been considered, mostly in the context of natural gas storage [47, 48, 20, 49]. A non exhaustive list of possible CG for H_2 storage in underground reservoirs are: the CO_2 captured from flue gases or other industrial gaseous effluents and stored permanently in those reservoirs; the flue gases themselves, emitted from gas- or coal-fired power plants (typically composed of N_2, O_2 and 10-15% CO_2); the natural gas of a seasonal gas storage or a depleted gas reservoir; town gases. In this work, for the sake of simplicity, we start by considering CGs made up of a pure compound (CO_2, CH_4 or N_2), and then extend the results to mixtures of these gases, or to other gases.

In this study, we examine and discuss a storage scheme (see Fig.2.1) in which H_2 is stored at the top of an existing denser CG, itself in contact with an underlying aquifer. The reservoir has top and lateral sealing boundaries: it could be for instance an anticline structure with a dome or crest [50, 51]. Water (or brine) is present as an irreducible phase that wets the pore walls throughout the gas column and connects the seal rock (caprock) to the underlying aquifer, which is initially fully saturated with water. The aquifer is hydrostatically pressured. The vertical well allows injection/withdrawal of the H_2 in the upper region of the reservoir. We consider here storage conditions such that H_2 and the CG are fully miscible. One crucial aspect to consider in this storage scheme is the extent of mixing between the two gas layers. The H_2-CG mixing zone, also referred to as the front, has a tendency to spread over time due to repeated sequences of injection and withdrawal of the H_2. Gas mixing dynamics play a significant role in determining the efficiency and safety of UHS. Thus, the mixing has to be minimized to avoid or limit expensive treatment of the produced gas.

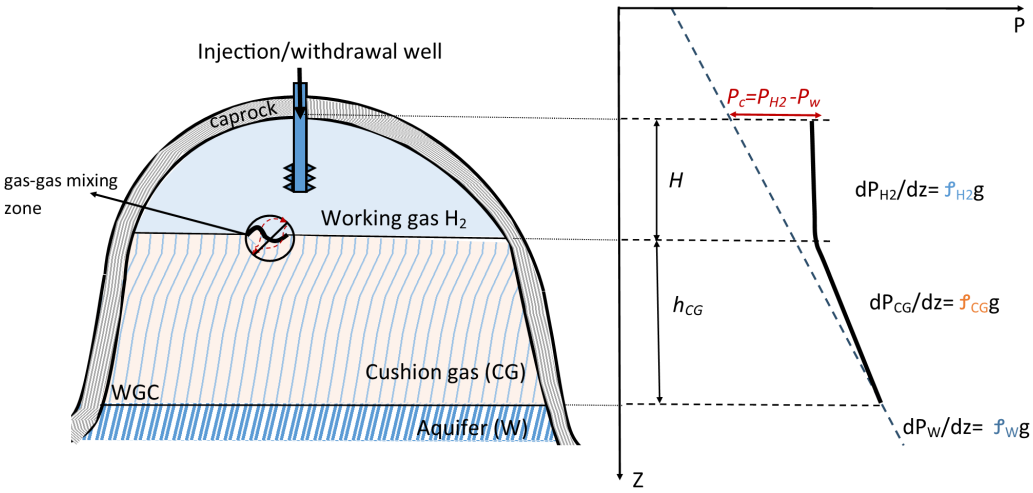

FIGURE 2.1: Pressure profile along the gas stored in the reservoir. The right side profile depicts the water and gas pressure variations with depth, while the left side shows the reservoir structure and storage gas layers.

Two important issues are addressed in this chapter. The first issue is the storage capacity of H_2, specifically focusing on the maximum height at which the H_2 column can be safely stored.

This maximum height is determined by calculating the pressure in the H_2 phase at the top of the gas column, positioned just beneath the caprock. To ensure safety, it is crucial that this pressure remains below the capillary entry or displacement pressure of H_2 into the brine-saturated caprock. Note that the capillary pressure is a measure of the pressure required to force H_2 overcome capillary pressure and displace brine within the caprock's pores. To clarify, the capillary entry pressure is the minimum overpressure in the (non-wetting) gas phase (compared to brine pressure) required for the gas phase to intrude into the seal rock wetted and saturated with brine . The evaluation of the maximum storage height is presented in section 2.3, and it takes into consideration a typical seal rock setting with varying CGs and thicknesses. This analysis assumes limited mixing between the CG and H_2.

Section 2.4 examines the conditions under which the assumption of limited mixing between the CG and H_2 holds true. A simple criterion is derived to determine whether the downward displacement of the CG by H_2 can, despite the unfavorable viscosity contrast, be stabilized by gravity. This criterion depends solely on the reservoir permeability and the density-to-viscosity relationship of H_2-CG mixtures at reservoir conditions. To provide clarity, these two issues are discussed once the relevant fluid/rock properties are presented and discussed in section 2.2.

2.2 Relevant fluid/rock properties.

We first present and discuss the key properties that are relevant to UHS. We initiate the discussion by presenting the densities and viscosities of the pure fluids of interest under typical storage conditions [52]. These conditions encompass a range of pressures P between $5 - 25\,\text{MPa}$ and temperatures T within the $298 - 373\,K$ range, which accurately represents the diverse offshore and onshore storage conditions. Then, we examine the corresponding mixtures that form the H_2-CG mixing zone. We then shift our focus on molecular diffusion, which determines the rate at which a gas-gas mixing zone spreads in the reservoir. This set of properties is needed and used in section 2.4 to assess the extent of mixing between the H_2 and CG layers. Finally, we address the interfacial properties that are relevant to both the safety and storage capacity of the H_2 storage (section 2.3).

2.2.1 Pure fluids' properties

The density of H_2 ranges from 3 to $18\,kg/m^3$ under the conditions we have considered. These values are significantly smaller, often by one order of magnitude or more, when compared to the densities of CH_4, N_2 and CO_2 under the same P and T. As a first approximation, these gases are treated as ideal gases (IG) by their limiting behavior at low pressure (or low density). An approximation in this context is to consider the compressibility factors as equal to 1 or, equivalently, to assume ideal gas behavior. This approximation allows us to reasonably estimate the density, denoted as ρ hereafter, for most of these gases within the specified T and P ranges. Using the IG law, the density is written as the following:

$$\rho \approx \frac{P\,M}{R\,T}, \tag{2.1}$$

where $R = 8.3145\, J/K\, mol$ and M denotes the molar weight of the fluid.

While this approximation offers a convenient and straightforward equation, it is important to note that this law does not hold for supercritical or liquid CO_2. Therefore, in many of the numerical calculations presented in subsequent sections of this chapter, we utilize the GERG-2008 model [53] as a thermodynamic model to predict the densities of both pure fluids and their mixtures. Further details on this model can be found in section 3.4.2.

Consequently, the ratio of CG density to H_2 density is approximately equal to the ratio of their respective molar weights: $\frac{\rho_{CG}}{\rho_{H_2}} \approx 8$ (when CG=CH_4), and $\frac{\rho_{CG}}{\rho_{H_2}} \approx 14$ (when CG=N_2). On the other hand, CO_2 is significantly denser, particularly when it exists as a supercritical fluid (with densities ranging from 400 to $750\, kg/m^3$) and even more so when it is a liquid (with densities in the range of $700 - 950\, kg/m^3$). These substantial differences in density can significantly influence the occurrence of gravity override, a phenomenon where less dense fluids tend to flow at the top of a structure. While the opposite phenomena, known as density underride, is when more dense fluids prefer to flow at the bottom of the structure. This downdip displacement of the denser fluid by the lighter gas H_2 during injection becomes unstable at a critical velocity. Above this critical velocity, gravity override occurs, underscoring the critical importance of comprehending density variations in porous reservoirs [54].

The viscosity of H_2 is not significantly different from that of the CG, except when the CG is supercritical or liquid CO_2. At about $10\, \mu Pa.s$, the viscosity of H_2 is weakly dependent on temperature and almost independent of pressure. At $T = 298\, K$ and $P = 5$ MPa, the viscosity of H_2 is $8.8 \mu\, Pa.s$, while at $T = 373\, K$ and $P = 25$ MPa, it is $10.7\, \mu Pa.s$ [52]. Under similar T and P conditions, viscosities generally range in the increasing order: H_2, CH_4, vapor CO_2, N_2. Whereas, the viscosity of liquid or supercritical CO_2 is 2 to 10 times higher than that of H_2.

The ratio of CG viscosity to H_2 viscosity, denoted $M_r = \frac{\mu_{CG}}{\mu_{H_2}}$, spans the following intervals: $1.35 - 2.1$ (for $CG = CH_4$), $1.7 - 1.9$ (for $CG =$ gaseous CO_2) and $2.1 - 2.5$ (for $CG = N_2$). M_r represents the mobility ratio of a H_2 phase displacing the CG. In general M_r smaller than one results in a stable displacement. When the magnitude of M_r is greater than one, it indicates that there is a high potential for front instability and viscous fingering, particularly in configurations where gravity can be neglected [55].

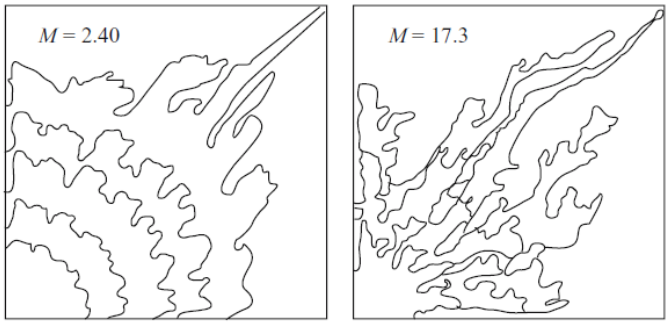

FIGURE 2.2: Displacement fronts for two different values of the mobility ratio in a porous reservoir. The injection point is located at the lower left corner [55].

Fig.2.2 illustrates how the mobility M_r influences the development and configuration of the finger patterns. Viscous fingering is triggered by minor disturbances arising from microscopic variations in the permeability field, even when the porous medium appears uniform on a larger scale [56]. Since the destabilizing influences outweigh the stabilizing ones, these small disturbances persist and grow into significant finger-like structures.

2.2.2 Mixtures of H_2 with CH_4, N_2 or CO_2

As to densities, the same ideal gas law approximation that holds for pure compounds also holds for the corresponding mixtures. Therefore, the density of mixtures such as H_2-CH_4 and H_2-N_2 can be approximated using Eq.(2.1), where M represents the molar-averaged molecular weight, calculated as $M = yM_{H_2} + (1-y)M_{CG}$, with y denoting the H_2 molar fraction and M_{CG} representing the molar weight of the CG. This approximation is also suitable for H_2-rich mixtures of H_2 and CO_2. However, this approximation is not valid for CO_2-rich mixtures: for instance, experimentally, the addition of only 2 mol.% H_2 to pure CO_2 lowers the density by as much as 25% [57]. This is a complexity in the behaviour that is much better accounted for by GERG-2008 equation.

Wilke's equation [58, 59] is a useful method to calculate the viscosity of low-density gas mixtures based on the viscosities of their individual components, μ_{H_2} and μ_{CG}. The equation is given by :

$$\mu_m = \frac{y\mu_{H_2}}{y + (1-y)\phi_{H_2,CG}} + \frac{(1-y)\mu_{CG}}{1 - y + y\phi_{CG,H_2}}, \tag{2.2}$$

with

$$\phi_{CG,H_2} = \frac{\left[1 + {M_r}^{1/2}\left(\frac{M_{H_2}}{M_{CG}}\right)^{\frac{1}{4}}\right]^2}{\left[8\left(1 + \frac{M_{CG}}{M_{H_2}}\right)\right]^{\frac{1}{2}}}, \tag{2.3}$$

or, as proposed by Herning and Zipperer (HZ) [60]

$$\phi_{CG,H_2} = \left(\frac{M_{H_2}}{M_{CG}}\right)^{1/2}. \tag{2.4}$$

The term $\phi_{H_2,CG}$ can be derived by reversing the roles of CG and H_2 in the preceding two equations, and substituting M_r with $1/M_r$ in Eq.(2.3).

Eq.(2.2) provides a reasonably accurate approximation of the viscosity of gas mixtures within the conditions of our study, correctly predicting limits for pure H_2 and pure CG. However, it has its limitations, particularly when dealing with denser gases. For the scope of this research, Eq.(2.2) is adequate for most systems under consideration, with the exception of gas mixtures containing a substantial amount of dense CO_2.

To evaluate the appropriateness of the Wilke model for our specific mixture systems, we conducted a comparative analysis. We compared the Wilke model with other models, including the SuperTRAPP model (or *Extended Corresponding State* (ECS) model) implemented in REFPROP, Dean and Stiel (using Simulis Thermodynamics), and Wilke (HZ). We also considered recent

experimental data for CO_2-rich mixtures ($y = 0.07$ and 0.2) [61]. A more detailed discussion of this analysis is provided in Appendix A.

The overall conclusion from this section is that the ECS model shows potential suitability for describing the viscosity of the system, particularly in the case of CO_2-rich mixtures. However, the Wilke model remains acceptable for all systems except those with a high CO_2 fraction.

The choice to use the ideal gas equation (for density) and the Wilke equation (for viscosity) were primarily driven by their simplicity and ease of integration into the equations used for deriving the analytical stability criterion in section 2.4. This stability criterion, which relies on both density and viscosity, would have been challenging to derive using more complex models like GERG-2008 or SuperTRAPP.

In summary, the low density and viscosity of H_2 can lead to displacement instability, resulting in a low volumetric displacement efficiency due to viscous fingering and gravity segregation. Gravity segregation occurs due to the differences in densities and mobilities between the displacing and displaced fluids. It is worth noting that fingering can result in a large contact area between the H_2 and the other fluid, increasing the mixing zone. On the other hand, gravity segregation can be utilized to maintain the segregation of different gases.

2.2.3 Hydrodynamic dispersion between the H_2 and CG

The hydrodynamic dispersion, D', responsible for mixing is composed of molecular diffusion and mechanical dispersion. Molecular diffusion is considered as a slow phenomena responsible for gas-gas mixing. Mutual molecular diffusion coefficients between two gases describe how the gas-gas mixing zone spreads over elapsed time t in the absence of flow. In a 1D geometry, this spreading is proportional to the square root of $D'\,t$, where molecular diffusion Eq.(2.5) is an essential component, as expressed in Eq.(2.18). D_{diff} is the diffusion coefficient. Typically, D_{diff} is no greater than 1 cm^2/s under near-ambient conditions and in the absence of a solid phase [62, 59]. D_{diff} strongly decreases with increasing pressure, following the relationship $D_{\text{diff}} \approx \frac{C}{P}$, where C is a constant usually below unity (D_{diff} in cm^2/s, P in bar) [59]. In a porous medium, the solid phase hinders fluid motion, and the effective molecular diffusion coefficient, D_m, depends on porosity, saturation state and tortuosity of the rock. D_m is D_{diff} divided by a factor τ, the tortuosity coefficient:

$$D_m = D_{\text{diff}}/\tau. \tag{2.5}$$

The values of τ depends on the degree of heterogeneity. For granular media, τ is typically ≈ 1.4, while for highly heterogeneous media, it can be several units.

Effective gas-gas diffusion coefficients D_m in porous media, are less than 0.01 cm^2/s for the gases and pressures of interest in this study. This corresponds to a front spreading below 1 m over a 10-year period starting with a sharp front at $t = 0$. This front spreading occurs between H_2 and CG CH_4, CO_2 and N_2 that are either at rest or moving very slowly, with no injection or withdrawal of H_2 from the reservoir. Molecular diffusion, which accounts for additional spreading due to fluid motion through the pore space, is analyzed and discussed in next section 2.4. Note

that in the contrast to this phenomena, the mixing due to the movement of the fluids in the porous medium is called mechanical dispersion. The mechanical dispersion coefficient ($D_{\text{disp},L}$ or $D_{\text{disp},T}$), where the subscript L refers the longitudinal direction and the subscript T refers the transverse direction, depends on the velocity, V, and direction of flow. The longitudinal hydrodynamic dispersion composed of these two terms (molecular diffusion and mechanical dispersion) can be formulated as follows:

$$D'_L = D_m + (D_{dispL})^m = \frac{D_{\text{diff}}}{\tau} + (\alpha_L||V||)^m. \tag{2.6}$$

Where α_L is the dispersivity in [m], $||V||$ is the mean interstitial velocities in the principle direction, and the exponent m, empirically found to be very slightly larger than 1, is considered here to be equal to $m = 1$. More details about dispersive phenomena is also examined in the section 6.3.3.3.

2.2.4 Interfacial properties

The trapping of a non-aqueous phase beneath the seal rock, typically a tight porous medium saturated with brine, primarily occurs due to capillary forces. For this phenomenon to be effective in preventing the non-aqueous phase (gas) from leaking, the *Interfacial Tension* (IFT) between the aqueous and non-aqueous phases, noted as $\gamma_{w,nw}$, needs to be sufficiently high. Additionally, the porous rock must remain wetted by water, which means that the contact angle, θ, at the triple (mineral/brine/non-aqueous phase) line must remain low, influencing the seal's effectiveness in retaining the stored gas, as illustrated on the left side of Fig.2.3. For instance, a high IFT and low θ promote the formation of a stable non-aqueous phase beneath the seal rock, effectively sealing the gas. In contrast, low IFT or unfavorable θ can jeopardize this stability, leading to gas migration and potential leakage.

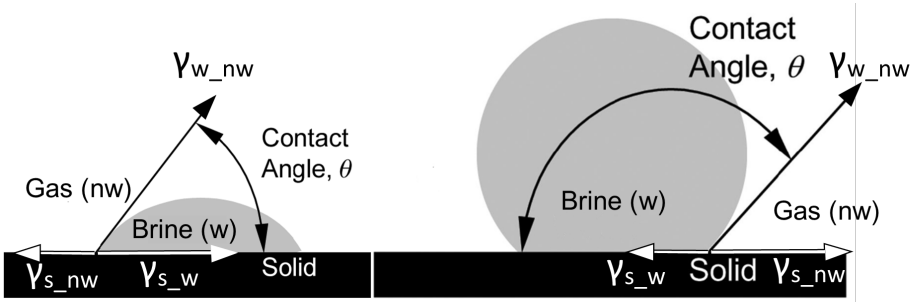

FIGURE 2.3: Two fluids exhibiting different wettability: Left represent the water-wet case, whereas the right is the water dewetting example. The contact angle serves as an inverse measure of wettability (modified after [63]).

Extensive experimental efforts have been undertaken over the past two decades to characterize these two interfacial properties, $\gamma_{w,nw}$ and θ , using various non-aqueous phases such as CO_2, N_2, CH_4 and, more recently, H_2. Typical values of γ_{w,CO_2} range from 20 to 35 mN/m under reservoir conditions. Notably, these values are significantly lower (about half) compared to the values measured for CH_4, N_2, or H_2 under similar conditions [64, 65, 66, 67, 68, 69]. Likewise,

CO_2 exhibits the most pronounced alteration of the water-wet character of typical seal rock minerals [70, 71, 72], compared to other CG or pressurized H_2. These observations are derived from contact angle measurements, conducted using techniques like the tilted plate technique [73] or the captive bubble method [74, 75, 76]. Furthermore, IFTs and contact angles can be inferred from capillary pressures obtained through two-phase (water and H_2) corefloods experiments or mercury injection tests. The results from these experiments are found to be consistent with the directly measured IFTs and contact angles [24].

In summary, IFT and θ are fundamental parameters that define the safety, stability, and efficiency of gas storage systems. These properties directly influence sealing mechanisms and gas migration within the reservoir. Recent studies have attempted to investigate the effect of CO_2 as a CG on the IFT of the (brine - H_2 - CO_2) system at reservoir conditions using the pendant drop technique [77], while others have explored $\gamma_{rock,gas}$ [78, 79]. It is worth noting that these studies are relatively recent, and not included in this work. This area of research remains active, and ongoing investigations are expanding our understanding of IFT properties in gas storage systems.

2.3 Assessment of caprock integrity and storage capacity: cushion gas effects

A successful UHS is based upon several crucial factors, including caprock integrity and storage capacity, both being closely related. Caprock integrity ensures that the stored gas remains contained within the reservoir, preventing migration or leakage. Additionally, understanding storage capacity is essential for optimizing the efficiency of the reservoir. In this section, we provide an assessment of caprock integrity and UHS capacity in presence of a CG (CO_2, H_2, and CH_4). We start by evaluating the capillary entry pressure in the presence of H_2 compared to other gases. This sets the stage for the subsequent methodology section, where we present the equations utilized to calculate storage height concerning different CGs. The impact of CGs on storage capacity is discussed in the results and discussion section.

It is reminded here that trapping of a non-wetting phase under a brine-saturated rock is ensured as long as the pressure in the non-wetting phase (P_{nw}) does not exceed that in the brine (P_w) by a quantity equal to the capillary entry (or displacement) pressure of the non-wetting phase into the seal rock, which from Laplace equation is equal to

$$P_{ce,nw} = P_{nw} - P_w = \frac{2\gamma_{w,nw}cos(\theta)}{R} \ . \tag{2.7}$$

where R is representative of the largest pore thresholds in the seal rock.

As stated in the section above, the water/H_2 IFT is significantly higher than the other gases like water/CO_2 IFT and caprock minerals are more water-wet in presence of H_2 than in presence of CO_2 [80, 81]. A straightforward consequence of these physical differences is the potential enhancement of the caprock sealing and therefore the safety of UHS. When considering the storage of pure CO_2, if the upper portion of the CO_2 column is replaced or mixed with one of the

gases mentioned (CH_4, H_2), the IFTs in contact with the caprock will increase compared to the IFTs of pure water and CO_2. This increase in IFT improves the sealing efficiency of the caprock, as it raises the capillary entry pressure Eq.(2.7). A similar conclusion can be drawn, although to a lesser extent, when injecting H_2 at the top of reservoirs with other gases for example a CH_4-bearing reservoir.

In the context of UHS in porous media, the addition of H_2 to the top of a gas column leads to an increase in the height of the stored fluid, resulting in an elevation of the buoyancy pressure. This pressure differential arises from the difference in densities between water and the stored gas, considering that water remains as an irreducible phase alongside the gas. The maximum pressure is encountered at the top of the column, and this pressure must not exceed the capillary entry pressure of H_2 into the seal rock to maintain the gas's containment. To calculate this pressure and analyze the scenario, certain assumptions are made. It is assumed that there is limited spreading of the mixing zone between H_2 and the CG during the storage period of H_2. This assumption is considered valid for permeable and homogeneous reservoirs, as discussed in section 2.4.

Fig.2.1 illustrates this situation by presenting profiles of water and gas pressures versus depth. The dashed and solid lines represent the water (or brine) pressure and gas pressure, respectively. The kink in the gas pressure profile corresponds to the change in gas density ρ_g as the profile crosses the H_2/CG mixing zone. The slope of the gas pressure versus depth z follows the hydrostatic law: $\frac{dP_g}{dz} = \rho_g\, g$, which is much lower than the water pressure gradient $\frac{dP_w}{dz} = \rho_w\, g$. The difference between these two pressures, known as capillary pressure, defines the overpressure in the gas (non-wetting) phase compared to the water. This overpressure also represents the buoyancy pressure and depends on the gas pressure profile down to the *Water-Gas Contact* (WGC). The overpressure in the gas phase is at its maximum at the top of the gas column, just below the brine-saturated seal rock. For the stored H_2 to remain trapped in the reservoir, it is essential that this overpressure does not exceed the capillary entry (or displacement) pressure of H_2 into the seal rock Eq.(2.8). This relationship ensures the integrity and safety of the storage system.

$$P_{ce,H_2} = \frac{2\gamma_{w,H_2} cos(\theta)}{R}\ . \tag{2.8}$$

This pressure can be determined experimentally or estimated using measurements conducted with a more convenient gas, such as N_2, or by performing mercury intrusion measurements, and then using the relation

$$P_{ce,H_2} = \frac{P_{ce}\,\gamma_{w,H_2}\,cos(\theta)}{\gamma'\,cos(\theta')},$$

where γ' and θ' are the IFT between brine and the non-wetting phase (either N_2 or liquid mercury), and the contact angle in the wetting phase, respectively. The contact angle is often assumed to be equal for two different water/gas systems and has a typical value of 40° for liquid mercury and its vapour.

2.3.1 Methodology

To assess the impact of CGs on storage capacity, we consider various scenarios involving different CGs. We first consider a scenario in which the entire gas column consists of H_2, part of it serving as a CG that is not counted in the storage capacity as depicted at left of the Fig.2.4.

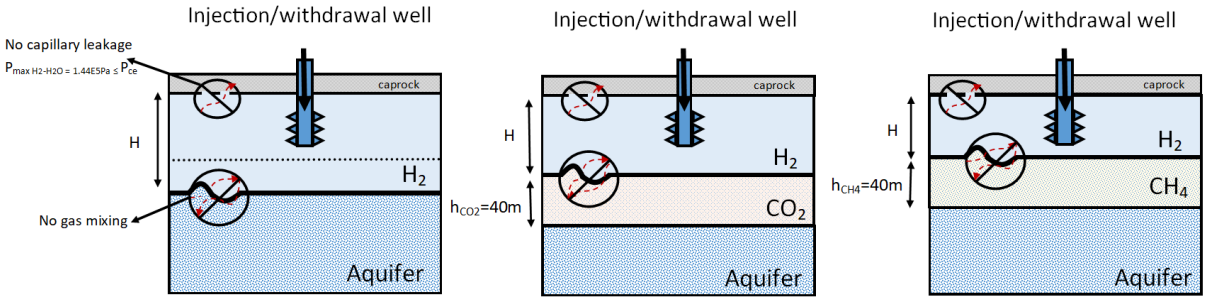

FIGURE 2.4: H_2 storage schemes with different CGs: Left scheme represents the scenario where only H_2 is stored. In Scenario 2, depicted in the middle, CO_2 serves as the CG. On the right scenario 3 shows CH_4 acting as the CG. Each scenario represents the maximum height (H) for safe H_2 storage beneath the seal rock.

Other configurations with other CGs will be compared, the middle and right scheme in the Fig.2.4 respectively for CO_2 and CH_4. The goal is to evaluate how the choice and the height of CG affects the maximum height (H) of safe H_2 storage beneath the seal rock.

We make the assumption that the reservoir is permeable enough (k larger than 100 mDarcy) to disregard the difference between the water-gas contact (WGC -the maximum depth where free gas is present) and the *Free Water Level* (FWL), defined as the depth where pressure in the water phase is equal to the pressure in the other, the gas phase. Thus, there is no free gas at the FWL, and it is located slightly below the WGC. At the FWL, the pressure in the brine phase equals the gas pressure extrapolated to below the WGC. Given these assumptions, the maximum height of H_2 (H) that can be stored safely in the aquifer is calculated as follows:

$$H = \frac{P_{ce,H_2}}{g(\rho_w - \rho_{H_2})} \ . \tag{2.9}$$

The value of H is determined by the competition between two adverse pressures: the buoyancy pressure that causes the gas to rise, and the capillary entry pressure of the caprock. The capillary entry pressure of H_2 into the seal rock, is given by Eq.(2.8). This equation is applicable to any gas, and particularly to CO_2, provided that the entry pressure and density of the stored gas are used instead of those of H_2 (e.g., CO_2 [82, 83]).

When a CG other than H_2 is used, as depicted in Fig.2.1, the height of H_2 can be calculated using the following equation:

$$H = \frac{P_{ce,H_2} - (\rho_w - \rho_{CG})g h_{CG}}{(\rho_w - \rho_{H_2})g} \ . \tag{2.10}$$

h_{CG} refers to the CG height. Eq.(2.10) is equivalent to Eq.(2.9) when the effective capillary entry pressure is P_{ce,H_2} minus the buoyancy pressure exerted by the CG: $(\rho_w - \rho_{CG})g\, h_{CG}$. If

the CG is made up of H_2, then the aforementioned equation is equivalent to Eq.(2.9) with the replacement of H by the total of H_2, which is $H + h_{CG}$.

It is important to note that in all these calculations, we have assumed complete wetting of the caprock minerals by water or brine, i.e., $\theta = \theta'$. The capillary entry pressure, P_{ce,H_2}, has been corrected for T and P that differ from T_{ref} and P_{ref} by considering this equation:

$$P_{ce,H_2}(T,P) = P_{ce,H_2}(T_{ref},P_{ref})\frac{\gamma_{w,H_2}(T,P)}{\gamma_{w,H_2}(T_{ref},P_{ref})} \ . \tag{2.11}$$

The values of $\gamma_{w,H_2}(T,P)$ used in this equation are obtained from recent measurements in the temperature range of 298 to 372 K and pressure range of 5 to 25 MPa, which are within the range of interest for our calculations [68].

2.3.2 Results and discussions

In this section, we present the findings from our analysis of H_2 storage capacity with different CGs and a chosen CG height of 40 m. The study considered various gases, pressures and temperatures to assess the impact of CG density and temperature on storage capacity.

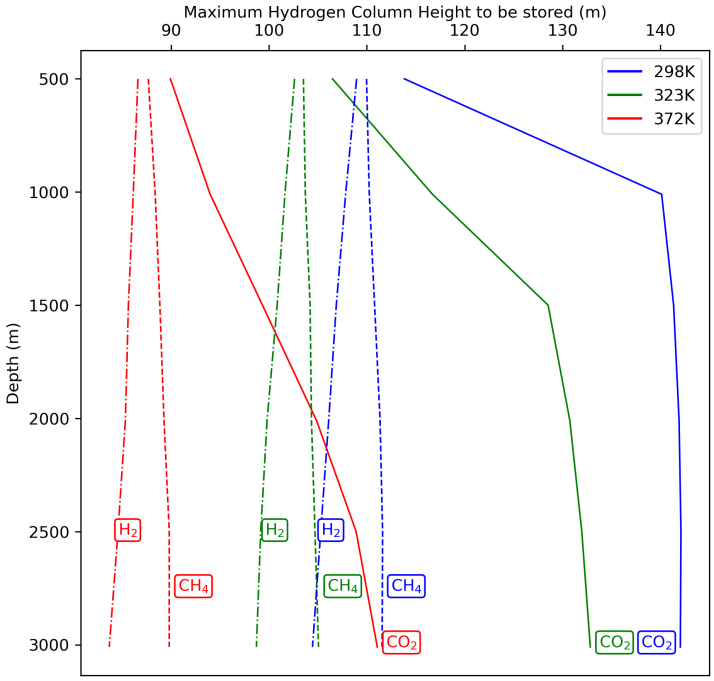

FIGURE 2.5: H_2 storage heights H at various reservoir pressures from 5 to 25 MPa (following the hydrostatic gradient 100m = 1MPa) and temperatures $T = 298\,K$ (blue for cold reservoirs), $T = 323\,K$ (green for warm reservoirs) and $T = 298\,K$ (red for hot reservoirs), calculated by Eq.(2.10) using the water/H_2 IFTs measured by Chow et al. [68] and the densities available on the NIST web site. Cushion gas height is of $h_{CG} = 40\,m$. Densities are considered constant over the whole gas column. Conditions of partial mixing of CO_2 and H_2 are not considered.

Fig.2.5 displays the maximum heights, H, of H_2 that can be safely stored, considering a CG with a height of $h_{CG} = 40\,m$. The storage height was calculated for a range of pressures from

5 to 25 MPa and three temperature scenarios: $T = 298\,K$ for relatively cold reservoirs, $372\,K$ for hot reservoirs, and $323\,K$ for warm reservoirs. The selected seal rock has an entry pressure, $P_{ce,H_2} \approx 1.5$ MPa at reference conditions, where $T_{ref} = 298\,K$ and $P_{ref} = 5$ MPa, corresponding to a hydrostatically-pressurized reservoir with a water depth of 500 m.

The study reveals an order in H_2 storage capacity with different CGs. Notably, when H_2 is stored with a CG, the maximum storage capacity is observed with CO_2, followed by CH_4, and H_2 itself. Note that when H_2 is used as a CG for itself, the storage capacity is the smallest, as the CG height must be subtracted from the total storage height.

The importance of CG density in determining H_2 storage capacities cannot be overstated. Fig.2.5 demonstrates that the storage capacity of H_2 is significantly influenced by the density difference between the aqueous phase and the CG. Since H_2 is the lightest of all the considered CGs, using it as a CG for itself results in the smallest storage capacity. In contrast, when denser gases such as CO_2 are used as the CG, storage capacity is significantly higher. This effect is especially pronounced at lower or moderate temperatures when carbon dioxide can exist as a dense liquid or supercritical fluid. Temperature is another crucial factor affecting H_2 storage capacities. Storage capacity decreases with rising temperature, primarily due to the dominant influence of the IFT between brine and H_2. The change in temperature results in variations in brine/H_2 IFT, further affecting the storage capacity.

To put these findings into perspective, we can express storage capacity in terms of energy per unit area (e.g., $A = 1\,km^2$) through the following expression:

$$\text{Energy per area } E = \rho_{H_2} e H \ . \tag{2.12}$$

This provides a more comprehensive view of the energy storage potential. The gravimetric energy density of H_2, e, is equal to $120 kJ/g$ [52].

In conclusion, this study highlighted that CG density and the reservoir temperature significantly impact UHS capacity. The choice of CG significantly impacts the available storage capacity, with denser gases, such as CO_2, offering the highest capacity, followed by CH_4. H_2 as a CG for itself has the lowest storage capacity.

This methodology provides valuable insights for UHS, where optimizing caprock integrity and storage capacity is essential. However, it is important to acknowledge that these calculations are based on various simplifications and further sophisticated modelling is required to validate these outputs.

2.4 Spreading of the gas-gas mixing zone

The spreading of the gas-gas mixing zone is primarily due to dispersive phenomena, as discussed in the section 2.2.3. Mechanical dispersion is an unavoidable factor in this process. However,

the extent of mixing can be minimized by preventing viscous fingering. Achieving this involves careful consideration of velocity rates during downward vertical displacements of the denser CG (CO_2, CH_4 or N_2) by H_2 injected in upper positions in the reservoir. The first part of this section focuses on calculating the rate conditions required for this displacement. In the second part, we delve into the inescapable mixing caused by hydrodynamic dispersion and the consequent spreading of the mixing zone over time. This section provides essential insights into the extent of mixing zone spread, which can be utilized to optimize injection strategies and mitigate the adverse effects of gas-gas mixing.

2.4.1 Rate conditions for viscous fingering avoidance (front stability)

Despite having a mobility ratio larger than 1, as discussed in section 2.2.4, the favorable density contrast, where H_2 is lighter than the CG, acts as a barrier against viscous fingering. This holds true as long as the injection rate of the H_2 is maintained at a sufficiently low level. The rate conditions for immiscible displacements, such as H_2 displacing water, are well-established, as outlined by Paterson (1983) [84].

In the case of a downward displacement of a given fluid by another immiscible, lighter, and less viscous (or more mobile) fluid, stability is maintained when the Darcy velocity does not exceed a critical value. This critical value, denoted as U_{im}, is determined by the following equation:

$$U_{im} = \frac{g\Delta\rho}{\Delta(1/\lambda)}, \tag{2.13}$$

Here, g is the acceleration due to gravity, $\Delta\rho = \rho_w - \rho_{H_2}$ is the density difference between the displaced and displacing phases (brine and H_2), and $\Delta(1/\lambda)$ is the difference between the inverse mobilities of the two phases, brine (w) and gas. For H_2 displacing brine, $\Delta(1/\lambda)$ can be expressed as:

$$\Delta(1/\lambda) = \frac{1}{\lambda_w} - \frac{1}{\lambda_{H_2}} = \frac{\mu_w}{k_w} - \frac{\mu_{H_2}}{k_{H_2}}$$

Where $k_w = kk_{rw}$ and $k_{H_2} = kk_{rH_2}$ are the permeabilities of brine and H_2 on the brine-rich side and on the H_2-rich side of the front, respectively.

We calculated critical downward velocities U_{im}, using the relative permeabilities k_{rw} and k_{rH_2} recently measured by Yekta and coworkers [24] in a $k = 50$ mDarcy sandstone under various (shallow and deep) storage conditions. These velocities range from a few centimeters to tens of centimeters per day, which corresponds to acceptable volumetric injection rates $Q < SU_{im}$. Here, S is the area of the water/H_2 contact, which is assumed to be horizontal. However, if the contact makes an angle α with the horizontal (dip angle), the right-hand side of the equation should be multiplied by $\cos(\alpha)$.

The classical result described above [85] is obtained by analyzing whether a small protrusion at the front between the displacing (upper) and displaced (lower) phases is suppressed or amplified, i.e., whether the front is stable (no fingering) or unstable (fingering occurs). In the stable situation the pressure gradient is smaller in the upper phase than in the lower phase, and in the unstable situation, the gradient is larger. The critical velocity U_{im} mentioned earlier is determined by the

condition in which both gradients are equal. If the velocity is below this critical value, the front is stable, and if it is above, the front is unstable, leading to fingering.

When the two phases are completely miscible but mixing between them is disregarded, meaning that the gas/gas front remains sharp, Eq.(2.13) can be simplified to:

$$U_{im} = kg\frac{\Delta\rho}{\Delta\mu}, \tag{2.14}$$

Where $\Delta\rho = \rho_{CG} - \rho_{H_2}$ and $\Delta\mu = \mu_{CG} - \mu_{H_2}$ are the density and viscosity differences between the two immiscible phases.

However, because the gas/gas front is not completely sharp and there is a transition zone where fluid composition gradually changes from pure H_2 at the top to pure CG at the bottom, the reasoning should be applied to any porous layer of thickness dz and to the layer below it [86]. As a result, the stability condition is $U < U_m$ with:

$$U_m = kg\left(\frac{d\rho}{d\mu}\right)_{min} = kg/\left(\frac{d\mu}{d\rho}\right)_{max}. \tag{2.15}$$

Here, $(\frac{d\rho}{d\mu})_{min}$ represents the minimum value of $\frac{d\rho}{d\mu}$ when fluid composition varies over the gas-gas mixing zone. This condition is more stringent than the stability condition for immiscible displacement ($U_m < U_{im}$). Dumore [86] first derived this condition for miscible liquid/liquid (oil/solvent) displacements and observed that $(\frac{d\rho}{d\mu})_{min}$ is achieved when the fraction of the most viscous liquid (i.e., oil) is maximum, meaning that the onset of instability occurs in the bottom part of the miscible front.

A simple analytical expression is obtained for the maximum downward velocity U_m that ensures front stability during H_2 injection sequences and can be expressed as:

$$U_m = \frac{kgP}{RT}\frac{M_{CG} - M_{H_2}}{\mu_{CG}/\phi_{CG,H_2} - \mu_{H_2}\phi_{H_2,CG}}. \tag{2.16}$$

This expression is obtained by writing $\frac{d\rho}{d\mu}$ as the quotient of $\frac{d\rho}{dy}$ and $\frac{d\mu}{dy}$, where y is the H_2 molar content of the H_2-gas mixture of interest. It assumes that densities and viscosities are approximated by the ideal gas law and Wilke's model, respectively, and that the minimum value of $\frac{d\rho}{d\mu}$ over the interval of fluid compositions occurs for $y \to 1$, i.e., in the upper, H_2-rich part of the mixing zone (discussed next). U_m is proportional to the permeability k of the reservoir. It is a fraction of the value in the absence of mixing, $U_{im} = kg\frac{\rho_{CG}-\rho_{H_2}}{\mu_{CG}-\mu_{H_2}}$ Eq.(2.14):

$$\frac{U_m}{U_{im}} = \frac{M_r - 1}{\frac{M_r}{\phi_{\mathrm{CG},H_2}} - \phi_{H_2,\mathrm{CG}}}. \tag{2.17}$$

The ratio U_m/U_{im} thus depends only on fluid properties and not on reservoir properties.

Tables 2.1 and 2.2 provide values of $\frac{U_m}{U_{im}}$ and U_m as calculated from Eqs.(2.16) and (2.17) at the limits of the temperature and pressure intervals chosen in this study, obtained within the above low-density approximation (IG+Wilke model). We consider a range of T and P from

Table 2.1: The ratio of U_m to U_{im} calculated for different CGs and T and P conditions, obtained within the low-density approximation (IG+Wilke model).

Temp(K)	298	298	373	373
Pressure (MPa)	5	25	5	25
H_2-CO_2	0.119	0.453	0.121	0.241
H_2-CH_4	0.173	0.340	0.175	0.268
H_2-N_2	0.196	0.242	0.196	0.224

Table 2.2: Maximum velocity U_m (m/day) for a stable downward displacement of various cushion gases (CO_2, CH_4, and N_2) displaced by H_2 for various T and P conditions. Reservoir permeability $k = 1$ Darcy.

Temp (K)	298	298	373	373
Pressure (MPa)	5	25	5	25
$H_2 - CO_2^*$	1.64	3.63	1.61	3.21
H_2-CH_4	1.45	3.75	1.94	2.97
H_2-N_2	0.88	3.07	1.98	2.26

* The values in the first row of the table are approximate and further discussed and corrected in the subsequent table (see Table 2.3).

298 to 373 K and 5 to 25 MPa, representative of various storage conditions, from shallow cold (offshore) reservoirs to deep and hot (onshore) reservoirs

The values of U_m lies in the range of a few meters per day (m/day) in reservoirs with permeability $k = 1$ Darcy. In reservoirs with permeability different than 1 Darcy, the value of U_m must be multiplied by the number of Darcies of the reservoir. These values are considerably higher than practical flow rate values, including when the front angle α is high and approaches 90°. To provide an example, we consider an aquifer spanning an area of 1 km^2 with 10 wells, each injecting about 100 000 Nm^3 of H_2 per day (which is equivalent to 20 000 m^3 of H_2 per day at reservoir conditions with $P \approx 5$ MPa) against a CG comprising CH_4 or N_2. In this case, the H_2 Darcy velocity is about $U = 2$ cm/day, which is about two orders of magnitude below the limit U_m (see Table 2.2 for exact values). If the mixing front is not horizontal, the above values of U_m must be multiplied by $cos(\alpha)$. It is noteworthy that while there appears to be no clear trend with T, U_m increases with pressure, indicating that the front might be more stable at higher pressure.

However, these calculated values are based on the following approximations: i) approximating the densities and viscosities of the mixtures with H_2 using Eq.s (2.2) and (2.3) is justifiable, and ii) $\frac{d\rho}{d\mu}$ is a monotonically decreasing function of y. First approximation, the two expressions for density and viscosity are valid for low-density gases. This approximation provides fairly accurate predictions for all H_2-CG mixtures of interest but it should not be used under high pressure conditions and/or when a CO_2 CG is supercritical or liquid. To that end, more accurate models have been used to calculate $d\rho/d\mu$ and its minimum value for the three mixtures and the T and P conditions of interest, namely the GERG-2008 [53] for densities and models for viscosities that

are presented and discussed in the Appendix.A.1. These results are presented in the Table.2.3. As to the H_2-CH_4 and H_2-N_2 mixtures, the density vs. viscosity behaviors and the velocity limits are found to be very close to those listed in Tables 2.1 and 2.2. As to the H_2-CO_2 mixtures, the previously used IG models fail to predict densities, especially for low H_2 molar fractions y in the mixture, a feature that is much better accounted for by GERG-2008 equation [53]. Likewise, Eq.(2.2) does not account for the viscosities of CO_2-rich H_2-CO_2 mixtures, as is easily checked by comparison with recent experimental data [61]. Alternative, more accurate viscosity models have been employed in this work for all H_2-CG mixtures investigated, including the SuperTRAPP model, the Dean and Stiel model, and Wilke's model with a Herning-Zipperer exchange coefficient. These models are presented and discussed in the AppendixA.1. The GERG-2008 and SuperTRAPP models have been used to update the U_m values presented and compared within the IG+Wilke models in Table 2.3. Interestingly, the IG+Wilke models provide values of U_m in the same range as those obtained with the more accurate (GERG-2008+SuperTRAPP) models.

These models also were used to check the second approximation, if the $\frac{d\rho}{d\mu}$ is a monotonically decreasing function of y. Some of the results, for H_2-CO_2 mixtures, are depicted in Fig.2.6, where $kg\frac{d\rho}{d\mu}$ is represented over the whole interval of compositions y for four different sets of temperatures and pressures. It was observed that the quantity $kg\frac{d\rho}{d\mu}$ exhibits distinct behaviors under varying pressure and temperature conditions. At a lower pressure of 5 MPa and temperatures of $298\,K$ and $372\,K$, $kg\frac{d\rho}{d\mu}$ decreases monotonically with y. In these cases, the minimum is located at $y = 1$ indicating that instability is initiated in the upper region of the mixing zone.

However, the situation changes when the pressure is elevated to 25 MPa. Under these higher pressure conditions, $kg\frac{d\rho}{d\mu}$ exhibits a different pattern with a maximum in the interval $y = [0, 1]$. The location of the global minimum depends on temperature: for the isotherm at $298\,K$, the global minimum is situated at $y = 0$, while for the isotherm at $372\,K$, it is at $y = 1$. When the minimum is located at $y = 0$, it means that if the fluid velocity reaches or slightly exceeds the limit U_m, the fingering process is initiated in the bottom, at the CO_2-rich part of the mixing front.

Table 2.3: The limit velocity, U_m, calculated for the system H_2-CO_2 mixtures at various T and P conditions using the low-density approximation (Wilke+IG) and the more exact GERG2008 model for densities with SuperTRAPP model for viscosities.

Temp(K)	298	298	323	323
Pressure (MPa)	5	25	5	25
Wilke+IG	1.64	3.63	1.61	3.21
SuperTRAPP+GERG2008	1.03	3.71	0.92	4.51

Based on these observations, when the CO_2 CG is in a liquid or supercritical state, the behavior of the system exhibits similarities to miscible liquid/liquid (e.g., oil/solvent) systems: When U reaches the limit value U_m, the onset of instability occurs in the lower part of the mixing zone [86]. However, in all other cases where both CG and H_2 are gases (including dense gases), the instability sets in the upper region of the mixing zone where H_2 is the fluid saturating the

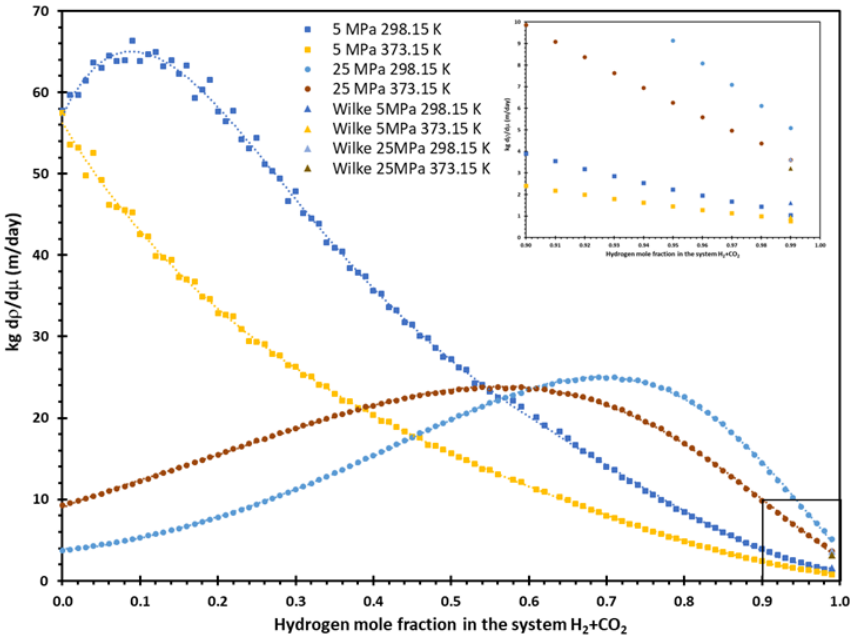

FIGURE 2.6: Values of $k\,g\frac{d\rho}{d\mu}$ as a function of the molar H_2 content y in the CO_2-H_2 mixtures for various temperature and pressure conditions. Densities are those of the GERG-2008 model [53]. Viscosities values are determined using the SuperTRAPP model [87, 88, 89].

porous medium. A more detailed description of how instability and fingers develop once they have been initiated goes beyond the scope of this study.

A general comment is in order here. Density increases with viscosity in very different manners for contrasted gas/gas and liquid/liquid mixtures as composition of the mixture changes. At given T and P, the density of two contrasted gases may differ by one order of magnitude or more, whereas their viscosity ratio rarely exceeds 2 or 3: this is for instance the case of H_2 and the CGs of interest here (see section 2.2). However, two liquids, one viscous and dense and the other lighter and less viscous, usually exhibit a limited density difference (say, a factor ≤ 2) yet their viscosities may differ by orders of magnitude. Stated otherwise, much larger values of $\frac{d\rho}{d\mu}$ are expected as composition varies in gas/H_2 mixtures than in oil/solvent mixtures. Gas/H_2 fronts are therefore expected to be stable for a range of H_2 velocities or injection rates, and/or over a much larger range of reservoir permeabilities and inclination angles α, and to be much larger than that of liquid/liquid fronts. This is one of the most important results of this study, and a strong argument in favor of storing H_2 on top of a denser, more viscous gas acting as a CG.

The scenario where CO_2 is utilized as a CG in low-temperature reservoirs (with T in the range of $298\,K$) does not correspond to full miscibility between the two phases. In a pressure range near the CO_2 critical pressure (around 7.3 MPa) that increases as the temperature decreases, CO_2 and H_2 do not mix completely and instead form two separate phases: a CO_2-rich (liquid) phase and an H_2-rich (gaseous) phase [90]. This phase separation takes place for relatively high overall CO_2 contents, such as at the base of the H_2-CO_2 front (refer to chapter5). The implications of this phase separation on the stability and extent of the H_2-CO_2 front are worth exploring in further research, although such an investigation is outside the scope of this study.

The above approach, Eq.(2.15) to (2.17), can be easily extended to any WG-CG pair by substituting the density, molar weight and viscosity of the WG at storage conditions to those of H_2. If the WG and CG are not pure components but mixtures of components, then the densities, molar weights and viscosities of the corresponding mixtures must be used in these equations instead of those of the H_2 phase and CG.

It is worth reminding that capturing the fingering instability described above by means of numerical reservoir simulations is a task that requires the use of fine grids and complex finite difference schemes. Additionally, introducing some "noise" or irregularities in the permeability field is necessary [91]. Besides finger selection when the instability arises is another issue that is not addressed here. This selection is obtained by determining the wavelength of maximum amplification in a Fourier analysis of the front deformation. This width is expected to depend on various parameters, such as dispersion and the variations of viscosity with density in the mixing zone [92].

2.4.2 Front spreading by hydrodynamic dispersion

When the injection rate satisfies the conditions established in the previous subsection for stable displacement, dispersion is the main factor responsible for front spreading. Dispersion is defined for one phase with a gradient of tracer molecules; this is referred to as tracer dispersion. However, it can also be defined for two miscible phases that may differ in density and viscosity, as long as the concentration or composition profile in the mixing zone can be described by a convection-dispersion differential equation. This is the case in practice whenever the front is stable (no viscous fingering). Although data on dispersion coefficients are scarce, the available information [93, 94, 95], mostly acquired with miscible liquid/liquid systems [94, 95], indicates that dispersion coefficients are similar, or even reduced (relative to tracer dispersion coefficients) when buoyancy is significant compared to viscous forces [94]. Therefore, we assume that the dispersion of a stable H_2/CG front is similar to tracer dispersion, even though the densities and viscosities of the two phases (H_2 and CG) are contrasted.

The longitudinal tracer dispersion is controlled by molecular diffusion at low flow rates U, and by the heterogeneities of the porous medium at high U (for large Peclet numbers). The expression of D' that characterizes the dispersive spreading of the front, Eq.(2.6), has been presented and discussed in the previous section 2.2. The longitudinal dispersivity α_L, which is approximately equal to the length scale of permeability heterogeneities, is typically small (on the order of a few grain sizes) for homogeneous granular media but can be much larger in real reservoirs, especially when they are heterogeneous. Tracer tests conducted in-situ, such as push-pull tests, can provide practical means of determining α_L. This condition is met for dispersivities α_L in the meter range and practical injection rates ranging from a few centimeters to decimeters per day. Assuming, that H_2 withdrawn or injected at rates of U and $-U$, respectively, the extension $Z(t)$ of the H_2/CG transition zone is expected to increase with the time t spent during those sequences as follows:

$$Z(t) \approx \sqrt{D'_L t} \approx \sqrt{(D_m + \alpha_L |U|)t} \approx \sqrt{(\alpha_L |U|)t} \ . \tag{2.18}$$

If molecular diffusion is neglected (high enough Peclet numbers), the quantity $Z(t)$ is proportional to the square root of the cumulative volume circulated over the time t, which is $|U|t$ the sum of the injected and withdrawn H_2 (both counted positively).

For continuous injection and withdrawal operations without shut-in periods, and with $|U| \approx 1$ cm/day and $\alpha_L \approx 1$ m, the extension of the H_2/CG mixing front after one year does not exceed a few meters. One approach to reduce the contamination of produced H_2 is to consider that some of the H_2 (i.e., the bottom of the H_2 column) is part of the CG. This approach is implemented in some natural gas aquifer storage, where the CG is comprised of natural gas at the top and another inert gas (e.g., N_2) at the bottom [47].

2.5 Conclusion

The stability and dispersion of miscible fronts between H_2 and various CGs have been analyzed in storage configurations where H_2 is stored on top of the CG in laterally- and top-bounded reservoirs. These fronts turn out to be stabilized by gravity in a wide range of injection rates, with a maximum rate that depends only on reservoir permeability, the inclination angle of the front with respect to the horizontal, and how the density and viscosity of the H_2-CG mixtures are related. This relation controls the onset and presumably the development of the instability that occurs when this maximum rate is reached or exceeded in the upper, H_2-rich region of the front - one exception is when the CO_2 is supercritical. The analysis shows that these fronts remain stable in a large range of medium-to-high permeability and homogeneous reservoirs, and the spreading of the H_2-CG fronts remains within acceptable limits under practicable H_2 injection rates. This approach can be straight forwardly extended to more complex WG-CG systems.

Furthermore, the trade-off between buoyancy forces and capillary properties of the seal rock with respect to water and brine and the gas present, has been examined to determine H_2 storage capacities for various CGs. Denser CG have lower density difference with brine, resulting in reduced buoyancy forces and increased storage capacities. Therefore, storage capacities decrease in the following order with the CG: CO_2, N_2, CH_4 and H_2. This approach can be easily extended to any WG/CG couple, including when the WG and CG are mixtures.

In summary, the use of CO_2 as CG for H_2 storage in aquifers or depleted gas reservoirs offers significant benefits over using H_2 or other inert gases (N_2, CH_4). Not only does it save a large amount of H_2, but it also enhances the safety of storage by reducing the buoyancy force transmitted to the top of the reservoir. The use of CO_2 as CG is particularly advantageous due to its high density, relatively close to that of water or brine, especially under the low or moderate temperatures and high pressures encountered in deep offshore reservoirs. Also, the same reservoir can be used for permanent CO_2 storage in addition to being used as a CG for intermittent H_2 storage. Additionally, the presence beneath the seal rock of a lighter gas (H_2, CH_4, N_2, air, and their mixtures) with better-sealing interfacial properties compared to those of CO_2, enhances the security of CO_2 storage.

2.6 Limitations and Future Developments

It is worth noting that while our approach has provided valuable insights into UHS capacities with various CGs and injection rate velocities, certain limitations and complexities remain. As observed, each assumption we made was tailored to ideal gases, with exceptions required for substances like CO_2 in the liquid and supercritical state. These calculations, while well-established for simplified cases, might need adjustment for more complex real-world behavior. The description of density required the use of an EoS, and the viscosity necessitated a different model. Furthermore, the simplified treatment of parameters such as permeability, porosity, and other characteristics, which allowed us to estimate storage height and critical injection velocity, may not fully capture the intricate real-world physics and site-specific conditions.

What we have obtained so far represents theoretical and quantitative estimations that serve as a useful starting point. However, for a more in-depth understanding, further investigation is required. Addressing the complexities of reservoir processes necessitates the use of sophisticated numerical reservoir simulations. Additional equations that establish relationships between phase density and viscosity with pressure, temperature, and composition will be essential for addressing the more complex mixing behavior of gases and reservoir conditions accurately.

This analytical work serves as a prelude to the upcoming chapters. In the next chapter, we will delve into the evaluation and development of thermodynamic models aimed at describing the relevant system for reservoir numerical simulations. These models will provide a more comprehensive exploration of the thermodynamic properties and interactions involved in UHS in aquifers.

CHAPTER 3

Thermodynamic models: EoS overview and applications in UHS

The assessment of reservoir storage performance and optimization is a fundamental criterion in subsurface gas storage. It is essential to emphasize that the financial viability of such projects is linked to the purity of the produced H_2, in the context of UHS. The purity of the produced H_2 carries significant economic implications, as separation and treatment methods can substantially impact project costs, necessitating careful anticipation.

Given that gas mixing processes depend on various factors and are closely related to fluid properties within reservoirs, sophisticated simulations become a necessity. These simulations aim to provide a precise description of fluid mixture properties. In the realm of commercial reservoir modeling, options for thermodynamic models are often limited.

In this chapter, we explore various thermodynamic models and outline the process of selecting appropriate equations. Our focus shifts toward molecules relevant to the proposed UHS concept, specifically, the H_2 and CO_2 systems under the pressure and temperature conditions surrounding the critical point of pure CO_2. Therefore, the latter part of this chapter is dedicated to a study of the accuracy of three selected thermodynamic models (two cubic EoS and GERG-2008) in describing the density of this system. The results of these models are then compared to experimental data sourced from existing literature.

3.1 Introduction

Accurate reservoir simulation relies on the precise description of thermodynamic properties for the involved fluids and the reliable prediction of the behavior of individual components and the resulting mixtures. Among the simpler models, the properties of pure substances are modeled using the ideal gas law, which provides a straightforward relationship for gases under simplified conditions. This law yields simple equations like Raoult's law or Henry's law for liquid-vapor equilibria. The ideal gas law, a simple model, is valid primarily for gases under low pressures (less than 2 bar) and idealized conditions.

However, to model phase equilibria and calculate various thermodynamic properties accurately, we turn to more complex EoS models. These models express experimentally measurable parameters-such as temperature (T), pressure (P), and volume (V) in the form of a function, denoted as $f(P, T, V) = 0$.

In the case of pure components, the EoS takes the form:

$$P\,V = N_{\text{tot}}\,R\,T\ ;\ Z = \frac{P\,V}{N_{\text{tot}}\,R\,T} = 1 \tag{3.1}$$

Here, $N_{\text{tot}} = \sum_i N_i$ and Z represents the compressibility factor, accounting for deviations from ideal gas behavior. In the ideal gas case, Z equals 1. In non-ideal systems, Z deviates from 1, reflecting interactions among molecules. These deviations from ideality can occur due to factors such as molecular size, intermolecular forces, and non-sphericity of molecules

However, when dealing with multi-component mixtures, the relationship Eq.(3.1) evolves into the well-known EoS for mixture of ideal gas:

$$P(T, V, \boldsymbol{N}) = \frac{R\,T\,\sum_i N_i}{V} \tag{3.2}$$

In this equation, P represents pressure, T is the temperature, V represents the volume, and $\boldsymbol{N} = (N_i)_i$ stands for the number of moles for each component.

The function P is a homogeneous function of degree 0 in (V, N_{tot}). For an ideal gas, the state is characterized by a lack of molecular interactions. In such a scenario, individual molecules neither encounter nor are influenced by each other. This model assumes the absence of attractive or repulsive forces among gas molecules, and ideal gas energy and enthalpy depend only on T.

It is important to note that not all gases perfectly conform to these simplifications. Some systems may exhibit deviations from ideal behavior due to the presence of inter-molecular forces and molecular interactions. In such cases, it becomes more convenient to employ alternative methods capable of determining the actual properties of real fluids, particularly in challenging regions, such as those close to branches of the curve representing liquid and gas.

Consequently, a variety of models have been introduced, with ongoing research continually refining and developing these models. The following section will provide a discussion of these existing thermodynamic models.

3.2 Overview about the possible thermodynamic models

The challenge of thermodynamics, particularly equilibrium conditions between phases, were addressed over a century ago by the two famous American scientists, Gibbs and Lewis. However, the history of thermodynamic modeling traces back to the inception of EoS, a foundational approach to thermodynamics introduced by Van der Waals. This approach entails formulating mathematical relationships that describe variations in pressure, temperature, and molar volume [96]. Throughout the years, various other models have been developed, as illustrated in the table below. These models are often based on general principles or theories, and many fall into multiple categories, as shown in Fig.3.1.

We can categorize them into classical models, including Cubic EoS, which are further divided into conventional mixing rules, excess Gibbs energy models, and advanced mixing rules. Another category involves Association theories, such as the CPA EoS and the SAFT EoS. Additionally, there are activity models like Unifac and NRTL, or the Virial equations, which are commonly employed in hydrocarbon applications.

The activity coefficient is a thermodynamic variable that quantifies a system's deviation from the behavior of an ideal solution by introducing a correction factor dependent on composition as expressed in the Eq.(3.3). For ideal gas, the activity coefficient is equal to 1.

$$\gamma_i = exp\left(\frac{\frac{\partial G^E}{\partial N_i}}{RT}\right) \tag{3.3}$$

Common activity coefficient models include the Van Laar equation, Wilson equation, NRTL (Non-Random Two-Liquid) equation, and UNIFAC (UNIQUAC Functional-group Activity Coefficient) model, among others.

The list of thermodynamic models is extensive, and it is beyond the scope of this work to provide a comprehensive overview of all of them. Our primary aim in mentioning these models is to identify the most suitable one for our specific application and the components under consideration. The selection of an appropriate model is a well-studied task, with numerous guidance papers available to assist users, especially those using commercial process software. These software packages offer a wide range of options based on predefined selection criteria. We will further explore this topic in the following section.

Equation of States			Activity Models		
VTPR		PC-SAFT g-SAFT S-PCSAFT e-PCSAFT	COSMO3D COSMOSAC		
PSRK, SWP	IAWPS		COSMO-RS	COSMOSPACE	
Mathias Huron-Vidal Mixing rules		PHCS, SAFT	Unifac, LiFAC	Koningsveld- Kleintjens Uniquac	e-NRTL Helgeson
Peng-Robinson	MBWR	Sanchez- Lacombe	ASOG Hansen	NRTL	Pitzer/Bromley Robinson/Stokes
Redlich-Kwon	BWR		Flory-Huggins Scatchard- Hildebrand	Wilson	Debeye-Huckel
vdWaals	Virial	Meyer		Van Laar Margules	
Cubic	**Empirical**	**Statistical**	**Predictive**	**Solvent**	**Electrolyte**

Year of introduction: 2000, 1990, 1975, 1950, 1925

FIGURE 3.1: An overview of some of the many EoS & Activity Models (from Dr. Gerard Krooshof, DSM-DTU summer school).

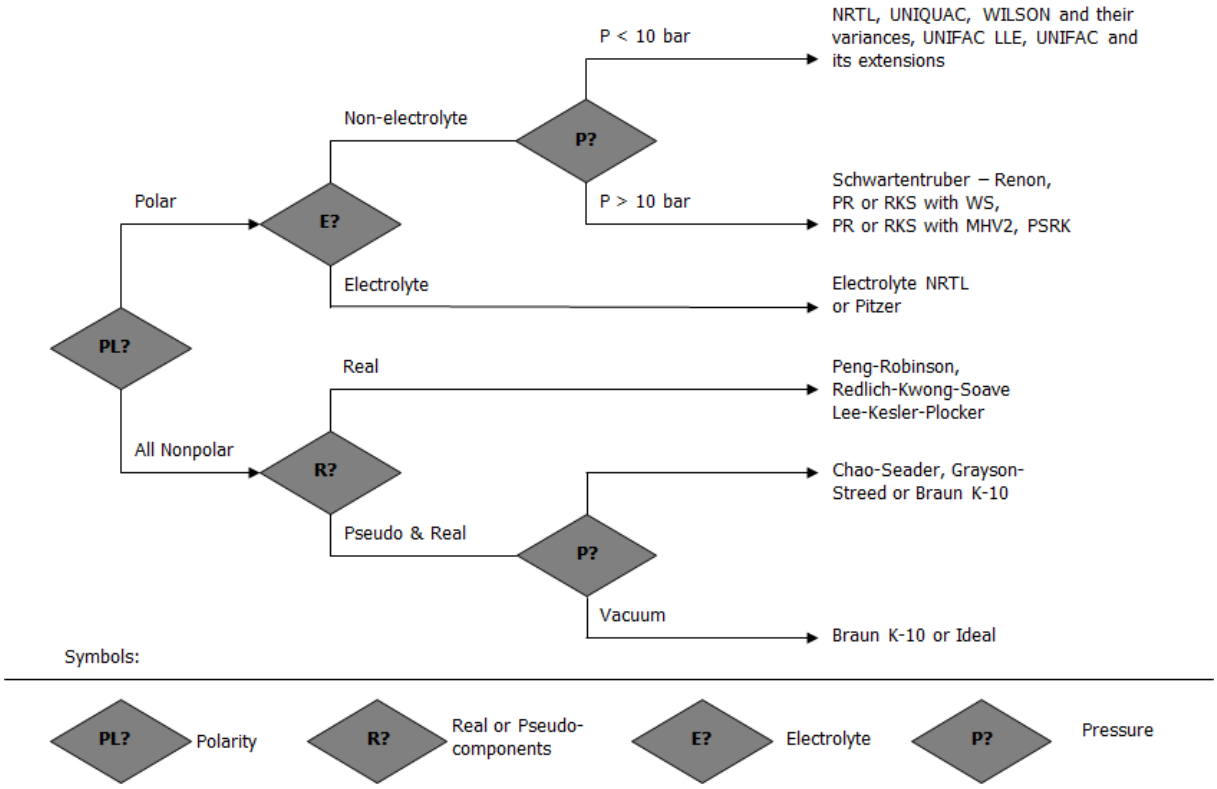

FIGURE 3.2: Use of decision trees for model selection [97].

3.3 Selecting the appropriate thermodynamic module

The pursuit of the "best" thermodynamic model is inherently relative in the realm of thermodynamics. While thermodynamics seeks beyond idealized models, the large diversity of compounds, mixtures, and the wide spectrum of conditions (concentration, temperature, and pressure), coupled with numerous potential phase equilibria (liquid-liquid, liquid-solid, vapor-liquid, and more), makes this task a complex challenge. Additionally, the choice of a thermodynamic model is profoundly influenced by specific study requirements, computational constraints, and other pertinent factors. To assist users in navigating this intricate landscape, commercial process simulators often offer a "decision tree" approach, as visually represented in Fig.3.2.

In this context, the process of selecting an ideal model begins with the evaluation of factors such as the polarity and ideality of the components within the system, alongside consideration of the prevailing pressure conditions. Given that both CO_2 and H_2 exhibit non-polar characteristics, and among the suggested models, cubic EoS appear highly relevant. Nevertheless, for a comprehensive evaluation, we will explore various models, including one that has recently garnered attention, GERG-2008. Our objective is to apply and evaluate these models, assessing their capability to provide accurate descriptions of the system under consideration.

3.4 Methodology

In this section, we direct our attention to a binary system composed of two distinct molecules: H_2 and CO_2 (Table 3.1). It is crucial to examine the behavior of this mixture, as highlighted by Carden and Paterson, and collect any available experimental data. However, it is important to acknowledge that there's a notable scarcity of experimental data pertaining to H_2 and, particularly, binary mixtures of H_2 and CO_2 under reservoir conditions.

Given the inconvenience of measuring every relevant parameter, we turn to computational models. However, it is vital to approach simulation results with a critical eye. EoS models can be rigorously tested for their accuracy in describing *Vapor-Liquid Equilibrium* (VLE) and fluid properties. The mixing process, crucial for our study, relies on fluid density and viscosity. Notably, a substantial density contrast between gases can partially mitigate mixing [54].

In this study, we specifically focus on fluid density, which is determined using EoS. we have selected three models for evaluation: two cubic EoS models (*Peng–Robinson* (PR) and *Soave-Redlich-Kwong* (SRK)) and GERG-2008.

A thorough review of the existing literature has unveiled limited density measurements at the pressures anticipated in UHS, particularly around the critical point of CO_2. The chosen reference experimental data corresponds to mixtures containing 0.07%, 0.1%, and 2% of H_2 in the system [99]. This selection of data is not only aligned with the reservoir conditions of the experiments but also considers the fraction of H_2 within the system. Indeed, when the system is enriched with H_2, it is closely approximated by ideal gas behavior. Conversely, introducing a small amount of H_2 into CO_2 significantly impacts the system's density. The density values derived from the SRK, PR, and GERG-2008 models will be compared to the experimental data to evaluate their accuracy.

We'll proceed by providing an in-depth explanation of these thermodynamic models. To describe the relevant system, we have developed computational codes for each equation, implemented in Fortran. These modules primarily produce density values, which will be rigorously compared to the chosen experimental data. The results of this comparison will be discussed in the following section.

We will start by introducing the fundamental concept of cubic EoS, delve into the specifics of the SRK and PR models, and conclude by elucidating the GERG-2008 model.

3.4.1 Cubic EoS

Cubic EoSs represent a fundamental pillar in thermodynamics and the most widely employed thermodynamic model. They are the default choice in a multitude of commercial reservoir simulation tools. The most renowned of these is the *Van der Waals* (VdW) EoS.

The classical form of the VdW equation Eq.(3.4) provides a starting point for comprehending fluid behavior. This equation, originally formulated by Nobel laureate Johannes Diderik van der Waals in 1873, represent a significant advancement. They accurately account for deviations from ideal gas behavior by considering intermolecular forces - both attractive and repulsive, which exert a significant influence on a fluid's volumetric and equilibrium properties.

$$P = \frac{RT}{v-b} - \frac{a}{v^2} \tag{3.4}$$

where R is the gas constant, T is the temperature, v is the molar volume. b the mixture co-volume and the attractive parameter, a, are functions of temperature and mixture composition.

The term $\frac{RT}{v-b}$ corrects for finite molecular volume (repulsive effect) through the parameter b depends on the molecular size. While the negative contribution to pressure via parameter a accounts for attractive intermolecular forces. When both a and b equal zero, the equation reverts to the ideal gas law.

The constants a and b, the VdW constants in the cubic EoS, are calculated based on the fluid's properties:

$$a = 0.421875\frac{R^2\,T_c^2}{P_c} \tag{3.5}$$

$$b = 0.125\frac{R\,T_c}{P_c} \tag{3.6}$$

Where, T_c is the critical temperature of the component. P_c is the critical pressure of the component.

Extension to mixtures: In a case of mixture of multi-component system, the parameters a and b are determined through various mixing rules. The most straightforward empirical correlation for the attractive term is quadratic, in terms of composition (mole fraction), such as Berthelot's representation:

$$a = \sum_i \sum_j x_i x_j a_{ij} \quad ; \quad a_{ij} = \sqrt{a_{ii}a_{jj}} \tag{3.7}$$

Note that x_i and x_j are the mole fractions of components i and j either in the liquid or the vapor phase. The cross-energy, a_{ij}, is the interaction energy between components i and j.

The parameter b in the repulsive term is the average fluid volume, represented as a linear function of composition:

$$b = \frac{1}{\boldsymbol{N}} \sum_i n_i b_i \tag{3.8}$$

where b_i are component-specific parameters.

The mixing rules in Eq.(3.7) and Eq.(3.8) can not be fitted to experimental data. However, another widely used method for determining a and b in mixtures involves fitting parameters. These are found in the VdW mixing rules Eq.(3.10), where a_{ij} and b_{ij} for the mixture are obtained using combining rules that consider the properties of individual components and their interactions Eq.(3.9).

$$a = \sum_i \sum_j x_i x_j a_{ij} \quad ; \quad b = \sum_i \sum_j x_i x_j b_{ij} \tag{3.9}$$

$$a_{ij} = \sqrt{a_{ii}a_{jj}}(1-k_{ij}) \quad ; \quad b_{ij} = \frac{b_{ii}+b_{jj}}{2}(1-l_{ij}) \tag{3.10}$$

Here, k_{ij} and l_{ij} are binary interaction parameters that are determined by fitting equilibrium data.

Usually the k_{ij} values are zero for mixtures with hydrocarbons. Although, over a limited temperature range, k_{ij} is often nearly independent of temperature, in the typical case, the temperature dependency must be accounted for. In certain cases, phase equilibrium calculations can be highly sensitive to the k_{ij} used. k_{ij} values for aqueous and other highly polar systems can be very high and they do not have a physical meaning. The representation of phase equilibria for such systems may not be satisfactory and/or may require two interaction parameters k_{ij} and l_{ij} for satisfactory correlation. l_{ij} equal to zero, reduces the Eq.(3.10) to the linear form given by the Eq.(3.8).

The best combining rules are the geometric mean for the cross-energy, a_{ij}, and the arithmetic mean for the cross co-volume parameter b_{ij}. In the case the arithmetic mean rule for the cross co-volume, as shown here Eq.(3.9), is used, then the mixing rule for the co-volume is a simple linear mixing rule with respect to concentration. The geometric mean rule for the cross-energy parameter has some theoretical foundation based on the theory of intermolecular forces.

Cubic EoS and Mixtures The name "cubic" arises from the fact that when these equations are solved for volume (V) or compressibility (Z), they yield third-degree polynomial equations. This results in three real solutions: the highest corresponds to the gas phase, the lowest to the liquid phase, and the middle root lacks physical significance because it is mechanically unstable.

Numerous adaptations of the original VdW equation have been introduced to accommodate specific molecule types. This diversity of models is chosen based on the characteristics of the components under study. Most modifications primarily focus on enhancing the attractive term and refining mixing rules. Two prominent modifications, SRK and PR, have become well-known and widely utilized in the field.

SRK (Soave-Redlich-Kwong) represents one of the earliest adjustments to the original VdW equation. Its primary goal was to accurately replicate vapor pressures of pure components and match experimental data. SRK significantly improved the description of intermolecular attraction between molecules by introducing the function $\alpha(T)$ in the attractive term [100]. The generalized SRK equation Eq.(3.11) incorporates the concept of molecular polarity related to molecular size for nonpolar compounds, denoted by the acentric factor ω :

$$P = \frac{R\,T}{v-b} - \frac{a\,\alpha(T)}{v(v+b)} \tag{3.11}$$

for pure components, a and b are determined as follows:

$$a = 0.42748\frac{R^2\,T_c^2}{P_c}\ ;\ b = 0.08664\frac{R\,T_c}{P_c}$$

The acentric factor ω plays a significant role, where:

$$\alpha(T) = \left(1 + (0.480 + 1.574\,\omega - 0.176\,\omega^2)\left(1 - \sqrt{\frac{T}{T_c}}\right)\right)^2$$

the mixing rules introduced in the Eq.(3.10) holds.

Although this equation became very popular, some shortcomings particularly when dealing with hydrocarbons giving specific volumes of the liquid phase that were 7%–27% too high with the deviations increasing as the critical point of the substance was approached.

PR (Peng-Robinson) brought further refinements to the attractive term, particularly for predicting liquid densities. It redefined the α function based on more extensive experimental data (Eq.(3.12)) [101]:

$$P = \frac{RT}{v-b} - \frac{a\,\alpha(T)}{v(v+b)+b(v-b)} \tag{3.12}$$

For pure components, a and b are calculated as follows:

$$a = 0.45724\frac{R^2\,T_c^2}{P_c}\ ;\ b = 0.0778\frac{R\,T_c}{P_c}$$

The $\alpha(T)$ function is redefined as:

$$\alpha(T) = \left(1 + (0.37464 + 1.54226\,\omega - 0.26992\,\omega^2)\left(1 - \sqrt{\frac{T}{T_c}}\right)\right)^2$$

It appears that the PR EoS outperforms SRK EoS in predicting liquid densities. This is mainly due to the fixed critical compressibility factor of the PR EoS.

Péneloux Constant Volume Translation The cubic EoS are considered the simple and efficient mathematical form that is easily manipulated to obtain thermodynamic properties and easily applicable to pure component as mixtures. They revealed one common shortcoming: a systematic overestimate of liquid density when compared to the experimental data [102]. To address this weakness, a variety of methods have been proposed. One of the simplest is the Péneloux constant volume translation [103]. This pseudo volume shift uses the Rackett Equation (3.13). This correction alters some properties, such as density and enthalpy. In addition, the validity of this correction is limited to a specific range within the liquid phase. The new volume or pseudo-volume is defined as V' and the correction constant here is noted c.

$$V' = V + c \quad \text{with} \quad c = \sum_i x_i\,c_i \tag{3.13}$$

The correlation term c is expressed in terms of compressibility factors Z_{RA}, critical temperature, and critical pressure of the components [104]. For the SRK EoS:

$$c_i = 0.40768\left(\frac{R\,T_{c,i}}{P_{c,i}}\right)(0.29441 - Z_{RA,i}) \tag{3.14}$$

For the PR EoS:

$$c_i = 0.406501\left(\frac{R\,T_{c,i}}{P_{c,i}}\right)(0.260484 - Z_{RA,i}) \tag{3.15}$$

Note that the temperature independent co-volume correction does not alter the prediction of phase behavior [105].

This volume correction is considered in our computational code here to help fit better the data.

Cubic EoS, although simple and efficient, exhibit some limitations, particularly in capturing the behavior of mixtures. This complexity arises due to the vast range of possible component combinations and the scarcity of experimental data under specific conditions. The presence of such data would undoubtedly enhance the development of these equations and provide valuable insights into resolving these shortcomings.

3.4.2 GERG-2008

In the quest for an EoS capable of accommodating a wide range of applications and providing highly accurate thermodynamic property calculations, Kunz *et al* [106] established the empirical multi-parametric GERG-2004 EoS. This was soon succeeded by the improved GERG-2008 [53]. The GERG-2008 equation is considered a reference for describing natural gas and its mixtures, making it a valuable tool for various applications. It distinguishes itself from the cubic EoS by the number of included terms.

The GERG-2008 equation builds upon its predecessor and offers a comprehensive framework for modeling the gas and liquid phases, VLE, and even the supercritical region. The main difference between GERG-2008 and its predecessor GERG-2004 lies in the number of terms included in the formulation. GERG-2008 is validated for a broad set of 21 components including CO_2 and H_2. The thermodynamic properties of these fluid mixtures are derived from the dimensionless Helmholtz free energy, as defined by Equation (3.16). Usually, the Helmholtz free energy is used as a dimensionless term ($\alpha = \frac{a}{RT}$). so, the equation is explicit in the Helmholtz free energy with the independent mixture variables density, temperature and molar composition.

3.4.2.1 Mathematical formulation

The Helmholtz free energy in GERG-2008 is a function of reduced density ($\delta = \frac{\rho}{\rho_c}$), the inverse of the reduced temperature ($\tau = \frac{T_c}{T}$), and the mixture composition (x). Here, ρ_c and T_c correspond to the critical density and temperature of the relevant fluid. This formulation aligns with the practical requirements of an EoS and enables the retrieval of thermodynamic properties for multi-component systems. However, it introduces increased complexity due to the calculation of various partial derivatives.

The GERG-2008 equation consists of two terms: the first term (α^o) is given for ρ, T, x and accounts for ideal gas behavior within the mixture, while the second term (α^r) represents the residual behaviour of the mixture. The equation is structured as follows:

$$\alpha(\delta, \tau, x) = \alpha^o(\rho, T, x) + \alpha^r(\delta, \tau, x) \tag{3.16}$$

where, the subscript o refers to pure substances.

The accuracy of this equation is closely tied to the description of the behavior of pure substances. Further complex correlation equations are used to describe the behavior of multi-components. The mathematical structure of pure component equations is formulated in a functional form of polynomial terms and in polynomial terms in combination with exponential

functions, resulting in complex expressions. The residual part also utilizes similarly polynomial terms and more sophisticated exponential functional forms to describe the mixture, primarily to improve the representation of properties in the extended critical region.

The ideal gas mixture equation is given by:

$$\alpha^o(\rho, T, x) = \sum_{i=1}^{N} x_i(\alpha^o_{oi}(\rho, T) + ln(x_i)) \tag{3.17}$$

This part of the equation describes the mixture of different ideal gases and includes the term $\alpha^o_{oi}(\rho, T)$, which is the dimensionless form of the Helmholtz free energy for the ideal gas of each individual component. The reduced Helmholtz free energy for the ideal gas component i is defined by:

$$\begin{aligned}\alpha^o_{oi}(\rho, T) = \frac{R^*}{R}[&\ln(\frac{\rho}{\rho_{c,i}}) + (n^o_{oi,1} + n^o_{oi,2}\frac{T_{c,i}}{T} + n^o_{oi,3}\ln(\frac{T_{c,i}}{T}) \\ &+ \sum_{k=4,6} n^o_{oi,k}\ln(|\sinh(\mathcal{V}^o_{oi,k}\frac{T_{c,i}}{T})|) \\ &+ \sum_{k=5,7} n^o_{oi,k}\ln\cosh(\mathcal{V}^o_{oi,k}\frac{T_{c,i}}{T}))],\end{aligned} \tag{3.18}$$

where, R and R^* represent the molar gas constant, equivalent to $8.314472\,J\,mol^{-1}\,K^{-1}$ and $8.314510\,J\,mol^{-1}\,K^{-1}$, respectively. The parameter $\mathcal{V}^o_{oi,k}$ and the coefficients $n^o_{oi,k}$ are provided for every component in the list.

The term α^r given in the Eq.(3.19), includes the reduced residual Helmholtz free energy for pure components, $\alpha^r_{oj}(\delta, \tau)$, and the double summation represents the departure function for binary mixtures, $\triangle\alpha^r(\delta, \tau, x)$. The latter term quantifies the interactions between different components and is characterized by a set of parameters tailored to specific system data, denoted as F_{ij} and $\alpha^r_{ij}(\delta, \tau)$. The residual function incorporates reduced variables such as σ, τ, and the molar composition of the mixture.

$$\begin{aligned}\alpha^r(\delta, \tau, x) = \alpha^r_{oj}(\delta, \tau) + \triangle\alpha^r(\delta, \tau, x)\sum_{i=1}^{N} x_i\alpha^r_{oi}(\delta, \tau) \\ + \sum_{i=1}^{N-1}\sum_{j=i+1}^{N} x_i x_j F_{ij}\alpha^r_{ij}(\delta, \tau) \quad , \quad F_{ij} = 1 \text{ for } i = j\end{aligned} \tag{3.19}$$

The linear combination function of the reduced residual Helmholtz free energy for pure substance is written as the following:

$$\begin{aligned}\alpha^r_{oi}(\delta, \tau) = &\sum_{k=1}^{K_{Pol}} n_{oi,k}\delta^{d_{oi,k}}\tau^{t_{oi,k}} \\ &+ \sum_{k=K_{Pol,i}+1}^{K_{Pol,i}+K_{Exp,i}} n_{oi,k}\delta^{d_{oi,k}}\tau^{t_{oi,k}}e^{-\delta^{c_{oi,k}}}.\end{aligned} \tag{3.20}$$

where, the coefficient $n_{oi,k}$ and the exponents $d_{oi,k}$, $t_{oi,k}$, and $c_{oi,k}$ are constant values given for every considered component. In this equation, K_{Pol} represents the number of polynomial terms, while K_{Exp} denotes the number of polynomial terms in combination with exponential expressions.

The maximum numbers of terms corresponds to the sum of K_{Pol} and K_{Exp}. The values of these coefficients and exponents depend on the specific pure component.

The $\alpha^r_{ij}(\delta,\tau)$ term is the part of the departure function $\triangle\alpha^r(\delta,\tau,x)$ that depends on the binary mixtures. For generalized binary mixtures, this parameter is fitted to the specific binary data. If this factor is zero, it indicates that the departure function was not developed for this mixture system. $\alpha^r_{ij}(\delta,\tau)$ incorporates $2K_{Pol}$ coefficient and $6K_{Exp}$ exponents and is expressed using a functional form of polynomial terms and exponential functions. The exponential term is more intricate than in Equation (3.20), including more coefficients in the expression. The expression for $\alpha^r_{ij}(\delta,\tau)$ is also expressed in terms of K_{Pol} and K_{Exp}, the number of terms used.

3.4.3 Parameterize the thermodynamic models for the H_2-CO_2 System

To explore the performance of different thermodynamic models and select the most appropriate equation for our application, the focus must be diverted towards the specific molecules present in the UHS, namely H_2 and CO_2. This selection is particularly relevant under the reservoir's pressure-temperature conditions. Our approach involved employing various thermodynamic models computed to solve equations, calculate volumes, and ultimately determine density values.

3.4.3.1 Cubic EoS parameterize

Concerning the cubic EoS, a generalized version is used to work for PR and SRK. The Péneloux corrections was taken into account for the both cubic EoS. Table 3.1 below provides a concise summary of the parameters used to parameterize the cubic EoS for the H_2-CO_2 system:

	H_2	CO_2
$T_c(K)$	31.76	304.2
P_c	1.276	7.377
ω	-0.062	0.351
M	2.0	44.01
k_{ij}	-0.1622	

Table 3.1: Cubic EoS parameters for the H_2-CO_2 system.

3.4.3.2 GERG-2008 model parameterize

In parallel with the cubic EoS, we also considered the GERG-2008 model. This model accommodates 21 components, including CO_2 and H_2. The Tables 3.2 and 3.3 display the relevant coefficients to this binary system. It is important to note that for the H_2-CO_2 mixture, the departure function is not developed due to limited data for regression. However, this lack of development is unlikely to significantly impact the results. Typically, the departure function makes a smaller contribution to the reduced residual Helmholtz free energy of the mixture compared to the contribution of the equations for the individual pure components [53].

		H_2	CO_2
	$T_c(K)$	33.19	304.1282
	$\rho_c(mol.dm^{-3})$	14.94	10.62497
	M	2.01588	44.0095
$\alpha^o_{oi}(\rho,T)$	$n^o_{oi,k=1}$	13.796443393	11.925152758
	$n^o_{oi,k=2}$	-175.864487294	-16.118762264
	$n^o_{oi,k=3}$	1.47906	2.50002
	$n^o_{oi,k=4}$	0.95806	2.04452
	$n^o_{oi,k=5}$	0.45444	-1.06044
	$n^o_{oi,k=6}$	1.56039	2.03366
	$n^o_{oi,k=7}$	-1.37560	0.01393
	$\mathcal{V}^o_{oi,k=4}$	6.891654113	3.022758166
$\alpha^r_{oj}(\delta,\tau)$	K_{Pol}	5	4
	K_{Exp}	9	18
	$n_{oi,k=1}$	$0.53579928451252 \cdot 10^{1}$	0.52646564804653
	$n_{oi,k=2}$	$-0.62050252530595 \cdot 10^{1}$	$-0.14995725042592 \cdot 10^{1}$
	$n_{oi,k=3}$	0.13830241327086	0.27329786733782
	$n_{oi,k=4}$	$-0.71397954896129 \cdot 10^{-1}$	0.12949500022786
	$n_{oi,k=5}$	$0.15474053959733 \cdot 10^{-1}$	0.15404088341841
	$n_{oi,k=6}$	-0.14976806405771	-0.58186950946814
	$n_{oi,k=7}$	$-0.26368723988451 \cdot 10^{-1}$	-0.18022494838296
	$n_{oi,k=8}$	$0.56681303156066 \cdot 10^{-1}$	$-0.95389904072812 \cdot 10^{-1}$
	$n_{oi,k=9}$	$-0.60063958030436 \cdot 10^{-1}$	$-0.80486819317679 \cdot 10^{-2}$
	$n_{oi,k=10}$	-0.45043942027132	$-0.35547751273090 \cdot 10^{-1}$
	$n_{oi,k=11}$	0.42478840244500	-0.28079014882405
	$n_{oi,k=12}$	$-0.21997640827139 \cdot 10^{-1}$	$-0.82435890081677 \cdot 10^{-1}$
	$n_{oi,k=13}$	$-0.10499521374530 \cdot 10^{-1}$	$0.10832427979006 \cdot 10^{-1}$
	$n_{oi,k=14}$	$-0.28955902866816 \cdot 10^{-2}$	$-0.67073993161097 \cdot 10^{-2}$
	$n_{oi,k=15}$	–	$-0.46827907600524 \cdot 10^{-2}$
	$n_{oi,k=16}$	–	$-0.28359911832177 \cdot 10^{-1}$
	$n_{oi,k=17}$	–	$0.19500174744098 \cdot 10^{-1}$
	$n_{oi,k=18}$	–	-0.21609137507166
	$n_{oi,k=19}$	–	0.43772794926972
	$n_{oi,k=20}$	–	-0.22130790113593
	$n_{oi,k=21}$	–	$0.15190189957331 \cdot 10^{-1}$
	$n_{oi,k=22}$	–	$-0.15380948953300 \cdot 10^{-1}$

Table 3.2: GERG-2008 parameters for the H_2-CO_2 system provided in [53].

The next section will examine the limitations and accuracy of these models within the CO_2 and H_2 system under the proposed UHS conditions. These findings will guide us in selecting the model that best captures the system's behavior.

3.5 Results of EoS accuracy evaluation

In this section, we present the results of our accuracy assessment for various EoS applied to the CO_2 and H_2 system, with a specific focus on conditions near the critical point of CO_2. To provide a comprehensive evaluation of these EoS models, we extended our analysis to a wider range

of pressure and temperature conditions. Density calculations for the mixture were performed at the exact temperature, pressure, and molar composition as the experimental data. The accuracy of these predictions was then assessed by comparing them with the experimental data reported by Sanchez-Vicente et al. [99]. To quantify the accuracy of our predictions, we calculated the relative error, expressed as the percent deviation from the experimental measurements.

Since the experimental measurements were conducted along isotherms, the calculated points are represented by the blue dots in Fig.3.3, forming vertical lines. In the figures presented, the letters attributed to each column denote the H_2 mole fraction in the system: the right column corresponds to 0.02, the middle column to 0.075, and the left column to 0.1. Additionally, the rows represent the different EoS used: the first row corresponds to GERG-2008, the second row to PR, and the last row to SRK. Figures 3.3a, 3.3b, and 3.3c depict the relative error between the GERG-2008 equation and experimental data. Notably, the maximum error observed with the GERG-2008 equation is 17.5%, primarily concentrated around the critical point of the mixture. This showcases the remarkable accuracy of the empirical GERG-2008 equation across a wide range of temperature and pressure conditions. The error exhibited by the GERG-2008 equation varies with the H_2 fraction in the system, albeit without significant changes in behavior, except for a minor shift towards higher pressure as H_2 fraction increases. On the other hand, Figures 3.3d, 3.3e, 3.3f, 3.3g, 3.3h and 3.3i show the relative error between the cubic equations (SRK and PR), after applying volume correction. These cubic EoS models exhibit slightly extended errors over a broader range of pressure and temperature. Although the maximum error reached with the cubic EoS is 16%, it remains relatively close to the maximum errors observed with the equation GERG-2008. Notably, both the PR and SRK models yield similar behavior and results.

However, on average, the GERG-2008 equation maintains an average error as low as 1.3591%. In contrast, the alternative equations, such as the PR equation with an average error of 2.7845% and the SRK equation with an average error of 6.0009%, display higher deviations from experimental data. The cubic EoS models seem to struggle in accurately predicting density when the H_2 fraction is very low, while the GERG-2008 equation's accuracy experiences only a minor, non-significant reduction as the H_2 fraction increases in the system. Particularly, when considering scenarios focused around the critical point of CO_2 and under conditions relevant to UHS, the GERG-2008 equation emerges as the preferable choice for accurately describing the system's behavior.

Given these findings, we recommend the adoption of the GERG-2008 equation for UHS analysis purposes.

		H_2	CO_2			H_2	CO_2
$\alpha^r_{oj}(\delta,\tau)$	$d_{oi,k=1}$	1	1	$\alpha^r_{oj}(\delta,\tau)$			
	$d_{oi,k=2}$	1	1				
	$d_{oi,k=3}$	2	2				
	$d_{oi,k=4}$	2	3				
	$d_{oi,k=5}$	4	3		$c_{oi,k=5}$	–	1
	$d_{oi,k=6}$	1	3		$c_{oi,k=6}$	1	1
	$d_{oi,k=7}$	5	4		$c_{oi,k=7}$	1	1
	$d_{oi,k=8}$	5	5		$c_{oi,k=8}$	1	1
	$d_{oi,k=9}$	5	6		$c_{oi,k=9}$	1	1
	$d_{oi,k=10}$	1	6		$c_{oi,k=10}$	2	1
	$d_{oi,k=11}$	1	1		$c_{oi,k=11}$	2	2
	$d_{oi,k=12}$	2	4		$c_{oi,k=12}$	3	2
	$d_{oi,k=13}$	5	1		$c_{oi,k=13}$	3	3
	$d_{oi,k=14}$	1	1		$c_{oi,k=14}$	5	3
	$d_{oi,k=15}$	–	3		$c_{oi,k=15}$	–	3
	$d_{oi,k=16}$	–	3		$c_{oi,k=16}$	–	3
	$d_{oi,k=17}$	–	4		$c_{oi,k=17}$	–	3
	$d_{oi,k=18}$	–	5		$c_{oi,k=18}$	–	5
	$d_{oi,k=19}$	–	5		$c_{oi,k=19}$	–	5
	$d_{oi,k=20}$	–	5		$c_{oi,k=20}$	–	5
	$d_{oi,k=21}$	–	5		$c_{oi,k=21}$	–	6
	$d_{oi,k=22}$	–	5		$c_{oi,k=22}$	–	6
	$t_{oi,k=1}$	0.500	0.000				
	$t_{oi,k=2}$	0.625	1.250				
	$t_{oi,k=3}$	0.375	1.625				
	$t_{oi,k=4}$	0.625	0.375				
	$t_{oi,k=5}$	1.125	0.375				
	$t_{oi,k=6}$	2.625	1.375				
	$t_{oi,k=7}$	0.000	1.125				
	$t_{oi,k=8}$	0.250	1.375				
	$t_{oi,k=9}$	1.375	0.125				
	$t_{oi,k=10}$	4.000	1.625				
	$t_{oi,k=11}$	4.250	3.750				
	$t_{oi,k=12}$	5.000	3.500				
	$t_{oi,k=13}$	8.000	7.500				
	$t_{oi,k=14}$	8.000	8.000				
	$t_{oi,k=15}$	–	6.000				
	$t_{oi,k=16}$	–	16.000				
	$t_{oi,k=17}$	–	11.000				
	$t_{oi,k=18}$	–	24.000				
	$t_{oi,k=19}$	–	26.000				
	$t_{oi,k=20}$	–	28.000				
	$t_{oi,k=21}$	–	24.000				
	$t_{oi,k=22}$	–	26.000				
$\triangle\alpha^r(\delta,\tau,x)$	F_{ij}	0					
	$\alpha^r_{ij}(\delta,\tau)$	–	–				

Table 3.3: (continued) GERG-2008 parameters for the H_2-CO_2 system provided in [53].

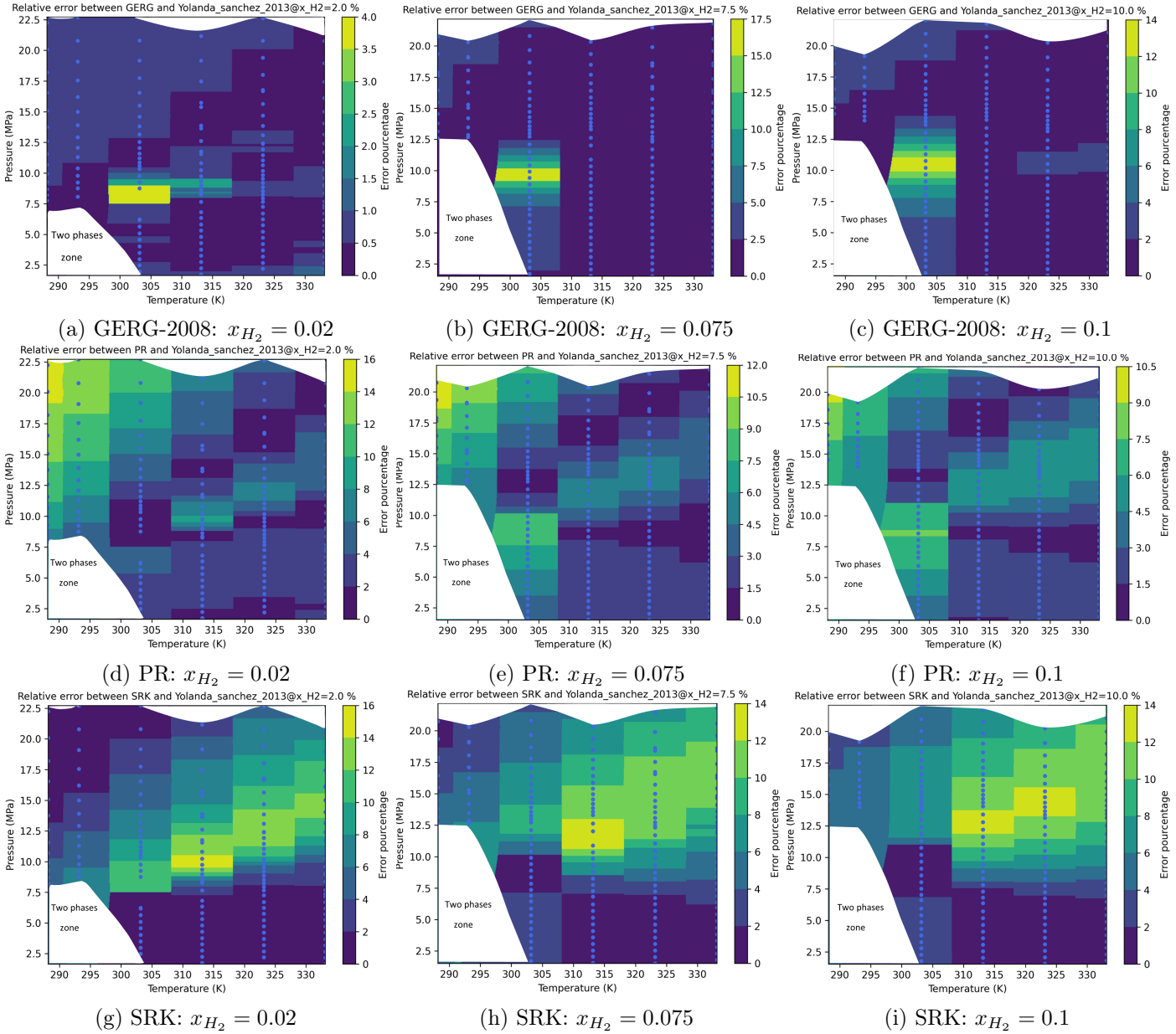

(a) GERG-2008: $x_{H_2} = 0.02$ (b) GERG-2008: $x_{H_2} = 0.075$ (c) GERG-2008: $x_{H_2} = 0.1$

(d) PR: $x_{H_2} = 0.02$ (e) PR: $x_{H_2} = 0.075$ (f) PR: $x_{H_2} = 0.1$

(g) SRK: $x_{H_2} = 0.02$ (h) SRK: $x_{H_2} = 0.075$ (i) SRK: $x_{H_2} = 0.1$

FIGURE 3.3: Relative errors between different EoS and experimental data for the density of CO_2 and H_2 mixtures at various mole fractions of H_2.

3.6 Conclusion

This chapter has provided an exploration of different thermodynamic models and their applicability in modeling the behavior of the CO_2 and H_2 system under UHS conditions. Our objective was to select the most suitable EoS for accurately predicting the thermodynamic properties of this system.

Cubic EoS, including the PR and SRK models, have long been regarded as efficient tools for phase equilibrium and fluid properties calculations. However, recent studies and comparisons have unveiled certain limitations associated with these models. For instance, these cubic EoS have shown deficiencies in accurately predicting properties in the liquid phase, especially for helium or H_2-rich mixtures, mainly related to the strong quantum effect exhibited [107].

On the other hand, the GERG-2008 EoS, developed specifically for natural gas and its mixtures, has demonstrated better accuracy in various studies, outperforming the cubic EoS for most mixture systems [108]. The GERG-2008 equation remains a powerful tool for modeling phase equilibria and thermodynamic properties of mixtures.

One noteworthy observation from the set of experimental data, which focused on the CO_2 and H_2 system under UHS conditions, revealed intriguing behaviors. Notably, even a small inclusion of 2% H_2 in the system led to a significant reduction in the mixture's density, up to 25% compared to pure CO_2 under identical conditions.

In terms of accuracy, our results showed that while cubic EoS models are generally reliable, they tend to struggle when predicting density at very low H_2 fractions in the system. In contrast, the GERG-2008 equation maintained its accuracy, with only minor and non-significant reductions as the H_2 fraction increased.

The GERG-2008 equation's capacity to handle a wide range of pressures and temperatures, coupled with its proven ability to provide highly accurate descriptions of the CO_2 and H_2 system, particularly under UHS-relevant conditions, makes it the most suitable choice to guide further UHS investigations and simulations. Based on these findings, we recommend adopting the GERG-2008 equation for the UHS simulations.

3.7 Limitations and Future Developments

3.7.1 Model Limitations

While the GERG-2008 equation exhibits several advantages, it also has its limitations, as outlined below:

- **Pressure Overestimation:** The GERG-2008 model tends to overestimate pressure values along the phase envelope, particularly at high temperatures [109]. The increase in temperature helps better accuracy at low pressure. However, this model prediction deviate at higher pressure, typically beyond 30 MPa. This limitation may impact the accuracy of pressure predictions in certain conditions that for instance deviate from common reservoir conditions.

- **Challenging Conditions Near Critical region:** The GERG-2008 equation faces challenges when applied near the critical region of CO_2-rich mixture. In such regions, its predictive accuracy might be compromised.
- **Limited Data for CO_2+H_2 System:** The multi-parametric GERG-2008 model was originally formulated for natural gas. While the component pair CO_2+H_2 is included in its component list, the lack of experimental data available for this system during equation development was reported. Consequently, departure functions for this specific binary system were not developed. Although the GERG-2008 equation offers impressive precision for various systems, it might not be optimized for the behavior of the CO_2-H_2 mixture.
- **Computational Time:** Achieving the higher precision offered by the GERG-2008 equation comes at the cost of increased computational time. In fact, the computational time can be 2 to 6 times higher compared to traditional PR cubic EoS [108]. This extended computation time is primarily due to the GERG-2008 EoS's requirement for iterative calculations of molar density in both the liquid and vapor phases within an inner loop during VLE calculations, making it a slower option for such simulations.

These limitations should be taken into consideration when choosing the appropriate model for a specific application, as the ideal model depends on the specific system, conditions, and computational resources available.

3.7.2 Future developments

Recently, a new mixture equation has been proposed for the H_2+CO_2 system, and other mixtures characterized by a high hydrogen content [109]. This equation is based on a careful selection of the most accurate data from previously conducted experimental studies. Furthermore, ongoing experimental measurements are being conducted at Ruhr University Bochum to provide additional data for this system. While these measurements are still in progress and their data are not yet available, preliminary results indicate that the new equation performs better than the GERG-2008 model. In fact, it reduces the deviations from almost all available data sets, signifying a potential improvement over the existing GERG-2008 model.

As part of this effort, a binary-specific equation of state has been developed to address the unique characteristics of the H_2+CO_2 system. This involves the addition of a departure function to the GERG-2008 equation, enhancing its representation of the system's behavior. These developments suggest that there is room for refining equations of state to better capture the properties and phase behavior of this binary system.

The primary objective of this chapter has been to assess the accuracy of various thermodynamic models and select the most suitable one for implementation in the open-source reservoir simulator. While the GERG-2008 model has been identified as the most accurate, it is important to consider its computational demands, both in terms of development time for coding and actual simulation runtime. The idea of pre-computed tables for reservoir pressure-temperature conditions was briefly discussed as a potential optimization for using GERG-2008 but has not been explored further.

Taking into account the limitations and advantages of each thermodynamic model, as well as the development timeline for the research project and computational requirements, the decision has been made to initially integrate a cubic EoS model. Cubic EoS strike a balance between accuracy and computational efficiency, making them a pragmatic choice for the next chapter of this research.

CHAPTER 4

UHS simulations with ComPASS

ComPASS (Computing Parallel Architecture to Speed up Simulations) stands as an open and evolving platform, employing advanced numerical methods to discretize non-isothermal multi-phase multi-component Darcy flows on generic unstructured meshes [110]. Initially, ComPASS was primarily employed for hydrothermal modeling. However, its scope has expanded significantly to encompass a wider range of applications and to address multi-physics scenarios [111, 112, 113, 114, 115]. For instance, in the context of nuclear waste storage, ComPASS has been utilized to model the de-saturation of storage zones at the interface with ventilation galleries [116, 117].

While our future plans include extending its capabilities to UHS usage, the current focus of this simulator remains on describing water and its vapor, involving two components, two-phases systems governed by the ideal gas law. However, as discussed in the previous chapter, certain case studies involve components that deviate significantly from ideal behavior. To address these complexities and broaden the application scope of ComPASS, the development of a more sophisticated thermodynamic model was deemed essential.

In this upcoming chapter, we delve into the development of this thermodynamic model within ComPASS. This exploration will provide insights into the changes made and the challenges encountered during its implementation. Then in numerical section, the module is tested on several 1D and one 3D test cases.

4.1 Introduction

A wide array of numerical tools is available for modeling UHS. These options span from commercial software widely used in the petroleum industry to open-source codes primarily used for scientific purposes. Each tool varies in its physical model, numerical scheme, and user interface, as detailed in Table.4.1. Among the diverse simulator options, ComPASS stands out as a parallel multiphase multi-component thermal flow simulator. ComPASS employs the Vertex Approximate Gradient (VAG) scheme for 3D spatial discretization and is coded in Fortran 90+, C++, and Python, which is used for simulation scripts and various other functionalities. The visualisation of outputs is provided through Paraview.

	ComPASS	$DuMu^x$	TOUGH	CMG	Eclipse
Commercial tool			✓	✓	✓
Open source	✓	✓			
User interface				✓	✓
Programming language	Fortran C++ python	C++	Fortran		Fortran
Parallelization	✓	✓	✓	✓	-
Compositional multi-phase flow	✓	✓	✓	✓	✓
Thermodynamic laws	Ideal gas	cubic EoS GERG-2008*	cubic EoS	cubic EoS	cubic EoS
Non-isothermal flow	✓	✓	✓	✓	
Molecular diffusion		✓	✓	✓	✓
Mechanical dispersion			✓	✓	
Bio-chemical reactions		✓	REACT	✓	✓
Fractures	✓	✓		✓	
Spatial discretization method**	FV	FV	FV	FD	FD
Time discretization	Implicit	Implicit	Implicit	-	-
Wells	✓	✓	✓	✓	✓

* Under consideration
**FV: Finite Volume, FD:Finite Difference.

Table 4.1: Overview of commonly used tools for modeling UHS reservoirs.

The initial goal behind the development of ComPASS was to create geothermal simulator utilizing unstructured meshes. This simulator is designed to function within parallel distributed architectures while also considering fractures represented as co-dimension surfaces integrated with the surrounding matrix domain [114].

The selection of ComPASS for this PhD research was based on several factors. Firstly, ComPASS offers flexibility beyond that of commercial software. The tool's open-source nature allows users to access and modify the source code, enabling adaptations and enhancements to the model. Secondly, it is an in-house tool within the research institution where the PhD was conducted and it is in the institution's interest to further develop this tool for additional applications. Additionally, the proximity of the development team within this institution facilitated technical support and collaboration, making it a practical choice for the research.

The subsequent section 4.2, provides a general introduction to the governing equations. It begins with an overview of the hydrodynamic laws employed. This section will also explain the different formulations used for multi-phase compositional Darcy flows and the procedures governing phase transitions in the simulation of multi-phase flow.

In section 4.3, we delve into a detailed description of the equations governing ComPASS. Following this, the methodology section, section 4.4, outlines the development requirements of the thermodynamic model, the resulting modifications to the tool's implementation, and adjustments made to the phase transition algorithm to accommodate this model.
The results, section 4.5, will then showcase the numerical tests conducted to validate this model. It is important to note that the selection of the thermodynamic model was discussed in detail in section 3.3.

4.2 Multiphase compositional model: mathematical description

Numerical reservoir simulations of the storage model are built upon mathematical formulations that couple compositional multiphase flow with physical laws based on different models. These equations collectively form a complex, nonlinear system that must be efficiently solved to accurately describe the behavior of the reservoir. In this section, we present the key mathematical equations:

- The mole balance of each component+ thermal balance,
- the pore volume balance,
- the hydrodynamic laws,
- the thermodynamic laws.

The complexity of the system also depends on the number of components and phases considered.
To reiterate, fluids in the model can be in liquid, gaseous, or supercritical phases where a phase is a region of the fluid where the fluid properties are relatively consistent. In contrast, an interface arises when two or more phases come into contact, creating distinct regions with different properties. These interfaces, characterized by IFT (as introduced in section 2.2.4), act as boundaries between coexisting fluid phases, with variations in pressure within each phase. Multiple components can coexist within a single phase, and each component can also exist in different phases, and partition between phases at their interfaces.

The hydrodynamic laws encompass a set of differential equations derived by ensuring the molar conservation of each component. Specifically, generalized Darcy's law determines the velocity of a multiphase flow. These conservation laws, along with the thermal balance, will be explained in the upcoming subsection. These equations necessitate the incorporation of closure equations that ensure the nonlinear system to be well-posed. A significant challenge lies in accounting for phase transitions and phase transfer, which arise from the change-of-phase reactions assumed to be at thermodynamic equilibrium. Various formulations have been proposed to address this issue. The second subsection will delve into a limited body of literature concerning the most commonly used formulations.

To accurately describe the flow, it is imperative to include the thermodynamic aspect. This entails precisely delineating the evolution of the fluid mixture composition within the reservoir. This is achieved through the equilibrium equations described in the final subsection.

4.2.1 Conservation laws

The hydrodynamic model describes the flow and transport of various components within the porous media. Let $\mathcal{C}$ denote the set of chemical components (such as water, CO_2, H_2, and more), and consider a compositional model for a two-phase flow wherein α represents the phase within the set $\mathcal{P} = \{l, g\}$, with l for liquid phase and g for gas phase.

In this framework, we address the molar balance equation Eq.(4.1) for each component alongside the thermal balance equation (enthalpy advection and Fourier law) Eq.(4.2). It is essential to note that this framework does not consider diffusion.

$$\phi \partial_t n_i + \operatorname{div}\left(\sum_{\alpha \in \mathcal{P}} x_i^\alpha \zeta^\alpha \mathbf{q}^\alpha\right) = 0, \quad i \in \mathcal{C}. \tag{4.1}$$

Where $\mathbf{q}^\alpha$ is given the generalized Darcy's law, written as follow:

$$\mathbf{q}^\alpha = -\frac{kr^\alpha}{\mu^\alpha}\Lambda(\nabla P^\alpha - \rho^\alpha \mathbf{g}).$$

Here,

$$\rho^\alpha = (\sum_{i \in \mathcal{C}} x_i^\alpha M_i)\zeta^\alpha,$$

and

$$n_i = \sum_{\alpha \in \mathcal{P}} x_i^\alpha \zeta^\alpha S^\alpha.$$

Note that the ratio $-\frac{kr^\alpha}{\mu^\alpha}$ represents the mobility ratio presented in the section 2.
Whereas, the thermal balance is written as:

$$\phi \partial_t E_f + (1-\phi)\partial_t E_r + \operatorname{div}\left(\sum_{\alpha \in \mathcal{P}} h^\alpha \zeta^\alpha \mathbf{q}^\alpha - \lambda \nabla T\right) = 0; \tag{4.2}$$

with:

$$E_f = \sum_{\alpha \in \mathcal{P}} S^\alpha \zeta^\alpha e^\alpha; \tag{4.3}$$

$$e^\alpha = \left(\sum_{i \in \mathcal{C}} M_i x_i^\alpha\right) E^\alpha; \tag{4.4}$$

$$h^\alpha = \sum_{i \in \mathcal{C}} x_i^\alpha h_i^\alpha = \left(\sum_{i \in \mathcal{C}} M_i x_i^\alpha\right) H^\alpha. \tag{4.5}$$

Let $N_\mathcal{P}$ represent the number of phases and $N_\mathcal{C}$ represent the number of components present. The system corresponds to $2N_\mathcal{P} + N_\mathcal{C} N_\mathcal{P} + 1$ dependent variables, which arise from the diverse pressure (P^α) and saturation (S^α) of each phase, as well as the mole fraction of each component present in each phase (x_i^α), together with the temperature. However, the conservation laws (Eq.4.1-4.2) only furnish $N_\mathcal{C} + 1$ equations. In the instance of two phases and two components, such as in our example case, the total count of unknown variables will amount to nine, while the conservation equations will involve three equations. To successfully solve these equations, the system must be mathematically well-posed, implying that the count of unknowns must align with

the number of equations. This is achieved thanks to closure equations represented in Eq.(4.6), which take into account the relations between capillary pressure, volume conservation (phase saturation), and the equality of fugacities for each component in the different phases. Various formulations have been proposed to handle the resulting system of partial differential equations and local nonlinear equations. However, the main difficulty in these formulations persists in managing the appearance and disappearance of phases during the fluid, mass, and heat flows occurring in many of the multi-component and non-isothermal systems of interest. This will be the focus of the forthcoming section, where we will present several well-known formulations designed to tackle this issue.

4.2.2 Different formulations for modelling systems

Multiple formulations have been explored for compositional Darcy flows, encompassing both isothermal and non-isothermal scenarios. Different formulations exist for modeling two-phase compositional Darcy flows that account for phase transitions. These formulations diverge in terms of their choice of primary variables and equations, as well as their approach to managing phase changes - a significant challenge in this type of modeling. Formulations can be categorized into those with a change in the set of primary variables and those with persistent variables. In these formulations, temperature is considered as a variable. However, for the sake of simplification, it is omitted from the discussion and treated as if the processes are isothermal.

Formulations with a change in the set of primary variables adapt their primary variables and equations based on the present phases, which can vary spatially and temporally. One well-known formulation within this category is the Coats formulation (also referred to as the natural variables formulation), which depends on pressure, saturation, and molar fractions of the present phases, denoted as PSC (Pressure Saturation Concentration) [118]. Various other combinations of dependent persistent variables exist, such as pressure, saturation, and fugacities with complementarity conditions, referred to as PSF (Pressure Saturation Fugacities) hereinafter, [119]; gas pressure and liquid pressure, denoted as PPF (Pressure of gas Pressure of liquid Fugacities) [120]; and capillary pressure and gas pressure as primary variables [121]. Another study suggested the extension of saturation to negative values [122].

Comparisons between these different formulations can be found in the literature [123, 124, 112]. Although the natural variable formulation finds substantial use in reservoir simulation, alternative simulators have embraced diverse formulations. For instance, PSF formulation with complementarity conditions, was selected to simulate H_2 migration in nuclear waste storage studies [125].

The Natural Variable Formulation PSC uses what is commonly referred to as the switch of variable. This approach employs a set of unknowns defined by phase pressure (P^α), phase saturation (S^α), and molar fractions of components ($X^\alpha = (x_i^\alpha)_{i \in C}$) within each phase $\alpha \in Q$, where Q represents the set of present phases ($Q = \{g\}$ or $Q = \{l\}$ or $Q = \{g, l\}$) at each time-space point.

The previously outlined conservation equation system (4.14.2) is assumed to be in a system in local thermodynamic equilibrium and will be completed with the local closure laws typically encompassing the following constitutive relations:

$$\begin{cases} \sum\limits_{\alpha \in Q} S^{\alpha} = 1, \\ \sum\limits_{i \in \mathcal{C}} x_i^{\alpha} = 1, \quad \alpha \in Q, \\ P^{\alpha} - P^{\beta} = P_c^{\alpha,\beta}, \quad \alpha \neq \beta, \quad (\alpha, \beta) \in Q^2, \\ f_i^{\alpha} = f_i^{\beta}, \quad \alpha \neq \beta, \quad (\alpha, \beta) \in Q^2. \end{cases} \tag{4.6}$$

Here, S^{α} is the saturation, and $P_c^{\alpha,\beta}$ the capillary pressure in the phases$(\alpha, \beta) \in Q^2$ (Pa).

The system becomes constrained by one pore volume balance equation, $N_{\mathcal{P}}$ component mole balance equations, $N_{\mathcal{P}} - 1$ capillary pressure relations, $(N_{\mathcal{P}} - 1)N_{\mathcal{C}}$ equilibrium equations, and one thermal balance equation. For instance, in the case of two components and two phases, this yields the requisite 6 equations. The balance of equations and unknowns aligns with the number of phases.

The set Q, which accounts for phase transitions, is usually determined through a negative flash computation (for additional details, please refer to the appendix B). On a first approach, this computation should be performed at every Newton iteration step, making this formulation time-intensive and resource-intensive.

The partitioning of components across phases is considered to be at equilibrium, as it assumes that the timescale for mass transfer is greater than that of the flow. Should this not hold true, a kinetic term would be introduced to account for mass transfer. To accurately represent the physical evolution of components and mixtures, thermodynamic laws are engaged and introduced in the subsequent section.

The complementarity condition formulation PSF has a significant advantage compared to the previous one. It employs a fixed set of equations and unknowns, defined by the phase pressure P^{α}, the phase saturation S^{α} with $\alpha \in \mathcal{P}$, and the component fugacities f_i, where $i \in \mathcal{C}$ [119]. This means that the set of equations and unknowns remains constant and independent of the present phases, eliminating the need for a flash calculation. In fact, the flash is replaced with a non-linear system resolution for each phase separately.

By replacing the component molar fractions with fugacities $f_i^{\alpha}(P, X^{\alpha}), i \in \mathcal{C}$, the number of unknowns is reduced to $2N_{\mathcal{P}} + N_{\mathcal{C}}$ (+1 when including temperature). The component molar fractions are computed from the fugacities and the phase pressure, defined as the solution $\tilde{X}^{\alpha} = \tilde{x}_i^{\alpha}$, $i \in \mathcal{C}$, and $\alpha \in Q$, of a nonlinear system incorporating complementarity conditions to handle phase appearance and disappearance.

The key concept here is that a fluid phase appears or disappears if a physical quantity exceeds a given threshold. This approach transforms phase transitions into complementarity constraints, eliminating the need for negative flash calculations. The transition conditions are formulated as a set of local inequality constraints, which are integrated into the nonlinear solver using a nonlinear complementarity function.

The presence of a phase is determined by the saturation of that phase being greater than zero and the sum of the extended molar fractions equaling one. Conversely, the absence of a phase is determined by the saturation of that phase being equal to zero, and the sum of the molar fractions being less then one. This is effectively expressed through the complementarity expression :

$$min\left(S_\alpha, 1 - \sum_{i=1}^{N_\mathcal{C}} \tilde{x_i^\alpha}\right) = 0. \tag{4.7}$$

In the case of two phases $\mathcal{P} = \{l, g\}$, this formulation involves $N_\mathcal{C} + 5$ unknowns, including fugacities, pressure, and saturation. To close the system, it employs $N_\mathcal{C} + 1$ equations for conservation laws, along with one closure equation for capillary pressure, two complementarity conditions, which determine the presence of existing phases as stated in Eq.(4.7), one equation for the pore volume balance, and final one for the thermal balance.

The Pressure-Pressure formulation PPF initially was introduced for the case of two components [120], and afterwards extended to encompass general compositional two-phase flows. This expansion incorporates the use of fugacities in conjunction with the phase pressures. In this refined framework, the phase pressure P^α is extended for $\alpha = \{l, g\}$ even in the absence of that phase, and the capillary function $P_c(S_l)$ is extended by its monotone graph. Consequently, phase transitions are simplified to $S_l = (P_c)^{-1}(\tilde{P}_g - \tilde{P}_l)$, and the need for inequality constraints is eliminated.

In previous studies, a comparison was conducted between different formulations, such as PSC and PSF, revealing that the use of the PSF formulation with pressure, saturation, and fugacities as the primary unknowns introduces greater non-linearities into the system. Their numerical tests indicated that while both formulations yield similar physical results with fairly consistent behavior, certain exceptions were observed, such as in condensate gas test cases and near the critical point. In these scenarios, the complementarity formulation outperformed the PSC in terms of the number of time steps and Newton iterations required for convergence [124].

Another study compared the PSC, PSF, and PPF formulations, concluding that all three formulations offer equivalent definitions of phase transitions for gas-liquid thermodynamic models. Subsequently, a numerical comparison was performed to assess the solution accuracy and convergence behavior of the Newton-type nonlinear solver across various 1D and 3D test cases, including cases involving gas appearance and liquid disappearance. They concluded that the PSF and PSC formulations exhibited superior performance compared to the PPF formulation in the context of compositional gas-liquid Darcy flows, based on their suite of numerical experiments [123].

4.3 Multiphase compositional model in ComPASS

Different fluid physics modules exist in ComPASS, each denoted by specific names. These modules determine the number of phases and components, as well as the matrix representing the presence of components in phases. The following modules are distinguished:

- Immiscible2ph: Two phases (liquid and gas) and two components (water and air). Only water is present in the liquid phase, and air in the gas phase.
- Linear water: One phase (liquid) and one component (water).
- Water2ph: Two phases (liquid and gas) and one component (water).
- Diphasic: Two phases (liquid and gas) and two components (water and air). All components can be present in all phases.

In the context of this work, at least two components are required in the two possible phases. Therefore, our development will be based on the existing Diphasic module. The following section provides a detailed description of the existing mathematical and numerical diphasic model.

4.3.1 The compositional model formulation in the Diphasic module

The Diphasic module is originally defined for two components: water denoted as 'w', which can vaporize in the gas phase and another gaseous component (air or other gas) $j \in \mathcal{C} \setminus w$ that can dissolve in the liquid phase. This module comes with default physical properties including phase densities, viscosities, enthalpies, and component molar masses.

The number of unknowns in this module and the choice of main variables (temperature, pressure, and component molar fractions) are not fixed, which corresponds to the PSC formulation. The arbitrary number of unknowns depends on the number of the present phases ($2N_{\mathcal{P}}+N_{\mathcal{C}}N_{\mathcal{P}}+1$). Thus, the unknowns are defined based on the phase context: liquid, gas, or diphasic ($Q = \{g\}$ or $Q = \{l\}$ or $Q = \{g, l\}$). In contrast to the natural variable Coats-type formulation, this module handles phase transitions differently. It doesn't rely on the typical negative flash; instead, it employs the approach of phase appearance and disappearance established in the PSF formulation.

In addition to the molar conservation laws, thermodynamic relations are taken into consideration. It is assumed that each component achieves thermodynamic equilibrium between the two phases ($\alpha = \{l, g\}$, $\alpha \in \mathcal{P}$), which is represented by equal fugacities. The disappearance of a phase is determined by phase saturation, akin to the complementarity conditions described in Eq.(4.7).

Since the module is based on water and ideal gas mixtures, the need for a flash calculation is eliminated, avoiding the addition of a nonlinear problem. Several simplifications have been made to avoid this flash calculation.

The local closure equations are expressed as follows:

$$\begin{cases} \sum\limits_{\alpha \in \mathcal{P}} S^{\alpha} = 1, \\ \sum\limits_{i \in \mathcal{C}} x_i^{\alpha} = 1, \quad \alpha \in Q, \\ P^{\alpha} - P^{\beta} = P_c^{\alpha,\beta}, \quad \alpha \neq \beta, \quad (\alpha, \beta) \in Q^2, \\ f_i^{\alpha} = f_i^{\beta}, \quad \alpha \neq \beta, \quad (\alpha, \beta) \in Q^2. \end{cases} \tag{4.8}$$

Fugacities are calculated based on the ideal gas assumption. For the components in the gas phase, fugacities $f_i^g(X^g, P^g, P^l)$ are given by Dalton's law:

$$f_i^g = x_i^g P^g, \quad i \in \mathcal{C}. \tag{4.9}$$

Fugacities of components in the liquid phase depend on the component involved. For the dissolution of gaseous components in the liquid phase, fugacities are determined by Henry's law:

$$f_j^l = c_j^l H_j(T), \quad j \in \mathcal{C} \backslash \{w\}. \tag{4.10}$$

For water in the liquid phase, the fugacity is expressed using Raoult-Kelvin's law:

$$f_w^l = c_w^l P_{sat}(T) \exp\left(\frac{-(P^g - P^l)}{\zeta^l(P^l) R\, T}\right), \tag{4.11}$$

where P_{sat} is the vapor pressure of the water component given in Pa by the Clausius-Clapeyron equation.

$$P_{sat}(T) = 100 \exp\left(46.784 - \frac{6435}{T} - 3.868\, log(T)\right). \tag{4.12}$$

Based on these equations Eq.4.9-4.11, the equality of fugacities and the mole balance of each component, constitute a linear equation system. The algorithm in the Diphasic module begins by assigning a context and then proceeds to check each step for the appearance or disappearance of phases based on the following criteria:

$$\begin{cases} \text{If} \quad f_j^l + f_w^l > P_g, \quad \{l\} \to \{l, g\}, \quad \text{then } S_g = 0, \quad S_l = 1. \\ \text{If} \quad x_j^l + x_w^l > 1, \quad \{g\} \to \{l, g\}, \quad \text{then } S_g = 1, \quad S_l = 0. \\ \text{If} \quad S_g < 0, \quad \{l, g\} \to \{l\}, \quad \text{then } S_l = 1. \\ \text{If} \quad S_l < 0, \quad \{l, g\} \to \{g\}, \quad \text{then } S_g = 1. \end{cases} \tag{4.13}$$

The calculation of fugacities and the criteria for phase appearance and disappearance are based on ideal mixture assumptions. Nevertheless, it is important to note that this ideal mixture assumption doesn't hold for all components. To achieve a more accurate determination of fluid density and precise evaluation of phase equilibria, a more sophisticated approach for calculating fugacities is necessary. Additionally, a more refined method is required for handling phases. This sets the stage for the upcoming section, which delves into the integration of the thermodynamic module into ComPASS. It outlines the necessary adjustments for this integration, along with the simulator's approach to managing phases.

4.3.2 Numerical implementation

The mathematical equations presented earlier (comprising closure equations and flow equations) are discretized using fully implicit Euler integration in time and a finite volume scheme with node-centered discretization, known as the Vertex Approximate Gradient scheme (VAG) in the spatial domain [126].

The reservoir's volume mesh, denoted as M_h, is subdivided into numerous control volumes, represented by $cv \in CV$ (as shown in Fig.4.1a). The previously introduced laws apply within

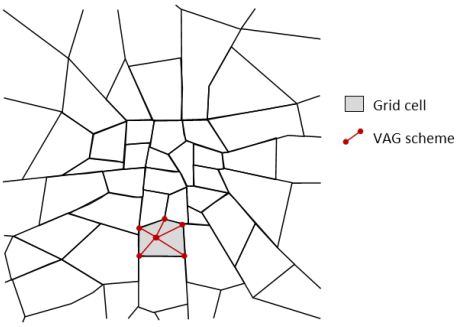

(a) 2D Grid Cell Representation in the VAG Scheme.

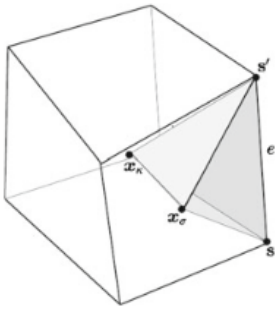

(b) 3D Tetrahedral Representation of the VAG Concept. [126]

FIGURE 4.1: Visualization of VAG Schemes in 2D and 3D.

these control volumes. The VAG scheme proposes a discretization based on tetrahedral sub-meshes, with x_K representing the cell center. Therefore each control volume is decomposed into tetrahedron (as illustrated in Fig.4.1b).

The process of discretization in space and time results in a nonlinear equation at each time step. The number of equations is equal to the number of control volumes multiplied by the number of primary variables, referred as the degrees of freedom.

The iterative procedure employed to solve this equation system follows the algorithm described below:

1. **Initialization:** The problem begins with the initialization of the grid, definition of initial conditions, and loading of the relevant fluid physics (Immiscible2ph or diphasic, etc.) .

2. **Time Stepping:** The defined time period is divided into a series of time steps. Each time step encompasses various Newton iterations for distinct control volumes.

3. **Newton Iterations:** The Newton iterations aim to solve the equation system as described below.

   a) Calculate the Jacobian matrix and the vector of residuals.

   b) the result is a linear equation system that could be solved to find the change in solution, denoted as δX_h : $J(X_h)\delta X_h = -R(X_h)$, where J is the Jacobian matrix, X_h is the set of unknowns, δX_h represents the change in the solution vector, and R is the residual vector.

   c) Update the solution: $X_{h+1} = X_h + \delta X_h$.

   d) Convergence is defined as the maximum relative or absolute error between the new solution vector and that of the previous iteration.

4. **Simulation Completion:** When the convergence criterion is met, the solution is recorded, and a new time step begins. The simulation continues until the final simulation time is reached.

The set of unknowns can be divided into two distinct categories. The first category consists of a set of unknowns, denoted as X_h^n, representing the vector of discrete unknowns across the entire mesh. The remaining unknowns belong to the second category, where X_{cv}^n represents the vector of unknowns within the volume $cv \in CV$ at the time step n of the discrete times. The X_h^n unknowns are directly tied to conservation laws, while the X_{cv}^n set of unknowns is effectively resolved through closure conditions. Consequently, the non-linear system takes the following form:

$$\begin{pmatrix} R_{\text{cv}}(X_h^n) \\ F_{\text{cv}}(X_{\text{cv}}^n) \end{pmatrix}_{cv \in CV} = 0, \tag{4.14}$$

Where $R_{\text{cv}}(X_h^n)$ is the set of discrete conservation equations, and $F_{\text{cv}}(X_{\text{cv}}^n)$ is the set of discrete closure equations and thermodynamic equilibrium equations, with specifics tailored to the context within each control volume $cv \in CV$.

At each discrete time step, and by excluding the time step, n, subscript for simplification, the non-linear system is resolved through the iterative Newton algorithm. In every iteration of this algorithm, a corresponding linear system must be addressed and resolved:

$$\begin{pmatrix} \frac{\partial R_{\text{cv}}}{\partial X_h} \\ \frac{\partial F_{\text{cv}}}{\partial X_{\text{cv}}} \end{pmatrix}_{cv \in CV} \delta X_h = - \begin{pmatrix} R_{\text{cv}}(X_h) \\ F_{\text{cv}}(X_{\text{cv}}) \end{pmatrix}_{cv \in CV}, \tag{4.15}$$

Within this equation, $\frac{\partial R_{\text{cv}}}{\partial X_h}$ signifies the Jacobian of the system R_{cv}, and $\frac{\partial F_{\text{cv}}}{\partial X_{\text{cv}}}$ signifies the Jacobian of the system F_{cv}. Meanwhile, δX_h represents the discrepancy between the vector X_h in the current iteration and that in the subsequent iteration.

To simplify the computational process and reduce the matrix size, X_{cv} is divided in two groups. The first set of $N_{\mathcal{C}} + 1$ unknowns referred to as the primary unknowns, X_{cv}^p , and the remaining unknowns are grouped as the secondary unknowns denoted as X_{cv}^s. This is applied for every control volume and depends on the phases present. In ComPASS framework, the primary unknowns encompass the pressure of a single phase, temperature, molar fractions of $N_{\mathcal{C}} - 2$ components within the phase, and saturation. In scenarios involving a single phase, primary variables shift to encompass pressure, temperature, and the molar fractions of $N_{\mathcal{C}} - 1$ components within the phase. The complementary unknowns are determined through closure equations.

In the gas phase:

$$\begin{aligned} X_{\text{cv}}^p &= \{P^g, T, (x_i^g)_{i=1,N_{\mathcal{C}}-1}\}, \\ X_{\text{cv}}^s &= \{S_g, x_{N_{\mathcal{C}}}^g\}. \end{aligned}$$

In the liquid phase:

$$\begin{aligned} X_{\text{cv}}^p &= \{P^l, T, (x_i^l)_{i=1,N_{\mathcal{C}}-1}\}, \\ X_{\text{cv}}^s &= \{S^l, x_{N_{\mathcal{C}}}^l\}. \end{aligned}$$

In the biphasic context:

$$
\begin{aligned}
X^p_{\text{cv}} &= \{P^g, T, S^g, (x^g_i)_{i=1,N_C-2}\},\\
X^s_{\text{cv}} &= \{S^l, P^l, x^g_{N_C-1}, x^g_{N_C}, (x^l_i)_{i=1,N_C}\},\\
&\text{or}\\
X^p_{\text{cv}} &= \{P^g, T, S^g, (x^l_i)_{i=1,N_C-2}\},\\
X^s_{\text{cv}} &= \{S^l, P^l, x^l_{N_C-1}, x^l_{N_C}, (x^g_i)_{i=1,N_C}\}.
\end{aligned}
$$

In the context of our specific system (H_2-CO_2), the ideal gas approximation we mentioned earlier breaks down. Consequently, employing a more complex thermodynamic model becomes imperative to accurately predict fluid properties and predict phase equilibria in such fluid mixtures. This will be the task treated in the next section.

4.4 Methodology

In this section, we delve into the methodology used for implementing SRK EoS and adapting it into ComPASS to handle phase transitions.

The choice of the SRK/PR EoS was based on its proven accuracy and versatility in modeling phase equilibria section 3.5. It offers a robust model for our reservoir simulator. Among the array of potential thermodynamic models explored in section 3.2, it became apparent that, for diverse gas mixtures, the multi-parametric GERG-2008 equation offers greater accuracy. While the numerical thermodynamic model code was formulated and utilized to generate Fig.3.3, further consultation and evaluation led us to opt for a conventional cubic EoS model integration. This decision was motivated by two principal factors. Firstly, it was chosen to avoid the potential convergence challenges associated with the GERG-2008 equation. Secondly, considering the anticipated time commitment for this task, a pragmatic approach was taken, commencing with the cubic EoS.

Therefore, the next section will delve into the development of the autonomous cubic SRK/PR EoS module and its integration with ComPASS. Subsequently, it will address the necessary adaptations for the existing flash algorithm that is grounded in the ideal gas theory. We will begin with the mathematical description of the chosen EoS and phase transition, and afterwards discuss the numerical implementation with developmental considerations.

4.4.1 Mathematical description

This section concerns the implementation of a thermodynamic module for a cubic EoS that can accommodate both the PR or SRK variants (as discussed in the section 3.4.1). The model was developed to be adaptable to either ramification of the cubic EoS, allowing flexibility in selecting either the PR or SRK formulations. This independent module is based on a general equation, which is detailed in Appendix C.4.1 and includes the equations specified in Eq.(3.11) and Eq.(3.12).

The primary purpose of the thermodynamic model is to provide fugacity coefficients, which play a crucial role in predicting phase equilibria in multi-component systems. While fugacity

coefficients do not directly govern transport properties like viscosity and thermal conductivity, they indirectly influence phase compositions, densities, and intermolecular interactions, making them essential for phase equilibrium predictions, such as vapor-liquid equilibrium or liquid-liquid equilibrium.

The fugacity is a measure of the partial molar Gibbs residual energy of real gas, that provides the value of the chemical potential for the real gas. In fact, it has the unit of pressure and it is considered as an effective pressure. The relationship between the fugacity and the measured pressure is defined by the fugacity coefficient. For a component i in a mixture, the fugacity f_i can be expressed as:

$$f_i^\alpha = \varphi_i^\alpha x_i P^\alpha \tag{4.16}$$

When a component behaves as an ideal gas, the fugacity is equal to $x_i P$, and the fugacity coefficient remains at unity, simplifying the fugacity calculation.
In general, for a component i in mixtures, the fugacity f_i is related to its molar density n_i (moles per unit volume) and the compressibility factor, Z, by the equation:

$$f_i = n_i \cdot \frac{RT}{V} \cdot Z$$

Where V is the molar volume (volume per mole) of the phase. In the case of ideal gas ($Z = 1$), the fugacity-density relation simplifies to:

$$f_i = n_i \cdot \frac{RT}{V}$$

However, for real fluids mixtures, the fugacity of a component i can be related to the chemical potential using the following equation:

$$\boldsymbol{\mu}_i(T, P, \boldsymbol{N}) - \boldsymbol{\mu}_i^{\text{ideal},0}(T, P, \boldsymbol{N}) \equiv RT \ln \frac{f_i(T, P, \boldsymbol{N})}{x_i\, P^\alpha} = RT \ln \varphi_i(T, P, \boldsymbol{N}) \tag{4.17}$$

In this equation, $\boldsymbol{N} = (N_i)_i$ is the number of mole for each component. $\boldsymbol{\mu}_i^{\text{ideal},0}(T, P)$ is the chemical potential of an ideal gas. For a more detailed exploration of how the ideal gas contribution is explicitly calculated, please refer to Appendix C.2.1.4.

In the module Diphasic of ComPASS, the fugacity of ideal gas was considered equal to the pressure and the fugacity coefficient was set to one as in Eq.(4.9). Now, an EoS is required to estimate the fugacity. The EoS such as SRK or PR provides an equation for pressure as a function of temperature, molar volume, and composition, allowing the determination of fugacity and fugacity coefficients.

4.4.1.1 Fugacity from a cubic EoS

The fugacity is a derived property that relies on the residual Helmholtz free energy using Eq.(4.18). In fact, the residual Helmholtz is the result of the integration in volume of the pressure equation at constant temperature and composition $P(T, V, \boldsymbol{N})$. Prior to the integration, the pressure term in Eq.(C.3) as described in Appendix C, section C.2.1, is substituted with the pressure explicitly provided by the EoS, as shown in Eq.(C.49). This integration process ultimately yields the

expression provided in Eq.(C.53). The fugacity coefficient, φ_i, is determined for each component i and for the different phases using the following equation:

$$ln(\varphi_i^\alpha) = \frac{1}{RT}\left(\left.\frac{\partial A^{\text{res}}}{\partial \boldsymbol{N}}\right|_{T,V}\right)_i - \ln Z \tag{4.18}$$

4.4.1.2 Derivation of thermodynamic properties for cubic EoS

This cubic EoS are represented as pressure-explicit forms, $P = P(T, V, \boldsymbol{N})$. In this formulation, pressure is the dependent variable, while temperature and molar volume serve as the independent variables. Note that some EoS may be expressed in terms of volume, $V = V(T, P)$, derived from extensive experimental volumetric data, which are rarely available. In most of the cases, the EoS equations are pressure explicit, as is the case for our application.

However, ComPASS is built on a framework that employs the variable $(T, P, \boldsymbol{N})$ where the pressure replaces volume compared to the typical formulation of EoS. This requires then the computation of the function $V(T, P, \boldsymbol{N})$ based on the function $P(T, V, \boldsymbol{N})$. Initially, thermodynamic variables are presented as functions of $(T, V, \boldsymbol{N})$ but are subsequently transformed into functions of $(T, P, \boldsymbol{N})$. This transformation process is further elaborated in Appendix C.2.3. Actually, the Jacobian vector R_{cv}: $\frac{\partial R_{\text{cv}}}{\partial X_h}$ written in the Eq.(4.15) comprises the set of partial derivatives of the conservation equations with respect to the primary variables $(T, P, \boldsymbol{N})$. As such, we require the expression and the derivatives of quantities such as density, chemical potential, internal energy (U), enthalpy (H), and Gibbs free energy (G). These derivations are initially developed from the provided function $(T, V, \boldsymbol{N})$ as detailed in the appendix C.2.2.1. Subsequently, through the transformation developed in Appendix C.2.3, we obtain the necessary quantities to populate the Jacobian matrix.
Furthermore, we account for the Péneloux volume translation, as defined in section 3.4.1, and discuss its impact on derivatives in section C.4.3. These developments are essential to meet the requirements of the Newton method and the main algorithm used in ComPASS.

4.4.1.3 Phase equilibria

The cubic EoS provides predictions for the fugacity coefficient, φ_i, for each component (i) in a mixture. These coefficients play a pivotal role in understanding the equilibrium properties of the fluid, governing phase behavior and other thermodynamic properties. Phase transitions are important in reservoir simulation, as they dictate the behavior of fluids under varying conditions. Phase transition adaptation to handle the phase equilibria -the appearance and disappearance of the phase- remains the challenge here to replace the combination of Raoult's law and Henry's law. In this section, we represent the methods used to determine phase composition, transition, and transfer, tailored to the consideration of non-ideal gas mixtures.

The phase composition is calculated through the assumption that the phases are in thermodynamic equilibrium, referring to equal fugacities. To accurately represent phase transitions, we have integrated principles of thermodynamic equilibrium into our model. This ensures that phases coexist at the same pressure and temperature, adhering to thermodynamic laws. Throughout

each Newton iteration, we continually update phase compositions and various hydrodynamic parameters.

To address phase appearance and disappearance during transitions, we have modified complementarity conditions, as initially defined in section 4.3.1. These conditions guarantee consistency between phase saturation and component molar fractions. In addition to considering saturation and concentration conditions, we have introduced capillary pressure conditions to account for the effects of capillary forces.

$$\begin{cases} \exists P^g_{eq}, x^g_{i\,\mathrm{eq}} : \left(f^l_{ref}(T, P^l_{ref}, x^l_{i\,\mathrm{ref}}) = f^g_{eq}(T, P^g_{eq}, x^g_{i\,\mathrm{eq}})\right) \wedge \left(P^g_{eq} \geq P^l_{ref}\right), \\ \quad \{l\} \rightarrow \{l, g\}, \quad \text{then } S_g = 0, \quad S_l = 1 \\ \exists P^l_{eq}, x^l_{i\,\mathrm{eq}} : \left(f^g_{ref}(T, P^g_{ref}, x^g_{i\,\mathrm{ref}}) = f^l_{eq}(T, P^l_{eq}, x^l_{i\,\mathrm{eq}})\right) \wedge \left(P^l_{eq} \geq P^g_{ref}\right), \\ \quad \{g \ \rightarrow \{l, g\}, \text{ then } S_g = 1,\ S_l = 0 \\ \text{If } S_g < 0,\ \{l, g\} \rightarrow \{l\}, \text{ then } S_l = 1 \\ \text{If } S_l < 0,\ \{l, g\} \rightarrow \{g\}, \text{ then } S_g = 1 \end{cases} \tag{4.19}$$

where $f^\alpha_{ref}, P^\alpha_{ref}, x^\alpha_{i\,\mathrm{ref}}$ represent the fugacity, pressure, and the mole fraction of the components of the existing phase and the $f^\alpha_{eq}, P^\alpha_{eq}, x^\alpha_{i\,\mathrm{eq}}$ are the fugacity, pressure, and mole fraction of the components of the possible phase in equilibrium with the existing reference phase.

The conditions outlined here provide a robust framework for handling phase equilibria within the ComPASS model. Notably, we have explored the possibility of employing a negative flash, as briefly mentioned in section 4.2.2. A multiphase flash capable of handling at least three phases (Vapor-Liquid-Liquid equilibrium) was developed. Details of this thermodynamic flash are provided in the appendix B. While this code was initially designed for thermodynamic equilibrium with phases at identical pressures, we later adapted it to accommodate different phase pressures, thereby considering capillary forces. However, this endeavor encountered several challenges and complexities (the algorithm runs indefinitely in a loop), leading us to revert to the existing version of the algorithm.

Considering that the switch-variable formulation tends to be computationally expensive, requiring local solution of a nonlinear system of equations with the size of all thermodynamic quantities essential for solving the partial differential equations [119], such computational demands could potentially be impractical.

4.4.2 Numerical description

To integrate the cubic EoS model into the open-source tool, we have developed custom code modules responsible for calculating phase properties and properties of fluids based on the selected EoS. The model utilizes advanced numerical methods, enabling efficient solutions to complex phase transition problems. In this section, we will delve into the intricacies of these numerical methods and the strategies employed for their implementation.

The thermodynamic module was designed to be user-friendly and flexible, allowing users to have control over the model's behavior. Initially, the user specifies the choice of EoS branch (PR or SRK) and identifies the relevant components in the system under study. Furthermore, the model may require user input for interaction parameters. This crucial step involves structuring

data as a library of components and their properties. Each fluid component is characterized by key parameters, including P_c, T_c, ω, and M. This data organization is done in YAML (Yet Another Markup Language) format.
Additionally, this integration entails the development of independent functions and subroutines. These structures serve as an interface between the user and the underlying thermodynamic model, enabling users to define components and manipulate parameters. Even though crucial, the wrapping work (bridging the communication between FORTRAN and Python) is not our primary focus in this context. Instead, our emphasis lies on the phase transition algorithms, which present significant challenges.

Note that the EoS module's validity and accuracy were rigorously assessed through properties validation and comparative analyses against other existing codes and open-source simulators. We conducted comparisons with tools like Thermobank and other Python-based phase equilibrium calculation codes. Furthermore, to ensure the model's reliability, we performed numerical checks on the derivatives.

Concerning the phase equilibrium calculation, the code was also written in FORTRAN and implements a numerical algorithm for finding equilibrium conditions between two phases of a two-component fluid system. The code aims to find the equilibrium pressure (P_{eq}^{β}) and composition ($x_{i\mathrm{eq}}^{\beta}$) of the second phase (β) that is in equilibrium with a reference phase (α) at a given temperature (T), reference pressure (P_{ref}^{α}), and reference composition ($x_{i\mathrm{ref}}^{\alpha}$).

In the above, the algorithm follows an iterative approach to converge to the equilibrium state. The following gives an overview of the main components and steps in the code.
The main subroutine performs the equilibrium calculation for one attempt, taking the reference phase and equilibrium phase as inputs and iteratively adjusting the equilibrium pressure and composition of the other phase. It uses a Newton-Raphson type of iteration to find the roots of a function. In this case, the function being reduced to zero is the difference in fugacities between the reference and equilibrium phases. The algorithm aims to find the pressure and composition that cancel this function and therefore finds the equilibrium pressure and composition.

However, a challenge in finding these equilibrium solutions may arise due to discontinuities or holes in the Newton's solution domain, requiring the algorithm to be guided to reach a stable solution. Here we first detail the Newton Raphson iteration process, accompanied with the stability test. Afterwords, there is a retry mechanism incorporated to handle situations of instability or non-convergence. The Newton-Raphson-like approach converges towards stable equilibrium and provides informative feedback through the 'INFO' variable:

1. It calculates the fugacity of the reference phase (f_{ref}^{α}) using the provided thermodynamic model and data (T, P_{ref}^{α}, $x_{i\ \mathrm{ref}}^{\alpha}$). It also checks the stability of the reference phase (INFO = 1 : target state for reference phase is not stable).

2. It initializes the equilibrium pressure (P_{eq}^{β}) and composition ($x_{i\ \mathrm{eq}}^{\beta}$) using the provided initial guesses (P_{eq0}^{β}, $x_{i\ \mathrm{eq0}}^{\beta}$).

3. The loop iterates for a maximum number of iterations or until the desired convergence is achieved. In each iteration:

- It calculates the fugacity of the current candidate state for equilibrium phase (f_{eq}^{β}).
- It computes the derivatives and differences of the fugacities to update the equilibrium pressure and composition based on Newton-Raphson strategy.
- If the composition goes beyond the bounds [0, 1], it adjusts it to be within those bounds.

4. If the desired convergence is achieved, the subroutine returns with the updated equilibrium conditions. If convergence is not achieved within the maximum number of iterations, appropriate INFO codes are set (-1 or -2) to indicate the status.

   - INFO $= -1$: non convergence, newton iteration encountered an unstable state for equilibrium phase
   - INFO $= -2$: non convergence, maximum iteration number exceed.

The algorithm provides additional handling for instability or non-convergence through a retry mechanism to the equilibrium search process.
If instability is encountered during the Newton iteration (INFO $= -1$) or the equilibrium phase is unstable (INFO $= 2$), it adjusts the initial guesses for pressure and composition based on the last stable values and retries the calculation. The iteration process is retried to navigate around potential solution gaps. The number of retries is controlled by the retry parameter. If after retries, convergence is not achieved (INFO $\neq 0$), the INFO code is set to -1 to indicate failure.

Overall, this code is used to find equilibrium conditions for a multi-component fluid system by iteratively adjusting the pressure and composition of the equilibrium phase. It accounts for cases where the initial guesses or initial equilibrium state are not suitable for convergence, and it attempts to refine these guesses to achieve convergence. It incorporates stability checks, iterative methods, and a retry mechanism to ensure convergence and robustness in finding the equilibrium state.

Based on the equilibrium calculation established earlier, we update the existing phases whether transitioning from one phase to a two-phase mixture or one phase system persists. Depending on the outcome (INFO value), the subroutine updates the properties of the reservoir object accordingly. If successful equilibrium is achieved between the reference phase and the potential other phase, it switches the system to a diphasic context, updates phase saturation and component fractions for gas and liquid phases.

As represented in the section 4.3.1, the switching between diphasic states is based on checking the saturation levels of both the liquid and gas phases. The saturation values control the phase context and phase saturation. If one of the phases vanishes (negative saturation), the system switches to the phase that remains.

The following figures (Fig.4.2 and Fig.4.3) visually depict the behavior of bubble and dew states respectively, under specific thermodynamic conditions (in this case T =290K). These figures present a comprehensive view of the equilibrium states of a mixture H_2-CO_2 in terms of pressure, and H_2 mole fraction. Each figure consists of two subplots, where the left subplot illustrates the equilibrium pressure of the corresponding phase and the right subplot illustrates

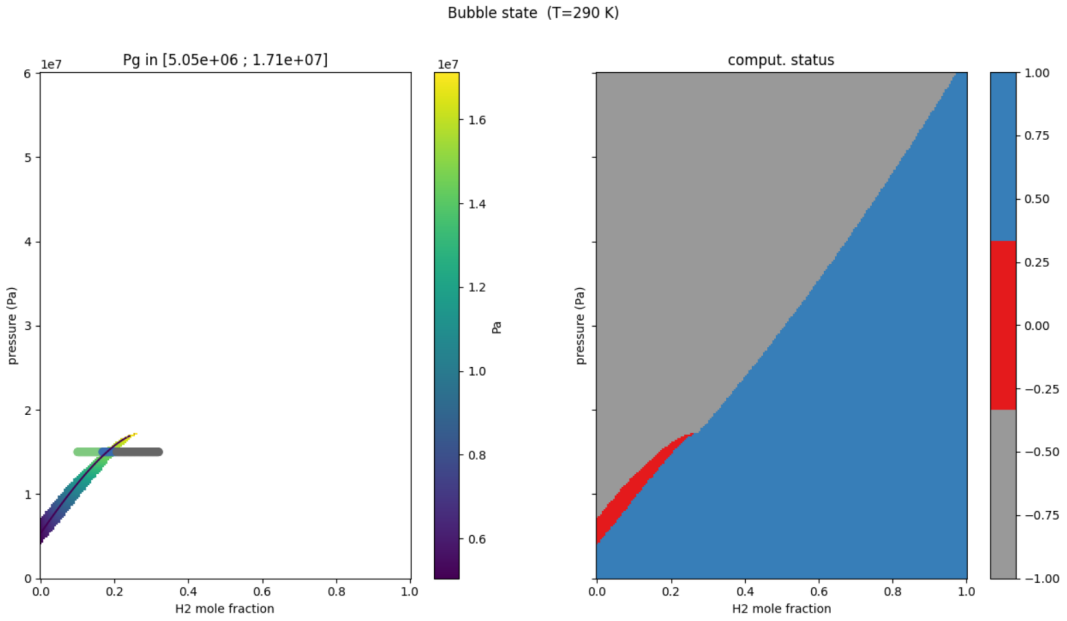

FIGURE 4.2: Equilibrium behavior of a CO_2 and H_2 mixture at a temperature of 290K, highlighting the gas phase equilibrium pressure in the left subplot, along with computational details in the right subplot. The black line indicates points of equal pressure for the two phases, suggesting a potential two-phase system.

the computational status. The color-coded pseudo-color plots in the subplots at left display the calculated values of the equilibrium pressures of the gas (P_g in Fig.4.2) or the liquid (P_l in Fig.4.3) phases. The black line represents the points where the two phases pressures are equal, and therefore possibility to shift into a two phase system, provided that the entry pressure

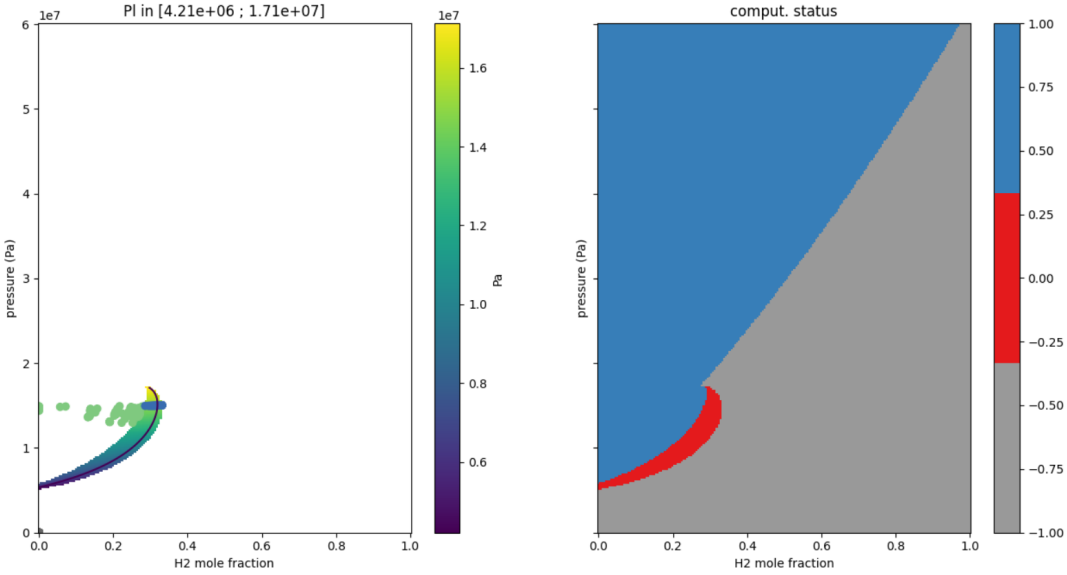

FIGURE 4.3: Equilibrium behavior of a CO_2 and H_2 mixture at a temperature of 290K, highlighting the liquid phase equilibrium pressure in the left subplot, along with computational details in the right subplot. The black line indicates points of equal pressure for the two phases, suggesting a potential two-phase system.

condition is included. The color code of the right subplots corresponds to the computational status of convergence (referring to INFO defined previously), aiding in the visual assessment of the solution's reliability. Additionally, in the left subplots, we have illustrated the calculated bubble and dew state points at a fixed pressure $1510^6 Pa$. These points represent the equilibrium pressure values determined during the Newton iterations. The color code was added to indicate their computational status - green for "INFO=1" and gray for "INFO=0".

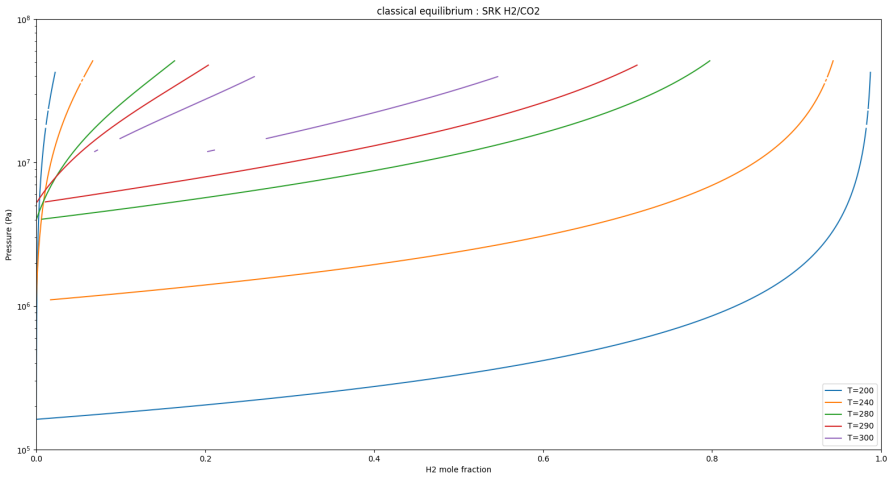

FIGURE 4.4: The dew and bubble curves at various temperatures (200 K, 240 K, 280 K, 290 K, and 300 K), presented in a pressure versus H_2 mole fraction diagram. These curves vividly depict the evolution of phase equilibria as temperature varies.

The Fig.4.4 is another plot that showcases the dew and bubble curves for varying temperatures (200 K, 240 K, 280 K, 290 K, and 300 K). This plot is presented as a pressure versus H_2 mole fraction diagram. These curves provide a clear depiction of how the phase equilibria evolve as the temperature changes. The plot includes regions, at high pressure, where equilibrium could not be found due to the non convergence of the algorithm. This observation offers insights into the limitations and challenges of the computational approach when using cubic EoS.

Overall, these figures provide valuable insights into the phase equilibria of the mixture at various compositions and pressures, facilitating a deeper understanding of the system's behavior under different conditions, while also addressing scenarios where equilibrium could not be established due to instability issues.

To verify the accuracy of the adapted SRK model associated to the phase transition and transfer, we conducted extensive validation tests against known phase behavior data. These tests ensured that the model faithfully reproduced phase transitions in reservoir simulations. In the following section we run examples that test the phase behavior and transition under different conditions.

4.5 Results

In this section, we present the results of the simulations conducted in ComPASS. Given our primary focus on testing and understanding the challenges arising from the physical aspects, we maintain a straightforward geometry, including quasi 1-D flow in homogeneous media, and gradually move towards more complex 3D simulations.

Due to the nature of these test cases, which required a two-phase well module not present in the used version of ComPASS, we made necessary additions to the code and equations. Specifically, we introduced a volumetric matter source, analogous to the existing heat source within the tool. This adjustment transformed the molar balance Eq.(4.1), as shown in Eq.(4.20). It is worth noting that, as of this version, the simulator does not account for hydrodynamic dispersion or diffusion.

$$\phi \partial_t n_i + \operatorname{div}\left(\sum_{\alpha \in \mathcal{P}} x_i^\alpha \zeta^\alpha \mathbf{q}^\alpha\right) = \mathcal{F}_i, \quad i \in \mathcal{C}. \tag{4.20}$$

The following test cases are presented to address specific challenges and gain insights into the behavior of our model under different conditions.

4.5.1 Case study 1: one-component (CO_2), two-pressure initial state

In this case study, we examine 1-D two-phase flow involving CO_2 within two adjacent homogeneous zones (Ω_1 and Ω_2). The media characteristics include a porosity of 0.15, permeability of $5^{-14} m^2$, bulk and thermal conductivity of $2\,W/m/K$. Each of these zones is characterized by uniform pressures, and they begin in a state of disequilibrium. Specifically, the right zone Ω_1 contains CO_2 in its liquid state, marked by a distinct liquid pressure. In contrast, the adjacent left zone Ω_2 contains CO_2 in its gaseous state, with a different gas pressure, as illustrated in Fig.4.5. The flow occurs due to the relaxation of this initial disequilibrium state. It is important to note that there's no interaction between this enclosed system and the external environment, and gravitational effects are neglected. Additionally, throughout the domain, the volumetric source terms for both components are set to zero.

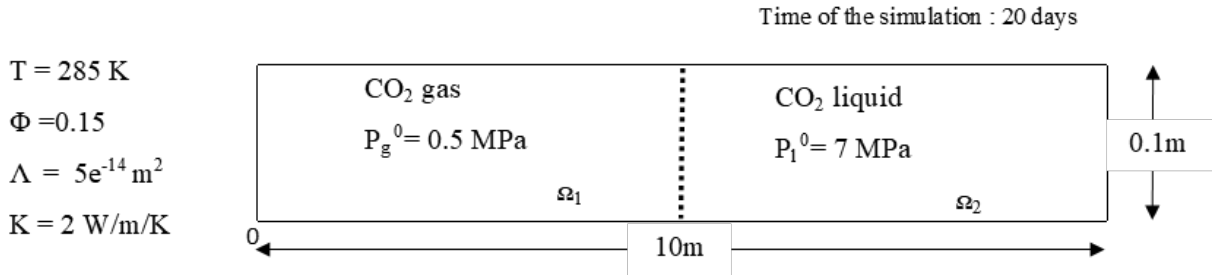

FIGURE 4.5: Case study 1: Domain properties and Boundaries.

As shown in Fig.4.6, the saturation front of gas, initially located at $x = 5\,m$, moves towards the abscissa $x = 10\,m$ as the system evolves from its initial state to an equilibrium state, after 20 days. In this case, there is no phase change; rather, the system is evolving towards thermodynamic equilibrium.

It is well-established that, due to the local mechanical equilibrium of the porous medium, the pressures of the liquid and gas phases must be continuous. Our focus here is on the return to this mechanical equilibrium for a system that starts with initial conditions that do not adhere to pressure continuity.

As expected, the behavior of the cell pressure curve demonstrates that the initially unbalanced system (mechanical imbalance due to the discontinuity of gas pressure) evolves towards a stationary equilibrium state. In this case, the equilibrium state is uniform, given the absence of material injection or withdrawal.

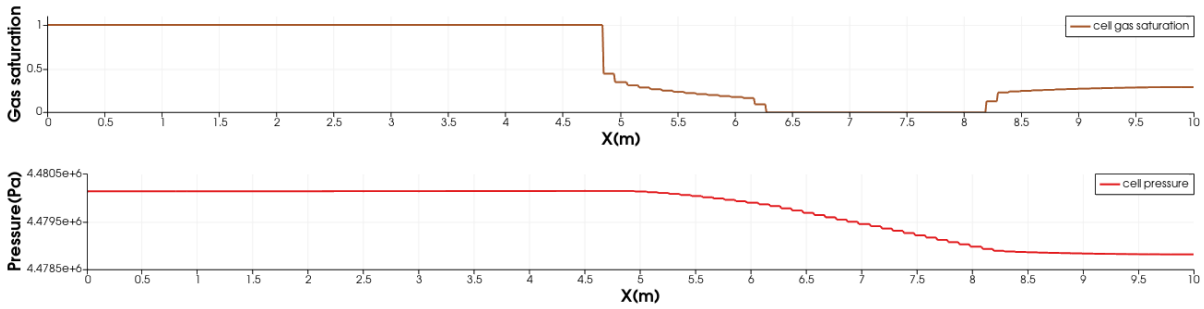

FIGURE 4.6: Pressure and saturation profile following the length of the domain at end time of the simulation (20 days).

4.5.2 Case study 2: Phase change in a saturated gas phase (CO_2)

In this case study, we initially explore the behavior of a CO_2 gas-saturated media. The media characteristics include a porosity of 0.15, permeability of $5^{-14}m^2$, bulk and thermal conductivity of $2\,W/m/K$. The volumetric source term for the CO_2 and for H_2 is set to zero throughout the domain. Injection in this case is represented by a volumetric flow rate introduced through Neumann boundary conditions. This test case aims to demonstrate the model's ability to account for the appearance of a liquid phase from a completely saturated gas state due to changes in pressure.

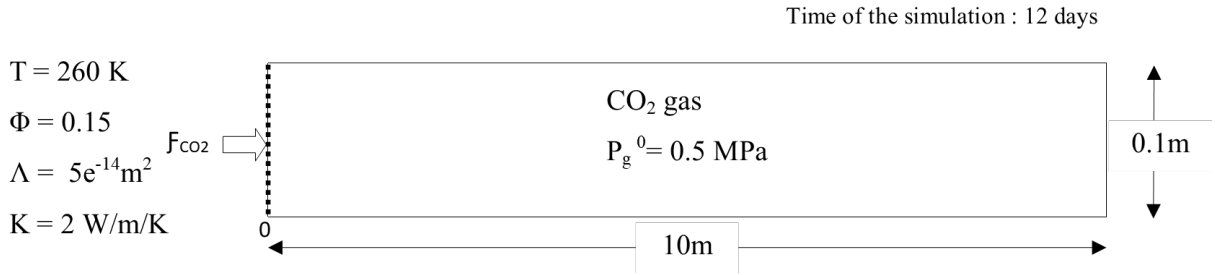

FIGURE 4.7: Case study 2: Domain properties and Boundaries.

As the simulation progresses, variations in pressure trigger the phase change of the fluid. The system transitions through an unsaturated state where both gas and liquid phases coexist along the axis. Eventually, a diphasic zone forms from $0.91\,m$ to $1.52\,m$, followed by a fully liquid-saturated zone (Fig.4.8).

The initial pressure is set at 0.5 MPa, and it increases over time to reach 2.5 MPa. This pressure change induces the phase change of the gas to the liquid phase, initially as a thin layer on top of the gas. As the pressure continues to rise to 6 MPa by the end of the simulation, the liquid region thickens. At the conclusion of the simulation, two distinct phases are formed, separated by a diphasic zone.

The addition of matter to the system, represented by the non-zero Neumann boundary condition, leads to an increase in pressure. Eventually, the pressure reaches the saturation pressure of CO_2 at this temperature, and the simulation algorithm successfully manages the appearance of a liquid phase in this single-component enclosed system.

4.5.3 Case study 3: Two-component, two-pressure initial state

In this case study, we examine a system enclosed without any mass exchange with the external environment. The volumetric source terms for both components are set to zero throughout the domain. Gravity effects are neglected. The media characteristics include a porosity of 0.15, permeability of $5\,^{-14}m^2$, bulk and thermal conductivity of $2\,W/m/K$. The system consists of two components, namely CO_2 and H_2. The initial conditions are set out of equilibrium, with distinct pressures in two adjacent zones (Ω_1 and Ω_2). The left zone Ω_1 contains CO_2 in its gaseous state at a pressure of 0.5 MPa, while the adjacent right zone Ω_2 contains H_2 in its gaseous state at a different pressure of 0.2 MPa (Fig.4.9).This initial condition introduces a mechanical imbalance due to the pressure discontinuity, as the pressures of the liquid and gas phases must be continuous. This case aims to observe the behavior of such a system and its evolution towards equilibrium. The flow is produced by relaxation of the initial non equilibrium.

However, there are no phase changes occurring. Instead, the main emphasis is placed on observing how pressure continuity is eventually achieved throughout the system. In Fig.4.10, we can visually track how the pressures and saturation profiles evolve along the length of the domain at the end of the simulation, representing the system under mechanical equilibrium.

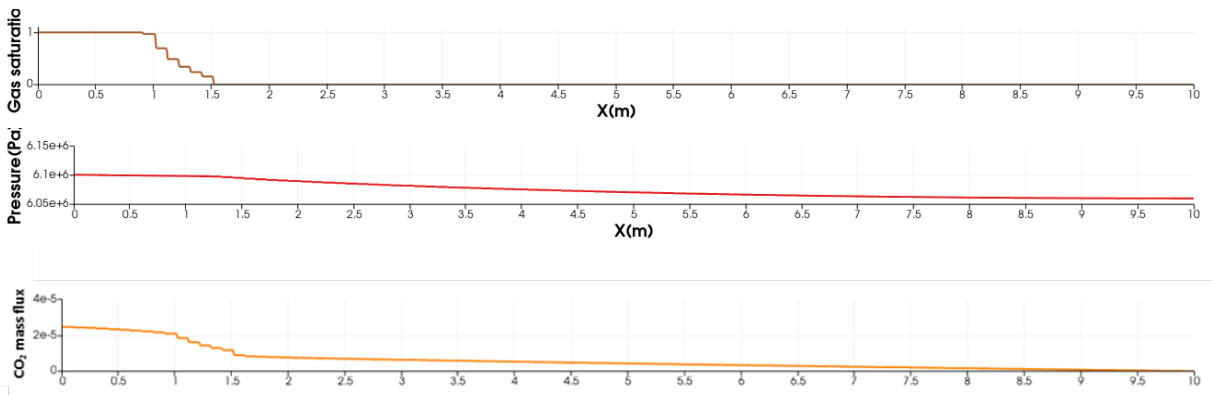

FIGURE 4.8: Pressure, saturation profile following the length of the domain at end time of the simulation (12 days).

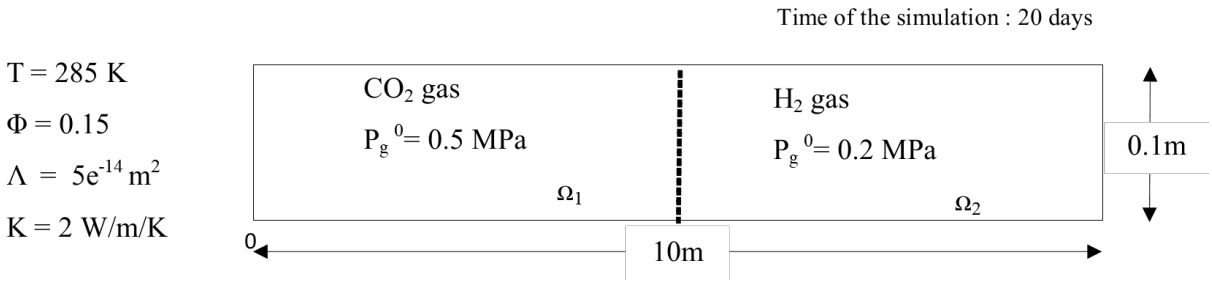

FIGURE 4.9: Case study 3: Domain properties and Boundaries.

4.5.4 Case study 4: Gas phase saturated media with phase change

This case study begins with a fully saturated gas phase of CO_2 in the media. The media characteristics include a porosity of 0.15, permeability of $5^{-14}m^2$, bulk and thermal conductivity of $2\,W/m/K$. The volumetric source term for the CO_2 and for H_2 is set to zero throughout the domain. The H_2 injection is represented by a volumetric flow rate introduced through Neumann boundary conditions. This test aims to demonstrate the model's capability to handle phase changes and the appearance of the CO_2 liquid phase.

The simulation shows that, initially, there is a gas phase from 0 to $4.7\,m$, with the first $3.5\,m$ consisting of only H_2, followed by a zone from $3.5\,m$ to $4.7\,m$ with a gas mixture of H_2 and CO_2. Beyond $4.7\,m$, a diphasic zone exists, with a small fraction of H_2 up to $7.5\,m$, primarily composed of CO_2 in the gas phase but also containing the liquid phase. At the simulation's end, the CO_2 has transformed into the fluid state (gas with liquid properties) at a temperature of $290\,K$ and a pressure of 6 MPa.

4.5.5 Case study 5: Three-dimensional two-phase flow

In this case study, we explore three-dimensional two-phase flow in homogeneous zones. The media characteristics include a uniform pressure of 5 MPa, temperature $290\,K$, a porosity of 0.15, permeability of $5^{-14}m^2$, bulk and thermal conductivity of $2\,W/m/K$. The initial state consists of a CO_2 gas phase saturating the entire media volume of $100 \times 100 \times 100\,m^3$. Dirichlet boundary conditions are set at the top and minimum of the x-axis, while a volumetric source term for H_2 is located in the center of the domain. Dirichlet boundary conditions are applied at the minimum

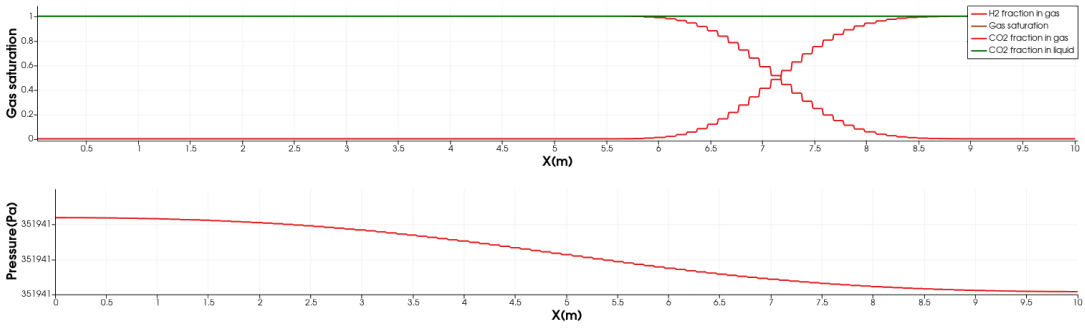

FIGURE 4.10: Pressure, saturation profile following the length of the domain at end time of the simulation (20 days).

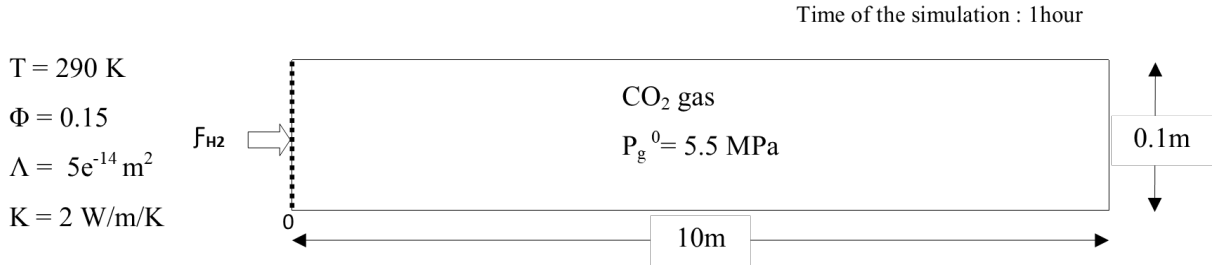

FIGURE 4.11: Case study 4: Domain properties and Boundaries.

and maximum of the x-axis. The simulation is conducted for one hour, with output recorded every minute.

In Fig.4.13, we can observe variations in gas saturation with different mole fraction compositions in this phase, as well as liquid saturation with mole fraction compositions in the liquid phase, depicted at the half time of the simulation. Continuous injection of H_2 mass leads to the formation of a H_2 bubble in the gas state. At a distance from the bubble, the CO_2 is also in the gas state. The front contact zone is the mixing region between CO_2 and H_2. With increasing pressure (between 5.4 MPa and 7.8 MPa), a small fraction of liquid appears in this zone, representing the coexistence of two phases: liquid and gas, with a minimum gas representation of about 86%. The gas phase shows a gradual presence of H_2 that diminishes with increasing distance from the injection point, along with an increasing CO_2 fraction. The liquid phase primarily consists of CO_2, with a negligible fraction of H_2.

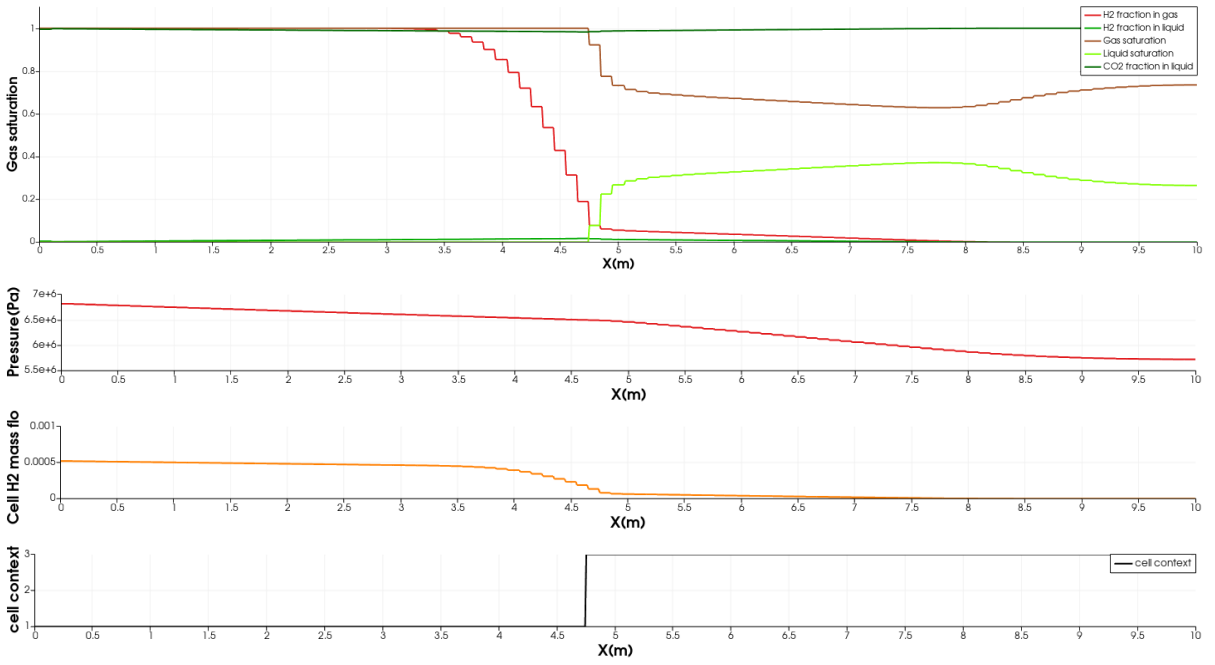

FIGURE 4.12: Pressure, saturation profile following the length of the domain at end time of the simulation (1hour).

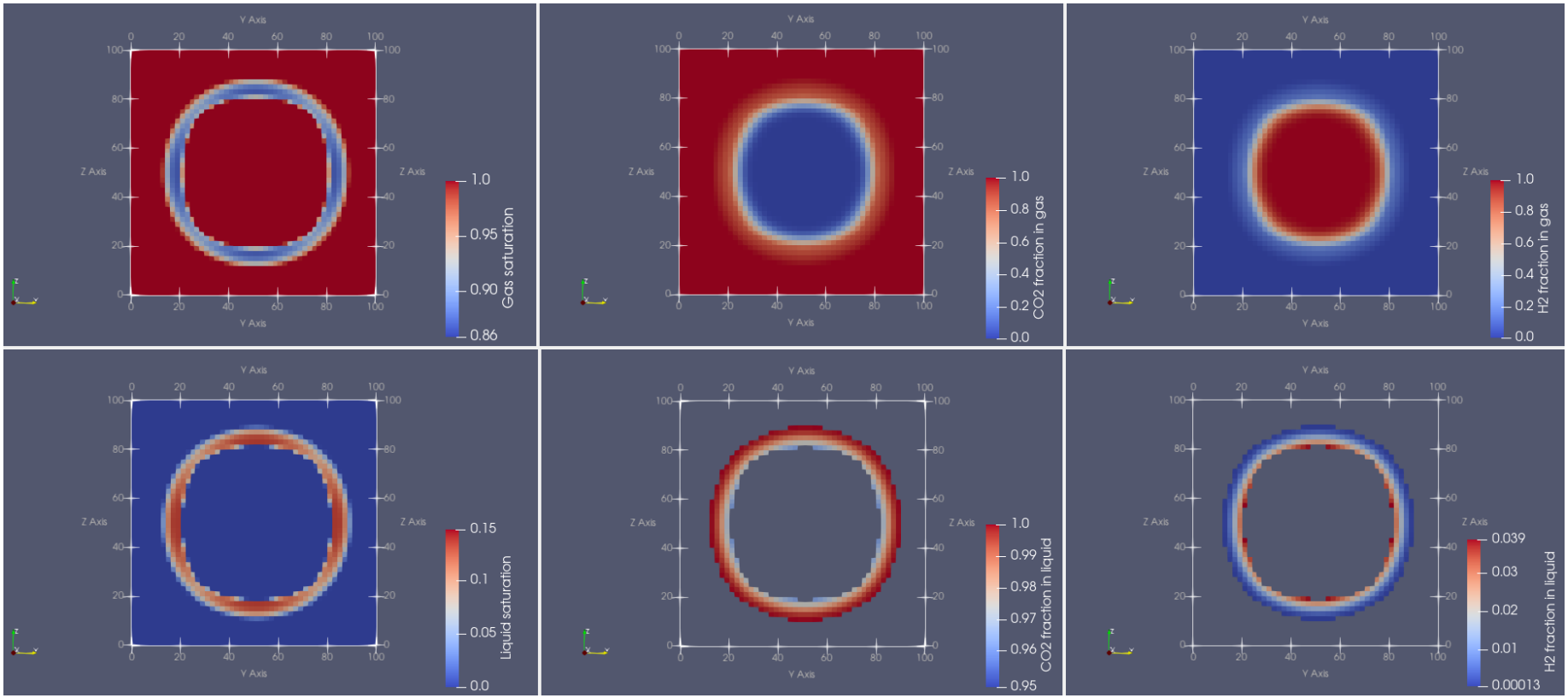

FIGURE 4.13: Phase amounts and phase compositions in H_2 injection into CO_2 simulation: variations in gas and liquid saturation, as well as mole fraction compositions in each phase.

4.6 Conclusion

In this chapter, we have presented a comprehensive overview of the implementation and testing of a cubic EoS model within ComPASS. Our primary objective was to integrate a thermodynamic model capable of handling phase transitions and fluid properties within the existing ComPASS framework.

We began by discussing the theoretical foundations of cubic EoS, emphasizing their role in predicting phase equilibria and thermodynamic properties. The derivation of fugacity coefficients, the Helmholtz free energy, and other thermodynamic variables were explained in detail. Additionally, we highlighted the challenges of integrating a pressure-explicit EoS into the ComPASS framework, where the standard formulation employs temperature, pressure, and mole numbers as primary variables.
The numerical implementation section mentioned the developments that enabled users to define components, manipulate properties, and focused on the algorithm modifications to simulate phase transitions efficiently. We described the use of advanced numerical methods, iterative algorithms, and convergence criteria to handle complex phase behavior crucial for reservoir simulation.
Throughout this chapter, we presented a series of case studies to validate and demonstrate the capabilities of the implemented EoS model and the phase transition code within ComPASS. These case studies included scenarios with varying initial conditions, pressure imbalances, and phase transitions. In case study 1, we observed how a two-phase CO_2 system evolved from initial out-of-equilibrium conditions to achieve pressure continuity within porous media. This case highlighted the importance of pressure balance. Case study 2 showcased the model's ability to handle the appearance of the liquid phase in a saturated gas state. The simulation effectively captured the phase transition triggered by pressure changes, demonstrating its capability to handle phase appearance. In case study 3, the system evolved to contain two components, CO_2 and H_2, each initially at different pressures. The simulation reached pressure continuity, without phase changes. Case study 4 injected H_2, into a fully saturated CO_2 gas phase. The simulation successfully captured the phase transition, demonstrating the model's capacity to handle multi-phase multi-component systems. Finally, case study 5 extended the analysis to a 3D scenario, highlighting the model's performance in complex, three-dimensional flow conditions under continuous mass injection.

In conclusion, the successful integration and testing of the cubic EoS module within ComPASS offer a consistent tool for simulating phase transitions, fluid behavior, and mass transport in porous media. This model could be used in a wide range of reservoir simulation applications, including carbon sequestration, and geothermal reservoir analysis.

4.7 Limitations and Future Developments

4.7.1 Model Limitations

We acknowledge that the current implementation of the cubic EoS model in ComPASS has certain limitations. These limitations are essential to recognize and address for future simulator developments and enhancements:

- **Phase Equilibria Flash:** The current implementation includes a flash calculation for two phases (gas and liquid), but it can be expanded to handle more phases. Enhancing the flash calculation capabilities can provide more flexibility and enable more complex reservoir simulation systems.

- **Modeling water:** While the SRK/PR model is a versatile choice for most systems, it doesn't accurately represent the properties of water, primarily due to its polar nature. Accurate modeling of phase equilibria in aqueous solutions using a cubic EoS necessitates additional efforts. Modifications and extensions to the SRK/PR model, such as those proposed by Soreide and Whitson (SW EoS), can address this limitation. The SW EoS introduces different binary interaction coefficients for different brine-gas systems, enabling more accurate predictions for systems containing water and brine. Integrating such enhanced models into ComPASS could extend its applicability to reservoirs containing aqueous solutions.

- **Computation and Calculation Capacity:** ComPASS development is ongoing, and the module integrated into ComPASS is not yet optimized or rigorously tested for optimization. To handle more extensive and complex reservoir simulations, continuous improvement in computational efficiency and capacity is required.

The flexibility, accuracy, and efficiency of the implemented model make it a valuable addition to the ComPASS framework, facilitating advanced reservoir simulations for both research and industrial purposes. Compass development was time consuming and calculation capacities are for the moment limited.

4.7.2 Future Developments

In order to address these limitations, we suggest potential avenues for future development and enhancement of the thermodynamic module and its integration within the open-source reservoir simulation tool.

- **Multi-Phase Multi-Component Transition:** Expanding the actual two-phase transition code to support multi-phase and multi-component systems is a challenging but valuable task. This functionality could be implemented for various scenarios application. Extending ComPASS in this direction will provide more comprehensive insights into complex reservoir behavior.

- **Taking water into account**: Integrating models accurate for systems involving water, brine, and real gas, as well as the solubility, can extend ComPASS's applicability to reservoirs containing aqueous solutions, allowing for accurate modeling in scenarios where water plays a significant role.

- **Computational Efficiency:** The computational efficiency of the implemented cubic EoS model should be rigorously evaluated. This evaluation could lead to optimizations aimed at enhancing simulation speed. Improving computational efficiency is essential to handle larger and more complex simulations.

- **Temperature-Dependent Péneloux Correction:** Exploring the temperature-dependent Péneloux correction could be interesting to evaluate, as it may enhance the model's accuracy in different temperature regimes. The code's flexibility was intended to allow for the incorporation of temperature dependency.

- **Integration of GERG-2008 Model:** Another potential future development is the integration of the GERG-2008 model into the tool. Comparing this model with the cubic EoS in terms of accuracy and computational costs will provide valuable insights. This expansion would broaden the tool's applicability.

- **Diffusion and Dispersion:**Adding the terms for diffusion and dispersion is necessary for improving the results of simulations. Integrating these processes into the model can enhance its capabilities in capturing the transport and spreading of components within the reservoir.

- **Benchmarking:** An ideal future step is to benchmark ComPASS with other open-source codes and commercial simulators. This benchmarking process will validate ComPASS's performance and accuracy against established reservoir simulation tools, ensuring its reliability for various applications.

It is worth noting that ComPASS is an evolving tool, and the alignment of work elaborated in this thesis with the latest version is an essential initial step in these potential future developments. While the suggested future developments hold promise for enhancing its capabilities, they are currently considered as potential areas for improvement. At present, these aspects may make ComPASS less suitable for handling complex simulations, particularly for scenarios involving H_2 storage with detailed reservoir characteristics.

In the context of this work, we benefit from a realistic geological model to test the concept of UHS. However, given the need for sophisticated simulations, we have chosen to use a commercial tool, CMG GEM. This decision is driven by the desire to thoroughly assess UHS efficiency and feasibility in the subsequent chapter, where we will explore these aspects in greater detail.

CHAPTER 5

Strategies for minimizing mixing: phase diagram and conceptual configurations for UHS[1]

Before proceeding with specific site-based numerical simulations in the next chapter, the behavior of the H_2-CO_2 system under a wide range of pressure and temperature conditions must be thoroughly understood. This comprehension serves as a foundational requirement for the identification of critical points and phase transitions that may occur during reservoir simulations. This chapter aims to compile the knowledge crucial for making informed predictions during numerical simulations. Given that the primary concern when using CO_2 or any gas other than H_2 as a CG is the potential for mixing and contamination of the H_2 asset, this work also investigates the conditions under which this mixing may occur. The objective of this chapter is to delineate the range of storage conditions and identify the optimal reservoir conditions, including pressure, temperature, and reservoir architecture, to limit the mixing zone. To achieve this, a study of the phase diagram of the H_2-CO_2 system is elaborated upon, and the results of numerical simulations are presented, while laying the foundational concepts that guide the study.

5.1 Introduction

Building on the earlier discussion regarding the influence of CG compressibility and volume on H_2 storage efficiency, it is crucial to delve into the interactions between CO_2 and H_2 within the reservoir. In fact, the pressure dynamics within the storage are significantly influenced by the injection and withdrawal actions, resulting in pressure fluctuations. Here, the compressibility and volume of the CG, enable the injection of larger amounts of H_2 without overpressurizing the reservoir. CO_2 is highly compressible near its critical point, suggesting its potential to serve as an excellent CG, especially under conditions where the reservoir temperature and pressure

[1]This chapter is derived from an article entitled "Underground H_2 Storage in Aquifers: Evaluating reservoir conditions with CO_2 as a cushion gas", which was reviewed currently under correction.

Table 5.1: Literature harvest of the VLE data of the system CO_2-H_2.

Author	range T(K)	range P(MPa)
Kaminishi and Toriumi (1966) [127]	233.15-298.15	5.06-20
Spano et al. (1968) [128]	219.9-289.9	0.269-20
Streett et al. (1983) [129]	220-290	0.9-172
Bezanehtak et al. (2002) [130]	278.15-298.15	0.1-183.94
Fandiño et al. (2015) [131]	218.15-303.15	0.5–15.4

align with those of CO_2's critical point [49]. However, the introduction of H_2 into this scenario may introduce potential alterations to the gas mixture's characteristics and flow behavior within the reservoir. These alterations could have consequences, impacting the efficiency of the storage operations and the extent of the mixing zone. Therefore, conducting a comprehensive study of CO_2-H_2 system becomes imperative to understand the reservoir's fluid behavior and effectiveness.

In this context, our focus shifts to identifying the ideal reservoir conditions in terms of pressure and temperature for achieving UHS in aquifers while employing CO_2 as a CG. Our research approach will primarily rely on experimental data, notably VLE data. By analyzing the phase diagram of the CO_2-H_2 system under storage conditions, our objective is to gain a thorough understanding of how H_2 influences CO_2 and the resulting mixture within the reservoir. This study aims to predict the system's behavior across varying reservoir temperature and pressure scenarios while pinpointing the Pressure-Temperature (P-T) region that might minimize the extent of the mixing zone between CO_2 and H_2. Furthermore, we will complement these investigations with conceptual and numerical studies to validate the findings and enhance our comprehension of how this system behaves within the reservoir.

5.2 Methodology

Experimental data for pure CO_2 and H_2 are well-documented and extensively studied, and their phase diagrams are widely known. The phase diagram of CO_2 is particularly very well known due to its relevance in the context of CCS, where storage conditions often fall within the range of 7 to 15 MPa and temperatures above $305.15\,K$, typically operating under supercritical conditions [99]. However, it is noteworthy that experimental data for the CO_2-H_2 binary system are relatively scarce, especially within the specific pressure and temperature conditions pertinent to CCS. This scarcity arises from the method's complexity and the challenges associated with conducting experiments under these conditions. Nonetheless, understanding the thermodynamic behavior of this binary system is essential to UHS, especially when CO_2 is employed as the CG. Therefore, this research starts with a review of the available experimental data from the literature pertaining to the CO_2-H_2 system. These data are specifically gathered under conditions of pressure ranging from 0.6 to 15 MPa and temperatures spanning from $293.15\,K$ to $313.15\,K$. The summary of currently accessible VLE data is provided in the Table 5.1.

5.3 Results

5.3.1 Study of the collected experimental data

The summary of references provided in Table 5.1 encompasses a collection of VLE data for the CO_2-H_2, a topic of interest in this study. Notably, the earliest data on this system date back to the 1960s, with contributions from researchers such as Kaminishi and Toriumi (1966), Spano et al. (1968), and Yorizane et al. (1970). However, the most comprehensive study of this system occurred about 15 years later, conducted by Streett et al. (1983). Nevertheless, some discrepancies were noted between the results for the liquid phase in more recent studies and earlier reports. The work of Fandiño et al. (2015) played a crucial role in resolving these disparities.

Their work revealed that the phase behavior of this binary system falls under Type III in the Scott and van Konynenburg classification. This type is attributed to this mixture due to the substantial difference in the volatility of its components and to its deviation from Raoult's Law in the liquid phase. This confirms its non-ideality, hinting at a more intricate phase behavior, as we will explore further in this study. Furthermore, this work points out that this system can present three-phase equilibrium, the Solid-VLE curve intersects the VLE zone at a temperature of 235 K and pressure of 198 bars.

In addition to VLE data, other studies have reported measurements of the mixture's density. This is a critical aspect, as changes in density, coupled with fluid properties, are indicative of phase transitions. Mixture density is also relevant to the mixture behaviour description and for the awareness about the fluid state in the reservoir. The phase change, is by all means dependent on the temperature and pressure conditions and the molar fraction. The set of density experimental data reported by Sanchez-Vicente et al. demonstrated that a 2% concentration of H_2 can reduce the density of the mixture by 25% compared to that of pure CO_2 under the same conditions. Consequently, alterations in the composition of the system can induce significant changes in fluid properties, potentially enabling a new phase to appear.

5.3.2 Phase diagram of the binary System H_2-CO_2

The compilation of data (Table 5.1) has resulted in the construction of a phase diagram for the binary system of H_2-CO_2, as presented in Fig.5.1. This diagram showcases the relationship between pressure, temperature, and the mole fraction of H_2 across a range of isotherms, spanning from 220 K to 303 K.

Blue points correspond to the experimental data illustrating the contour of the phase envelopes and exhibit the join of two curves: the bubble and the dew curves. These curves intersect at critical points, depicted in red in Fig.5.1, which are characteristic of specific compositions. The black curve shown as a pressure-temperature (P-T) projection represents the critical locus, linking the critical points of different mixture compositions.

The location of a point in the phase diagram, defined by a particular temperature and pressure, determines the state of the system. When such a point falls within the envelope formed by the blue data points, the system is within a VLE zone. Beyond this envelope and above the bubble curve, a mixture with a higher concentration of CO_2 exists in the liquid phase. Below the dew

curve and when the system contains a significant fraction of H_2, the fluid exists in a gaseous state.

At a constant temperature, variations in composition correspond to different pressure thresholds controlling the phases present. When the pressure surpasses this threshold, a fluid with distinct properties emerges, and the system is in the single-phase region. The behavior of this region is contingent on the mole fraction of H_2 in the system. Changes in temperature shift the critical point of the mixture through an increase in the mole fraction of H_2 in the system, accompanied by elevated pressure.

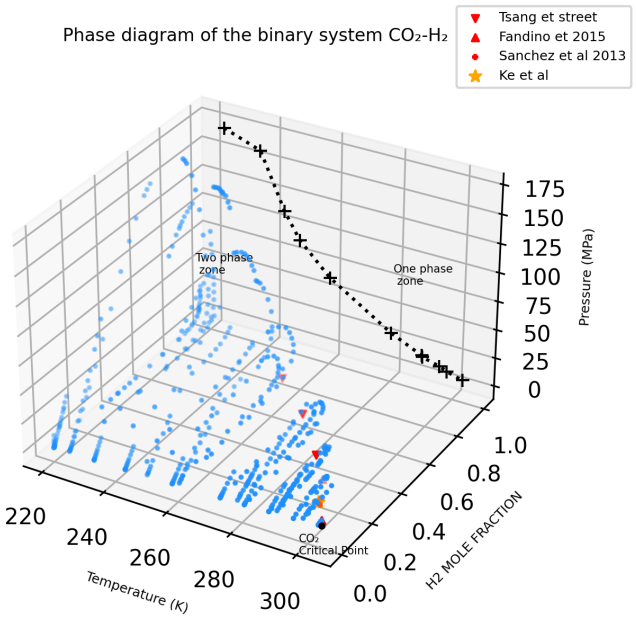

FIGURE 5.1: Phase diagram of the binary mixture H_2-CO_2.

The VLE region of the binary system CO_2-H_2 is confined within specific boundaries. At high pressures and temperatures, the VLE region is defined by the critical locus of the mixture, represented by the black curve in Fig.5.1. On the other hand, the lower pressure limit of the VLE region is demarcated by the curve associated with pure CO_2.

The critical locus curve is particularly informative because it provides insights into the state of the mixture (whether it is in a gaseous, liquid, or supercritical state) and, intriguingly, it establishes the lowest feasible conditions in terms of temperature and pressure that are compatible with the single-phase region. This black pressure-temperature (P-T) curve corresponds to the critical point of the mixture and is associated with specific molar concentrations of H_2 and CO_2 within the system. Thus, each point on this curve corresponds to a precise percentage of H_2 in the system.

During previous experiences of underground storage, CO_2 is mixed with heavier molecules or with molecules with similar properties that displaces slightly the critical temperature of the mixture T_c to higher values with temperature change. In this system, the H_2 has a very low T_c ($33.18\,K$) [133] compared to the T_c of CO_2 ($304.2\,K$) [134]. Reduced amounts of H_2 decrease severely the temperature of the mixture for a low pressure variation ($7.2 - 10\,\text{MPa}$).

Under storage conditions where the temperature is less than the critical temperature of pure CO_2 ($304.2\,K$), a two-phase flow system can form. This system consists of a CO_2-rich liquid phase and an H_2-rich gas phase. This behavior, illustrated in the 5th case study in Chapter 4, also in the Fig.3.3 and validated through the phase diagram analysis, highlights the potential for two-phase flow in UHS scenarios. The impact of this two-phase behavior on the mixing zone and its implications for storage has not been explored yet.

This phase behavior is especially relevant when the storage temperature is below the critical temperature of pure CO_2. In most storage conditions, CO_2 is maintained under supercritical state. However, these conditions have significant consequences for fluid behavior in the reservoir and, as such, the impact on the mixing zone needs further investigation. The capacity of numerical simulators, along with the associated thermodynamic models, to accurately describe this system has been discussed in a previous section (refer to section 3.5). While storage conditions are often designed to maintain CO_2 in a supercritical state, it is important to understand the potential scenarios where this may not be the case. In the next section, conceptual static schemes will be elaborated to predict the behavior of the reservoir under different conditions. Additionally, the impact on the mixing zone will be further discussed with initial numerical simulations, and examples from real reservoirs will be cited to demonstrate the relevance of such conditions.

Understanding how different phases can form and impact the reservoir is crucial for optimizing storage strategies and ensuring safe and efficient UHS.

5.4 Modeling of UHS with CO_2 as cushion gas

5.4.1 Conceptual Models

The behavior of the reservoir in response to the injection of H_2 and its interaction with CO_2 can be understood through conceptual models. When H_2 is injected into the reservoir, it spreads spatially, primarily driven by buoyancy forces and influenced by reservoir properties. As it migrates away from the well, the concentration of H_2 decreases until it encounters the CG. This contact between the two fluids defines the mixture zone within the reservoir. The front of this contact zone consists of a large fraction of CO_2 mixed with a reduced H_2 portion. Therefore, it is interesting to focus on the effect that a small fraction of H_2 can have when put in contact with CO_2 [135, 99]. By analyzing the pressure-temperature-composition diagram of the CO_2 - H_2 system and tracking the evolution of density within the system, it becomes evident that, under specific conditions of pressure, temperature, and mole fraction, the resulting mixture can transition from a single-phase state to a two-phase regime (Fig.5.1).

In this section, we present three different reservoir conditions at varying temperatures ($290\,K$, $298\,K$, and $303\,K$) in proximity to the critical point of CO_2 (Fig.5.2). Regarding pressure, we have chosen 10 MPa because it intersects the VLE zone and falls within the operational range of reservoir storage conditions. At 10 MPa, the VLE zone changes with temperature and the mole fraction of components. Outside the biphasic zone, the components form a single fluid, with the fluid state being either liquid or gas depending on the pressure regime. At the $290\,K$

isotherm and with an H_2 molar fraction between 0.5 and 0.35, the phase envelope falls within the biphasic zone for pressures between 8 MPa and 20 MPa. This implies that, under 10 MPa, a coexistence of liquid and gas phases occurs. On the liquid side, we find pure CO_2 and CO_2-rich mixtures, while on the gas side, there are pure H_2 and H_2-rich mixtures. At 298 K, the VLE zone narrows down, remaining relevant only between pressures of 7.2 and 10 MPa. For temperatures exceeding 303 K, the VLE zone vanishes. This indicates that, at such conditions, CO_2 transitions into a supercritical fluid, presenting gas-like properties. However, when combined with H_2, the properties of the CO_2-rich phase are altered. Even though H_2 lightens the density of the original CO_2, the mixture retains a single-phase state, ultimately extending the scope of the mixing zone.

Regarding the mixing zone, we previously discussed in section 2.4 that viscous fingering and gravity segregation are the main phenomena responsible for mixing. When addressing viscosity, the simple criteria established for the front mixing in order to avoid fingering is more stringent in miscible displacement compared to immiscible displacement, as discussed in section 2.4.1. In cases of partial miscibility, we expect the displacement front to exhibit an intermediate behavior between complete miscibility and immiscible displacement. The conditions for front stability are less stringent under partial miscibility conditions, i.e., the front in such conditions is more stable under practical H_2 injection rates. Gravity segregation is the other significant process, resulting from differences in densities. This effect can be used to keep fluids segregated, which forms the basis of the following conceptual scenarios. The density difference between phases becomes more pronounced, leading to segregation due to the gravity-override phenomenon [9].

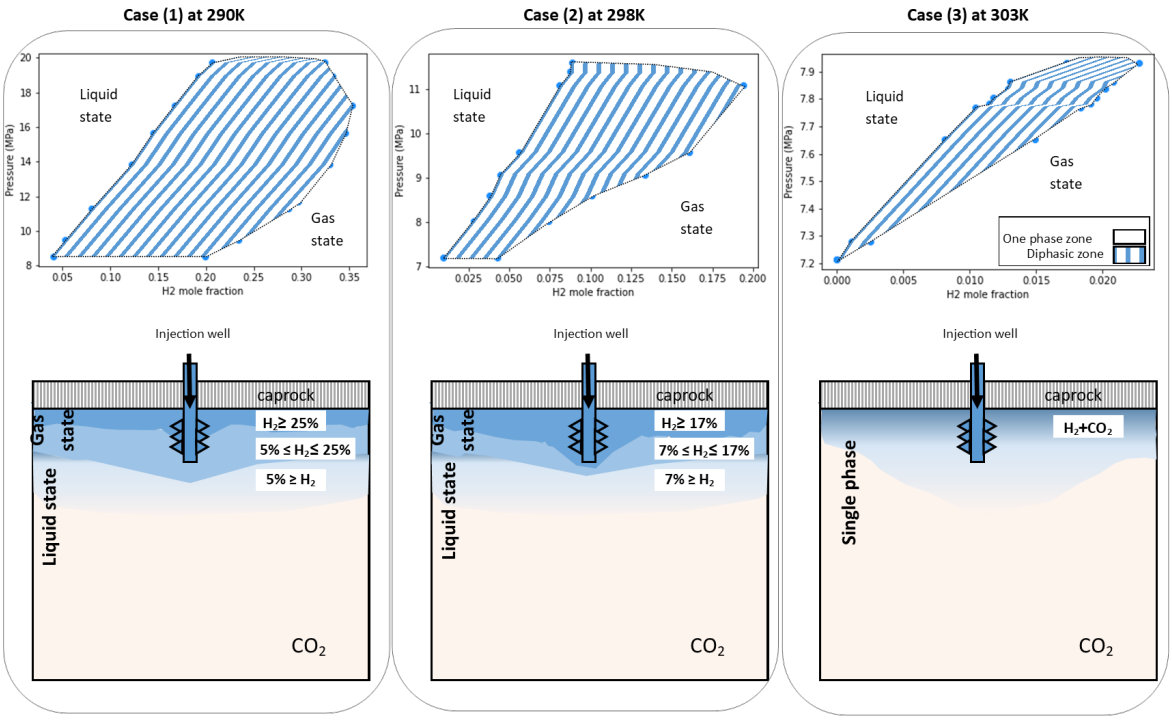

FIGURE 5.2: The phase envelope and static scenarios, which are associated with various reservoir conditions and denoted as case 1 to case 2, pertain to the UHS in aquifers.

To illustrate these mechanisms and the three reservoir conditions, conceptual cases are depicted in Fig.5.2. All three models are considered at a pressure of 10 MPa, with each case corresponding to a different isotherm through the phase diagram. Cases (1) and (2) are reservoir conditions where the separation of components into two phases is anticipated. These two cases differ in the range of H_2 fractions considered in the phase envelope. Wider phase envelopes at lower temperatures result in a higher proportion of H_2 in case (1) compared to case (2). Under such conditions, the pure CG exists in a liquid state, and when it comes into contact with injected H_2, the mixing zone divides into two phases with different densities. The liquid CO_2 phase, lightened by the H_2 fraction, settles on top of the CG, followed by the gas phase composed of H_2 contaminated with CO_2, with more pure, lighter H_2 on top.
Case (3) involves temperatures above the critical point of CO_2, which means it is situated in the single-phase zone. The reservoir pressure exceeds the cricondenbar of the phase envelope, and thus, the mixture exists as a miscible fluid in a single phase. H_2 lightens the original density of pure CO_2 but remains in a single phase, which we predict will enhance the extent of the mixing zone, as represented here.

These conceptual models help us understand how H_2 and CO_2 interact, influencing fluid behavior and potentially affecting the mixing zone and storage capacity. We'll further investigate this impact through initial numerical simulations and refer to reservoir conditions to validate the existence of such scenarios.

5.4.2 Numerical Modeling

To explore the conceptual models proposed earlier, three numerical case studies were conducted using the compositional simulator CMG/GEM [136], with SRK cubic equation of state. Molecular diffusion, H_2 dissolution in brine and geochemical reactions were all neglected in the calculations presented here as the main focus is on the thermodynamic behaviour. The storage scenario was simulated in a 3D cubic grid ($50*50*50$) homogeneous and isotropic with local refined cells around the well, a permeability of $1000\,mD$ and a porosity of 0.2. To simulate an infinite aquifer, the cells at the grid boundaries were multiplied by a very large number and can be considered as infinite in volume. The relative permeability is represented in Fig.5.3. Capillary pressure were correlated using the Brooks-Corey correlation. The WGC is defined shallower than the minimum elevation, and the aquifer is initially fully water saturated. The simulation began with the CO_2 CG emplacement followed by the H_2 injection at a constant rate and takes place at the top center of the reservoir. The purpose of this simulation was not to entirely displace the original fluids in place but rather to create a CG bubble around the well and examine the system's behavior after H_2 injection.

Interpreting the results of the simulations, it is evident that a third phase, characterized by the presence of water, gas, and liquid (CO_2 in the liquid form), can be successfully represented. This is illustrated in Fig.5.4 for scenarios (d) and (c). The Fig.5.4, shows no liquid CO_2 under the 3rd case scenario which is coherent since the H_2-CO_2 system is in a single phase. When comparing the H_2 or CO_2 concentration across the three scenarios in Fig.5.4 (a, b, c) and (g, h, i), which helps us evaluate the extent of the mixing zone, it becomes apparent that the contamination

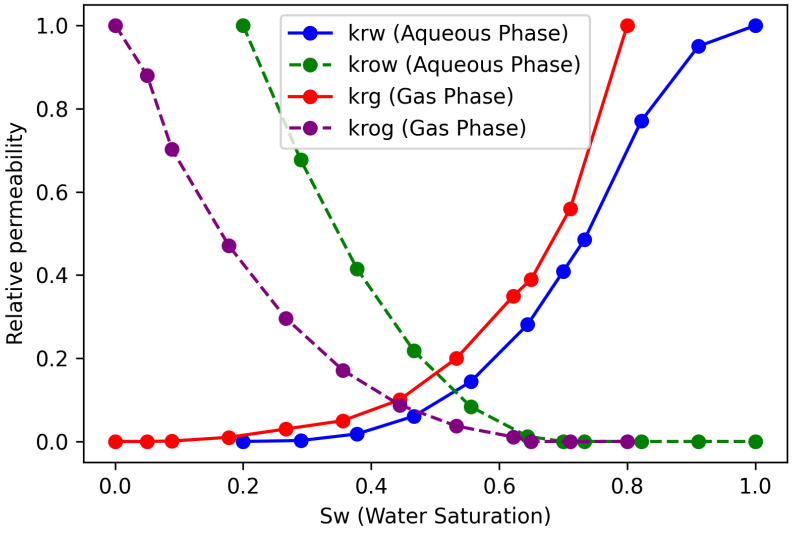

FIGURE 5.3: Relative Permeabilities for three phases used for this model (krw, krow, krg, krog); with krw (Relative Permeability of Wetting Phase), krow (Relative Permeability of Non-Wetting Phase), krg (Relative Permeability of Gas Phase), and krog (Relative Permeability of Oil and Gas).

of the H_2 is notably higher in Fig.5.4 (c) and (i), corresponding to case (3). Interestingly, the vertical spreading appears to occur more rapidly in Fig.5.4 (i) compared to (g) and (d).

These observations suggest that mixing is more significant in scenario (3), where the H_2-CO_2 system remains in a single phase. This finding supports the adoption of the first case scenario for UHS, which suggests utilizing reservoirs with temperatures below the critical temperature of CO_2. Fortunately, such conditions are commonly found in existing aquifers.

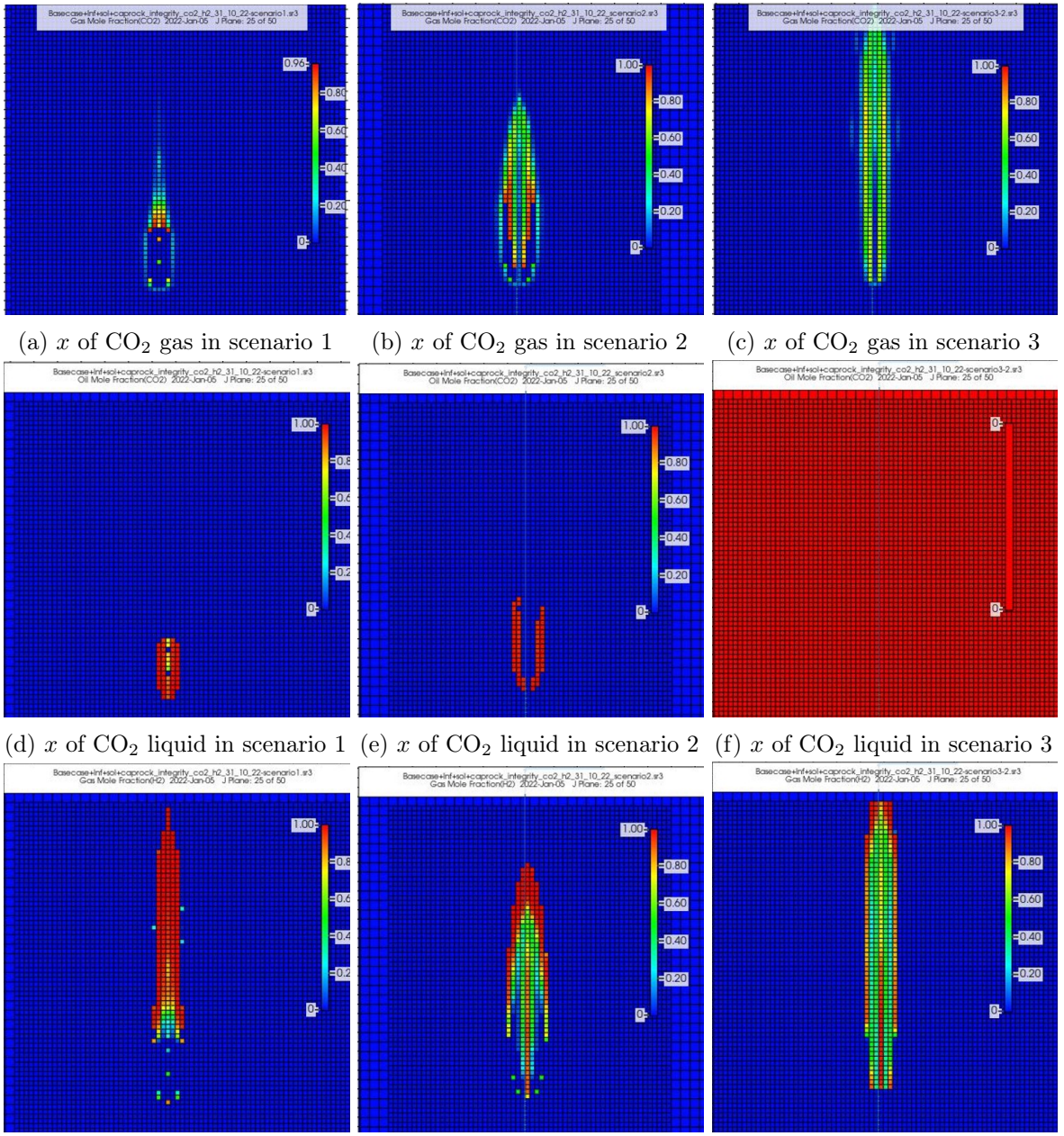

(a) x of CO_2 gas in scenario 1 (b) x of CO_2 gas in scenario 2 (c) x of CO_2 gas in scenario 3

(d) x of CO_2 liquid in scenario 1 (e) x of CO_2 liquid in scenario 2 (f) x of CO_2 liquid in scenario 3

(g) x of H_2 gas in scenario 1 (h) x of H_2 gas in scenario 2 (i) x of H_2 gas in scenario 3

FIGURE 5.4: Mole fractions (x) of different gases in various scenarios.

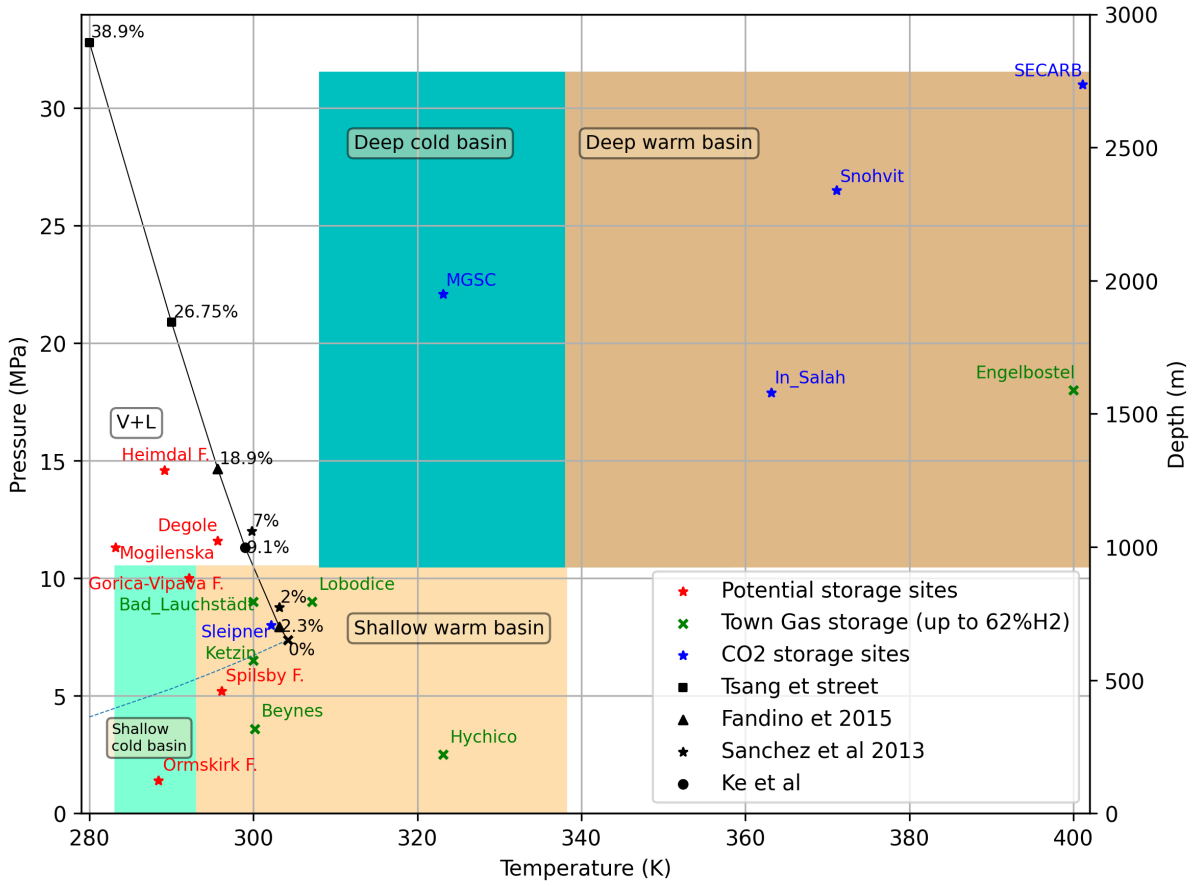

FIGURE 5.5: The diagram displays four relevant regions for CCS and town gas storage. The critical temperatures and pressures of the CO_2-H_2 system, obtained from experimental data, are marked by a solid line denoting the critical locus and displaying the corresponding percentage of H_2 above each point. The point marked with 0% indicates the pure CO_2 critical point. The saturation line of pure CO_2 is represented by a dashed curve, while V+L indicates vapour and liquid. The red asterisks depict formations with the potential to be utilized as future H_2 storage sites.

Fig.5.5 illustrates the reservoir conditions that have been previously used for CCS and Natural town gas storage. It highlights several aquifers that have served as storage for carbon sequestration or natural gas, with relatively high H_2 percentages.

These reservoirs have been identified and analyzed in previous studies [137, 138, 8, 139, 140]. These reservoirs can be classified into four types, including deep or shallow cold basins and deep or shallow warm basins, which are represented by different colored rectangles. The critical locus is depicted in this diagram to delineate the vapor-liquid zone and indicate the critical percentage of H_2 in the mixture. Using this limit, we can locate the position of potential reservoirs/formation that meet the necessary conditions for a two-phase system, enabling the proposed storage concept of UHS. It is clear that few existing storage facilities meet these requirements. However, these conditions match those of deep cold basins, which are more commonly associated to offshore reservoirs.

To further expand the list of potential aquifers suitable for UHS, we made use of the Hystories project data, which is designed to map aquifers in Europe based on their salinity and temperature

[141]. We leveraged this database to identify potential UHS sites and formations, considering their pressure and temperature that support two-phase flow, and included them in the figure. The following list provides additional information about the selected formations:

- The Gorica-Vipava saline aquifer is an onshore aquifer located in the southwest of Slovenia. It has a gross thickness of 400 m and can be found at a depth of 900 m. The aquifer has a temperature of 292.15 K and a pressure of 9 MPa.

- The Degole aquifer trap formation is located in Latvia and has a gross thickness of 52 m. It starts at a depth of 1045 m and has a pressure of $11 - 11.6$ MPa and a temperature of 295.65 K.

- The Mogilenska storage formation of the Polish aquifer has a pressure and temperature of $0.5 - 28$ MPa and $283.15\,K - 364.15\,K$, with an average temperature and pressure of $324.15K$ and 11.35 MPa. It can be found at depths ranging from 50 m to 1135 m.

- In the United Kingdom, there are three formations: the Spilsby Sandstone Unit 1, the Heimdal Sandstone Unit, and the Ormskirk Sandstone Unit 2. The Spilsby Sandstone Unit 1 can be found at depths ranging from 20m to 1135m (avg. 500 m) with a pressure range of 0.2 to 11.7 MPa (avg. 5.2 MPa) and a temperature range of 281.15 K to 313.15K (avg. 296.15 K). The Heimdal Sandstone Unit has a depth range of 223 m to 2621 m (avg. $1422m$), a pressure range of 2.3 to 27 MPa (avg. 14.6 MPa), and a temperature range of 289.15 K to 373.15 K (avg. 331.15 K). It has a thickness of 949.9 m (avg. $88.97m$). The Ormskirk Sandstone Unit 2 has a minimum depth of 114.39 m (avg. 133.97 m) and a maximum depth of 147.89 m. Its pressure ranges from 1.2 to 1.6 (avg 14 MPa), and its temperature ranges from 287.22 K to 289.64 K (avg. 288.43 K).

While the aquifers mentioned earlier serve solely as examples, it is important to note that there are several other potential UHS sites worldwide, particularly offshore, that may exhibit conditions suitable for generating and maintaining two-phase conditions for H_2 and CO_2 during UHS cycling and thereby reduce mixing effects. Such conditions may also arise due to the pressure variation in the reservoir caused by injection influence, leading to crossing the phase envelope and resulting in phase segregation. Thus, it is crucial to consider the possibility of phase separation during any hydrodynamic study at potential UHS sites, even if the site conditions are not specifically selected to facilitate two-phase flow. Proper consideration of phase separation can enhance the understanding of the storage capacity and performance of the site, leading to more effective and efficient UHS design and implementation.

5.5 Conclusion

Through our comprehensive analysis of the phase behavior of the H_2-CO_2 system, we have brought to the forefront the potential for a two-phase system to exist under specific pressure-temperature conditions. Our study delves into the implications of these distinct behaviors on the mixing

phenomenon and the possibility of the occurrence of gravity override, a process that can segregate fluids based on density differences.

The results of initial numerical modeling demonstrate that under these conditions, the phase separation occurring at the front of the mixture might act as a buffer, reducing mixing of the CG with the injected H_2, while also observing a delay in the upward buoyant flow of H_2. These observations could play a crucial role in optimizing the operational efficiency of UHS.

By evaluating various storage sites, both existing and potential, including offshore and onshore formations, we have identified several locations that meet the criteria for two-phase flow in UHS. This validates the relevance and potential significance of this phase behavior for UHS and confirms that such conditions can be found in real-world reservoirs.

Overall, offshore reservoirs in cold sedimentary basins meeting these conditions, i.e., located between 7 and 10 MPa and below $300\,K$, may present attractive prospects for potential UHS sites. Furthermore, when situated near offshore wind farms, the possibility of storing H_2 locally could lead to cost savings and significantly enhance project efficiency.

5.6 Limitations and Future Developments

In this chapter, we have conducted an exploration of the phase diagram of the H_2-CO_2 system and the proposed concepts for UHS. However, a more realistic reservoir model is essential for a comprehensive evaluation. Real reservoirs exhibit heterogeneous geological characteristics, and operational parameters must be taken into account to assess the practicality of the proposed concepts.

Our examination of dynamic parameters was limited, and a more in-depth analysis is required to evaluate the purity of the produced gas and to study the extent of the mixing phenomenon. Parameters such as injection rate, reservoir heterogeneity, and the cyclic operation period can significantly influence the extent of the mixing zone under these conditions. Therefore, a dynamic study that considers these factors is necessary to identify the optimal storage scenario with minimal mixing. This scenario will be further compared to situations where only a single phase is present.

In the following chapter, we will perform exhaustive numerical simulations using realistic reservoir models under conditions where CO_2 and H_2 coexist as a single phase. The aim of this investigation is to shed more light on the best storage scenarios for these conditions.

CHAPTER 6

Numerical simulations in a realistic reservoir[1]

This chapter presents the results of comprehensive numerical simulations utilizing the GEM modeling tool from Computer Modelling Group (CMG) to investigate the feasibility of seasonal UHS with CO_2 as a cushion gas in a realistic aquifer with a well-defined geological structure. The primary focus of the study is to address the challenge of efficiently recovering pure H_2 in UHS, as the contamination and recovery of the cushion gas significantly impact the economic viability of the project. The research aims to analyze and understand how various parameters, including operational, geological, and reservoir-related factors (e.g., injection and production rates, heterogeneity, gas solubility, etc.), influence the performance of the H_2 storage system, with the ultimate goal of identifying optimal storage scenarios. However, it is important to note that no geochemical considerations have been incorporated into this analysis.

6.1 Introduction

In this study, a realistic geologic model of actual natural gas reservoir is used as case study. A sensitivity analysis of different parameters will be conducted to study their impact on the volume of gas produced and the degree of purity of this later. We use the commercial reservoir simulator GEM from the Computer Modelling Group (CMG). The temperature, pressure of the aquifer suggest that the system H_2-CO_2 remains in the gas phase under storage conditions.

This chapter begins with a summary of recently published numerical simulations research papers related to UHS in aquifers. It then presents the methodology used, including a detailed description of the reservoir, the base case scenario, and the relevant parameters considered in the simulations. The results of each parameter study are analyzed, discussing their impact on gas recovery and quality. The discussion section explores the impact of associating different factors

[1]This chapter is derived from an article entitled "H_2 storage with CO_2 cushion gas in aquifers: Numerical simulations and performance influences in a realistic reservoir model" accepted with revision at the International Journal of Energy Storage

and their effects on UHS performance. Finally, the conclusion summarizes the main findings of the simulations, highlights effective scenarios, and suggests potential areas for further research.

6.2 Literature review

Previous research has extensively studied the UHS in aquifers using various simulation software codes. These studies explored the capacity of storage systems, geochemical reactions, and the impact of different factors. Some notable studies that have examined UHS in saline aquifers include the following:

- Comsol was used in a 3D model to study the well configuration for three annual cycles of UHS with H_2 as a CG for itself. The research estimated a maximum H_2 recovery ratio of 78%, representing a global energy efficiency of 30%. Notably, in this study, The CG was deemed unnecessary when H_2 is stored in steeply dipping structures. The major challenge identified in this storage was due to coning effect and massive water intrusion. Efficient H_2 recovery was achieved when the production wells are shallow and located beneath the caprock [142].

- This work considered a hypothetical site with a realistic geological structure, with N_2 used as the CG. They demonstrated the capacity of porous media to store significant quantities of H_2 and meet the required energy demands. The simulations were conducted using Eclipse (E300) [143].

- Using DuMux, this study explored the hydrodynamic effects due to H_2 injection and compared it to CH_4. For H_2 storage, an initial quantity of H_2 was introduced into the reservoir. In the case of the CH_4 scenario, an equivalent amount of CH_4 was injected, although it was not explicitly designated as CG. It appears that at low injection rates, gravitational forces dominated, resulting in the uniform displacement of water by H_2. Conversely, at high injection rates, viscous forces became dominant, leading to unstable displacement. Notably, at higher injection rates, lateral fingering spreading of H_2 was observed to occur faster than when CH_4 is injected [144].

- This work used TOUGH2 PetraSim to assess the feasibility of UHS (with H_2 as CG) in the Suliszewo aquifer in Poland. The authors deduced that the recovered amount of the total injected H_2 increases with the increase of number of withdrawal cycles and highlighted the possible issue of water management concerning the water withdrawed during the H_2 production [145].

- This research investigated the impact of caprock availability and H_2 injection rate on H_2 recovery and leakage in UHS in heterogeneous 3D model using TOUGH2. They revealed that caprock presence and lower injection rates enhance H_2 recovery while higher injection rates increase H_2 leakage [146].

- This study focused on analyzing the injection and storage of H_2 in an open saline aquifer, with a particular emphasis on investigating the role of H_2 CG. It was demonstrated that

CG plays a significant role in controlling the injectivity of H_2, as well as influencing the storage capacity. Additionally, geological parameters such as reservoir permeability and depth need to be taken into account when determining the capacity of CG as WG in the aquifer [147].

- The study aimed to address unstable displacement and potential chemical reactivity caused by microorganisms consuming H_2. The model DuMuX was used to simulate the evolution of a hypothetical UHS system in a depleted gas reservoir and revealed that hydrodynamic and bio-chemical effects are different compared to natural gas storage [148].

- In this paper, the authors leveraged data previously utilized to evaluate CO_2 storage potential in the UK, to assess H_2 storage capacity in gas fields and saline aquifers. They assumed H_2 CG requirement of 50%. Through their sensitivity analysis, they determined that sites characterized by low temperatures and sealing rocks capable of withstanding high pressures are favored locations for efficient storage [149].

Upon examination of the relevant studies, it became apparent that many of the literature studies do not take into account the utilization of CG for UHS in aquifers. In most of these analyses, H_2 is acting as a CG for itself and there exists no extensive numerical simulation study exploring UHS with CO_2 as CG, particularly one carried out in a realistic geological model – this is a distinctive advantage of the present work.

6.3 Methodology

The aim of this study is to conduct an extensive sensitivity analysis. The commercial simulation software GEM of Computer Modelling Group (a courtesy of CMG) [150] was used to model the non-isothermal and multi-phase flows of a mixture of brine (water), CO_2, and H_2 in a realistic aquifer model. The model used served for natural gas storage and it is further discussed in the following first subsection 6.3.1. A straightforward operational approach involves starting with a reservoir with CG that is already injected before proceeding with the injection and production of H_2. Therefore, the reservoir was initially filled with CG. Then, the reservoir was left shut-in for one month to reach equilibrium.
Afterward, some storage cycles with seasonal injection and withdrawal were simulated to represent a real case study where the operator plans to inject without a shut-in period after each operation. The injection and production data are depicted in the second subsection 6.3.2.

The current model does not account for geochemical and bacterial reactions, and the methanation reaction is not activated. However, it is crucial to consider these processes, as they involve methanogenic and acetogenic microorganisms capable of consuming H_2 and CO_2 to produce CH_4 and acetate, respectively [43, 32, 40]. Geomechanics was not included to consider the changes in porosity and permeability, as well as the caprock integrity. The fluid behaviour (PVT) is operated based on a cubic EoS (PR1998) [101].

In this work, the analysis revolves around the base case as described in 6.3.2 and explore various scenarios by adjusting the input parameters mentioned in the subsection 6.3.3. The objective is to understand how these changes influence the purity and the H_2 volume recovered.

6.3.1 Reservoir description:

This study benefits from a realistic reservoir model based on the characteristics of a practical reservoir, capable of yielding results that closely resemble real-world situations in porous media. Petrel was utilized to generate the precise 3D static model.

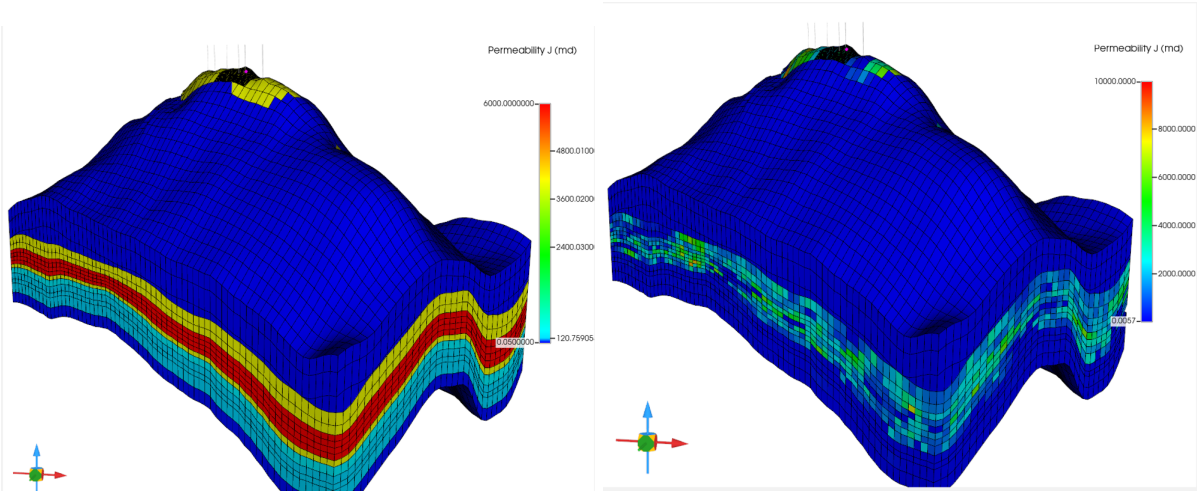

FIGURE 6.1: Reservoir Model: horizontal permeability in both layered simple model (the base case at left) and heterogeneous (right).

The reservoir is an anticline with the top located at a depth of 380 m under sea level, with the temperature of 40°C and hydrostatic pressure of 55 bar. The structure has an extent of the 900 m and has an approximate thickness of 50 m. The WGC is defined at 430 m. A hydrostatic pressure distribution is assumed throughout the reservoir starting at this contact. The 3D structure of the reservoir is depicted in Fig.6.1. The model consists of 213 180 grid blocks, with grid refinement around the well achieved by dividing each cell into $11 * 11 * 10$ cells.

The model encompasses five different types of rocks, representing various horizons within the reservoir (Table 6.1). The lower part of the model simulates a substantial aquifer, enabling sufficient inflow or outflow volume to maintain the flow rates of the wells at the top. The aquifer is numerically simulated with a thickness of 200 m, porosity of 0.25, and permeability of 10 Darcy. The proportion of CG to WG initialized at the reservoir conditions has been determined to prevent water breakthrough during the back production cycles. Therefore the reservoir starts at 42 bars with $2.3\,10^9\,Std\,m^3$ CG in place. In order to model the two-phase flow of CO_2-brine, relative permeability curves are adapted from experimental data produced for CH_4-brine and tailored to different rock types as represented in the Fig.6.2. While the adaptation is not specifically designed for CO_2, it provides a close approximation. Capillary pressure data was calculated using a standard Brooks & Corey function. As a first approach, there is one well situated at the top layer of the structure, which serves as both the injection and production well. Well

Table 6.1: Different reservoir rock types characteristics.

Rock type	Average porosity (%)	Average permeability (Darcy)	Lithology
1	30	4.6	Clean Sand
2	28	3	Clean Sand
3	24	0.092	Carbonated Sandstone
4	16	0.01	Degraded sandstone
5	7	0.00036	Poor reservoir facies

perforations are located in the upper layer of the anticline. The injection and production flow rates are controlled based on pressure buildup and release, ensuring that the reservoir pressure remains within safe limits to prevent fracturing. The maximum and minimum allowable *Bottom Hole Pressure* (BHP) for injection and production are 100 bars and 1 bar, respectively. In the event of a violation of these BHP limits, the simulator automatically adjusts the well flow rate to bring the pressure within the specified range.

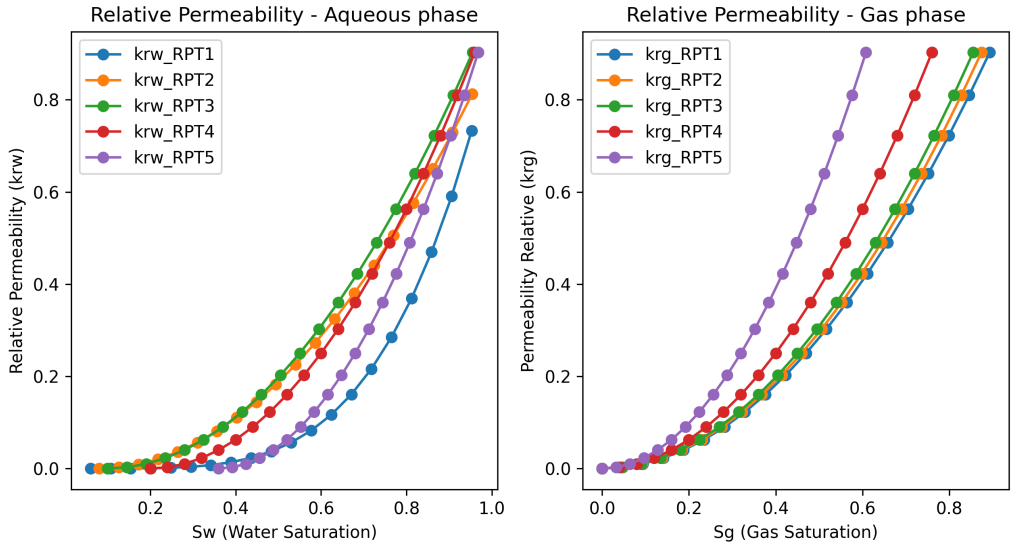

FIGURE 6.2: Two-phase relative permeabilities for different rock types in the model. Left, the relative permeabilities as a function of water saturation. Right, the relative permeabilities as a function of the gas saturation. The different curves represent the five different rock types present in the model.

6.3.2 Base case scenario description:

A simplistic base case scenario was used as reference (Fig.6.1 left). This base case relies on a homogeneous layered model with equal vertical and horizontal permeability, ranging between 5×10^{-5} Darcy and 6 Darcy, and a porosity varying from 4% to 35% for different layers.

The reservoir is initially filled with brine, and the CG is introduced during the model setup. Following this, H_2 injection and production take place. The specific injection and production

data are detailed in Table 6.2. There was no shut-in period between the injection and production phases. The simulation commences on 01-06-2023, and the well remains shut-in until the start of the H_2 injection phase on 01-07-2023. The project duration spans four years, ending on 28-06-2027.

Table 6.2: H_2 injection and production data.

Event	Event length (months)	Injection rate ($Stdm^3/Day$)	Production rate ($Stdm^3/Day$)
1	6	1522800	0
2	6	0	1522800

6.3.3 Sensitivity analyses

When a CG other than the WG is used, minimizing mixing between the different gas components is a major challenge. The front spreading between the WG and CG depends on the nature of the CG chosen and the contrast of its physical properties compared to those of the WG. (the density, viscosity difference; the mobility ratio) and the coupled process of molecular diffusion and mechanical dispersion. Molecular diffusion is a slow phenomena that is generally proportional to the concentration gradient but also depends on saturation, tortuosity and the porosity of the reservoir. Mechanical dispersion is governed by the velocity of the fluid.

The sensitivity analyses consist in changing input parameters of the base case to investigate the impact of: residual saturation; solubility of H_2 in the aqueous phase; diffusivity and diffusion; dispersion; reservoir heterogeneities; operational scenarios; and injection-well strategy.

6.3.3.1 Residual saturation

In underground storage processes, considering fluid-rock interactions is crucial as it directly impacts storage capacity and efficiency. When WG is stored in aquifers, the injection and withdrawal processes are controlled by WG-brine transport physics, involving "forced" drainage during injection and "spontaneous and forced" imbibition during withdrawal [151]. However, relative permeability hysteresis can have a dual effect: while it may reduce the H_2 withdrawal factor, it can improve the H_2 withdrawal purity [152]. Previous hysteresis trapping studies have shown that this parameter decreased the H_2 recovery factor by 0.37% in a single cycle of production and withdrawal when compared to their base case without hysteresis [15].

Here, the H_2 injection will be preceded by the injection of CO_2, which will come into contact with the brine. The CO_2-brine relative permeability curves significantly influence the capillary trapping of CO_2 in the reservoir, which has been extensively studied in various works related to carbon capture and storage [153]. With the presence of multiple gases, the hysteresis describing the relationship between gas saturation and pressure during injection and withdrawal is expected to become more complex.

In this study, CH_4-brine relative permeability curves was used, as H_2-CO_2 brine relative permeability curves are not available.

6.3.3.2 Solubility in the aqueous phase

H_2 solubility was studied in saline solutions under reservoir conditions, and experimental data were used to supplement the lack of data for UHS. Various thermodynamic approaches have been developed to enhance the prediction of H_2 solubility and improve the models used in reservoir simulation software [154]. In the GEM simulation software, the gas solubility trapping in the aqueous phase was selected to be based on the general Henry's law based on the fugacity formula, the equation is as the following:

$$f_{iw} = x_{iw} * H_i \tag{6.1}$$

where, x_{iw} is the mole fraction of the component $i = H_2$ in the aqueous phase, f_{iw} is the fugacity of the component (i) in the aqueous phase and H_i is the Henry constant for the component, calculated as follows:

$$lnH_i = lnH_i^0 + \frac{v_i^\infty (P - P_i^0)}{RT} \tag{6.2}$$

H_i^0 is the reference Henry's law constants of the components (kPa) at the reference pressure P_i^0 (kPa). v_i^∞ is the partial molar volume of the component i in the aqueous phase at infinite dilution (l/mol) and P is its partial pressure in the gas phase under equilibrium conditions, R is gas constant, and T is temperature. The Henry constant is a function of pressure, where H_2 solubility in aqueous phase increases with rising pressure and decreases with increasing temperature and salinity [155]. Comparatively, carbon dioxide exhibits the highest solubility in water (0.169 g/100 g), followed by CH_4 (0.0023 g/100 g), while H_2 has very low solubility (0.00016 g/100 g) [156].

According to 157, the reference Henry's Law constant is set to $3.3 \times 10^{-4}\, mol/m^3 Pa$ and $37.7 \times 10^{-6}\, mol/m^3 Pa$ at a reference temperature of 298.15 K for CO_2 and H_2, respectively.

Since CO_2 dissolution is a long process and could have a significant impact on the volume of the CG, in this work, it was preferred to also investigate the viability of the CG. Therefore, simulations were conducted over a period of 10 years. The CO_2 solubility was taken as a function of pressure, temperature, and salinity. The solubility model for CO_2 was enhanced by making the Henry's constant dependent on temperature, pressure, and salinity. The simulation results have already demonstrated the efficiency of this enhanced model for CO_2, as they were compared to data from the literature [156].

The simulation for this parameter involved running the model with activated H_2 solubility and comparing it to the base case. Additionally, the impact of CO_2 solubility on the lifetime of the CG was assessed.

6.3.3.3 Dispersive Phenomena

This section discusses the phenomena responsible for mixing.

a) Physical Processes

Hydrodynamic dispersion comprises molecular diffusion and mechanical dispersion, the main two processes controlling the mixing between the WG and the CG. Molecular diffusion dominates

during quiescence, such as in scenarios with shut-in period, when there is no flow or exceedingly low flow. Conversely, mechanical dispersion predominates during periods of flow (injection or withdrawal). At reservoir scale, due to its dependency to velocity, hydrodynamic dispersion is a phenomenon that requires considering all flow mechanisms, including heterogeneities, as well as the influence of gravity on the flow stability [158].

Molecular diffusion is usually considered as a slow phenomena that is proportional to the concentration gradients [54]. The molecular diffusion process depends on the physical properties of the concerned molecule and the substrate (porosity, tortuosity, etc). The molecular diffusion coefficient for H_2 in its gaseous state is relatively high, approximately $10^{-6}\, m^2/s$ [9]. On the other hand, the diffusion coefficient for H_2 in pure water is lower, estimated at $5.13 \times 10^{-9}\, m^2/s$ at 25°C [13, 17]. Comparatively, H_2 is more diffusive than CH_4 and CO_2, with coefficients of 1.85×10^{-9} and $1.6 \times 10^{-9}\, m^2/s$, respectively.
In previous studies on seasonal H_2 storage in depleted gas reservoirs, minimal H_2 losses from dissolution and diffusion were reported, reaching as low as 0.1% [17].
It is important to emphasize that in this case study, the reservoir is composed of a mixture of gases, necessitating consideration not only of the diffusion of CO_2 in the aqueous phase but also that of H_2 in the gas phase.

In the section 6.4.3, we compare the base case with several scenarios where different molecular diffusion mechanisms are activated. One scenario involves the molecular diffusion of CO_2, while the others focus on the diffusion of H_2 in the gas and water phases, and the final scenario encompasses both phenomena. By examining these scenarios, we aimed to understand the impact of molecular diffusion on the storage process and the overall behavior of the reservoir.

Mechanical dispersion phenomenon is initiated by the movement of fluid in porous media, primarily influenced by flow velocity and direction [9]. Accurately predicting the mechanical dispersion process necessitates characterizing the dispersivity coefficient of the field site. However, this parameter is challenging to be determined due to the laboratory's incapacity to reproduce such irregularities (mainly natural heterogeneities that cause irregular flow at the field scale). Laboratory measurements typically identify dispersivity coefficients at the scale of a few millimeters or centimeters. Nevertheless, field tracer tests can be employed to determine the mechanical dispersion coefficient [54].

The simulations were conducted (section 6.4.4) with varying dispersivity coefficient values ranging from few centimeters to meters. The choice of an intentionally high and probably non-realistic dispersivity coefficient for this site was made to investigate the effect of increased dispersion. It is worth noting that in this study, the longitudinal and transverse dispersivity coefficients remain the same for all layers.

b) Numerical impact

If the hydrodynamic process is disabled in the model, numerical dispersion is likely still in effect in the simulation, causing the observed mixing effect between the two gases. Although inherent to the approximation of modeling techniques, numerical dispersion can be compared

to hydrodynamic dispersion. Typically, hydrodynamic dispersion values in porous aquifers are within the range of 10-100 m [159, 39]. In some cases, numerical dispersion can be substantial enough to completely dominate the true physical dispersion. Reducing the size of cells, especially in the front contact zone, can help mitigate numerical dispersion.

Comparing simulations in which mechanical dispersion is activated with simulations where this process is disabled will enable an evaluation of numerical dispersion.

In this section, the reference case that will be used is the base case including heterogeneities defined in the next section.

6.3.3.4 Geological heterogeneities

In previous works, it was highlighted that the impact of the CG on the recovery process was closely related to the permeability of the reservoir [15]. In fact, geological heterogeneities is a factor that can significantly impact the dispersion of the fluid in the porous media. A geostatisticaly distributed heterogeneous model for permeability field was used. The model is composed of 5 different rock fluid types with different level of heterogeneities Fig.6.3. The porosity was also distributed over the different layers and it ranges from 0.07 to 0.3.

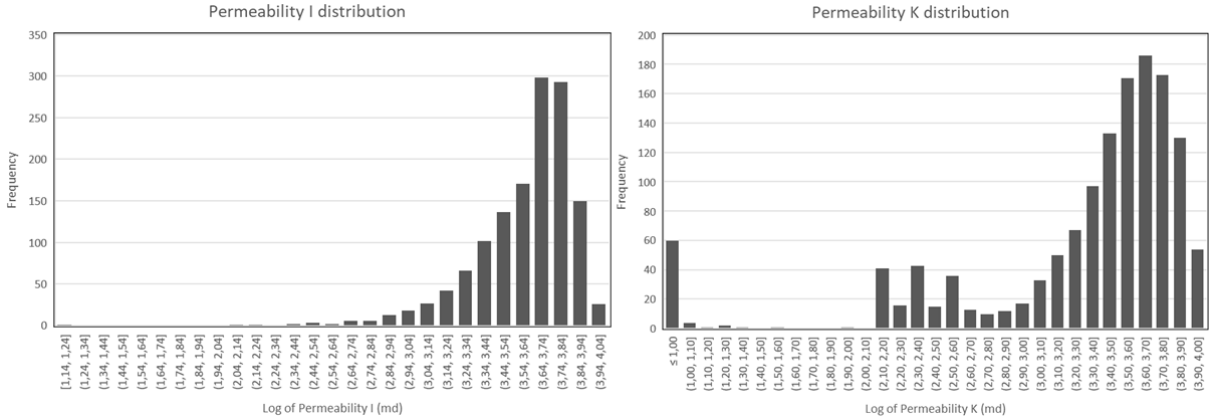

FIGURE 6.3: Permeability distribution for both Horizontal (left) and vertical direction (right).

6.3.3.5 Operational scenario

The base study involved multiple storage injection and withdrawal cycles with constant rates. In this section, we will explore the reservoir's performance by evaluating operational parameters and studying their impact on the storage process. The injection rate, production rate, and the time interval of the process will be modified, as shown in Table 6.3. Each scenario is defined by its event length, injection rate, shut-in duration, and production rate. Scenario A (Base case) maintains a seasonal event length without shut-in periods, injecting and producing H_2 at a constant rate. Scenario B and scenario C both have an event length of 3 months, and the same injection and production rates as the scenario A. The difference arises in scenario C, where a shut-in duration of 3 months is introduced. In contrast, scenario D maintains a 6-month event length with the same injection rate as the base case, but halves the production rate. Similarly, scenario E maintains the 6-month event length and injection rate, but reduces the production rate

by third the production case of the base case. Scenario F deviates in its injection rate, operating at half the rate of the base case, while maintaining a 6-month event length and no shut-in period. Lastly, scenario G mirrors scenario F, equalizing both the injection and production rates at half of the rates seen in the base case.

Table 6.3: H_2 Operational schedule data.

scenario	Event length (months)	Injection rate ($Stdm^3/Day$)	Shut-In (months)	Event length (months)	Production rate ($Stdm^3/Day$)
A (Base case)	6	1522800	0	6	1522800
B	3	1522800	0	3	1522800
C	3	1522800	3	3	1522800
D	6	1522800	0	6	761400
E	6	1522800	0	6	507600
F	6	761400	0	6	1522800
G	6	761400	0	6	761400

* Scenario A is the base case defined earlier in this work.

6.3.3.6 Well configuration

For the sake of simplicity, the base case in this study involves a single well that serves both as an injector and producer through the same perforations. Inspired by the selective technology [144] which involves deep perforation injection and shallower perforation production, we also explore a dual-well configuration. In this arrangement, one well operates as an injector at a greater depth, while the other serves as the producer at a shallower level. This study evaluates the effectiveness of these distinct scenarios.

Scenario A represents the base case with a single well configuration, while Scenario H explores a model with two distinct wells for injection and production as explained earlier. Scenario I replicates the base case but with a reduced production rate, and Scenario J follows the dual-well concept with a reduced production rate as well.

The impact of perforation location on the recovery of H_2 is also investigated in this section, considering the findings that shallower perforations may influence the injection process [21]. This section will explore the impact of the perforations' location on the recovery of H_2.

6.4 Results

For all the treated scenarios, the hydrodynamics of the H_2 plume reflect the density contrast between H_2 and CO_2, as demonstrated by the upward migration of H_2 beneath the caprock. The anticline structure of this model enhances the accumulation of H_2 and prevents its lateral spreading. In this section, we will discuss the impact of the previously mentioned parameters on the efficiency of H_2 storage and recovery.

6.4.1 Effect of hysteresis

The hysteresis trapping was added to the base case to investigate its potential impact on production behavior. The hysteresis did not affect the recovery factor of H_2 when compared to the base case. Similarly, when heterogeneity was applied to the base case and to the base case with hysteresis, it also did not seem to have a notable impact on the results. The unchanged behavior observed in both cases was actually expected, as the input data does not consider the mixture of gases and is primarily controlled by gases displacement around the well (driven by the mobility ratio), which is far from the water contact (even though it may indirectly influence the reservoir).

6.4.2 Effect of solubility in the reservoir

Solubility is considered an important process since even a small amount of H_2 dissolved in water can trigger biological activity [144]. Numerical simulations were conducted with H_2 solubility activated and compared to the base case scenario. However, negligible impacts were observed on the volume and the purity of the H_2 produced. On the other hand, the solubility had a slight impact on the bottom-hole pressure of the injection-production well, as depicted in Fig.6.4. Activating the solubility model resulted in a small reduction in the bottom-hole pressure due to the dissolution of gases in the aqueous phase within the reservoir.

Evaluating the effect of CO_2 dissolution on H_2 recovery is complex. The solubility of CO_2 is important, and it may lead to a relatively slow consumption of the CG, subsequently affecting the pressure provided by this gas to ensure the necessary pressure required for production. After 5 years, the well pressure dropped by 0.8% of its initial pressure. Further investigation may be needed to determine whether a refill of the CG is required, depending on the potential time scales of the storage.

Due to the negligible effect of H_2 solubility and the computational time required by the CO_2 solubility model, we have not considered this process in the subsequent simulations conducted in this study.

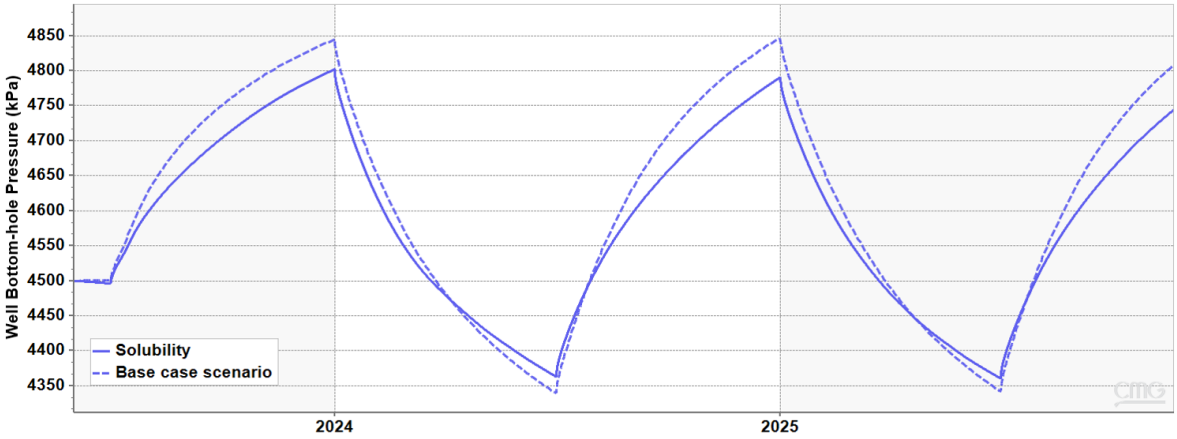

FIGURE 6.4: Comparison of bottom-hole pressure between the base case model and the model with solubility of H_2 and CO_2 activated.

6.4.3 Effect of molecular diffusion

The modeling process, taking into account diffusion, was time-consuming with convergence difficulties due to the complexity of the problem. Despite this challenge, simulations were conducted considering the molecular diffusion of H_2 in gas using the Sigmund correlation [160], and the molecular diffusion coefficient of H_2 and CO_2 in the aqueous phase was also taken into account, along with the presence of reservoir heterogeneities.

Accounting for diffusion in gas and aqueous phase did not significantly impact the results compared to the same case when diffusion was deactivated. This finding suggests that other dominant factors may overshadow the influence of molecular diffusion in the gas and aqueous phases. However, it is important to acknowledge that this parameter should not be overlooked in further investigations, even though it is common to deactivate it in simulations.

6.4.4 Effect of mechanical dispersion

The Fig.6.5 represents the H_2 mole fraction and the cumulative gas volume during the first production cycle. Various curves are present, each representing a different dispersivity coefficient, alongside the curve for the reference case. It is evident that the degree of mixing is notably influenced by the dispersivity coefficient. The H_2 mole fraction in the produced gas consistently remains below or equal to the H_2 mole fraction produced in the base case, although these values approach the base case values as the cycle nears its end. The same behavior is observed for cumulative gas withdrawal. This indicates that an increasing value of the dispersivity coefficient lead to pronounced mechanical dispersion, consequently increasing the mixing of CO_2 with H_2. The simulation conducted with a dispersivity coefficient of 0.10 m nearly overlaps the reference case curve, suggesting that numerical dispersion is very small. This is mainly due to local grid refinement around the well and in the contact zone between the two fluids.

When the dispersivity coefficient was set to greater than 1 meter, the impact of mechanical dispersion became significant. The 2D reservoir view in Fig.6.6 illustrates the H_2 mole fraction at the midpoint of the production period. Comparing the two profiles, it is evident that the H_2 fraction in the model with activated mechanical dispersion (Fig.6.6, left) is notably lower than in the base model with heterogeneity (Fig.6.6, right). Only a small portion of pure H_2 remains trapped beneath the cap rock.

The dispersion coefficient for the relevant site of our study appears to be on the order of 1 meter, and the mechanical effect of this value is not significant. Therefore, within the context of this research, numerical dispersion will be considered analogous to mechanical dispersion

Mechanical dispersion is also closely linked to flow velocity. Reduced velocities at greater distances from the well diminish the dispersion effect [39]. This aligns with other research highlighting the significant impact of injection and production rates on mixing between nitrogen and CH_4 [161]. Therefore, the mixing observed here may be minimized by reducing injection and production rates. It is important to note that, alongside molecular diffusion, mechanical dispersion amplifies mixing of gas components [9].

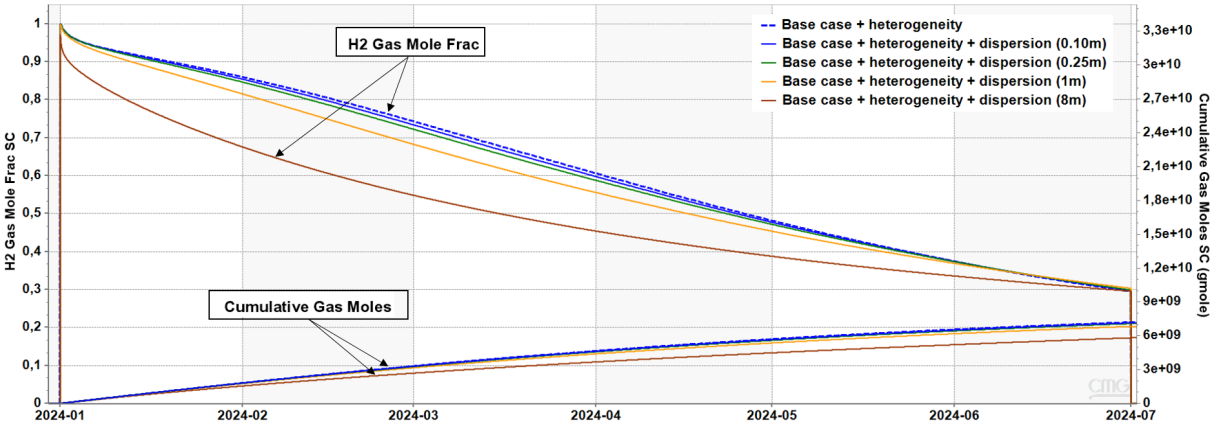

FIGURE 6.5: H_2 mole fraction recovered and cumulative H_2 mass produced-impact of activating mechanical dispersion.

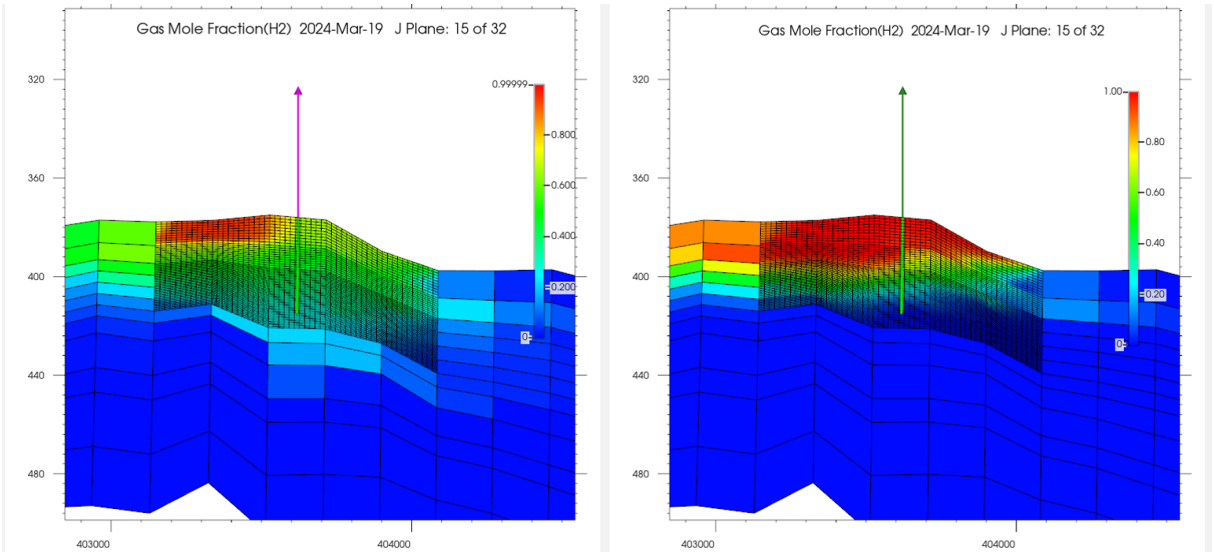

FIGURE 6.6: IK 2D view representing the H_2 mole fraction comparison between the mechanical dispersion (8m) activated model (left) and the heterogeneous base case (right).

However, it is important to mention that activating this parameter significantly increases computational time for the simulator (requiring up to 48 hours to simulate 300 days, compared to an average of 15 hours) and often leads to convergence challenges. Despite its importance, the substantial time cost associated with activating this parameter makes it unfeasible to conduct simulations for testing purposes.

6.4.5 Effect of heterogeneity

As can be observed in Fig.6.7, during production in the base case scenario, the amount of H_2 stored in the aquifer decreases unless the wells are shut down due to upconing (see Fig.6.8 right).

The CG/WG mixing zone reaches the production well, leading to an increase in CO_2 mole fraction production in the lower part of the well. This negatively impacts the efficiency of H_2 production, as the injected H_2 tends to rise and becomes less abundant in the lower regions.

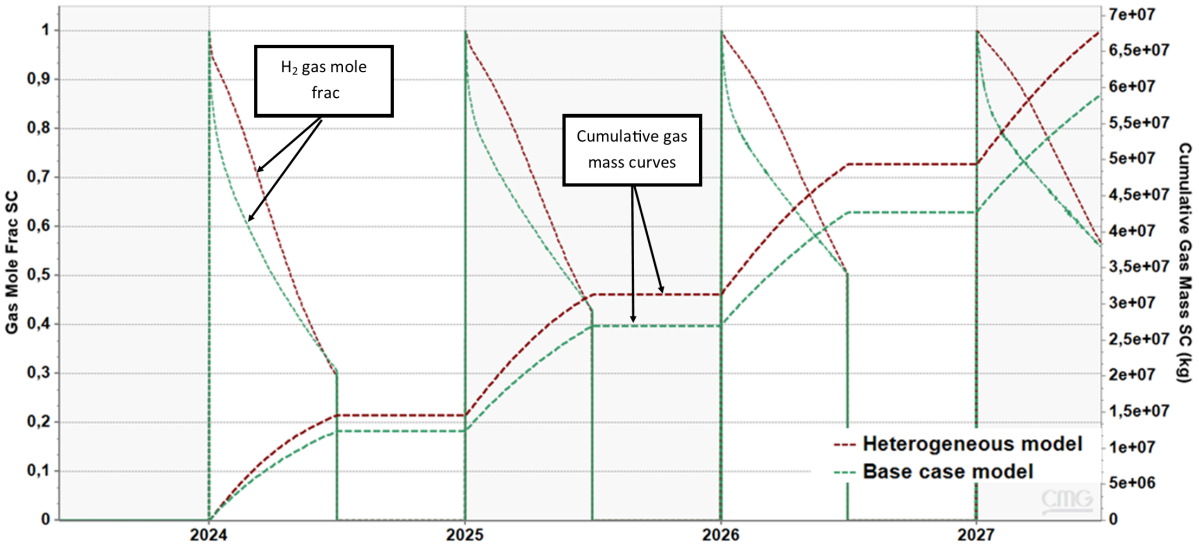

FIGURE 6.7: H_2 mole fraction recovered and cumulative H_2 mass produced-impact of adding heterogeneity.

When heterogeneity of this model is introduced, the heterogeneous permeability field significantly impacts well productivity, especially due to the effect of vertical permeability on coning. As depicted in Fig.6.7, before reaching the same H_2 mole fraction at the end of each cycle, we achieve a higher H_2 mole fraction with the heterogeneous model. This is further confirmed by the cumulative withdrawn volume of H_2, which is higher for the heterogeneous case. The mitigation of the coning effect due to the incorporation of this reservoir heterogeneities, is illustrated on the left side of Fig.6.8. Heterogeneity, in this case, promotes a non-uniform gas distribution [143].

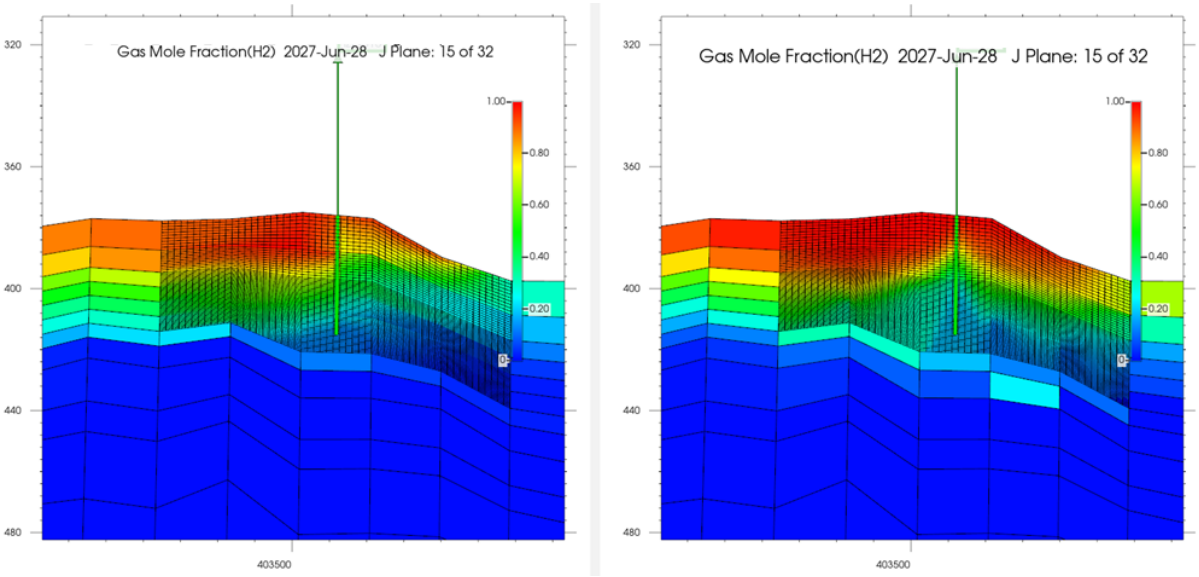

FIGURE 6.8: IK 2D view representing the H_2 mole fraction comparison between the heterogeneous model (left) and the base case (right).

6.4.6 Effect of the operation strategy

The injection and production rate, as well as the cycle duration (Fig.6.9) have a significant impact on both the quality and quantity of the produced H_2.

Among the scenarios, E and G represent the highest and lowest mole fraction of H_2 recovery at the end of the production cycle, respectively. When compared to the base case, scenarios C, F, and G exhibit lower H_2 fraction in the produced gas, as well as less cumulative volume. Conversely, scenarios E and D exhibit better H_2 mole fraction compared to the base case, albeit with different cumulative volumes (D more volume than E). Notably, scenario B represents the only case with both improved H_2 fraction and cumulative volume.

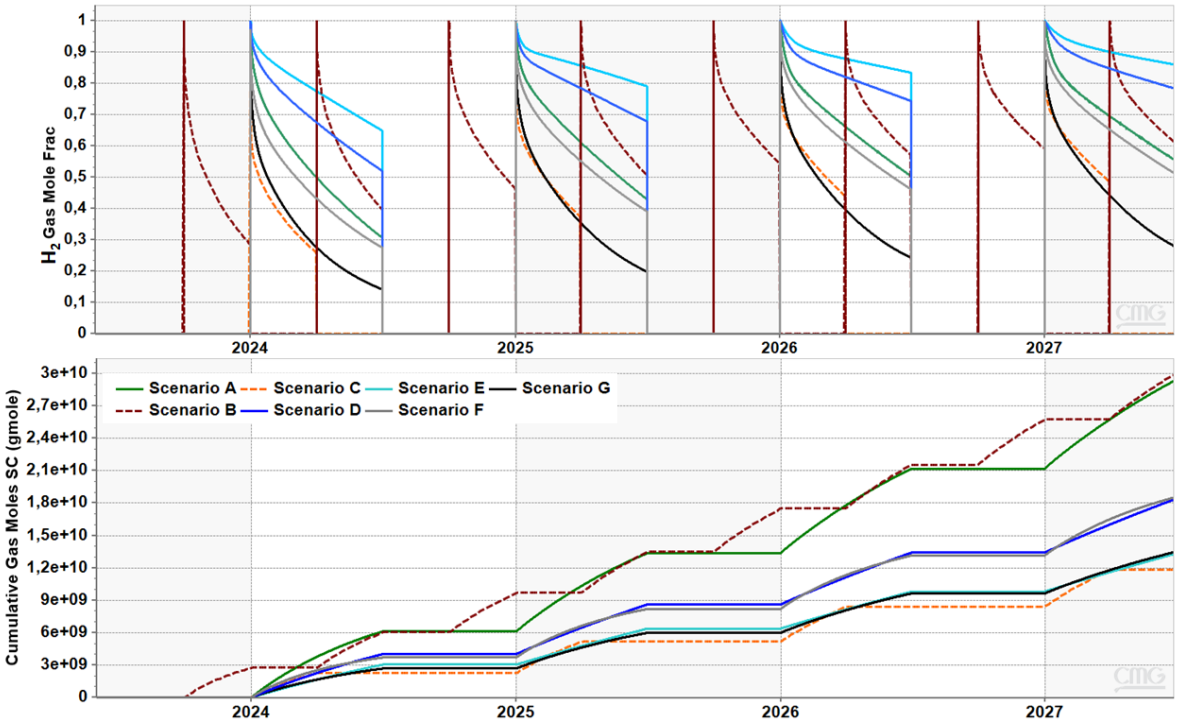

FIGURE 6.9: H_2 gas fraction withdrawn for every considered scenario (up) and the corresponding cumulative H_2 gmole (down)- Effect of the operation strategy.

In the scenarios F and G the quantity of injected H_2 is reduced, however, also reducing the production rate, as in case G, seems to enhance the quality of the produced gas. For instance, producing at half the rate of the injection rate leads to 62.4% of the base case quantity produced, while producing at a rate equivalent to one-third of the injection rate results in 45.2% of the base case quantity produced for the same injection-production cycles period. Scenarios B and G represent the same quantities injected and withdrawn, but over different periods of time and at different rates. In Scenario B, double the quantity is injected and withdrawn compared to Scenario G, but within half the time frame. Comparing these two scenarios highlights the impact of the injection rate on the reservoir dynamics, illustrating a trade-off between gravity segregation and viscous fingering.

Gravity override is predominantly observed in most cases, with H_2 naturally tending to migrate to the top of the structure. This displacement is dependent on the velocity and can

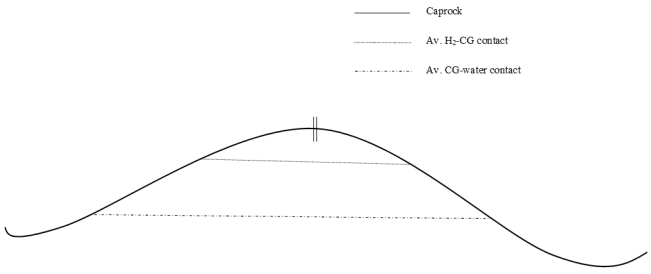

(a) Slow injection: gravitational forces dominate

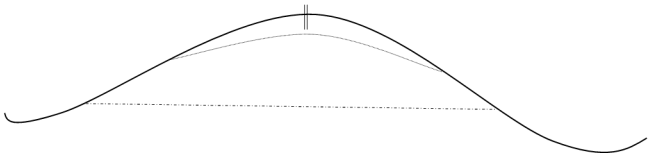

(b) Fast injection: viscous forces dominate

FIGURE 6.10: A schematic representation of the gas spreading depending on the injection rates. (Figure modified from [84])

become unstable at a critical velocity, thereby affecting gas distribution, as depicted in Fig.6.10 [84].

In Fig.6.11, the left side illustrates the H_2 fraction in Scenario B after 3 months of injection, while the right side shows the same for Scenario G after 6 months of injection. This figure represents the gas distribution beneath the caprock. Notably, when the injection rate is lower, the lateral spread is more significant due to the prevailing gravitational forces.

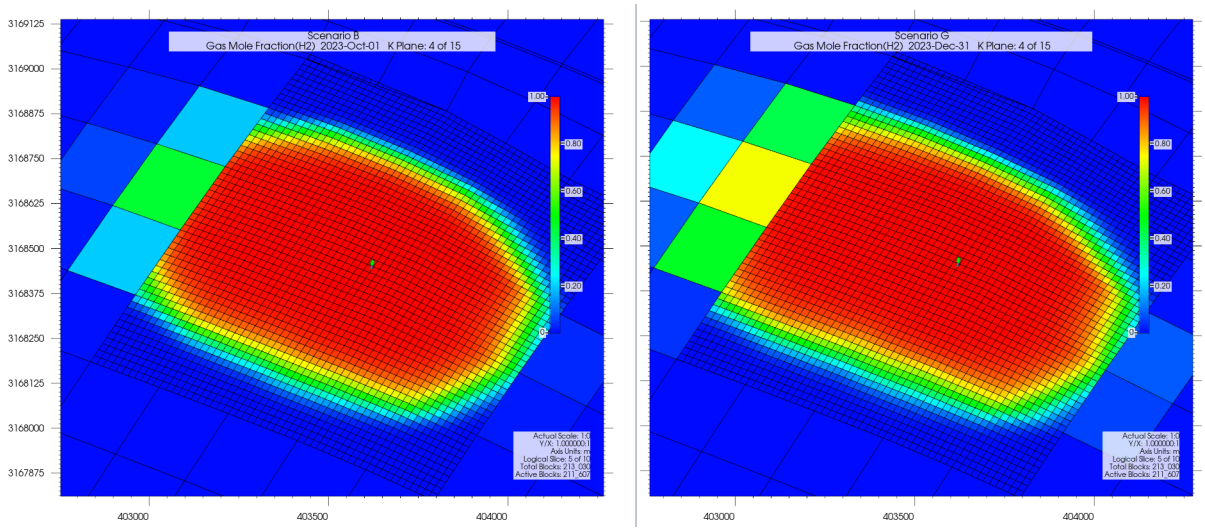

FIGURE 6.11: Plane view depicting a comparison of H_2 mole fraction between scenario B (left) and scenario G (right). The visual highlights the distinct variations in H_2 distribution resulting from the difference in injection rate.

Scenario C presents a case with both low quality and quantity, mainly due to the shut-in period. Interestingly, the rest time between operations not only enhances mixing but also provides

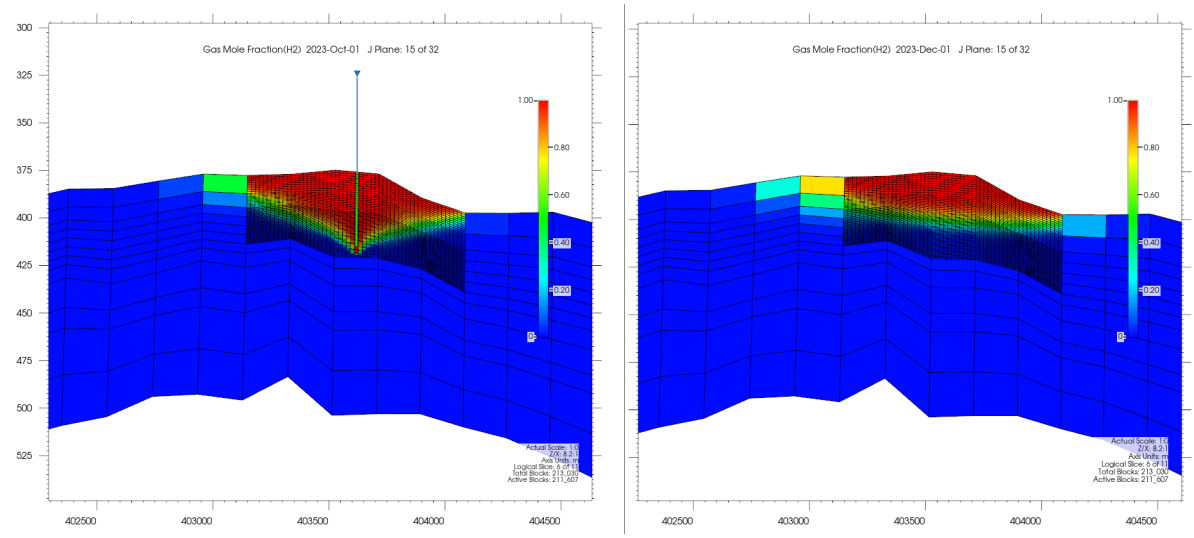

FIGURE 6.12: IK 2D view depicting a comparison of H_2 mole fraction between scenario B (left) and scenario C (right). The visual highlights the distinct variations in H_2 distribution resulting from the different operational conditions, showcasing the effects of the shut-in period in scenario C.

time for H_2 to migrate laterally beneath the caprock. This migration reduces the vertical height of the H_2 layer under the caprock and increases the contact of the CO_2 fraction with the well perforation, as illustrated in Fig.6.12. The left view is depicted immediately after the injection phase of scenario B, while the right view shows the situation one month after the injection phase.

During the shut-in period, as observed in the figure, gravity forces had sufficient time to establish layering based on density, leading to a change in the shape of the plume around the well.

The most favorable scenario appears to be when reducing the injection and withdrawal periods. However, it remains uncertain whether this approach is practical for real-case applications and whether it aligns with seasonal storage plans.

6.4.7 Effect of well configuration

The results, here shown in Fig.6.13 indicate that the use of different perforations in Scenario H and J, did not have a substantial impact on either the fraction or the quantity of produced H_2 when compared to the base cases (Scenarios A and I, respectively).

Scenario H closely resembles Scenario A, with the H_2 fraction and cumulative volume of produced gas exhibiting minimal differences. Similarly, Scenario J closely mirrors Scenario I, with slight variations in H_2 fraction and cumulative volume.

These findings suggest that the concept of employing deep perforations for injection and restricting production to the upper part of the reservoir, did not significantly alter the overall performance of the H_2 storage process. However, these slight differences observed between scenarios may still carry practical implications that require further investigation for real applications.

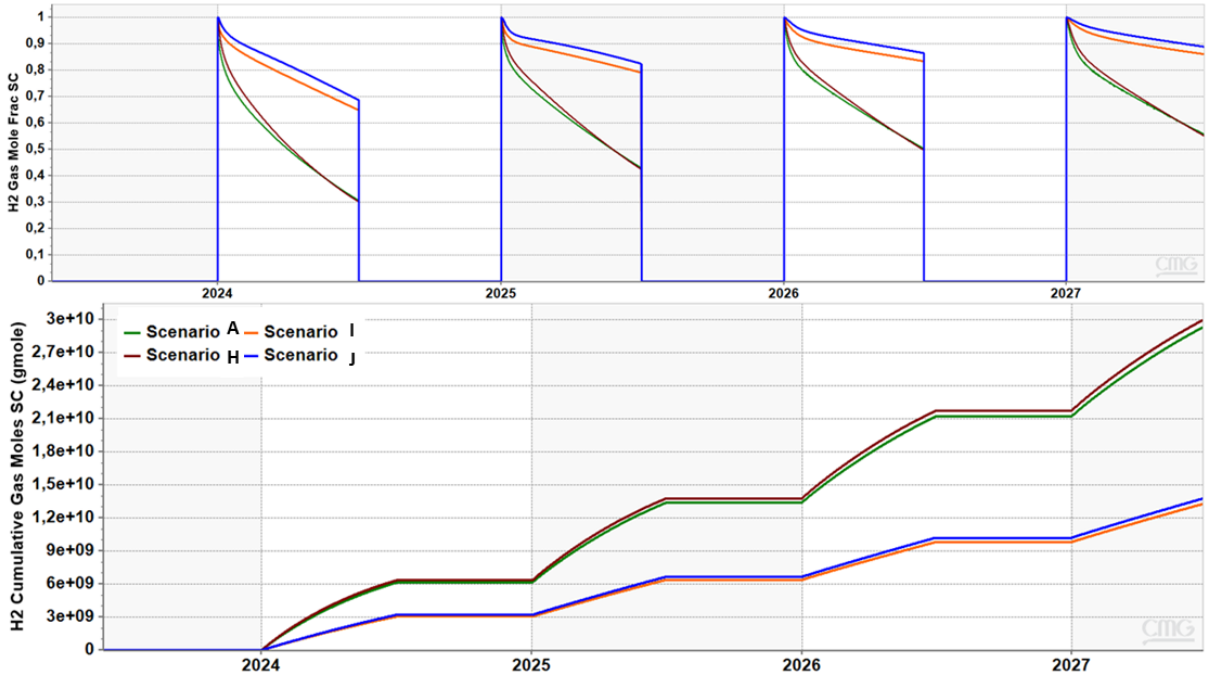

FIGURE 6.13: H_2 gas fraction withdrawn for every considered scenario (up) and the corresponding cumulative H_2 gmole (down)- Effect of the well configurations.

6.5 Discussion

Based on the above sensitivity study, we identified the most significant parameters with a considerable impact on gas purity and/or quantity. These key parameters include heterogeneity, production rate, and cycle duration. In this section, we conducted simulations by combining two or three of these identified processes, as outlined in Table 6.4. The main goal of these simulations is to determine the most effective scenario by evaluating the combined effects of these parameters.

To assess the effectiveness of each scenario, we employed a Hydrogen Productivity Index, defined as the ratio of cumulative H_2 produced to cumulative H_2 injected (Eq.6.3).

$$\text{H}_2\text{productivity index} = \frac{\text{Cumulative H}_2\text{produced}}{\text{Cumulative H}_2\text{injected}} \times 100 \tag{6.3}$$

Additionally, the withdrawal quality of the H_2-expressed as a gas mole fraction of the total gas produced-complements this recovery factor. These parameters collectively serve as a crucial metrics for evaluating the performance of each scenario in terms of H_2 recovery during the storage process.

The Fig.6.14 showcases two plots. On the left, we observe the H_2 mole fraction selected at the end of the withdrawal period and its corresponding standard cumulative gas produced volume. The cycle numbers are also indicated on the curves. This plot reveals two distinct reservoir behaviors: one that delivers large volumes (composed of less than 70% H_2) and the other behavior that delivers higher-quality gas but with a limited volume due to a reduced production rate. Scenarios A, B', C', and E' are associated with delivering large volumes, whereas scenarios D', F', and G' focus on delivering high-quality gas.

Table 6.4: Simulations details.

Process	Heterogeneity	Event length*	Production rate**
Scenario B'	✓		
Scenario C'		✓	
Scenario D'			✓
Scenario E'	✓	✓	
Scenario F'	✓		✓
Scenario G'	✓	✓	✓

Scenario A is the base case defined earlier in this work.
* The event length is reduced from 6 months to 3 months of injection and 3 months withdrawal.
** The production rate is defined as third of the injection rate $507600 Stdm^3/Day$.

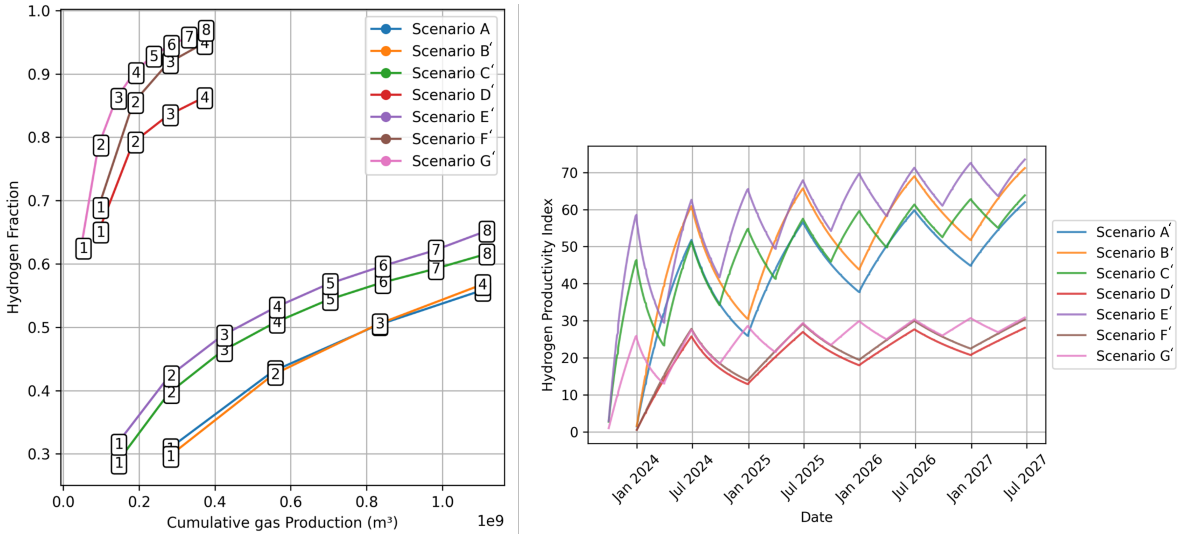

FIGURE 6.14: Dynamics of H_2 Productivity. Left: H_2 mole fraction at the end of the withdrawal period and the corresponding standard cumulative volume of the produced gas. The numbers represent the cycle numbers. Right: the H_2 productivity index as function of time.

On the right side, we present a graph illustrating the H_2 Productivity Index's behavior over time. Notably, scenarios B', C', and E' exhibit higher productivity indices, indicating that despite not having the best gas quality, a significant quantity of the injected H_2 is effectively recovered. It is important to highlight that the quality of the produced H_2 improves with each cycle, a trend consistent with findings from other studies. Towards the end of the last cycle, scenarios B' and E' surpass a productivity index of 70%, making them potential economically viable and practical options for real-world applications.

6.6 Conclusion

This study has focused on investigating the key parameters that impact the viability and effectiveness of UHS in aquifers, using CO_2 as a CG, through numerical simulations. Various scenarios were explored by adjusting input parameters, such as residual saturation, H_2 solubility in the aqueous phase, diffusion, dispersion, reservoir heterogeneities, operational scenarios, and

injection-well strategy, to understand their influence on gas recovery and quality. The simulations revealed that heterogeneity, cycle duration, and production rate play crucial roles in enhancing gas quality and cumulative recovered volume.

- Heterogeneities enhanced the quality of the recovered gas by suppressing the coning effect. Note that this finding is site specific.
- Producing at a slower rate, while keeping the injection rate and period constant, effectively reduces the mixing between the two gases. This results in the mixing zone being pushed further away from the well, allowing for the production of less contaminated H_2. This conclusion is consistent with findings from other studies [162].
- Reducing the cycle duration helps to quickly recover the injected H_2 and limits the time for the gas to migrate and mix.
- Mechanical dispersion can have a significant impact on the mixing zone, and its effect closely depends on the dispersivity coefficient. Characterizing this parameter for each specific site is essential for assessing the profitability of the storage project.

To evaluate the combined effects of these parameters, the H_2 Productivity Index was analyzed. The scenario with heterogeneity and an increased number of cycles per year demonstrated higher efficiency. Furthermore, it was observed that gas quality improves with each cycle, potentially reaching economically viable levels by the end of the last cycle in certain scenarios. However, further investigations are recommended to explore the long-term behavior of gas quality and stability over extended simulation periods.
The challenge in UHS lies in striking a balance between the quality and quantity of the produced gas. Achieving high gas quality often requires accepting a lower gas quantity, and vice versa. Therefore, it is essential to conduct an economic analysis, which involves calculating the LCOHS, taking into account both the CapEx and OpEx factors [14]. CapEx includes the initial investment costs, such as the cushion gas investment, while OpEx covers ongoing operational costs from the first day of the project.

By integrating technical insights from this study with the economic analysis, better decision-making and planning can be achieved in industrial applications. This approach can help identify promising scenarios for efficient and cost-effective UHS solutions.

6.7 Limitations and Future Developments

Although this study enhances our comprehension of UHS in aquifers, it is also constrained by few limitations that pave the way for further research points.

To deepen our understanding of the H_2-CO_2 system, particularly concerning phenomena like diffusion, solubility, and dispersion of hydrogen in CO_2, further experimental investigations are crucial. These experiments can provide real-world data and insights that support numerical modelling. Through these information, we can gain more accurate knowledge of how hydrogen

behaves with CO_2 under various conditions, ultimately improving our comprehension of this system.

Future research could expand this study to include analysis of geochemical and microbial activities within the reservoir. This knowledge will enable a better understanding of the potential implications of these phenomena on the reservoir

Regarding operational scenarios, the current study evaluates the performance of a single injection and withdrawal well positioned on the summit of the anticline. Thus, further research into the deployment of multiple wells, varied well configurations, and their impacts on UHS efficiency is intended. Strategies such as separating injection and withdrawal wells to recover hydrogen that has migrated to the top of the reservoir could be examined to avoid the injection point and the contact zone with the CG. This can be explored to optimize gas recovery and minimize mixing phenomena.

Expanding the scope of this work to consider the impact of storing other gases, such as CH_4, N_2 or mixtures, on the recovery and the purity of H_2 produced, is another promising way forward. The role and the effect of different CG have been explored for depleted oil reservoirs and partially depleted gas condensate reservoir, but there is a lack of research in the context of aquifers [16, 163]. This is being investigated as part of an undergoing PhD project.

Finally, the variation in site-specific strategies complicates direct comparisons. Each study site implements its own unique production strategy, including the use of different numbers of production wells. This diversity in operational approaches makes it challenging to make direct comparisons and highlights the need for standardized evaluation that allow for a more straightforward comparison of UHS projects across different sites.

CHAPTER 7

Conclusions

This thesis is organized into five main chapters: analytical investigation of the stability of H_2 -CG miscible fronts and storage capacities, thermodynamic models for mixtures of CO_2-H_2, the development of a thermodynamic model integrated into the ComPASS tool, evaluation of storage conditions, and the examination of key parameters influencing storage efficiency through numerical modeling. Detailed conclusions for each of these chapters can be found in sections 2.5, 3.6, 4.6, 5.5, and 6.6. Summarized the following conclusions can be drawn:

- Deep saline aquifers have emerged as potential UHS sites due to their widespread geographic distribution and significant storage capacities. Geological sites used for CCS where the CO_2 is stored permanently could serve as an ideal storage sites for UHS, offering potential cost savings. However, this approach presents multiple challenges, such as addressing hydrodynamic effects responsible for mixing between H_2 and the CG. Additionally, microbial and geochemical activities play a role, but these are outside the scope of this study, though literature provides substantial information. The primary challenge is to mitigate mixing and ensure the integrity of the storage. Identifying geologic and operational parameters that impact the mixing of CO_2 and H_2, while considering cost-effectiveness, is a novel contribution, as it has not been explored with a realistic geological model.

- The stability of miscible H_2-CG fronts when H_2 is injected and displaces various CGs has been analyzed in the context of UHS scenarios. We found, despite the unfavorable viscosity contrast, that these fronts tend to be stabilized by gravity in a broad range of practical injection rates. The maximum injection rate that ensure this stability is influenced by reservoir permeability, the inclination angle of the front with respect to the horizontal, and the relationship between the density and viscosity of H_2-CG mixtures. These fronts remain stable in reservoirs with medium-to-high permeability and homogeneous characteristics, ensuring the mixing zone stays within acceptable limits, particularly for practical H_2 injection rates. Additionally, the trade-off between buoyancy forces and capillary properties of the seal rock, considering different CGs, has been assessed to determine H_2 height storage capacities. We discovered that denser CGs, such as CO_2, having lower density differences

with brine, reducing buoyancy forces and increasing storage capacities. Therefore, storage capacities decrease in the order of CO_2, CH_4, and H_2. This analysis can be extended to any WG/CG combination, including mixtures. In summary, using CO_2 as the CG for UHS in aquifers or depleted gas reservoirs offers significant advantages over using H_2 or other inert gases like nitrogen or methane. This approach not only allows a substantial amount of H_2 to be stored but also enhances storage safety by reducing the buoyancy forces transmitted to the top of the reservoir. Furthermore, the same reservoir can serve dual purposes by being used for permanent CO_2 storage while also acting as a CG for intermittent H_2 storage. The presence of gas with these interfacial properties beneath the seal rock improves the security of CO_2 storage.

- A thorough examination of three thermodynamic models, including two cubic EoS and the GERG-2008 EoS, aimed to understand their accuracy in modeling the behavior of the CO_2-H_2 system under UHS conditions. The GERG-2008 EoS was identified as the most suitable model, considering its performance in accurately predicting the thermodynamic properties. This model is capable of handling a wide range of pressures and temperatures, especially under UHS-relevant conditions, making it the preferred choice for UHS simulations. While cubic EoS models are generally reliable and offer a balance between accuracy and computational efficiency, the GERG-2008 EoS stands out for its accuracy, particularly at low H_2 fractions.

- A thermodynamic model based on cubic equations of state was developed and integrated into the open-source reservoir simulator, ComPASS. Several case studies and thermodynamic properties were utilized to validate this module. The main challenge addressed during this task was related to phase appearance and disappearance. The integration of a cubic EoS model within ComPASS provides a consistent tool for simulating phase transitions, fluid behavior, and mass transport in porous media. This model can be applied in various reservoir simulation applications, including carbon sequestration and geothermal reservoir analysis.

- The phase diagram exploration of the system H_2-CO_2 has pointed the potential for a two-phase system in UHS under specific pressure-temperature conditions. This research is a preliminary analysis of how these behaviors affect mixing phenomena and the occurrence of gravity currents, a process that can segregate fluids based on density differences. First numerical modeling simulations showed that phase separation at the mixture front can reduce mixing of the CG with the injected H_2 and delay the rise of H_2 gas. This information can be crucial for optimizing UHS operational efficiency, and offshore reservoirs in cold sedimentary basins meeting the recommended conditions may be attractive prospects for UHS sites.

- Numerical simulations, utilizing the commercial tool GEM-CMG, were conducted to evaluate the effectiveness of UHS in aquifers, with a focus on the identification of key parameters influencing gas recovery and quality. The reservoir investigated corresponds to a realistic aquifer with a single well. The results highlight that the amount of recovered H_2 progressively

increases with successive withdrawal cycles. Several parameters were found to influence the quality and quantity of the produced gas for this reservoir (like production rate and cycle duration), with geological heterogeneities of that reservoir playing a crucial role in mitigating the coning effects. Short-period cycles were shown to enhance the Hydrogen Productivity Index, while the production rate impacted gas quality and the extent and location of the mixing zone. These findings demonstrate that UHS with CO_2 as a CG can be achieved with reasonable gas recovery parameters.

In conclusion, this thesis contributes to a deeper understanding of UHS. These insights can inform future UHS projects and enhance their efficiency and cost-effectiveness.

Analogies with Natural Hydrogen Observations: Observations from natural H_2 occurrences in conventional and unconventional reservoirs provide valuable insights for UHS. While the average concentration of H_2 in gases from conventional reservoirs is approximately 0.8%, the median concentration is as low as 0.01% [164]. However, exceptional cases with remarkably high concentrations of H_2 in both conventional and unconventional reservoirs have been reported, shedding light on the potential of natural UHS system. For instance, in Australia, concentrations ranging from 51% to 84% have been observed in the Adelaide area within the Gawler Craton, and up to 95.3% in the Meda field in the Canning Basin [165, 166]. In the Heins and Scott wells in Kansas, 31 gas samples showed H_2 concentrations ranging from 1.4% to 70% [167]. In the Bourakebougou area of Mali, gas with concentrations as high as 98% H_2 was discovered [168, 169]. Even more intriguing, a well in Kazakhstan encountered a free water flow containing 90% to 98% of molecular H_2 in dissolved gas [164].

Globally, there have been notable initiatives in exploring H_2, including the Hydroma project in Mali, where the exploitation of a natural H_2 field has enabled electricity production for a village. The NH2E project in the United States, which initiated drilling in Kansas in 2019, and SANTOS in Australia, with its plans for H_2 production in the Amadeus Basin, represent significant steps towards natural H_2 exploration. Additionally, the discovery of a natural H_2 field in Arizona by "Desert Mountain Energy" demonstrates the expanding interest in this field. However, it is important to note that scientific publications on these discoveries are limited, with the Malian project being a notable exception.

In France, potential operators such as 45-8 and ENGIE have included the exploration and production of natural H_2 in their corporate strategies. This emphasis on natural H_2 exploration underscores the growing recognition of its potential significance in the transition to decarbonized energy sources.

Understanding these natural H_2 phenomena and their geological characteristics provides a valuable foundation for UHS exploration and comprehension. The insights gained from these occurrences can be pivotal in shaping the strategies for UHS and support H_2 as an energy carrier for decarbonization.

APPENDIX A

Different Viscosity models

In this appendix, we begin by introducing various viscosity models that are utilized in this work. Subsequently, we compare the output results of these models for the H_2-CO_2system. As the viscosity model has an influence on the velocity limit calculation (refer to section 2.4), we provide an updated table and comparison specifically for the H_2-CO_2 system. A dedicated subsection is included for this purpose. In the following section, we briefly discuss the minimal impact of these models on the remaining systems examined in this study.

A.1 Review of possible/used viscosity models:

There are several methods for estimating the viscosity. A variety of methods have been developed to accurately estimate fluid viscosities for pure components or mixtures. These methods present advantages and limitations generally linked to their type, "empirical" requiring a lot of experimental data, or "predictive" with a solid theoretical background and requiring little or no experimental data to have more or less reliable data. Given the very limited available high-pressure viscosity data especially for the H_2-CO_2 system, predictive models are the most appropriate in this case. Among the best-known predictive models used to estimate the viscosities of high-pressure gas mixtures:

- the TRAPP (Transport Property Prediction) -type model (Eq.(A.1)) developed by Ely and Hanley [170] based on the extended corresponding state (ECS) theory and applicable to systems containing hydrocarbons, permanent gases, CO_2, H_2S and refrigerants. However, the original version (TRAPP) is not recommended for use at reduced temperatures (T/T_c) above 0.925, and in these conditions, its variant called SuperTRAPP (see book of Millat et al. 1996 [87]), which has been further refined and implemented under the generic name "ECS model", is preferable and is currently available in REFPROP (NIST's software). In REFPROP's SuperTRAPP model, a scaling factor has been added so that, at infinite dilution of each compound, the viscosity of the pure fluid is exactly reproduced [88].The definition and calculation details of each term in Eq.(A.1) can be found elsewhere in the

literature [89].

$$\begin{aligned}\Delta\mu(T,\varrho,x) &= \mu(T,\varrho,x) - \mu^*(T,x) \\ &= \Delta\mu(T_{\text{ref}},\varrho_{\text{ref}})F_\mu(T,\varrho,x)\ .\end{aligned} \tag{A.1}$$

- the model proposed by Dean and Stiel 1965 Eq.(A.2), which is simplest to implement, applies to high-pressure pure fluids and their mixtures, and is available in Simulis Thermodynamics (ProSim's software). Using a semi-theoretical approach, Predvoditelev [171] showed that residual viscosity $\Delta\mu(T,\varrho,x)$ is simply a function of density. Subsequent works have built on this finding, including those by Stiel and co-workers, and more recently by Galliero et al. 2005 [172], who introduced a temperature dependency as well. The Dean-Stiel version implemented on Simulis Thermodynamics uses the Brokaw model [173] to estimate the viscosity of gas mixtures at moderate pressure (or dilute-gas viscosity) $\mu^*(T,x)$.

$$\Delta\mu(T,\varrho,x) = \frac{10.8 * 10^{-5}(e^{1.439\rho_R} - e^{-1.11\rho_R^{1.858}}))}{\xi}\ . \tag{A.2}$$

In the next section, we test the two models mentioned above and compare them with the original Wilke model (Eq.(2.2) with expression (2.3)) and its simplified version with the Herning and Zipperer term (Eq.(2.2) with expression (2.4)).

A.2 Different viscosity models applied to the system H_2-CO_2

In this section, we apply the previously mentioned models to the H_2-CO_2 system and provide a comprehensive discussion on the comparison of the obtained results. Fig.A.1 depicts four different scenarios at various temperatures and pressures: 298 K, 5 MPa; 323.15 K, 5 MPa; 298 K, 25 MPa; and 323.15 K, 25 MPa. Each figure on the left represents a zoomed-in view on the right, focusing specifically on the H_2-rich system. The x-axis represents viscosity, while the y-axis represents density. The marked points indicate the density and viscosity of the mixture at specific fractions of hydrogen in the system. As the fraction of H_2 increases, the points ascend. Different models are presented for comparison in each scenario, alongside a set of experimental viscosity data that corresponds to our system of interest. In this analysis, a density model (GERG-2008 model [53]) is used to align the results.

It is observed that the SuperTRAPP model accurately predicts the viscosity of the system across all temperatures and pressures, while the Wilke model exhibits slight underestimations of viscosity for H_2-rich systems at 5 MPa, yet remains close to SuperTRAPP predictions. Since SuperTRAPP successfully describes the experimental data throughout this section, it will be considered as the reference model for the remaining analyses.

At 25 MPa, the Wilke model deviates from the SuperTRAPP description of the fluid, confirming that this approximation is only valid at low pressure. The Dean and Stiel model demonstrates a common behavior at 5MPa, correctly predicting systems rich in H_2 but deviating as the CO_2 fraction increases. At different temperatures but at 25MPa, this model exhibits an overall improvement in predicting the mixture and aligns with the SuperTRAPP curve at both extreme ends (CO_2-rich and H_2-rich), with a small deviation in between.

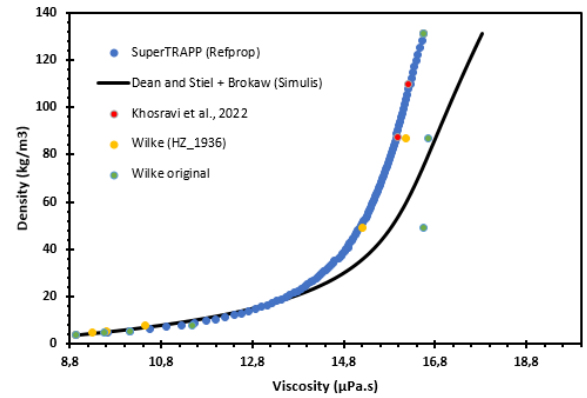

(a) 298K_5MPa

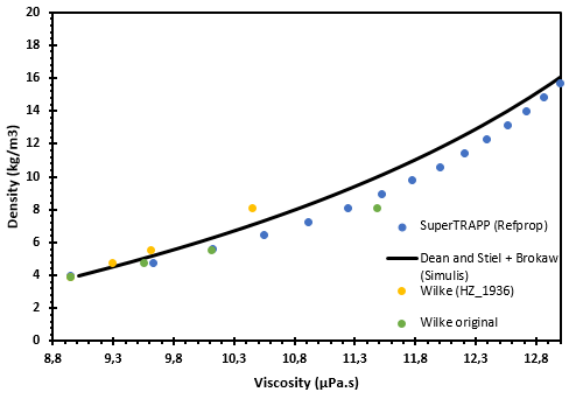

(b) 298K_5MPa zoom

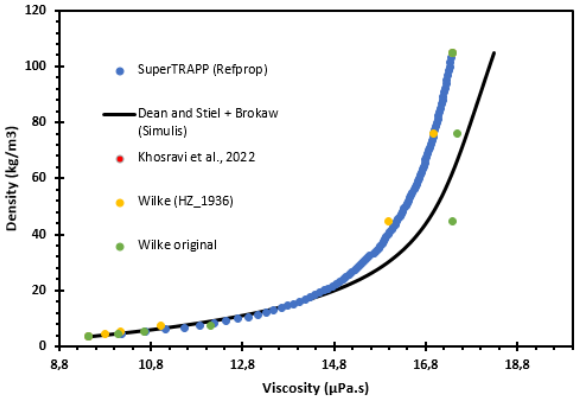

(c) 323K_5MPa

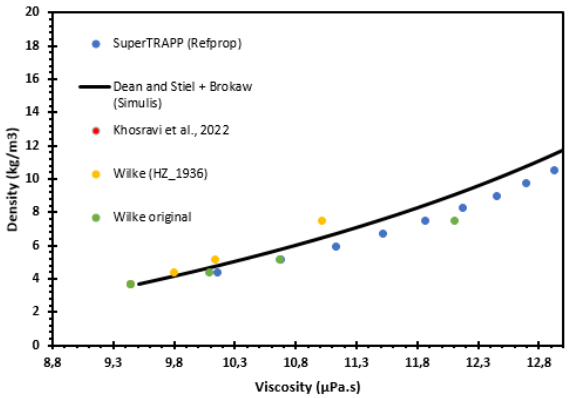

(d) 323K_5MPa zoom

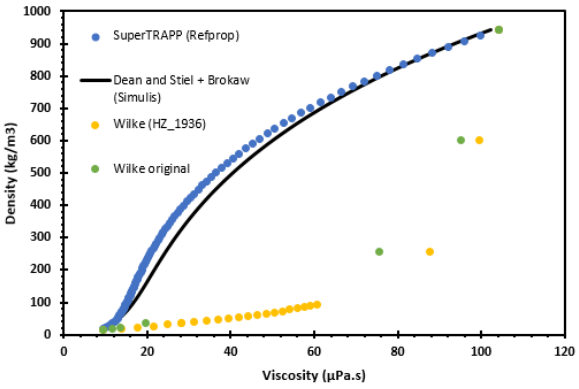

(e) 298K_25MPa

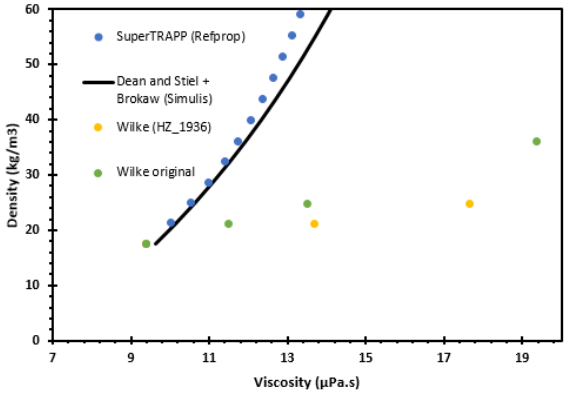

(f) 98K_25MPa zoom

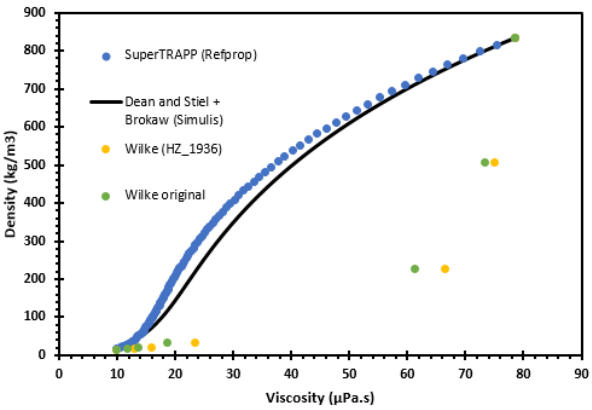

(g) 323K_25MPa

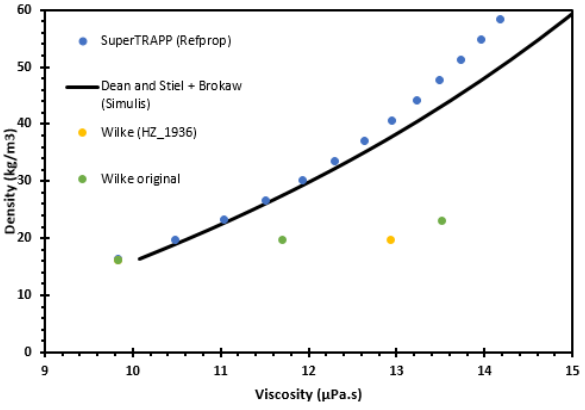

(h) 323K_25MPa zoom

FIGURE A.1: H_2-CO_2 density vs viscosity.

In conclusion, the Wilke model can be used as a simplified approximation, but it is not valid at high pressures. On the other hand, the Dean and Stiel model is the opposite behaviour of Wilke, and SuperTRAPP proves to be the most suitable model for this system. The expression $d\rho/d\mu$ was determined for various pressures and temperatures in Fig.A.2 using SuperTRAPP model. The curves are calculated under single-phase conditions (vapor, liquid or supercritical). Being close to the critical pressure of CO_2, the curves at 5 MPa are less smooth than those at 25 MPa, and this is linked to:

- most likely, the determination of the "shape factor" of the SuperTRAPP model, which is obtained iteratively (exact shape factor method) and is density-dependent, and care must be taken not to obtain incorrect roots in regions where there are several roots (non-convex problem) [88] and more precisely in the vicinity of the mixture's critical point.

- or/and, very less likely, the "scaling factor" used in REFPROP's implementation of Super-TRAPP model so that, at infinite dilution of each compound, the viscosity of the pure fluid is exactly reproduced [88].

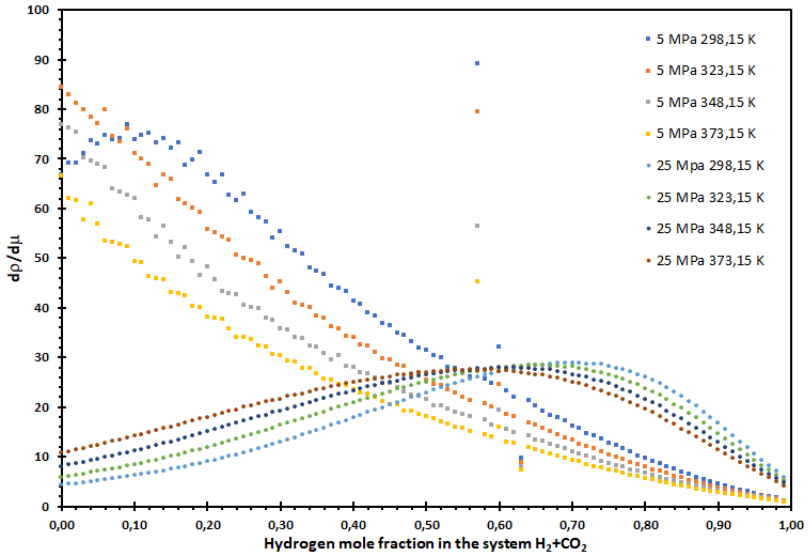

FIGURE A.2: $d\rho/d\mu$ at different pressure as a function of composition (or molar H_2 content) y of the H_2-CO_2 mixtures for various temperature and pressure conditions. Densities are those of the GERG-2008 model [53]. Viscosities values are determined using the SuperTRAPP model [87, 88, 89].

Since the viscosity model has an influence on the velocity limit calculation (as discussed in section 2.4), Table A.1 provides a comparison of velocity limit values calculated using different viscosity models for the H_2-CO_2 system, while GERG-2008 is used for density calculations. Based on the conclusion that SuperTRAPP is considered as the reference model, the resulting velocity limit will be considered as a reference to compare against values calculated using other viscosity models. For instance, the Wilke model appears to be a good approximation for describing this system.

Table A.1: Maximum velocity U_m (m/day) for a stable downward displacement of CO_2 displaced by H_2 for various T and P conditions with viscosity calculated with different models. Reservoir permeability k =1 Darcy. For other permeabilities these figures have to be multiplied by the number of Darcies of the reservoir.

Temp(K)	298	298	323	323
Pressure (MPa)	5	25	5	25
Wilke	1.64	3.63	1.61	3.21
Wilke(HZ_1936)	2.07	0.75	1.84	0.95
SuperTRAPP (Refprop)	1.04	5.09*	0.93	4.51
Dean and Stiel + Brokaw (Simulis)	1.68	6.16	1.45	5.50

* This value is discussed in the section 2.4.1 and corrected in Table 2.3.

A.3 Different viscosity models for the other systems

In contrast to the H_2-CO_2 system, the remaining systems examined in this study, namely H_2-CH_4 and H_2-N_2, show a minimal impact of the different viscosity models considered. Fig.A.3 clearly demonstrates that these systems adhere closely to the ideal gas law and the approximations made. As a result, the results obtained using the three models (SuperTRAPP, Dan&Stiel, and Wilke) are in close agreement for these systems. In contrast, the image (c) in the figure, representing the H_2-CO_2 system, displays significant deviation among the models. This discrepancy is the reason why we addressed this point in the previous section.

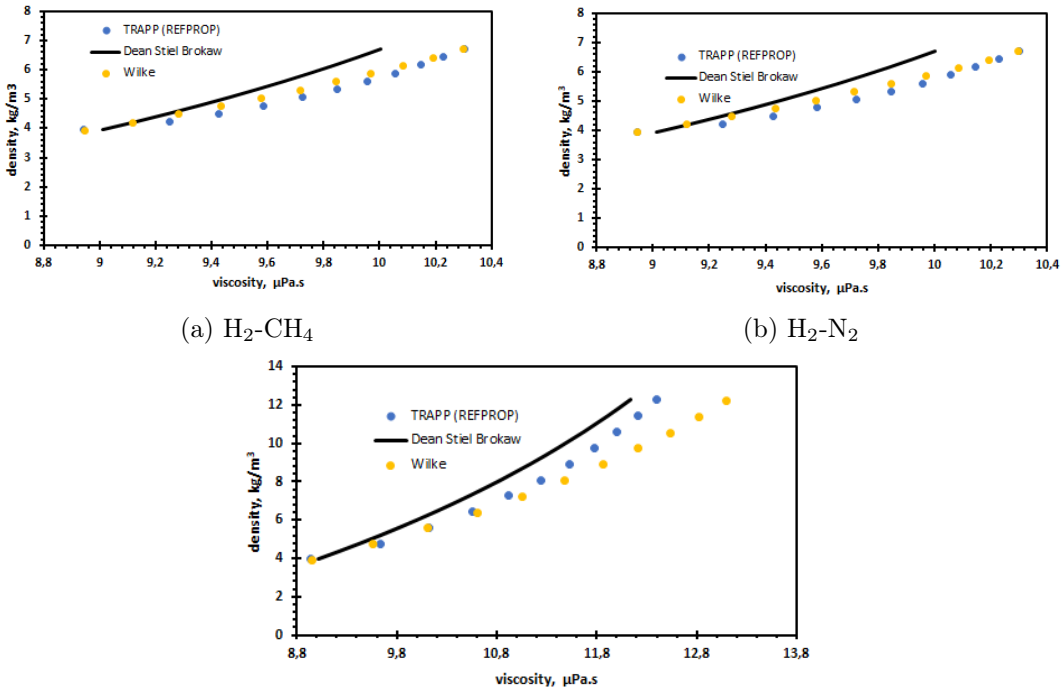

(a) H_2-CH_4

(b) H_2-N_2

(c) H_2-CO_2

FIGURE A.3: Density vs viscosity for different mixtures.

APPENDIX B

Phase equilibrium calculations

This chapter partially serves as the foundation for a three-week, Ph.D.-level course in numerical phase equilibrium calculation. The course was conducted as a summer school at DTU - Technical University of Denmark [174]. It provides an overview of two-phase and multiphase isothermal flash calculations along with their associated algorithms.

B.1 Introduction

The accurate prediction of multiphase equilibrium is based on the availability of an appropriate thermodynamic model and the use of a consistent equation to determine all phase properties. Phase equilibrium, often referred to as a flash calculation, is achieved when a set of equations is satisfied.

B.2 Mathematical method

As discussed in section 4.2, equilibrium is represented by the equality of chemical potentials or fugacities for each component in the phases. Thermodynamic models enable the calculation of component fugacities at a given temperature, pressure (or volume), and phase composition.

Let $N_{\mathcal{P}}$ represent the number of phases and $N_{\mathcal{C}}$ represent the number of components present. For $N_{\mathcal{P}} = 2$, we have $2N_{\mathcal{C}} + 1$ relations. $N_{\mathcal{C}}$ of these equations account for fugacity equality, while another $N_{\mathcal{C}}$ deal with material balance and are expressed as:

$$\boldsymbol{\beta} y_i + (1 - \boldsymbol{\beta}) x_i = z_i, i = 1..N_{\mathcal{C}},$$

Additionally, there is an extra relation stating that the sum of mole fractions of a component in different phases must be equal to unity:

$$\sum_{i=1}^{\mathcal{C}} (y_i - x_i) = 0.$$

On the other hand, we have $2N_{\mathcal{C}}+3$ unknowns denoted as $\{X, Y, T, P, \boldsymbol{\beta}\}$. To solve this problem, we require two specification equations in addition to the $2N_{\mathcal{C}}+1$ equations.

It is important to note that adding a phase to the system introduces $N_{\mathcal{C}}+1$ unknowns and $N_{\mathcal{C}}+1$ relations, thus the number of specifications needed remains at 2.

Generally, the set is accomplished by fixing two of these independent variables $(T, P, \boldsymbol{\beta})$or one of these variables and another overall property of the mixture (e.g., enthalpy, entropy, or total volume). This leads to different types of specifications and corresponding formulations of the equilibrium calculation. Specifications like (P, T), (P, H), (P, S), and (T, V) can be used, each resulting in a unique solution (minimization of a thermodynamic state function). However, choices such as $(T, \boldsymbol{\beta})$ or $(P, \boldsymbol{\beta})$ may yield multiple solutions. The most common equilibrium calculation type is the isothermal flash, which specifies T and P. It is widely used due to its reliability and the simplicity of its algorithm. The solution corresponds to the global minimum in Gibbs energy.

However, a method exists, primarily applied to the isothermal flash, that reduces the system of equations. This reduction is achieved by using equilibrium factors. This approach allows for the calculation of phase mole fractions X and Y from the K-factors and the phase fraction $\boldsymbol{\beta}$. The set of equations is replaced by $N_{\mathcal{C}}$ K-factor equations:

$$K_i = \frac{\varphi_i^l(T,P)}{\varphi_i^g(T,P)},$$

Additionally, the summation of mole relations leads to:

$$\sum_{i=1}^{\mathcal{C}} \frac{z_i(K_i-1)}{1-\boldsymbol{\beta}+\boldsymbol{\beta}K_i} = 0. \tag{B.1}$$

With the two specifications, we have $N_{\mathcal{C}}+3$ equations for $N_{\mathcal{C}}+3$ unknowns ($N_{\mathcal{C}}$ K-factors, $\boldsymbol{\beta}$, T, and P).

It is worth mentioning that this approach assumes that fugacity coefficients are independent of composition.

B.2.1 The governing equation for a multiphase flash

In a multiphase flash, α represents the phase within the set $\mathcal{P} = \{l_1, l_2, g\}$, with l_1, l_2 indicating liquid phases and g representing the gas phase. Here, $\alpha \in Q$, where Q denotes the set of present phases. To determine the phase distribution, the function $\mathcal{Q}(\boldsymbol{\beta}, z)$ evaluates the fraction of the feed, $\boldsymbol{\beta}$, and the mole fractions:

$$\mathcal{Q}(\boldsymbol{\beta}, z) = \sum_{i=1}^{N_{\mathcal{P}}} \boldsymbol{\beta}_\alpha - \sum_{i=1}^{N_{\mathcal{C}}} z_i \ln E_i, \quad E_i = \sum_{i=1}^{N_{\mathcal{P}}} \frac{\boldsymbol{\beta}_\alpha}{\varphi_i^\alpha} \tag{B.2}$$

with the constraints that $\boldsymbol{\beta} \geq 0$, which is reflected in the gradient vector:

$$g^\alpha = \frac{\partial \mathcal{Q}}{\partial \boldsymbol{\beta}_\alpha} = 1 - \sum_{i=1}^{N_{\mathcal{C}}} \frac{z_i}{E_i \varphi_i^\alpha}, \tag{B.3}$$

The hessian matrix, defined as:

$$g^{\alpha\beta} = \frac{\partial g^{\alpha}}{\partial \boldsymbol{\beta}^{\beta}} = \sum_{i=1}^{N_{\mathcal{C}}} \frac{z_i}{E_i^2 \varphi_i^{\alpha} \varphi_i^{\beta}}, \tag{B.4}$$

must be minimized to find the equilibrium solution.

B.3 Numerical methods

The challenge in such formulations lies in determining the number of phases in advance. When the number of phases is fixed to two, it is referred to as a two-phase flash, which relies on an iterative method to solve the system. When dealing with multiphase PT flash calculations, two types of flash models may be encountered.
The first is VLE calculation, which stands for vapor-liquid equilibrium. In this scenario, different pure components may be present as more phases, such as water. VLLE, on the other hand, occurs when demixing can take place in the liquid phase.
Phase equilibrium calculations involve solving a non-linear set of equations. Several suitable procedures have been reported in the literature [174], with successive substitution and the Newton-Raphson Method being two prominent methods.

B.3.1 Successive substitution method

Although this method can be time-consuming and may require numerous iterations for convergence, it remains one of the most practical options. Successive substitution doesn't calculate all solution quantities simultaneously. The sequence of iterations converges linearly, resulting in slower convergence rates.
This method is built on the implicit assumption of composition-independent fugacity coefficients. The algorithm alternates between determining the phase distribution and evaluating the fugacity coefficients at the composition estimate. The phase amounts and compositions are determined using the modified Rachford-Rice method, which solves Eq.(B.1):

$$g(\boldsymbol{\beta}) = \sum_{i=1}^{\mathcal{C}} \frac{z_i(K_i - 1)}{1 - \boldsymbol{\beta} + \boldsymbol{\beta} K_i} = 0. \tag{B.5}$$

This equation can also be solved using Newton's method, with $\boldsymbol{\beta}$ constrained to the range $[0, 1]$. Phase fractions are then determined using:

$$x_i = \frac{z_i}{1 - \boldsymbol{\beta} + \boldsymbol{\beta} K_i} \quad , \quad y_i = \frac{K_i\, z_i}{1 - \boldsymbol{\beta} + \boldsymbol{\beta} K_i}. \tag{B.6}$$

In cases where a feed contains a small quantity of an extremely volatile component like $H_2$and the solution is close to $\boldsymbol{\beta} = 0$ (indicating a subcooled liquid state), the derivative of g can exhibit significant magnitudes. This may necessitate a substantial number of iterations for convergence. The rate of convergence in successive substitution depends on the degree of non-ideality. To enhance convergence, better initial estimates are generated in such situations by setting upper

and lower $\boldsymbol{\beta}$ limits.

The primary objective of this method is to determine the number of components and assumed phases based on the overall composition, fugacity coefficients for the components in different phases, the fraction of the feed ($\boldsymbol{\beta}$), and the mole fractions for each phase. Yet, challenges arise when providing initial estimates for the fugacity coefficients and feed fractions since knowing the phases in advance can be difficult. The algorithm aims to introduce a $\boldsymbol{\beta}$ fraction for a phase initially presumed to be absent and potentially eliminate a previously assumed present phase. Moreover, obtaining initial estimates for the fugacity coefficients in liquid phases can also be challenging. To address this, the Wilson K-factor expression (Eq.(B.7)) can offer an adequate expression for approximating the equilibrium and offering initial estimates for the set of fugacity coefficients.

$$K_i^W(T,P) = \frac{P_{c,i}}{P} \exp\left(5.373(1+\omega_i)(1-\frac{T_{c,i}}{T})\right). \tag{B.7}$$

The K-factors can be converted into estimates for fugacity coefficients by assuming the vapor phase is ideal. Consequently, the fugacity coefficients in the liquid phase become equal to the K-factors.
The iterative algorithm follows these steps:

1. Calculation of Wilson K-factors: The Wilson coefficients are computed for each component in each phase. This computation relies on critical component properties, including (T_c, P_c, ω), as well as temperature and pressure data. The determination of fugacity coefficients is subsequently facilitated based on these K-factors. The phase fractions ($\boldsymbol{\beta}$) are initially set and categorized to denote the presence or absence of phases, guided by $\boldsymbol{\beta}$.

2. Gibbs free energy minimization: The algorithm iteratively engages in the minimization of the Gibbs free energy of the system by iteratively adjusting the phase fractions. This optimization process necessitates the resolution of the Rachford-Rice equation. Linear equation solutions are effectively implemented using LAPACK. The phase fractions are systematically updated to minimize the Gibbs free energy.

3. Nested iterations: Fugacity coefficients are updated in an iterative process. Phases are identified as either present or absent through comprehensive gradient calculations. The existence of phases is marked within a vector and assessed using Eq.(B.2) through Eq.(B.3). When the function $g^\alpha = 0$ and $\boldsymbol{\beta}^\alpha > 0$, it signifies that the phase is indeed present. Conversely, if $g^\alpha > 0$ and $\boldsymbol{\beta}^\alpha = 0$, it denotes that the phase is absent.

4. Phase composition calculation: The algorithm calculates phase compositions based on phase fractions and updated fugacity coefficients. Moreover, K-factors are dynamically adjusted for each component.

5. Convergence Criteria: The algorithm persists in its calculations until specific convergence criteria are successfully met. Convergence is ultimately determined based on the observed changes in fugacity coefficients.

B.3.2 The Newton-Raphson Method

The Newton-Raphson method is a widely used approach for solving nonlinear equations in phase equilibrium calculations. It linearizes and iteratively solves a set of equations, ensuring rapid and accurate convergence. However, it requires good initial estimates for the variables. To overcome this limitation, alternative convergence methods like successive substitution are used in the initial stages of calculations. Additional details on the method and its algorithm can be found in the literature [174].

B.3.3 The negative multiphase Rachford-Rice

The negative flash (P, Z), consists in the determination of the gas phase molar fraction, $\boldsymbol{\beta}^g$, under the conditions of fixed temperature, specific pressures (P^g and P^l), and a fixed component total molar fraction, z_i. It is notable that the molar fraction in the gas phase can, in fact, take on negative values. Within this context, a negative flash calculation is performed to ascertain the molar fraction of the gas phase.

The relationship governing the component molar fractions (z_i) takes the form of:

$$z_i = \boldsymbol{\beta}^g x_i + (1 - \boldsymbol{\beta}^g) y_i. \tag{B.8}$$

Here, the appearance and vanishing of phases are related to the sign of the gas phase molar fraction, denoted as the parameter $\boldsymbol{\beta}$. The classification of phase behavior under the negative flash conditions follows these distinctive patterns:

$$\begin{cases} \text{If} \quad \boldsymbol{\beta}^g \leq 0, \text{ a single-phase liquid state } \{l\} \\ \text{If} \quad \boldsymbol{\beta}^g \geq 1, \text{ a single-phase gas state } \{g\} \\ \text{Otherwise, two-phase coexistence, } \{l, g\} \end{cases} \tag{B.9}$$

For the case of negative flash, $\boldsymbol{\beta}^g$ can potentially assume values outside the conventional range of $[0, 1]$ of the Rachford-Rice solver defined earlier, the initial constraints on $\boldsymbol{\beta}$ must be redefined as follows:

$$\boldsymbol{\beta}_{min} = \frac{-1}{K_{max} - 1} \text{ and } \boldsymbol{\beta}_{max} = \frac{-1}{1 - K_{min}}.$$

Notably, a negative fraction in this context implies a subcooled liquid state, while a positive phase fraction signifies a superheated vapor state. The adaptation of the Rachford-Rice solver to accommodate the negative flash conditions ensures that this robust algorithmic approach can effectively handle a diverse range of phase behavior.

In the context of successive substitution, one technique for accelerating convergence is the utilization of the Dominant Eigenvalue Method. By comparing the performance of the unaccelerated method to the accelerated version, it becomes evident that the implementation of acceleration introduces a significant "jump" in the convergence process, effectively enhancing the convergence rate and reducing the number of iterations required. The Dominant Eigenvalue Method proves to be a valuable tool when using successive substitution to solve the equilibrium equations.

Another challenge encountered in the iterative flash calculation, particularly when utilizing EoS, is the presence of trivial solutions. These trivial solutions signify the potential existence of multiple solutions with identical phase compositions. These false solutions are more likely to arise when initial estimates are inaccurately specified.

In the context of phase behavior calculations, such as the PT flash, which involves minimizing the Gibbs free energy, it is crucial to ascertain whether the trivial solution corresponds to the true solution, which represents the global minimum of the Gibbs free energy. To address this, a stability analysis is imperative, and it involves assessing whether the specified temperature and pressure correspond to a single-phase region. This assessment relies on a stability analysis technique known as the tangent plane distance method, as described by Michelsen [174]. Additionally, an alternative approach to stability analysis is the negative flash method, which can provide insights into phase behavior and address stability concerns in scenarios where trivial solutions may be encountered.

APPENDIX C

EoS derivation:Helmholtz energy based EoS [1]

This appendix serves as supplementary material for the integration of a thermodynamic model into ComPASS (section 4.4. Notably, ComPASS is formulated using the variables $(T, P, \boldsymbol{N})$, with pressure replacing volume compared to the typical formulation of EoS. This necessitates the computation of the function $V(T, P, \boldsymbol{N})$ based on the function $P(T, V, \boldsymbol{N})$. The procedure is elaborated in section C.2.3.

In the first part of this appendix, we present thermodynamic variables expressed as functions of $(T, V, \boldsymbol{N})$. This initial presentation is covered in section C.2.1. Subsequently, these properties are transformed into functions of $(T, P, \boldsymbol{N})$.

In the second part of this appendix, we introduce a general equation that can accommodate both cubic EoS, specifically the PR and SRK formulations. This formulation is defined to pure substances and mixtures. Additionally, we address the formulation of derivatives in $(T, V, \boldsymbol{N})$. These expression can be eventually transformed into $(T, P, \boldsymbol{N})$.

This section concludes with a discussion of the Péneloux volume translation and its derivatives, which is detailed in Section C.4.3.

C.1 Introduction

We consider a model of EoS given in the form

$$P(T, V, \boldsymbol{N}) \tag{C.1}$$

where P denotes the pressure, T the temperature, V the volume and $\boldsymbol{N} = (N_i)_i$ the number of mole for each component.

The aim is to derive all the thermodynamic variables (and their derivatives) from the given of the function $P(T, V, \boldsymbol{N})$. In this formulation, pressure is the dependent variable, while temperature and molar volume serve as the independent variables. Note that some EoS may be expressed in

[1] This chapter is co-authored with Farid Smai (the first author).

terms of volume, $V = V(T, P)$, derived from extensive experimental volumetric data, which are rarely available. In most of the cases, the EoS equations are pressure explicit $P(T, V, \boldsymbol{N})$ [174]. The thermodynamic variables will be provided in two forms: (i) as functions of $(T, V, \boldsymbol{N})$ and (ii) as functions of $(T, P, \boldsymbol{N})$.

At first, a general derivation is developed, then it is applied to specific class of EoS.

C.2 General derivation

C.2.1 Helmholtz free energy from $P(T, V, \boldsymbol{N})$

C.2.1.1 First principle

The first principle of thermodynamics for a homogeneous fluid gives

$$\mathrm{d}U = T\mathrm{d}S - P\mathrm{d}V + \sum_i \mu_i \mathrm{d}N_i$$

where U denotes the internal energy, S the entropy and $\boldsymbol{\mu} = (\mu_i)_i$ the chemical potential of each components.

C.2.1.2 Helmholtz free energy

We introduce the Helmholtz free energy A as

$$A = U - TS$$

that satisfies, according to the first principle,

$$\mathrm{d}A = -S\mathrm{d}T - P\mathrm{d}V + \sum_i \mu_i \mathrm{d}N_i \ . \tag{C.2}$$

That equation gives the Helmholtz free energy as a function of $(T, V, \boldsymbol{N})$ and links its derivative to the pressure:

$$\left.\frac{\partial A}{\partial V}\right|_{T,\boldsymbol{N}} = -P(T, V, \boldsymbol{N}) \ .$$

This fits exactly the form (C.1) in which is given the EoS model. The latter equation can integrated along V to gives

$$A(T, V, \boldsymbol{N}) = -\int_V P(T, V, \boldsymbol{N})\mathrm{d}V \ .$$

The integration constant in this equation still need to be determined.

C.2.1.3 Residual Helmholtz free energy

The determination of the integration constant is based on the fact that the model should converge to the ideal gas model when the volume tends toward infinity :

$$A \xrightarrow[V\to\infty]{} A^{\mathrm{ideal}} \ .$$

By introducing the residual Helmholtz free energy A^{res} as the discrepancy between the EoS model and the ideal model, we get

$$A^{\text{res}} \equiv A - A^{\text{ideal}} \xrightarrow[V\to\infty]{} 0 \ .$$

For the ideal gas model, the pressure is given by

$$P^{\text{ideal}} = \frac{N_{\text{tot}}\, RT}{V} \quad \text{with} \quad N_{\text{tot}} = \sum_i N_i$$

thus the residual Helmholtz free energy is given by the integral

$$A^{\text{res}}(T, V, \boldsymbol{N}) = -\int_{+\infty}^{V} \left(P(T, V', \boldsymbol{N}) - \frac{N_{\text{tot}} RT}{V'} \right) \mathrm{d}V' \ . \tag{C.3}$$

The equation (C.3) can be explicitly calculated according to the explicit formula (C.1) of the model under consideration.

C.2.1.4 Ideal gas Helmholtz free energy

To get the full Helmholtz free energy, $A = A^{\text{res}} + A^{\text{ideal}}$, we need to explicit the ideal gas contribution. We use the following expression

$$A^{\text{ideal}}(T, V, \boldsymbol{N}) = \sum_i N_i \left(\mu_i^{\text{ideal},0}(T) + RT \ln\left(\frac{N_i RT}{P_0 V} \right) - RT \right) \tag{C.4}$$

where P_0 is a fixed reference pressure and

$$\mu_i^{\text{ideal},0}(T) \tag{C.5}$$

is the chemical potential of component i in hypothetical pure ideal gas state, at temperature T and pressure P_0. It must be stressed that different functions of temperature can be considered for the formulas (C.5), and that all of them will satisfy the ideal gas mixture model. The choice of the functions for the formulas (C.5) is part of the model as much as the choice of the function for the formula (C.1).

The molar heat capacity of the pure ideal gas state is defined by

$$c_{V,i}^{\text{ideal}} \equiv \frac{T}{N_i} \left. \frac{\partial S_i^{\text{ideal}}}{\partial T} \right|_{V,N_i}$$

It is linked to the functions $\mu_i^{\text{ideal},0}(T)$ by the following equation

$$c_{V,i}^{\text{ideal}}(T) = -T \frac{\mathrm{d}^2 \mu_i^{\text{ideal},0}}{\mathrm{d}T^2}(T) - R$$

The molar heat capacity is also written as

$$c_{V,i}^{\text{ideal}}(T) = \frac{1}{2} f_i(T) R$$

where $f_i(T)$ is the number of active degrees of freedom of the gas molecule i available to store heat energy ($f_i \geq 3$) [2]. Finally, we can constrain $\mu_i^{\text{ideal},0}$ with

$$\frac{\mathrm{d}^2}{\mathrm{d}T^2} \mu_i^{\text{ideal},0}(T) = \frac{-R}{2} \left(\frac{f_i(T) + 2}{T} \right) \ .$$

[2] see Wikipedia

Assuming $f_i(T)$ is constant, integration gives

$$\mu_i^{\text{ideal},0}(T) = R(T - T_0)\ln\left(\frac{P_0}{P_1}\right) - \frac{1}{2}(f_i + 2)RT\ln\left(\frac{T}{T_0}\right) \tag{C.6}$$

where T_0 is chosen arbitrarily as the temperature at which chemical potentials vanish and P_1 an arbitrary reference pressure.

Typically, it is assumed that: $\frac{\mathrm{d}}{\mathrm{d}T}\mu_i^{\text{ideal},0}(T_0) = 0$. Under the condition $\mu_i^{\text{ideal},0}(T_0) = 0$, this assumption implies that both enthalpy and entropy are set to zero at temperature T_0. It is worth noting that this specific hypothesis is a feature of the GERG-2004 standard.

Following this hypothesis, we can express the relationship as:

$$\mu_i^{\text{ideal},0}(T) = R\left(\frac{f_i + 2}{2}\right)\left(T - T_0 - T\ln\left(\frac{T}{T_0}\right)\right)$$

C.2.1.5 Summary

Summing equations (C.3) and (C.4), the Helmholtz free energy is explicitly given by

$$A(T, V, \boldsymbol{N}) = A^{\text{res}}(T, V, \boldsymbol{N}) + A^{\text{ideal}}(T, V, \boldsymbol{N}) \tag{C.7}$$

The input data of the EoS model are the function (C.1) that determines A^{res} and the functions (C.5) that determine A^{ideal}. Under certain conditions, especially when temperature range is moderate, the functions (C.5) are approximated by equation (C.6) that depends only on the scalar parameters $(f_i)_i$.

The derivatives of $A(T, V, \boldsymbol{N})$ are directly retrieved by summing the derivatives of $A^{\text{res}}(T, V, \boldsymbol{N})$ and $A^{\text{ideal}}(T, V, \boldsymbol{N})$. The ideal gas EoS is fully discussed in section C.3 and the derivatives of $A^{\text{ideal}}(T, V, \boldsymbol{N})$ are given by equations (C.40), (C.41), (C.42), (C.43) and (C.44).

C.2.2 Thermodynamic variables as $(T, V, \boldsymbol{N})$ function

For now, given a state $(T, V, \boldsymbol{N})$, we are able to compute the pressure, $P(T, V, \boldsymbol{N})$, thanks to equation (C.1) and the Helmholtz free energy, $A(T, V, \boldsymbol{N})$, thanks to equation (C.7). The other thermodynamic variables can be computed using the derivatives of the Helmholtz free energy. In this section, $A(T, V, \boldsymbol{N})$ and $P(T, V, \boldsymbol{N})$ are assumed to be explicitly known and all other quantities will be build on them. The derivatives of the thermodynamic variables are also computed.

C.2.2.1 Thermodynamic variables as derivatives of $A(T, V, \boldsymbol{N})$

From equation (C.2), we get

$$P(T, V, \boldsymbol{N}) = -\left.\frac{\partial A}{\partial V}\right|_{T,\boldsymbol{N}} \tag{C.8}$$

$$S(T, V, \boldsymbol{N}) = -\left.\frac{\partial A}{\partial T}\right|_{V,\boldsymbol{N}} \tag{C.9}$$

and

$$\boldsymbol{\mu}(T, V, \boldsymbol{N}) = \left.\frac{\partial A}{\partial \boldsymbol{N}}\right|_{T,V} \tag{C.10}$$

By definition, $A = U - TS$, using the former equation we get

$$U(T, V, \boldsymbol{N}) = A(T, V, \boldsymbol{N}) - T \left.\frac{\partial A}{\partial T}\right|_{V,\boldsymbol{N}} \tag{C.11}$$

The enthalpy is defined by

$$H = U + PV$$

Using equation (C.11), it comes

$$H(T, V, \boldsymbol{N}) = A(T, V, \boldsymbol{N}) + VP(V, T, \boldsymbol{N}) - T \left.\frac{\partial A}{\partial T}\right|_{V,\boldsymbol{N}} \tag{C.12}$$

The Gibbs free energy is defined by

$$G = A + PV$$

Using equation (C.1) and (C.7), it comes

$$G(T, V, \boldsymbol{N}) = A(T, V, \boldsymbol{N}) + VP(V, T, \boldsymbol{N}) \tag{C.13}$$

C.2.2.2 Entropy and derivatives

Entropy as a function of $(T, V, \boldsymbol{N})$ is given by equation (C.9). Its derivatives are

$$\left.\frac{\partial S}{\partial T}\right|_{V,\boldsymbol{N}} = - \left.\frac{\partial^2 A}{\partial T^2}\right|_{V,\boldsymbol{N}} \tag{C.14}$$

$$\left.\frac{\partial S}{\partial V}\right|_{T,\boldsymbol{N}} = \left.\frac{\partial P}{\partial T}\right|_{V,\boldsymbol{N}} \tag{C.15}$$

$$\left.\frac{\partial S}{\partial \boldsymbol{N}}\right|_{T,V} = - \left.\frac{\partial^2 A}{\partial T \partial \boldsymbol{N}}\right|_{V} \tag{C.16}$$

where P is introduced thanks to equation (C.8).

C.2.2.3 Chemical potential and derivatives

Chemical potentials as functions of $(T, V, \boldsymbol{N})$ are given by equation (C.10). Their derivatives are

$$\left.\frac{\partial \boldsymbol{\mu}}{\partial T}\right|_{V,\boldsymbol{N}} = \left.\frac{\partial^2 A}{\partial T \partial \boldsymbol{N}}\right|_{V} \tag{C.17}$$

$$\left.\frac{\partial \boldsymbol{\mu}}{\partial V}\right|_{T,\boldsymbol{N}} = - \left.\frac{\partial P}{\partial \boldsymbol{N}}\right|_{T,V} \tag{C.18}$$

$$\left.\frac{\partial \boldsymbol{\mu}}{\partial \boldsymbol{N}}\right|_{T,V} = \left.\frac{\partial^2 A}{\partial \boldsymbol{N} \partial \boldsymbol{N}}\right|_{T,V} \tag{C.19}$$

where P is introduced thanks to equation (C.8).

C.2.2.4 Internal energy and derivatives

Internal energy as a function of $(T, V, \boldsymbol{N})$ is given by equation (C.11). Its derivatives are

$$\left.\frac{\partial U}{\partial T}\right|_{V,\boldsymbol{N}} = -T \left.\frac{\partial^2 A}{\partial T^2}\right|_{V,\boldsymbol{N}} \tag{C.20}$$

$$\left.\frac{\partial U}{\partial V}\right|_{T,\boldsymbol{N}} = -P(T, V, \boldsymbol{N}) + T \left.\frac{\partial P}{\partial T}\right|_{V,\boldsymbol{N}} \tag{C.21}$$

$$\left.\frac{\partial U}{\partial \boldsymbol{N}}\right|_{T,V} = \left.\frac{\partial A}{\partial \boldsymbol{N}}\right|_{T,V} - T \left.\frac{\partial^2 A}{\partial T \partial \boldsymbol{N}}\right|_{V} \tag{C.22}$$

where P is introduced thanks to equation (C.8).

C.2.2.5 Enthalpy and derivatives

Enthalpy as a function of $(T, V, \boldsymbol{N})$ is given by equation (C.12). Its derivatives are

$$\left.\frac{\partial H}{\partial T}\right|_{V,\boldsymbol{N}} = V \left.\frac{\partial P}{\partial T}\right|_{V,\boldsymbol{N}} - T \left.\frac{\partial^2 A}{\partial T^2}\right|_{V,\boldsymbol{N}} \tag{C.23}$$

$$\left.\frac{\partial H}{\partial V}\right|_{T,\boldsymbol{N}} = V \left.\frac{\partial P}{\partial V}\right|_{T,\boldsymbol{N}} + T \left.\frac{\partial P}{\partial T}\right|_{V,\boldsymbol{N}} \tag{C.24}$$

$$\left.\frac{\partial H}{\partial \boldsymbol{N}}\right|_{T,V} = V \left.\frac{\partial P}{\partial \boldsymbol{N}}\right|_{T,V} + \left.\frac{\partial A}{\partial \boldsymbol{N}}\right|_{T,V} - T \left.\frac{\partial^2 A}{\partial T \partial \boldsymbol{N}}\right|_{V} \tag{C.25}$$

where P is introduced thanks to equation (C.8).

C.2.2.6 Gibbs free energy and derivatives

Gibbs free energy as a function of $(T, V, \boldsymbol{N})$ is given by equation (C.13). Its derivatives are

$$\left.\frac{\partial G}{\partial T}\right|_{V,\boldsymbol{N}} = V \left.\frac{\partial P}{\partial T}\right|_{V,\boldsymbol{N}} + \left.\frac{\partial A}{\partial T}\right|_{V,\boldsymbol{N}} \tag{C.26}$$

$$\left.\frac{\partial G}{\partial V}\right|_{T,\boldsymbol{N}} = V \left.\frac{\partial P}{\partial V}\right|_{T,\boldsymbol{N}} \tag{C.27}$$

$$\left.\frac{\partial G}{\partial \boldsymbol{N}}\right|_{T,V} = V \left.\frac{\partial P}{\partial \boldsymbol{N}}\right|_{T,V} + \left.\frac{\partial A}{\partial \boldsymbol{N}}\right|_{T,V} \tag{C.28}$$

where P is simplified thanks to equation (C.8).

C.2.2.7 Fugacity and derivatives

The fugacity, f_i, is sometimes favored over the chemical potential in some applications. It is defined by

$$RT \ln \frac{f_i}{P_0} = \mu_i - \mu_i^{\text{ideal},0}(T)$$

where $\mu_i^{\text{ideal},0}(T)$ is defined at equation (C.5). Using the equations (C.7), (C.10) and (C.41), we get an expression of fugacity as a function of $(T, V, \boldsymbol{N})$, not related to the ideal gas:

$$\ln \frac{f_i(T, V, \boldsymbol{N})}{P_0} = \frac{1}{RT} \left(\left.\frac{\partial A^{\text{res}}}{\partial \boldsymbol{N}}\right|_{T,V} \right)_i + \ln \left(\frac{N_i RT}{P_0 V} \right) \tag{C.29}$$

Using the fact, see equation (C.3), that

$$\left.\frac{\partial^2 A^{\text{res}}}{\partial V \partial \boldsymbol{N}}\right|_T = \frac{RT}{V} - \left.\frac{\partial P}{\partial \boldsymbol{N}}\right|_{T,V}$$

we compute the derivatives of the fugacity, depending on the derivatives of the EoS and the residual Helmholtz free energy, as follows

$$\frac{1}{f_i}\left.\frac{\partial f_i}{\partial T}\right|_{V,\boldsymbol{N}} = \frac{1}{T} + \frac{1}{RT}\left(\left.\frac{\partial^2 A^{\text{res}}}{\partial T \partial \boldsymbol{N}}\right|_V\right)_i - \frac{1}{RT^2}\left(\left.\frac{\partial A^{\text{res}}}{\partial \boldsymbol{N}}\right|_{T,V}\right)_i \tag{C.30}$$

$$\frac{1}{f_i}\left.\frac{\partial f_i}{\partial V}\right|_{T,\boldsymbol{N}} = -\frac{1}{RT}\left(\left.\frac{\partial P}{\partial \boldsymbol{N}}\right|_{T,V}\right)_i \tag{C.31}$$

$$\frac{1}{f_i}\left(\left.\frac{\partial f_i}{\partial \boldsymbol{N}}\right|_{T,V,\boldsymbol{N}}\right)_j = \frac{1}{RT}\left(\left.\frac{\partial^2 A^{\text{res}}}{\partial \boldsymbol{N} \partial \boldsymbol{N}}\right|_V\right)_{i,j} + \frac{\delta_{i,j}}{N_i} \tag{C.32}$$

where

$$\delta_{i,j} = \begin{cases} 1 & \text{if } i = j \\ 0 & \text{otherwise} \end{cases}$$

C.2.3 Thermodynamic variables as $(T, P, \boldsymbol{N})$ function

The previous section shows how knowing $A(T, V, \boldsymbol{N})$ enables the computation of all other thermodynamic variables as functions of $(T, V, \boldsymbol{N})$. An other popular state description is based on $(T, P, \boldsymbol{N})$, where the pressure replaces the volume. In this section, $P(T, V, \boldsymbol{N})$ is assumed to be explicitly known, we will see how the volume at first and then any other quantity can be expressed as a function of $(T, P, \boldsymbol{N})$.

C.2.3.1 Computing $V(T, P, \boldsymbol{N})$ and its derivatives

Knowing the function $P(T, V, \boldsymbol{N})$, computing the function $V(T, P, \boldsymbol{N})$ can be performed by solving the following implicit problem:

$$\begin{gathered} \text{Given } (T, P, \boldsymbol{N}) \text{ find } V(T, P, \boldsymbol{N}) \text{ such that} \\ P\left(T, V(T, P, \boldsymbol{N}), \boldsymbol{N}\right) = P \ . \end{gathered} \tag{C.33}$$

Solving that problem may require different kinds of methods depending on the properties of $P(T, V, \boldsymbol{N})$. We are not discussing those methods here and we just assume for now that we can solve the problem.

Deriving the equation of problem (C.33) according to $(T, P, \boldsymbol{N})$ gives

$$\begin{aligned} \left.\frac{\partial P}{\partial T}\right|_{V,\boldsymbol{N}} + \left.\frac{\partial P}{\partial V}\right|_{T,\boldsymbol{N}} \left.\frac{\partial V}{\partial T}\right|_{P,\boldsymbol{N}} &= 0 \\ \left.\frac{\partial P}{\partial V}\right|_{T,\boldsymbol{N}} \left.\frac{\partial V}{\partial P}\right|_{T,\boldsymbol{N}} &= 1 \\ \left.\frac{\partial P}{\partial \boldsymbol{N}}\right|_{T,V} + \left.\frac{\partial P}{\partial V}\right|_{T,\boldsymbol{N}} \left.\frac{\partial V}{\partial \boldsymbol{N}}\right|_{T,P} &= 0 \end{aligned}$$

Which gives the derivatives of $V(T,P,\boldsymbol{N})$ depending on the derivatives of $P(T,V,\boldsymbol{N})$:

$$\begin{cases} \left.\dfrac{\partial V}{\partial T}\right|_{P,\boldsymbol{N}} = -\left(\left.\dfrac{\partial P}{\partial V}\right|_{T,\boldsymbol{N}}\right)^{-1}\left.\dfrac{\partial P}{\partial T}\right|_{V,\boldsymbol{N}} \\ \left.\dfrac{\partial V}{\partial P}\right|_{T,\boldsymbol{N}} = \left(\left.\dfrac{\partial P}{\partial V}\right|_{T,\boldsymbol{N}}\right)^{-1} \\ \left.\dfrac{\partial V}{\partial \boldsymbol{N}}\right|_{T,P} = -\left(\left.\dfrac{\partial P}{\partial V}\right|_{T,\boldsymbol{N}}\right)^{-1}\left.\dfrac{\partial P}{\partial \boldsymbol{N}}\right|_{T,V} \end{cases} \tag{C.34}$$

C.2.3.2 Transitioning from $(T,V,\boldsymbol{N})$ to $(T,P,\boldsymbol{N})$

Let ξ be any thermodynamic variable that we know as a function of $(T,V,\boldsymbol{N})$: $\xi(T,V,\boldsymbol{N})$. By solving problem (C.33), we get $V(T,P,\boldsymbol{N})$. Thus ξ can be computed from $(T,P,\boldsymbol{N})$ by

$$\xi(T,V(T,P,\boldsymbol{N}),\boldsymbol{N}) \tag{C.35}$$

Deriving equation (C.35) with respect to $(T,P,\boldsymbol{N})$ gives

$$\begin{aligned} \left.\frac{\partial \xi}{\partial T}\right|_{P,\boldsymbol{N}} &= \left.\frac{\partial \xi}{\partial V}\right|_{T,\boldsymbol{N}}\left.\frac{\partial V}{\partial T}\right|_{P,\boldsymbol{N}} + \left.\frac{\partial \xi}{\partial T}\right|_{V,\boldsymbol{N}} \\ \left.\frac{\partial \xi}{\partial P}\right|_{T,\boldsymbol{N}} &= \left.\frac{\partial \xi}{\partial V}\right|_{T,\boldsymbol{N}}\left.\frac{\partial V}{\partial P}\right|_{T,\boldsymbol{N}} \\ \left.\frac{\partial \xi}{\partial \boldsymbol{N}}\right|_{T,P} &= \left.\frac{\partial \xi}{\partial V}\right|_{T,\boldsymbol{N}}\left.\frac{\partial V}{\partial \boldsymbol{N}}\right|_{T,P} + \left.\frac{\partial \xi}{\partial \boldsymbol{N}}\right|_{T,V} \end{aligned}$$

Using equations (C.34), we get the derivatives of $\xi(T,P,\boldsymbol{N})$ depending on the derivatives of $\xi(T,V,\boldsymbol{N})$ and $P(T,V,\boldsymbol{N})$

$$\begin{cases} \left.\dfrac{\partial \xi}{\partial T}\right|_{P,\boldsymbol{N}} = -\left.\dfrac{\partial \xi}{\partial V}\right|_{T,\boldsymbol{N}}\left(\left.\dfrac{\partial P}{\partial V}\right|_{T,\boldsymbol{N}}\right)^{-1}\left.\dfrac{\partial P}{\partial T}\right|_{V,\boldsymbol{N}} + \left.\dfrac{\partial \xi}{\partial T}\right|_{V,\boldsymbol{N}} \\ \left.\dfrac{\partial \xi}{\partial P}\right|_{T,\boldsymbol{N}} = \left.\dfrac{\partial \xi}{\partial V}\right|_{T,\boldsymbol{N}}\left(\left.\dfrac{\partial P}{\partial V}\right|_{T,\boldsymbol{N}}\right)^{-1} \\ \left.\dfrac{\partial \xi}{\partial \boldsymbol{N}}\right|_{T,P} = -\left.\dfrac{\partial \xi}{\partial V}\right|_{T,\boldsymbol{N}}\left(\left.\dfrac{\partial P}{\partial V}\right|_{T,\boldsymbol{N}}\right)^{-1}\left.\dfrac{\partial P}{\partial \boldsymbol{N}}\right|_{T,V} + \left.\dfrac{\partial \xi}{\partial \boldsymbol{N}}\right|_{T,V} \end{cases} \tag{C.36}$$

C.3 The ideal mixture of ideal gas

The ideal mixture of ideal gas is a model adapted for low density gas mixture. It is also a model used as a limit case for more realistic models. Equations (C.4)-(C.5) gives the general formula for the Helmholtz free energy depending on $(T,V,\boldsymbol{N})$. One special case, with simpler parameters, is also given by equations (C.4)-(C.6). The EoS for that model is

$$P^{\text{ideal}}(T,V,\boldsymbol{N}) = \sum_i N_i \frac{RT}{V} \tag{C.37}$$

In order to apply the results of the general derivation obtained in section C.2, we need to compute $V(T,P,\boldsymbol{N})$, the derivatives of $P(T,V,\boldsymbol{N})$ and the derivatives of $A(T,V,\boldsymbol{N})$.

C.3.1 Computing $V(T, P, \boldsymbol{N})$

This is straightforward for this model, the explicit formula is

$$V^{\text{ideal}}(T, P, \boldsymbol{N}) = \sum_i N_i \frac{RT}{P} \tag{C.38}$$

C.3.2 Derivatives of $P(T, V, \boldsymbol{N})$

We can compute that

$$\begin{cases} \left.\dfrac{\partial P^{\text{ideal}}}{\partial T}\right|_{V,\boldsymbol{N}} = \displaystyle\sum_i N_i \frac{R}{V} \\ \left.\dfrac{\partial P^{\text{ideal}}}{\partial V}\right|_{T,\boldsymbol{N}} = -\displaystyle\sum_i N_i \frac{RT}{V^2} \\ \left.\dfrac{\partial P^{\text{ideal}}}{\partial \boldsymbol{N}}\right|_{T,V} = \dfrac{RT}{V} \end{cases} \tag{C.39}$$

C.3.3 Derivatives of $A(T, V, \boldsymbol{N})$

The Helmholtz free energy for ideal mixture of ideal gas is given by equation (C.4):

$$A^{\text{ideal}}(T, V, \boldsymbol{N}) = \sum_i N_i \left(\mu_i^{\text{ideal},0}(T) + RT \ln\left(\frac{N_i RT}{P_0 V}\right) - RT \right)$$

Its derivatives are:

$$\left.\frac{\partial A^{\text{ideal}}}{\partial T}\right|_{V,\boldsymbol{N}} = \sum_i N_i \left(\mu_i^{\text{ideal},0\prime}(T) + R \ln\left(\frac{N_i RT}{P_0 V}\right) \right) \tag{C.40}$$

$$\left(\left.\frac{\partial A^{\text{ideal}}}{\partial \boldsymbol{N}}\right|_{T,V} \right)_i = \mu_i^{\text{ideal},0}(T) + RT \ln\left(\frac{N_i RT}{P_0 V}\right) \tag{C.41}$$

$$\left(\left.\frac{\partial^2 A^{\text{ideal}}}{\partial T \partial \boldsymbol{N}}\right|_{V} \right)_i = \mu_i^{\text{ideal},0\prime}(T) + R \ln\left(\frac{N_i RT}{P_0 V}\right) + R \tag{C.42}$$

$$\left.\frac{\partial^2 A^{\text{ideal}}}{\partial T^2}\right|_{V,\boldsymbol{N}} = \sum_i N_i \left(\mu_i^{\text{ideal},0\prime\prime}(T) + \frac{R}{T} \right) \tag{C.43}$$

$$\left(\left.\frac{\partial^2 A^{\text{ideal}}}{\partial \boldsymbol{N}^2}\right|_{T,V} \right)_{i,j} = \begin{cases} \frac{RT}{N_i} & \text{if } i = j \\ 0 & \text{otherwise} \end{cases} \tag{C.44}$$

When using the special case of $\mu_i^{\text{ideal},0}(T)$ given by equation (C.6), we have

$$\begin{aligned} \mu_i^{\text{ideal},0}(T) &= R(T - T_0) \ln\left(\frac{P_0}{P_1}\right) - \frac{(f_i + 2)}{2} R\, T \ln\left(\frac{T}{T_0}\right) \\ \mu_i^{\text{ideal},0\prime}(T) &= R \ln\left(\frac{P_0}{P_1}\right) - \frac{(f_i + 2)}{2} R \left(1 + \ln\left(\frac{T}{T_0}\right)\right) \\ \mu_i^{\text{ideal},0\prime\prime}(T) &= -\frac{(f_i + 2)}{2} \frac{R}{T} \end{aligned}$$

C.4 Cubic Equation of State

The cubic EoS are thermodynamic models that express the pressure as a function of temperature, volume and molar composition. Various ramifications and improvements were added after the first Van Der Waals EoS in 1873, namely Soave modification of Redlich–Kwong SRK and PR that took more importance than the others through time. In this document, we will focus on these two equations.

C.4.1 Model description

C.4.1.1 Cubic Equation of state for a pure component

The use of different versions of the cubic EoS impose the use of a more general equation that can include both PR and SRK formulation. The equation is expressed as follow:

$$P(T,v,x) = \frac{RT}{v-b} - \frac{a\alpha(T)}{(v+\delta_1 b)(v+\delta_2 b)} \tag{C.45}$$

The introduced constants (δ_1, δ_2) are present in the attractive term of the EoS and represent its volumetric dependence. We still distinguish as well the Temperature dependency of this term through $\alpha(T)$:

$$\alpha(T) = \left(1 + Q(w)\left(1 - \sqrt{\frac{T}{T_c}}\right)\right)^2 ;$$

For SRK:

$$\delta_1 = 1 \; ; \; \delta_2 = 0 \; ; \; Q(w) = 0.480 + 1.574\omega - 0.176\omega^2.$$

Whereas for PR:

$$\delta_1 = 1 + \sqrt{2} \; ; \; \delta_2 = 1 - \sqrt{2} \; ; \; Q(w) = 0.37464 + 1.54226\omega - 0.26992\omega^2.$$

knowing that ω is acentric factor for the component.
In this equation a and b are the mixture parameters. The values of these coefficients are slightly different for the two EoS and written as the following : For SRK:

$$a = 0.42748\frac{R^2T_c^2}{P_c} \; ; \; b = 0.08664\frac{RT_c}{P_c}$$

For PR:

$$a = 0.45724\frac{R^2T_c^2}{P_c} \; ; \; b = 0.0778\frac{RT_c}{P_c}$$

C.4.1.2 Cubic Equation of state for a mixture of multi-components system

The previous cubic equation (C.45) was developed for pure components without interaction between different compounds. In order to shift to an accurate description of the fluid properties in the mixture system, we extend the cubic EoS using mixing and combining rules. The most classical and the mostly used mixing rules are the Van der Waals that describes the mixture of the fluid as the follow:

$$a = \sum_i \sum_j x_i x_j a_{ij}(T) \quad ; \quad b = \sum_i \sum_j x_i x_j b_{ij} \tag{C.46}$$

where x_i and x_j are the mole fractions of the component i and j. The Van der Waals combining rules introduces k_{ij} the binary interaction parameter.

$$a_{ij}(T) = \sqrt{a_{ii}\alpha_{ii}(T)a_{jj}\alpha_{jj}(T)}(1-k_{ij}) \quad ; \quad b_{ij} = \frac{b_{ii}+b_{jj}}{2}(1-l_{ij}) \tag{C.47}$$

When b_{ij} is substituted in the eq (C.46), the mixture co-volume b is reduced to the following expression with often l_{ij}= 0 :

$$b = \sum_i x_i b_{ii}$$

It is known that this functional form of mixing rules is very useful but also represents some limitations. Vander Waals mixing rules are not able to describe all the possibles mixtures. Consequently, a number of works have proposed different non quadratic rules, e.g. Huron-Vidal mixing rule, and the more complex Wong-Sandler mixing rule...

The pressure written in the equation (C.45) can be expressed in extensive variables where we convert (x, v) to (n, V) as the following:

$$P(T,V,\boldsymbol{N}) = \frac{RT}{\frac{V}{N_{\text{tot}}}-b} - \frac{a\alpha(T)}{(\frac{V}{N_{\text{tot}}}+\delta_1 b)(\frac{V}{N_{\text{tot}}}+\delta_2 b)} \quad \text{with} \quad v = \frac{V}{N_{\text{tot}}};\ x_i = \frac{N_i}{N_{\text{tot}}} \tag{C.48}$$

whereas in the mixing rules :

$$a = \sum_i \sum_j x_i x_j a_{ij} = \frac{1}{N_{\text{tot}}^2} \sum_i \sum_j N_i N_j a_{ij}$$

$$b = \sum_i x_i b_{ii} = \frac{1}{N_{\text{tot}}} \sum_i N_i b_i$$

leading to:

$$P(T,V,\boldsymbol{N}) = \frac{N_{\text{tot}}RT}{V-\mathfrak{B}(\boldsymbol{N})} - \frac{\mathfrak{A}(T,\boldsymbol{N})}{(V+\delta_1\mathfrak{B}(\boldsymbol{N}))(V+\delta_2\mathfrak{B}(\boldsymbol{N}))} \tag{C.49}$$

where:

$$\mathfrak{A}(T,\boldsymbol{N}) = N_{\text{tot}}^2 a = \sum_{i,j} N_i N_j a_{ij}(T) \quad \text{and} \quad \mathfrak{B}(\boldsymbol{N}) = N_{\text{tot}} b = \sum_i N_i b_i$$

C.4.2 Thermodynamic variables as $(T, V, \boldsymbol{N})$ functions

C.4.2.1 Derivatives of $P(T, V, \boldsymbol{N})$

The pressure and its derivatives are written below:

$$\begin{cases} P_V = \left.\dfrac{\partial P}{\partial V}\right|_{T,\boldsymbol{N}} = -\dfrac{N_{\text{tot}}RT}{(V-\mathfrak{B})^2} + \dfrac{\mathfrak{A}(T)\left((V+\delta_1\mathfrak{B})+(V+\delta_2\mathfrak{B})\right)}{(V+\delta_1\mathfrak{B})^2(V+\delta_2\mathfrak{B})^2} \\ P_T = \left.\dfrac{\partial P}{\partial T}\right|_{V,\boldsymbol{N}} = \dfrac{N_{\text{tot}}R}{V-\mathfrak{B}} - \dfrac{\mathfrak{A}_T}{(V+\delta_1\mathfrak{B})(V+\delta_2\mathfrak{B})} \\ P_{\boldsymbol{N}} = \left(\left.\dfrac{\partial P}{\partial \boldsymbol{N}}\right|_{T,V}\right)_i = \dfrac{RT}{(V-\mathfrak{B})} + \mathfrak{B}_i\dfrac{N_{\text{tot}}RT}{(V-\mathfrak{B})^2} - \dfrac{\mathfrak{A}_i}{(V+\delta_1\mathfrak{B})(V+\delta_2\mathfrak{B})} \\ \qquad + \mathfrak{A}\mathfrak{B}_i\dfrac{(\delta_1(V+\delta_2\mathfrak{B})+\delta_2(V+\delta_1\mathfrak{B}))}{(V+\delta_1\mathfrak{B})^2(V+\delta_2\mathfrak{B})^2} \end{cases} \tag{C.50}$$

The first order partial derivatives of $\mathfrak{A}$ ans $\mathfrak{B}$

$$\begin{aligned}
\mathfrak{A}_T &\equiv \frac{\partial \mathfrak{A}}{\partial T} = \sum_i \sum_j N_i N_j \frac{\mathrm{d}a_{ij}}{\mathrm{d}T} \\
\mathfrak{A}_i &\equiv \frac{\partial \mathfrak{A}}{\partial N_i} = 2\sum_j N_j a_{ij} \\
\mathfrak{B}_i &\equiv \frac{\partial \mathfrak{B}}{\partial N_i} = b_i
\end{aligned} \tag{C.51}$$

The second order partial derivatives of $\mathfrak{A}$ and $\mathfrak{B}$

$$\begin{aligned}
\mathfrak{A}_{TT} &\equiv \frac{\partial^2 \mathfrak{A}}{\partial T^2} = \sum_i \sum_j N_i N_j \frac{\mathrm{d}^2 a_{ij}}{\mathrm{d}T^2} \\
\mathfrak{A}_{Ti} &\equiv \frac{\partial^2 \mathfrak{A}}{\partial \boldsymbol{N}_i \partial T} = 2\sum_j N_j \frac{\mathrm{d}a_{ij}}{\mathrm{d}T} \\
\mathfrak{A}_{ij} &\equiv \frac{\partial^2 \mathfrak{A}}{\partial \boldsymbol{N}_i \partial \boldsymbol{N}_j} = 2a_{ij} \\
\mathfrak{B}_{ij} &\equiv \frac{\partial^2 \mathfrak{B}}{\partial \boldsymbol{N}_i \partial \boldsymbol{N}_j} = 0
\end{aligned} \tag{C.52}$$

C.4.2.2 $F(T, V, \boldsymbol{N}, \mathfrak{A}, \mathfrak{B})$ and its derivatives

Based on the equation (C.3), we note the quantity F representing the general equation of the residual Helmholtz free energy, expressing the dependencies to $\mathfrak{A}$ and $\mathfrak{B}$ as a model parameters. Where $\mathfrak{B}$ is a function of the composition and $\mathfrak{A}$ is a function of temperature and composition. F can be written as the following:

$$\begin{aligned}
F = A^{\mathrm{res}} &= -\int_{+\infty}^{V} \left(P(T, V, \boldsymbol{N}) - \frac{N_{\mathrm{tot}} RT}{V} \right) \mathrm{d}V \\
&= N_{\mathrm{tot}} RT \ln \frac{V}{V - \mathfrak{B}(\boldsymbol{N})} + \frac{\mathfrak{A}(T, \boldsymbol{N})}{(\delta_1 - \delta_2)\mathfrak{B}(\boldsymbol{N})} \ln \frac{V + \delta_2 \mathfrak{B}(\boldsymbol{N})}{V + \delta_1 \mathfrak{B}(\boldsymbol{N})}
\end{aligned}$$

Let us define the function $F(T, V, \boldsymbol{N}, \mathfrak{A}, \mathfrak{B})$ as

$$F(T, V, N_{\mathrm{tot}}, \mathfrak{A}, \mathfrak{B}) = N_{\mathrm{tot}} RT \ln \left(\frac{V}{V - \mathfrak{B}}\right) + \frac{\mathfrak{A}}{\mathfrak{B}(\delta_1 - \delta_2)} \ln \left(\frac{V + \delta_2 \mathfrak{B}}{V + \delta_1 \mathfrak{B}}\right) \tag{C.53}$$

Deriving equation (C.53) gives

$$\begin{aligned}
F_T &\equiv \frac{\partial F}{\partial T} = N_{\mathrm{tot}} R \ln \left(\frac{V}{V - \mathfrak{B}}\right) = \frac{N_{\mathrm{tot}}}{T} F_N \\
F_N &\equiv \frac{\partial F}{\partial N_{\mathrm{tot}}} = RT \ln \left(\frac{V}{V - \mathfrak{B}}\right) \\
F_{\mathfrak{A}} &\equiv \frac{\partial F}{\partial \mathfrak{A}} = \frac{1}{\mathfrak{B}(\delta_1 - \delta_2)} \ln \left(\frac{V + \delta_2 \mathfrak{B}}{V + \delta_1 \mathfrak{B}}\right) \\
F_{\mathfrak{B}} &\equiv \frac{\partial F}{\partial \mathfrak{B}} = \frac{N_{\mathrm{tot}} RT}{V - \mathfrak{B}} - \frac{\mathfrak{A}}{\mathfrak{B}} \left(F_{\mathfrak{A}} + \frac{V}{(V + \delta_2 \mathfrak{B})(V + \delta_1 \mathfrak{B})} \right)
\end{aligned} \tag{C.54}$$

on the other hand, the second derivatives lead to:

$$
\begin{aligned}
F_{TN} &\equiv \frac{\partial^2 F}{\partial T \partial N_{\text{tot}}} = \frac{1}{T} F_N \\
F_{\mathfrak{B}T} &\equiv \frac{\partial^2 F}{\partial \mathfrak{B} \partial T} = \frac{N_{\text{tot}} R}{V - B} \\
F_{\mathfrak{B}\mathfrak{A}} &\equiv \frac{\partial^2 F}{\partial \mathfrak{B} \partial \mathfrak{A}} = \frac{1}{\mathfrak{B}^2(\delta_1 - \delta_2)} \ln \frac{V + \delta_1 \mathfrak{B}}{V + \delta_2 \mathfrak{B}} - \frac{V}{(V + \delta_1 \mathfrak{B})(V + \delta_2 \mathfrak{B})} \\
&= -\frac{1}{\mathfrak{B}} \left(F_{\mathfrak{A}} + \frac{V}{(V + \delta_1 \mathfrak{B})(V + \delta_2 \mathfrak{B})} \right) \\
F_{N\mathfrak{B}} &\equiv \frac{\partial^2 F}{\partial N_{\text{tot}} \partial \mathfrak{B}} = \frac{RT}{V - \mathfrak{B}} \\
F_{\mathfrak{B}\mathfrak{B}} &\equiv \frac{\partial^2 F}{\partial \mathfrak{B} \partial \mathfrak{B}} = \frac{N_{\text{tot}} RT}{(V - \mathfrak{B})^2} - \frac{\mathfrak{A}}{\mathfrak{B}} F_{AB} + \frac{\mathfrak{A}}{\mathfrak{B}^2} F_A \\
&\quad + \frac{\mathfrak{A}}{\mathfrak{B}} \frac{V}{(V + \delta_1 \mathfrak{B})(V + \delta_2 \mathfrak{B})} \left(\frac{1}{\mathfrak{B}} + \frac{\delta_1}{V + \delta_1 \mathfrak{B}} + \frac{\delta_2}{V + \delta_2 \mathfrak{B}} \right) \\
F_{TT} &\equiv \frac{\partial^2 F}{\partial T^2} = 0 \ ; \ F_{\mathfrak{A}T} \equiv \frac{\partial^2 F}{\partial \mathfrak{A} \partial T} = 0 \ ; \ F_{NN} \equiv \frac{\partial^2 F}{\partial N_{\text{tot}}^2} = 0 \ ; \\
F_{N\mathfrak{A}} &\equiv \frac{\partial^2 F}{\partial N_{\text{tot}} \partial \mathfrak{A}} = 0 \ ; \ F_{\mathfrak{A}\mathfrak{A}} \equiv \frac{\partial^2 F}{\partial \mathfrak{A}^2} = 0
\end{aligned}
\tag{C.55}
$$

on the other hand:

$$
\begin{aligned}
\left. \frac{\partial A^{\text{res}}}{\partial T} \right|_{V,\boldsymbol{N}} &= F_T + F_{\mathfrak{A}} \mathfrak{A}_T \\
\left(\left. \frac{\partial A^{\text{res}}}{\partial \boldsymbol{N}} \right|_{T,V} \right)_i &= F_N + F_{\mathfrak{B}} \mathfrak{B}_i + F_{\mathfrak{A}} \mathfrak{A}_i
\end{aligned}
$$

$$
\begin{aligned}
\left. \frac{\partial^2 A^{\text{res}}}{\partial T^2} \right|_{V,\boldsymbol{N}} &= F_{\mathfrak{A}} \mathfrak{A}_{TT} \\
\left(\left. \frac{\partial^2 A^{\text{res}}}{\partial T \partial \boldsymbol{N}} \right|_{V} \right)_i &= (F_{\mathfrak{B}T} + F_{\mathfrak{B}\mathfrak{A}} \mathfrak{A}_T) \mathfrak{B}_i + F_{\mathfrak{A}} \mathfrak{A}_{iT} + F_{TN} \\
\left(\left. \frac{\partial^2 A^{\text{res}}}{\partial \boldsymbol{N} \partial \boldsymbol{N}} \right|_{T,V} \right)_{i,j} &= F_{N\mathfrak{B}} (\mathfrak{B}_i + \mathfrak{B}_j) + F_{\mathfrak{B}\mathfrak{A}} (\mathfrak{B}_i \mathfrak{A}_j + \mathfrak{B}_j \mathfrak{A}_i) + F_{\mathfrak{B}} \mathfrak{B}_{ij} \\
&\quad + F_{\mathfrak{B}\mathfrak{B}} \mathfrak{B}_i \mathfrak{B}_j + F_{\mathfrak{A}} \mathfrak{A}_{ij}
\end{aligned}
$$

C.4.2.3 Derivatives of $A(T, V, \boldsymbol{N})$

These equations were previously derived, and this is simply a consolidation of the equations mentioned earlier.

$$
\begin{cases}
\left. \dfrac{\partial A}{\partial T} \right|_{V,\boldsymbol{N}} = \left. \dfrac{\partial A^{\text{res}}}{\partial T} \right|_{V,\boldsymbol{N}} + \displaystyle\sum_i N_i \left(\mu_i^{\text{ideal},0\prime}(T) + R \ln \left(\frac{N_i RT}{P_0 V} \right) \right) \\
\left(\left. \dfrac{\partial A}{\partial \boldsymbol{N}} \right|_{T,V} \right)_i = \left(\left. \dfrac{\partial A^{\text{res}}}{\partial \boldsymbol{N}} \right|_{T,V} \right)_i + \mu_i^{\text{ideal},0}(T) + RT \ln \left(\dfrac{N_i RT}{P_0 V} \right)
\end{cases}
\tag{C.56}
$$

$$\begin{cases} \left(\left.\dfrac{\partial^2 A}{\partial T \partial \boldsymbol{N}}\right|_V\right)_i = \left(\left.\dfrac{\partial^2 A^{\text{res}}}{\partial T \partial \boldsymbol{N}}\right|_V\right)_i + \mu_i^{\text{ideal},0\prime}(T) + R\ln\left(\dfrac{N_i RT}{P_0 V}\right) + R \\ \left.\dfrac{\partial^2 A}{\partial T^2}\right|_{V,\boldsymbol{N}} = \left.\dfrac{\partial^2 A^{\text{res}}}{\partial T^2}\right|_{V,\boldsymbol{N}} + \sum_i N_i\left(\mu_i^{\text{ideal},0\prime\prime}(T) + \dfrac{R}{T}\right) \end{cases} \tag{C.57}$$

$$\left(\left.\frac{\partial^2 A}{\partial \boldsymbol{N}^2}\right|_{T,V}\right)_{i,j} = \begin{cases} \left(\left.\frac{\partial^2 A^{\text{res}}}{\partial \boldsymbol{N}\partial \boldsymbol{N}}\right|_{T,V}\right)_{i,j} + \frac{RT}{N_i} & \text{if } i = j \\ \left(\left.\frac{\partial^2 A^{\text{res}}}{\partial \boldsymbol{N}\partial \boldsymbol{N}}\right|_{T,V}\right)_{i,j} & \text{otherwise} \end{cases} \tag{C.58}$$

C.4.2.4 Summary

The thermodynamic variables presented as functions of $(T, V, \boldsymbol{N})$ were initially defined in section C.2, along with their derivatives. By applying Eq.(C.36), which guarantees the transition from $(T, V, \boldsymbol{N})$ to $(T, P, \boldsymbol{N})$, we can transform these properties and their derivatives to be expressed in terms of $(T, P, \boldsymbol{N})$. Therefore, by utilizing the derivatives of the variable of interest in $(T, V, \boldsymbol{N})$ and the derivatives of $P(T, V, \boldsymbol{N})$, we can determine the derivatives of this variable in $(T, P, \boldsymbol{N})$.

C.4.3 Péneloux volume translation

C.4.3.1 Principle and consequences

The cubic EoS present a shortage when describing the density of the liquid phase. Therefore, some approaches were proposed to reduce the deviation from experimental data. The most common correction used is the Péneloux volume translation that suggests to shift mathematically the volume considered by the EoS by a constant C. Here we denote the quantities related to the uncorrected EoS with a hat, $\hat{\cdot}$. For instance, the volume seen by the EoS is $\hat{V} = V + C$, and the uncorrected EoS is $\hat{P}(T, V, \boldsymbol{N})$, as given in equation (C.49). The correction consists in applying the EoS $\hat{P}$ to the shifted volume $\hat{V}$ rather than directly to the "true" volume V. More formally, the corrected EoS, $P(T, V, \boldsymbol{N})$, is given by

$$\begin{cases} P(T, V, \boldsymbol{N}) = \hat{P}(T, \hat{V}(T, V, \boldsymbol{N}), \boldsymbol{N}) \\ \hat{V}(T, V, \boldsymbol{N}) = V + C(T, \boldsymbol{N}) \end{cases} \tag{C.59}$$

Here, we consider a general case where the translation volume, $C(T, \boldsymbol{N})$, depends on the temperature T and the mole composition $\boldsymbol{N}$ without further details ; see section C.4.3.2 for more details.

The volume translation can be propagated into the equations and the derivatives written above. First of all, the Helmholtz free energy, as the integral of the pressure with respect to the volume, gives

$$\begin{aligned} A(T, V, \boldsymbol{N}) &= -\int_{V_0}^{V} P(T, V', \boldsymbol{N})\mathrm{d}V' \\ &= -\int_{V_0}^{V} \hat{P}(T, \hat{V}(T, V', \boldsymbol{N}), \boldsymbol{N})\frac{\partial \hat{V}}{\partial V}(T, V', \boldsymbol{N})\mathrm{d}V' \\ &= -\int_{\hat{V}_0}^{\hat{V}(T,V,\boldsymbol{N})} \hat{P}(T, \hat{V}', \boldsymbol{N})\mathrm{d}\hat{V}' \end{aligned}$$

Thus, the Helmholtz free energy is given by the formula of the uncorrected Helmholtz free energy but where the shifted volume $\hat{V}$ replaces the volume V:

$$A(T,V,\boldsymbol{N}) = \hat{A}(T,\hat{V}(T,V,\boldsymbol{N}),\boldsymbol{N}) \tag{C.60}$$

Let $\hat{P}_T$, $\hat{P}_V$ and $\hat{P}_{\boldsymbol{N}}$ denote the uncorrected derivatives of $\hat{P}(T,V,\boldsymbol{N})$ given in equation (C.50) ; let $\hat{A}_T$, $\hat{A}_{\boldsymbol{N}}$, $\hat{A}_{TT}$, $\hat{A}_{T\boldsymbol{N}}$ and $\hat{A}_{\boldsymbol{NN}}$ denote the derivatives of the uncorrected Helmholtz free energy $\hat{A}(T,V,\boldsymbol{N})$; let C_T and $C_{\boldsymbol{N}}$ denote the derivatives of $C(T,\boldsymbol{N})$. From equations (C.59) and (C.60), the derivatives of the corrected pressure and Helmholtz free energy are

$$\begin{cases} \left.\dfrac{\partial P}{\partial T}\right|_{V,\boldsymbol{N}} = \hat{P}_T + \hat{P}_V C_T \\ \left.\dfrac{\partial P}{\partial V}\right|_{T,\boldsymbol{N}} = \hat{P}_V \\ \left(\left.\dfrac{\partial P}{\partial \boldsymbol{N}}\right|_{T,V}\right)_i = \left(\hat{P}_{\boldsymbol{N}}\right)_i + \hat{P}_V \left(C_{\boldsymbol{N}}\right)_i \end{cases} \tag{C.61}$$

$$\begin{cases} \left.\dfrac{\partial A}{\partial T}\right|_{V,\boldsymbol{N}} = \hat{A}_T - \hat{P} C_T \\ \left(\left.\dfrac{\partial A}{\partial \boldsymbol{N}}\right|_{T,V}\right)_i = \left(\hat{A}_{\boldsymbol{N}}\right)_i - \hat{P}\left(C_{\boldsymbol{N}}\right)_i \end{cases} \tag{C.62}$$

$$\begin{cases} \left.\dfrac{\partial^2 A}{\partial T^2}\right|_{V,\boldsymbol{N}} = \hat{A}_{TT} - 2\hat{P}_T C_T - \hat{P}_V C_T^2 - \hat{P} C_{TT} \\ \left(\left.\dfrac{\partial^2 A}{\partial T \partial \boldsymbol{N}}\right|_{V}\right)_i = \left(\hat{A}_{T\boldsymbol{N}}\right)_i - \hat{P}_T \left(C_{\boldsymbol{N}}\right)_i - \hat{P}_V C_T \left(C_{\boldsymbol{N}}\right)_i \\ \qquad\qquad - \left(\hat{P}_{\boldsymbol{N}}\right)_i C_T - \hat{P}\left(C_{T\boldsymbol{N}}\right)_i \\ \left(\left.\dfrac{\partial^2 A}{\partial \boldsymbol{N} \partial \boldsymbol{N}}\right|_{T,V}\right)_{i,j} = \left(\hat{A}_{\boldsymbol{NN}}\right)_{i,j} - \left(\hat{P}_{\boldsymbol{N}}\right)_i \left(C_{\boldsymbol{N}}\right)_j - \left(\hat{P}_{\boldsymbol{N}}\right)_j \left(C_{\boldsymbol{N}}\right)_i \\ \qquad\qquad - \hat{P}_V \left(C_{\boldsymbol{N}}\right)_i \left(C_{\boldsymbol{N}}\right)_j - \hat{P}\left(C_{\boldsymbol{NN}}\right)_{i,j} \end{cases} \tag{C.63}$$

A^{res} and derivatives

$$\Delta A_X^{\text{res}} = \Delta A_X + \left[A_X^{\text{ideal}}(T,\hat{V},\boldsymbol{N}) - A_X^{\text{ideal}}(T,V,\boldsymbol{N})\right]$$

C.4.3.2 About the translation factor dependencies

There are discussions in the literature about the form of the function $C(T,\boldsymbol{N})$, the simplest is $C(T,\boldsymbol{N}) = \sum_i N_i c_i$ [107].

C.4.4 Computing $V(P,T,N)$

The advantage of this type of equation that it can be reduced to the polynomial form and solved using the compressibility Factor $Z = \frac{PV}{N_{\text{tot}}RT}$ like the expression bellow:

$$Z^3 + ((\delta_1+\delta_2)\beta - \beta - 1)Z^2 + (\alpha - (\delta_1\delta_2)\beta^2 - (\beta+1)(\delta_1+\delta_2)\beta)Z - \beta(\alpha + \beta(\beta+1)(\delta_1\delta_2)) = 0 \tag{C.64}$$

with

$$\beta = \frac{P\mathfrak{B}}{N_{\text{tot}}RT} \; ; \; \alpha = \frac{P\mathfrak{A}}{N_{\text{tot}}^2R^2T^2}$$

For SRK:

$$Z^3 - Z^2 + (A - B - B^2)Z - AB = 0$$

with

$$A = 0.42748\frac{\alpha R^2 P_r}{T_r^2} \text{ and } B = 0.08664\frac{\alpha R P_r}{T_r}$$

For PR:

$$Z^3 - (1 - B)Z^2 + (A - 2B - 3B^2)Z - (AB - B^2 - B^3) = 0$$

with

$$A = 0.045724\frac{\alpha P_r}{T_r^2} \text{ and } B = 0.0778\frac{\alpha P_r}{T_r}$$

where P_r is the reduced pressure $P_r = \frac{P}{P_c}$ and T_r is the reduced temperature and $T_r = \frac{T}{T_c}$. The determination of the two terms A and B, will allow us to resolve the equation and conclude the roots Z using the Newton-Raphson method. the polynomial equation of order three will lead to three roots: the inferior is describing the liquid phase, the superior is describing the Vapour phase and the middle one has non physical meaning.

ANNEXE D

Résumé détaillé

D.1 Introduction

La transition vers des sources d'énergie durables, notamment en utilisant l'H_2 en tant que vecteur énergétique, est un sujet d'actualité et de recherche qui réunit différents spécialistes à l'échelle internationale. Il existe diverses "couleurs" de l'H_2, telles que le gris, le vert, le bleu et l'orange, en fonction de son origine et des émissions de CO_2 associées [5]. En 2021, l'H_2 était principalement issu des technologies de gazéification du charbon lignite (H_2 gris), de la biomasse, ou de l'extraction du gaz naturel par reformage du CH_4 à la vapeur (H_2 marron) [1, 2]. L'empreinte carbone de ces processus peut être réduite en les associant au stockage de CO_2 (H_2 bleu). Cependant, la diversité des sources et le système de "blending" ont rendu difficile la distinction entre ces différentes couleurs [3, 4].

D'autre part, malgré les efforts déployés pour réduire la consommation de combustibles fossiles, les émissions de CO_2 ont augmenté en raison de la croissance économique [1]. Cela souligne l'importance de la capture et du stockage du CO_2, une idée qui s'inscrit dans le cadre de ce travail en proposant un stockage double avec le CO_2 stocké de manière permanente.

Afin de promouvoir la réduction des émissions de CO_2, une solution envisagée serait de produire de l'H_2 à partir de sources d'énergie renouvelable [6]. En outre, si nous envisageons de remplacer progressivement les énergies fossiles par des sources d'énergie renouvelable, nous devrons alors équilibrer l'offre et la demande en convertissant l'excédent de production en énergie. Cependant, la production d'H_2, tout comme sa source, est intermittente, ce qui souligne la nécessité d'un stockage efficace de l'H_2. Dans ce contexte, le stockage souterrain d'H_2 (UHS) dans des aquifères émerge comme une solution prometteuse [8, 9]. Bien que le stockage en réservoirs épuisés soit une option plus réalisable en raison de la connaissance géologique approfondie de la structure du réservoir acquise lors de son l'exploitation, il présente des inconvénients tels que des capacités limitées, une distribution géographique restreinte et des préoccupations liées à la sécurité en raison de fuites potentielles à partir de puits abandonnés [12, 13, 14, 15, 16].

Les aquifères, des formations rocheuses poreuses et perméables remplies d'eau généralement salée, suscitent un intérêt croissant en tant que sites potentiels de stockage souterrain de gaz

[18]. Leurs caractéristiques géologiques sont similaires à celles des réservoirs d'hydrocarbures épuisés, mais leur utilisation est souvent plus coûteuse en raison du manque d'infrastructures et d'informations géologiques. Pour créer des pièges à gaz efficaces dans les aquifères, des structures géologiques telles que des anticlinaux avec une roche couverture imperméable et des pressions hydrostatiques et de seuil appropriées sont nécessaires [19]. Cependant, l'UHS dans les aquifères salins présente plusieurs défis, notamment la production d'eau et le maintien d'une pression de production suffisante [20, 21]. De plus, l'identification des divers paramètres géologiques et opérationnels influençant le mélange de CO_2 et d'H_2 affecte la rentabilité du projet [22, 23].

En résumé, le stockage de fluides dans le sous-sol et les modifications des propriétés naturelles des fluides d'origine peuvent entraîner des changements dans la pression et la distribution géomécanique des contraintes, favorisant la migration des fluides et les fuites. Une planification minutieuse et des stratégies d'atténuation sont cruciales pour le stockage de l'H_2.

Dans le stockage de gaz en aquifère, le CO_2 est nécessaire pour maintenir la pression du H_2, contribuant ainsi à l'intégrité structurelle du réservoir [19]. Le rapport CO_2/H_2 dans l'UHS des aquifères est une information essentielle, étant donné que des pertes de CO_2 et d'H_2 sont inévitables. Cependant, une fraction significative de CO_2 reste piégée en raison de l'hétérogénéité du réservoir, et elle ne peut pas être récupérée.

L'UHS dans les aquifères présente de nombreux défis, notamment des risques géologiques, géochimiques et microbiens, exigeant une exploration approfondie, des projets pilotes et des mises en œuvre commerciales pour être viables [25, 26]. L'H_2 est une molécule très réactive, susceptible d'engendrer des réactions géochimiques et microbiennes avec la roche environnante, ce qui peut altérer les propriétés du réservoir [24]. Cependant, sa faible solubilité limite sa réactivité, en particulier dans les réservoirs froids. Les réactions géochimiques sont sensibles à la température, avec des réservoirs plus froids présentant des risques moindres.

L'incertitude élevée dans les milieux poreux, en raison de l'hétérogénéité minérale et de la composition des fluides, constitue également un défi. La migration de l'H_2 à travers la roche couverture soulève des questions sur l'étanchéité et l'intégrité du réservoir pour éviter les fuites vers la surface. Parmi d'autres défis figurent l'optimisation des performances du réservoir, la sélection du site, le choix du CO_2, la comparaison de l'impact des types de CO_2 sur les taux de récupération de l'H_2 et la prise en compte des coûts associés. Les cycles saisonniers ont également un impact sur la migration et le mélange des fluides, et la perte de CO_2 peut devenir irrécupérable dans le réservoir. Des données supplémentaires collectées dans des conditions et des formations variées sont essentielles pour des prévisions précises sur le développement du panache d'H_2 et la définition de stratégies de production optimales. La nature corrosive de l'H_2 suscite des inquiétudes concernant les puits, les pipelines et les installations de surface, avec un risque de fuite d'H_2 provenant de puits mal bouchés ou abandonnés ou de forages non cartographiés, ce qui pourrait avoir des répercussions sur l'environnement, l'économie du projet et la sécurité.

D.2 Revue des projets

La recherche sur le stockage de l'H_2 dans les aquifères s'est concentrée sur les sites de stockage de gaz de ville, où le mélange gazeux peut contenir jusqu'à 60 % d'H_2, offrant ainsi des perspectives

intéressantes pour le développement de systèmes d'H_2. L'H_2 induit principalement des réactions d'oxydoréduction, telles que la réduction du fer, la réduction du sulfate, la méthanogénèse et l'acétogénèse, susceptibles de générer des gaz toxiques et corrosifs, tels que le H_2S. De plus, la méthanogénèse peut donner lieu à la formation de CH_4, ce qui modifie la composition du mélange gazeux.

Des expériences menées sur des sites de stockage de gaz de ville ont révélé des changements significatifs dans la composition du gaz au fil du temps, entraînant des pertes de gaz [33, 32, 31]. Ces changements semblent dépasser les seules réactions microbiennes. Par exemple, à Beynes, en France, on a observé la production de H_2S, probablement due à la réduction abiotique de la pyrite par des bactéries [28]. De même, à Lobodice, en République tchèque, des changements dans la composition du gaz se sont produits au cours des cycles d'injection et de retrait, entraînant une diminution des gaz acides et une augmentation de la production de CH_4 [29, 30, 30].

Il est essentiel de noter que le gaz de ville est composé de plusieurs molécules, ce qui le rend plus réactif que l'H_2 pur, voire plus réactif que l'association H_2-CO_2. Ces expériences fournissent des informations précieuses pour aborder les questions soulevées précédemment.

Au cours de la dernière décennie, de nombreux projets de recherche ont été initiés dans le domaine du stockage souterrain de l'H_2, en se penchant notamment sur les réservoirs de gaz épuisés. Parmi ces projets, on compte Hychico [33], HyUnder [34], H2STORE [35], ANGUS+ [36], HyInteger, ainsi que les projets Underground Sun Storage et Sun Conversion.

Hychico s'est concentré sur la production de CH_4 à partir de H_2 et de CO_2 en utilisant la méthanogénèse contrôlée, impliquant à la fois de l'H_2 pur et un mélange de gaz "pauvre". Cependant, la méthanogénèse s'est révélée être fortement influencée par des conditions expérimentales spécifiques, ne se produisant pas systématiquement [33].

HyUnder a examiné les principaux obstacles à l'adoption à grande échelle de l'UHS, tandis que H2STORE a étudié la faisabilité du stockage de l'H_2 à grande échelle dans les réservoirs poreux. ANGUS+ s'est penché sur la pré-faisabilité de UHS et de la méthanisation dans les réservoirs de gaz épuisés, prenant en compte des facteurs économiques, politiques et juridiques. HyInteger s'est focalisé sur les effets du métabolisme microbien sur l'intégrité des puits et le comportement des matériaux dans des conditions corrosives.

Les projets Underground Sun Storage et Sun Conversion ont observé la consommation microbienne de H_2 pendant le stockage combiné de gaz naturel avec ajout d'H_2 (provenant de sources vertes) et de CO_2 dans des gisements de gaz épuisés. Ces projets ont noté une légère modification de la perméabilité effective, peut-être due à une réduction concomitante de la saturation en eau.

Cependant, il est important de noter que la plupart de ces études se sont concentrées sur les réservoirs épuisés plutôt que sur les aquifères, ce qui soulève des défis techniques nécessitant une recherche plus approfondie. Pour aborder cette exploration, il est essentiel de définir la demande en stockage et les volumes nécessaires, de comparer les différents CGs du point de vue technique et économique, de déterminer le rapport H_2-CG optimal pour chaque scénario, d'évaluer l'intégrité du stockage et de comprendre comment l'activité géochimique et microbienne peut influencer la sécurité et l'économie du projet.

La performance du stockage est un autre aspect critique qui nécessite d'être exploré, les taux

d'injection et de production étant des paramètres clés pour répondre à la demande, étroitement liés à la pureté du gaz produit. Il est essentiel de bien comprendre le comportement des fluides à l'intérieur du réservoir et les processus de mélange en jeu. Une modélisation précise des réservoirs doit être validée et développée, mais les incertitudes liées aux résultats de ces modèles contribuent aux risques potentiels pour la sécurité et la rentabilité des projets. Les installations de surface et l'infrastructure des puits font partie intégrante de l'équation.

La recherche présentée ici explore une approche de stockage de l'H_2 dans les aquifères, où l'aquifère est rempli en permanence d'un CG tandis que l'H_2 est injecté et récupéré pendant les cycles d'exploitation. Cette approche, en utilisant l'H_2 soutenu par un autre CG comme le CO_2, peut améliorer la rentabilité de l'UHS en réduisant les coûts d'exploitation. En outre, elle offre la possibilité de réutiliser le CO_2 pour la séquestration souterraine, contribuant ainsi à la réduction des émissions de gaz à effet de serre.

Toutefois, des préoccupations subsistent concernant le mélange entre l'H_2 et le CO_2, ainsi que sur l'extension de la zone de mélange. L'étude utilise deux outils de simulation, un simulateur commercial de Computer Modelling Group (CMG) appelé GEM, et un code open-source, ComPASS, pour développer un modèle thermodynamique précis et évaluer l'efficacité du concept UHS. Cette recherche fournit un aperçu complet des conditions potentielles du réservoir, en évaluant l'état et le comportement du système CO_2-H_2, avec un accent sur la capacité de stockage et les capacités de récupération et pureté du gaz.

La thèse se concentre sur la comparaison des capacités théoriques de stockage dans des réservoirs poreux en utilisant l'H_2 comme CG et d'autres gaz tels que le CO_2, le gaz naturel (CH_4), le N_2, ou potentiellement des mélanges. Elle évalue la capacité du caprock et le mélange gazeux entre le CG et l'H_2, calculant ainsi une limite pratique pour les taux d'injection d'H_2 en fonction de la perméabilité du réservoir et des propriétés des fluides. La thèse discute également de différents modèles thermodynamiques et de leur pertinence pour décrire le comportement de densité du système H_2-CO_2. Elle conclut par une évaluation générale du comportement du système dans différentes conditions de température et de pression du réservoir, introduisant des scénarios statiques. La recherche utilise également le simulateur CMG avancé pour effectuer des simulations complètes sur un réservoir réaliste, évaluant l'influence des variables opérationnelles, géologiques et liées au réservoir sur les performances du système de stockage de l'H_2-CO_2. La thèse offre une perspective prospective sur les applications et les développements potentiels.

D.3 Approche analytique pour le calcul de capacité de stockage

Dans cette étude, nous nous penchons sur la question cruciale du mélange de gaz entre le CG et l'H_2, en explorant les stratégies de base pour minimiser ce phénomène.

Notre analyse fournit un critère simple pour calculer la limite pratique des taux d'injection de H_2. Cette limite sert de référence pour garantir la faisabilité opérationnelle des systèmes de stockage d'H_2 dans différents types de réservoirs. Nous avons examiné la stabilité et la dispersion des fronts miscibles entre H_2 et certains CGs dans des configurations de stockage où H_2 est stocké au-dessus du CG dans des réservoirs limités latéralement et par le haut. Il s'avère que ces fronts sont stabilisés par la gravité dans une large gamme de taux d'injection, avec un taux maximum qui

dépend uniquement de la perméabilité du réservoir, de l'angle d'inclinaison du front par rapport à l'horizontale, et de la manière dont la densité et la viscosité des mélanges H_2-CG sont corrélées. Cette relation contrôle le déclenchement et présumément le développement de l'instabilité qui se produit lorsque ce taux maximal est atteint ou dépassé dans la région supérieure du front, riche en H_2, à l'exception du cas où le CO_2 est supercritique. Notre analyse montre que ces fronts restent stables dans une large gamme de réservoirs homogènes et de perméabilité moyenne à élevée, et que la propagation des fronts H_2-CG reste dans des limites acceptables pour des taux d'injection de H_2 réalistes. Il est à noter que cette vitesse maximale est rarement dépassée dans les applications pratiques, même dans les scénarios impliquant des zones de mélange inclinées. Cette approche peut être directement étendue à des systèmes WG-CG plus complexes.

Ce chapitre propose également des approches analytiques pour réaliser une évaluation comparative des capacités de stockage dans les réservoirs poreux. Nous commençons par étudier un scénario dans lequel le H_2 est utilisé comme son propre CG. Par la suite, nous étendons notre analyse aux gaz plus denses, tels que le CO_2, le gaz naturel (CH_4) et le N_2. Cette étude implique une analyse de la capacité de la roche couverture, qui dépend de facteurs tels que la faible perméabilité et la pression d'entrée. Le compromis entre les forces de poussée et les propriétés capillaires de la roche étanche par rapport à l'eau, à la saumure et au gaz présents a été examiné pour déterminer les capacités de stockage d'H_2 pour différents CGs. Les CGs plus denses ont une différence de densité plus faible avec la saumure, ce qui réduit les forces de poussée et améliore les capacités de stockage. Par conséquent, les capacités de stockage diminuent dans l'ordre suivant avec la CG : CO_2, N_2, CH_4 et H_2. Cette approche peut être facilement étendue à tout couple WG/CG, y compris lorsque le WG et CG sont des mélanges.

En résumé, l'utilisation du CO_2 comme CG pour le stockage de l'H_2 dans les aquifères ou les réservoirs de gaz déplétés offre des avantages significatifs par rapport à l'utilisation du H_2 ou d'autres gaz inertes (N_2, CH_4). Elle permet non seulement d'économiser une grande quantité d'H_2, mais aussi de renforcer la sécurité du stockage en réduisant la force de poussée transmise à la partie supérieure du réservoir. La densité élevée du CO_2, relativement proche de celle de l'eau ou de la saumure, rend son utilisation comme CG particulièrement avantageuse, notamment dans les conditions de températures basses ou modérées et de pressions élevées que l'on rencontre dans les réservoirs offshore profonds. En conséquence, le même réservoir peut être utilisé pour le stockage permanent du CO_2 en plus d'être utilisé en tant que CG pour le stockage intermittent de l'H_2. La présence sous la roche de scellement d'un gaz plus léger (H_2, CH_4 , N_2, air et leurs mélanges) dont les propriétés interfaciales sont meilleures que celles du CO_2, augmente la sécurité du stockage du CO_2.

D.4 Étude du modèle thermodynamique et leur applicabilité au système H_2-CO_2

Par la suite, pour approfondir notre compréhension des complexités de l'UHS, nous avons entrepris une exploration de différents modèles thermodynamiques et de leur applicabilité à la modélisation du comportement du système CO_2 et H_2 dans les conditions de l'UHS. L'objectif consistait à

sélectionner l'équation d'état (EoS) la plus appropriée pour prédire avec précision les propriétés thermodynamiques de ce système.

Les EoS cubiques, notamment les modèles PR (Peng-Robinson) et SRK (Soave-Redlich-Kwong), ont longtemps été considérés comme des outils efficaces pour les calculs d'équilibre de phase et de propriétés des fluides. Cependant, des études et des comparaisons récentes ont révélé certaines limites associées à ces modèles. Par exemple, ces EoS cubiques ont montré des déficiences dans la prédiction précise des propriétés en phase liquide, en particulier pour l'hélium ou les mélanges riches en H_2, principalement en raison de l'effet quantique non-negligeable.

En revanche, l'EoS GERG-2008, développée spécifiquement pour le gaz naturel et ses mélanges, a démontré une meilleure précision dans diverses études, surpassant les EoS cubiques pour la plupart des systèmes de mélange. L'équation GERG-2008 reste un outil puissant pour la modélisation des équilibres de phase et des propriétés thermodynamiques des mélanges.

Les données expérimentales portant sur le système CO_2 et H_2 dans les conditions de l'UHS ont révélé des comportements intrigants. Même une faible introduction de 2 % de H_2 dans le système entraînait une réduction significative de la densité du mélange, jusqu'à 25 % par rapport au CO_2 pur dans des conditions identiques.

Quant à la précision, nos résultats ont révélé que bien que les modèles EoS cubiques soient généralement fiables, ils ont tendance à rencontrer des difficultés lorsqu'il s'agit de prédire la densité à de très faibles fractions d'H_2 dans le système. En revanche, l'équation GERG-2008 a maintenu sa précision, avec seulement des pertes de précision faibles et non significatives au fur et à mesure que la fraction de H_2 augmentait. La capacité de l'équation GERG-2008 à gérer une large gamme de pressions et de températures, associée à sa capacité prouvée à fournir des descriptions très précises du système CO_2 et H_2, en particulier dans des conditions pertinentes pour l'UHS, la rendent le choix le plus approprié pour guider les recherches et les simulations ultérieures de l'UHS.

À la lumière de ces résultats, nous recommandons d'adopter l'équation GERG-2008 pour les simulations UHS. Cependant, il est important de noter que le modèle GERG-2008 peut être exigeant en termes de temps de développement pour le codage et d'exécution de simulations réelles. En tenant compte des avantages et des inconvénients de chaque modèle thermodynamique, ainsi que du calendrier de développement du projet de recherche de la thèse, il a été décidé d'intégrer initialement un modèle EoS cubique dans ComPASS. Les EoS cubiques permettent un équilibre entre précision et efficacité de calcul, ce qui en fait un choix pragmatique pour la suite. Par conséquent, un module thermodynamique basé sur l'équation cubique a été intégré à l'outil de simulation open-source, ComPASS.

D.5 Simulations UHS avec ComPASS

ComPASS (Computing Parallel Architecture to Speed up Simulations) est un simulateur de modélisation d'écoulements multiphasiques et multicomposants en milieux poreux. Il s'agit d'un code open-source parallèle qui utilise des méthodes numériques avancées pour discrétiser les flux de Darcy multicouches non statiques sur des maillages non structurés génériques [110]. Initialement,

ComPASS était principalement utilisé pour la modélisation hydrothermale, mais sa portée s'est considérablement élargie pour englober un plus large éventail d'applications et pour traiter des scénarios multiphysiques [111, 112, 113, 114, 115].

Dans notre étude, nous avons présenté un aperçu complet de la mise en œuvre et des tests d'un modèle d'EoS cubique au sein de ComPASS. Notre objectif principal était d'y intégrer un modèle thermodynamique capable de gérer les transitions de phase et les propriétés des fluides.

Nous avons commencé par discuter des fondements théoriques des EoS cubiques, mettant en lumière leur rôle dans la prédiction des équilibres de phase et des propriétés thermodynamiques. Nous avons expliqué en détail la dérivation des coefficients de fugacité, l'énergie libre de Helmholtz, et d'autres variables thermodynamiques. De plus, nous avons mis en évidence les défis liés à l'intégration d'une EoS explicite en pression dans le cadre de ComPASS, où la formulation standard utilise la température, la pression et les nombres de moles comme variables primaires.

La section sur l'implémentation numérique a mentionné les développements qui ont permis aux utilisateurs de définir des composants, de manipuler des propriétés et de se concentrer sur les modifications de l'algorithme pour simuler efficacement les transitions de phase. Nous avons décrit l'utilisation de méthodes numériques avancées, d'algorithmes itératifs et de critères de convergence pour gérer le comportement de phase complexe, crucial pour la simulation de réservoir.

Tout au long de ce chapitre, nous avons présenté une série d'études de cas pour valider et démontrer les capacités du modèle EoS implémenté et du code de transition de phase au sein de ComPASS. Ces études de cas comprenaient des scénarios avec des conditions initiales variables, des déséquilibres de pression et des transitions de phase. Ces études de cas ont montré la capacité du modèle à gérer diverses situations, notamment la transition de phase provoquée par les variations de pression et des systèmes multi-composants multi-phases.

En conclusion, l'intégration et les tests réussis du module EoS cubique au sein de ComPASS fournissent un outil cohérent pour simuler les transitions de phase, le comportement des fluides et le transport de masse dans les milieux poreux. Ce modèle présente un large éventail d'applications potentielles, notamment dans la séquestration du carbone et l'analyse de réservoirs géothermiques.

D.6 Stratégies pour minimiser le mélange entre l'H_2 et le CO_2 : diagramme de phase et configurations conceptuelles

Nous avons élargi notre étude pour prendre en compte diverses conditions de pression et de température du réservoir. Cette analyse nous a permis de caractériser le comportement statique du système H_2-dioxyde dans ces conditions et de mettre en évidence la possibilité d'une séparation en deux phases : une phase dense riche en dioxyde et une phase riche en H_2. Nous avons étudié les implications de ces comportements distincts sur le mélange des gaz et la possibilité de la ségrégation gravitationnelle, un processus qui peut séparer les fluides en fonction de leurs différences de densité.

Les premiers résultats de notre modélisation suggèrent que dans ces conditions, la séparation de phase se produisant à l'avant du mélange pourrait agir comme un tampon, réduisant le mélange du CG avec l'H_2 injecté. De plus, nous avons observé un retard dans l'élévation de la

concentration d'H_2. Ces observations indiquent que l'optimisation de l'efficacité opérationnelle de l'UHS pourrait considérablement bénéficier de la prise en compte de ces phénomènes.

En poursuivant notre analyse à travers plusieurs sites de stockage actuels et futurs, qu'ils soient offshore ou onshore, nous avons identifié plusieurs endroits qui satisfont aux critères d'écoulement biphasique dans le contexte de l'UHS. Cela valide la faisabilité de cette approche et confirme qu'elle pourrait être mise en œuvre dans des scénarios réels.

Dans l'ensemble, les réservoirs extracôtiers situés dans les bassins sédimentaires froids, qui répondent à des critères spécifiques tels qu'une pression entre 7 et 10 MPa et une température inférieure à 300 K, présentent un potentiel intéressant pour les sites UHS. De plus, la proximité du stockage d'H_2 avec les parcs éoliens offshore pourrait générer des économies de coûts significatives et améliorer considérablement l'efficacité des projets.

D.7 Étude de simulations numériques dans un réservoir réaliste

Une étude d'un réservoir réaliste dans des conditions où le CO_2-H_2 coexistent en tant que système monophasé a été modélisée. L'utilisation de l'outil de modélisation GEM du CMG (Computer Modelling Group) permet de réaliser des simulations numériques complexes afin d'étudier la faisabilité d'un UHS saisonnier avec du CO_2 comme gaz de coussin dans un aquifère réaliste, doté d'une structure géologique bien définie. L'étude a pour objectif principal de relever le défi de la récupération efficace de l'H_2 pur dans l'UHS, car la contamination et la récupération du gaz de coussin ont un impact significatif sur la viabilité économique du projet. Ce travail de recherche vise à analyser et à comprendre comment divers paramètres comme des facteurs opérationnels, géologiques et liés au réservoir (p. ex., taux d'injection et de production, hétérogénéité, solubilité du gaz, etc.), influencent la pureté du système de stockage de H_2. Le but final étant d'identifier des scénarios de stockage optimaux. Cependant, il est important de noter qu'aucune considération géochimique n'a été intégrée à cette analyse.

À travers des simulations de réservoir exhaustives, divers scénarios ont été explorés en ajustant les paramètres d'entrée, tels que la saturation résiduelle, la solubilité de H_2 dans la phase aqueuse, la diffusion, la dispersion, les hétérogénéités du réservoir, les scénarios opérationnels et la stratégie de puits d'injection, afin de comprendre leur influence sur la le taux de récupération et la qualité du gaz. Les simulations ont révélé que l'hétérogénéité de ce site, la durée du cycle et le taux de production jouent un rôle crucial dans l'amélioration de la qualité du gaz et du volume cumulé récupéré.

- Les hétérogénéités ont amélioré la qualité du gaz récupéré en supprimant l'effet de conicité. Veuillez noter que cette constatation est propre au site.

- Produire à un rythme plus lent, tout en gardant le taux d'injection et la période constante, réduit efficacement le mélange entre les deux gaz. Il en résulte que la zone de mélange est plus éloignée du puits, ce qui permet de produire moins de H_2 contaminé. Cette conclusion concorde avec les conclusions d'autres études [162].

- La réduction de la durée du cycle permet de récupérer rapidement le H_2 injecté et limite le temps de migration et de mélange du gaz.
- La dispersion mécanique peut avoir un impact significatif sur la zone de mélange, et son effet dépend étroitement du coefficient de dispersivité. La caractérisation de ce paramètre pour chaque site spécifique est essentielle pour évaluer la rentabilité du projet de stockage.

D.8 Conclusion

Cette thèse explore le potentiel des aquifères salins profonds en tant que sites de UHS en raison de leur distribution géographique étendue et de leurs capacités de stockage importantes. Les sites géologiques utilisés pour la CCS, où le CO_2 est stocké en permanence, offrent des économies de coûts potentielles, mais cette approche présente des défis tels que le traitement des effets hydrodynamiques responsables du mélange entre l'H_2 et le gaz. Le principal défi consiste à atténuer le mélange et à assurer l'intégrité du stockage.

La stabilité des fronts miscibles entre le H_2 et différents CG a été analysée dans le contexte des scénarios UHS. L'étude a révélé que ces fronts ont tendance à être stabilisés par gravité dans une large gamme de taux d'injection pratiques, le taux d'injection maximal étant influencé par la perméabilité du réservoir, l'angle d'inclinaison du front par rapport à l'horizontale, et la relation entre la densité et la viscosité du mélange H_2-CG. Les CG plus denses, comme le CO_2, entraînent des différences de densité plus faibles avec la saumure, ce qui réduit les forces de flottabilité et augmente les capacités de stockage.

L'utilisation du CO_2 comme CG pour UHS dans les aquifères ou les réservoirs de gaz épuisés offre des avantages significatifs par rapport à l'utilisation de H_2 ou d'autres gaz inertes comme l'azote ou le CH_4 . Cette approche permet non seulement de conserver une quantité importante de H_2, mais également d'améliorer la sécurité de stockage en réduisant les forces de flottabilité transmises au sommet du réservoir. Le même réservoir peut servir à deux fins en étant utilisé pour le stockage permanent de CO_2 tout en agissant également comme CG pour le stockage intermittent de H_2.

Un modèle thermodynamique basé sur des équations d'état cubiques a été développé et intégré dans le simulateur de réservoir open source ComPASS. Le principal défi abordé au cours de cette tâche était lié à l'apparition et à la disparition des phases. L'intégration d'un modèle EoS cubique dans ComPASS fournit un outil cohérent pour simuler les transitions de phase, le comportement des fluides et le transport de masse dans les milieux poreux.

L'exploration du diagramme de phase du système H_2-CO_2 a montré le potentiel d'un système biphasé en UHS dans des conditions de pression-température spécifiques. Les simulations numériques ont montré que la séparation des phases au front du mélange peut réduire le mélange du CG avec le H_2 injecté et retarder la montée du gaz H_2. Ces résultats démontrent que l'UHS avec du CO_2 comme CG peut être atteint avec des paramètres de récupération de gaz raisonnables.

En conclusion, cette thèse contribue à une meilleure compréhension d'UHS. Ces connaissances peuvent éclairer les futurs projets d'UHS.

Bibliography

[1] E. Institute, Statistical review of world energy 2023 (72nd edition), Available online at: https://www.energyinst.org/statistical-review, 2023.

[2] D. F. Birol, World Energy Outlook 2022, Technical Report, International Energy Agency, 2022. URL: https://www.iea.org/reports/world-energy-outlook-2022.

[3] O. Olaniyi, J. Incer-Valverde, G. Tsatsaronis, T. Morosuk, Exergetic and Economic Evaluation of Natural Gas/Hydrogen Blends for Power Generation, Journal of Energy Resources Technology 145 (2023) 062701.

[4] I. Dincer, C. Acar, Review and evaluation of hydrogen production methods for better sustainability, International Journal of Hydrogen Energy 40 (2015) 11094–11111.

[5] F. Osselin, C. Soulaine, C. Fauguerolles, E. C. Gaucher, B. Scaillet, M. Pichavant, Orange hydrogen is the new green, Nature Geoscience 15 (2022) 765–769. Number: 10 Publisher: Nature Publishing Group.

[6] J. Incer-Valverde, A. Korayem, G. Tsatsaronis, T. Morosuk, "Colors" of hydrogen: Definitions and carbon intensity, Energy Conversion and Management 291 (2023) 117294.

[7] AFHYPAC - Th. A. (association francaise pour l'hydrogene et les piles), Mémento de l'Hydrogène: Fiche 3.2.1 Production d'Hydrogène par Électrolyse de l'Eau, Technical Report, 2017. URL: https://www.contrepoints.org/wp-content/uploads/2015/07/Lhydrog%C3%A8ne-cet-hallucinog%C3%A8ne-Annexe-1.pdf, révision : janvier 2017.

[8] M. Panfilov, Underground and pipeline hydrogen storage, in: Compendium of Hydrogen Energy, Elsevier, 2016, pp. 91–115. URL: https://linkinghub.elsevier.com/retrieve/pii/B9781782423621000043. doi:10.1016/B978-1-78242-362-1.00004-3.

[9] F. Feldmann, B. Hagemann, L. Ganzer, M. Panfilov, Numerical simulation of hydrodynamic and gas mixing processes in underground hydrogen storages, Environmental Earth Sciences 75 (2016) 1165.

[10] HyUnder, Assessment of the potential, the actors and relevant business cases for large scale and seasonal storage of renewable electricity by hydrogen underground storage in Europe – HyUnder, Executive Summary Grant agreement no.: 303417, 2014. URL: http://hyunder.eu/wp-content/uploads/2016/01/D8.1_HyUnderExecutive-Summary.pdf, accessed February 18, 2017.

[11] B. Sørensen, Underground hydrogen storage in geological formations, and comparison with other storage solutions, in: Hydrogen Power Theoretical and Engineering Int. Symp., Merida Technical University, 2007. Publisher's PDF, also known as Version of record.

[12] S. Foh, M. Novil, E. Rockar, P. Randolph, Underground Hydrogen Storage. Final Report. [Salt Caverns, Excavated Caverns, Aquifers and Depleted Fields], Technical Report, 1979. URL: https://doi.org/10.2172/6536941.

[13] C. Hemme, W. Van Berk, Hydrogeochemical Modeling to Identify Potential Risks of Underground Hydrogen Storage in Depleted Gas Fields, Applied Sciences 8 (2018) 2282. Number: 11 Publisher: Multidisciplinary Digital Publishing Institute.

[14] S. H. Yousefi, R. Groenenberg, J. Koornneef, J. Juez-Larré, M. Shahi, Techno-economic analysis of developing an underground hydrogen storage facility in depleted gas field: A Dutch case study, International Journal of Hydrogen Energy (2023) S0360319923018256.

[15] A. Safari, L. Zeng, R. Nguele, Y. Sugai, M. Sarmadivaleh, Review on using the depleted gas reservoirs for the underground H_2 storage: A case study in Niigata prefecture, Japan, International Journal of Hydrogen Energy 48 (2023) 10579–10602.

[16] M. Kanaani, B. Sedaee, M. Asadian-Pakfar, Role of cushion gas on underground hydrogen storage in depleted oil reservoirs, Journal of Energy Storage 45 (2022) 103783.

[17] A. Amid, D. Mignard, M. Wilkinson, Seasonal storage of hydrogen in a depleted natural gas reservoir, International Journal of Hydrogen Energy 41 (2016) 5549–5558.

[18] K. L. Anthonsen, N. P. Christensen, EU Geological CO_2 Storage Summary, Technical Report RAPPORT 2021/34, the Geological Survey of Denmark and Greenland for Clean Air Task Force, 2021.

[19] J. D. Arthur, N. Alleman, K. Andersen, A historical look at underground natural gas storage in america, Oil-Industry History (2016). Copyright © 2017 Petroleum History Institute.

[20] B. Misra, S. Foh, Y. Shikari, R. Berry, F. Labaune, The Use of Inert Base Gas in Underground Natural Gas Storage, volume All Days of *SPE Unconventional Resources Conference / Gas Technology Symposium*, 1988. doi:10.2118/17741-MS.

[21] N. Heinemann, M. Wilkinson, K. Adie, K. Edlmann, E. M. Thaysen, A. Hassanpouryouzband, R. S. Haszeldine, Cushion Gas in Hydrogen Storage—A Costly CAPEX or a Valuable Resource for Energy Crises?, Hydrogen 3 (2022) 550–563.

[22] S. M. Jafari Raad, Y. Leonenko, H. Hassanzadeh, Hydrogen storage in saline aquifers: Opportunities and challenges, Renewable and Sustainable Energy Reviews 168 (2022) 112846.

[23] H. B. Navaid, H. Emadi, M. Watson, A comprehensive literature review on the challenges associated with underground hydrogen storage, International Journal of Hydrogen Energy 48 (2023) 10603–10635.

[24] A. E. Yekta, J.-C. Manceau, S. Gaboreau, M. Pichavant, P. Audigane, Determination of Hydrogen–Water Relative Permeability and Capillary Pressure in Sandstone: Application to Underground Hydrogen Injection in Sedimentary Formations, Transport in Porous Media 122 (2018) 333–356.

[25] A. Lassin, M. Dymitrowska, M. Azaroual, Hydrogen solubility in pore water of partially saturated argillites: Application to callovo-oxfordian clayrock in the context of a nuclear waste geological disposal, Physics and Chemistry of the Earth, Parts A/B/C 36 (2011) 1721–1728.

[26] L. Truche, M.-C. Jodin-Caumon, C. Lerouge, G. Berger, R. Mosser-Ruck, E. Giffaut, N. Michau, Sulphide mineral reactions in clay-rich rock induced by high hydrogen pressure. application to disturbed or natural settings up to 250 c and 30 bar, Chemical Geology 351 (2013) 217–228.

[27] A. Yekta, Characterization of geochemical interactions and migration of hydrogen in sandstone sedimentary formations: Application to geological storage, Ph.D. thesis, 2017.

[28] Bourgeois, J. P., Aupaix, N., Bloise, R., Millet, J. L., Proposition d'explication de la formation d'hydrogène sulfuré dans les stockages souterrains de gaz naturel par réduction des sulfures minéraux de la roche magasin, Rev. Inst. Fr. Pét. 34 (1979) 371–386.

[29] P. ***S***migá***n***, M. Greksák, J. Kozánková, F. Buzek, V. Onderka, I. Wolf, Methanogenic bacteria as a key factor involved in changes of town gas stored in an underground reservoir, FEMS Microbiology Letters 73 (1990) 221–224.

[30] F. Buzek, V. Onderka, P. Van***c***ura, I. Wolf, Carbon isotope study of methane production in a town gas storage reservoir, Fuel 73 (1994) 747–752.

[31] J. Miocic, N. Heinemann, K. Edlmann, J. Scafidi, F. Molaei, J. Alcalde, Underground hydrogen storage: a review, Geological Society, London, Special Publications 528 (2023) SP528–2022.

[32] M. Panfilov, Underground Storage of Hydrogen: In Situ Self-Organisation and Methane Generation, Transport in Porous Media 85 (2010) 841–865.

[33] S. Dupraz, S. Stephant, A. Perez, C. Joulian, M. Blessing, L. André, E. Pérez, J. Bolcich, Patagonia Wind –Using Methanogenesis to Store Hydrogen on Large Scales, in: 22st World Hydrogen Energy Conference - WHEC 2018, Rio de Janeiro, Brazil, 2018. URL: `https://brgm.hal.science/hal-01742093`.

[34] Assessment of the potential, the actors and relevant business cases for large scale and seasonal storage of renewable electricity by hydrogen underground storage in Europe | HyUnder Project | Fact Sheet | FP7, 2023. URL: `https://cordis.europa.eu/project/id/303417`.

[35] L. Ganzer, V. Reitenbach, D. Pudlo, M. Panfilov, D. Albrecht, R. Gaupp, The H2STORE Project - Experimental and Numerical Simulation Approach to Investigate Processes in Underground Hydrogen Reservoir Storage, OnePetro, 2013. URL: https://dx.doi.org/10.2118/164936-MS. doi:10.2118/164936-MS.

[36] S. Bauer, A. Dahmke, O. Kolditz, Subsurface energy storage: geological storage of renewable energy—capacities, induced effects and implications, Environmental Earth Sciences 76 (2017).

[37] G. E. F. Tobin, K. Edlmann, N. Heinemann, Features, Events and Processes of geological hydrogen storage: Which pose highest risk for leakage? A three-scenario analysis: Depleted Gas Fields, Porous Aquifers and Salt Caverns., Technical Report EGU21-12754, Copernicus Meetings, 2021. URL: https://meetingorganizer.copernicus.org/EGU21/EGU21-12754.html. doi:10.5194/egusphere-egu21-12754, conference Name: EGU21.

[38] B. Uliasz-Misiak, J. Lewandowska-Śmierzchalska, R. Matuła, Selection of underground hydrogen storage risk assessment techniques, Energies 14 (2021) 8049. Number: 23 Publisher: Multidisciplinary Digital Publishing Institute.

[39] C. M. Oldenburg, L. Pan, Utilization of CO $_2$ as cushion gas for porous media compressed air energy storage, Greenhouse Gases: Science and Technology 3 (2013) 124–135.

[40] J. Tremosa, R. Jakobsen, Y. Le Gallo, Assessing and modeling hydrogen reactivity in underground hydrogen storage: A review and models simulating the Lobodice town gas storage, Frontiers in Energy Research 11 (2023) 1145978.

[41] R. Gholami, Hydrogen storage in geological porous media: Solubility, mineral trapping, H2S generation and salt precipitation, Journal of Energy Storage 59 (2023) 106576.

[42] P. Haddad, M. Ranchou-Peyruse, M. Guignard, J. Mura, F. Casteran, L. Ronjon-Magand, P. Sénéchal, M.-P. Isaure, P. Moonen, G. Hoareau, et al., Geological storage of hydrogen in deep aquifers–an experimental multidisciplinary study, Energy & Environmental Science 15 (2022) 3400–3415.

[43] E. M. Thaysen, T. Armitage, L. Slabon, A. Hassanpouryouzband, K. Edlmann, Microbial risk assessment for underground hydrogen storage in porous rocks, Fuel 352 (2023) 128852.

[44] G. Wang, G. Pickup, K. Sorbie, E. Mackay, Scaling analysis of hydrogen flow with carbon dioxide cushion gas in subsurface heterogeneous porous media, International Journal of Hydrogen Energy 47 (2022) 1752–1764.

[45] J. Scafidi, L. Schirrer, I. Vervoort, N. Heinemann, An open-source tool for the calculation of field deliverability and cushion-gas requirements in volumetric gas-reservoir storage sites, Geological Society, London, Special Publications 528 (2023) SP528–2022–71.

[46] N. Heinemann, J. Scafidi, G. Pickup, E. Thaysen, A. Hassanpouryouzband, M. Wilkinson, A. Satterley, M. Booth, K. Edlmann, R. Haszeldine, Hydrogen storage in saline aquifers:

The role of cushion gas for injection and production, International Journal of Hydrogen Energy 46 (2021) 39284–39296.

[47] Carriere1985, Mixing in Underground Storage Reservoirs, volume All Days of *SPE Annual Technical Conference and Exhibition*, 1985. URL: `https://doi.org/10.2118/14202-MS`. doi:`10.2118/14202-MS`, sPE-14202-MS.

[48] C. Walker, R. V. Huff, Feasibility of Inert-Gas Cushions in Gas Storages, 6531-6534, US Department of the Interior, Bureau of Mines, 1964.

[49] C. M. Oldenburg, Carbon dioxide as cushion gas for natural gas storage, Energy & Fuels 17 (2003) 240–246.

[50] A. Hassanpouryouzband, E. Joonaki, K. Edlmann, R. S. Haszeldine, Offshore geological storage of hydrogen: Is this our best option to achieve net-zero?, ACS Energy Letters 6 (2021) 2181–2186.

[51] A. Aftab, A. Hassanpouryouzband, Q. Xie, L. L. Machuca, M. Sarmadivaleh, Toward a fundamental understanding of geological hydrogen storage, Industrial & Engineering Chemistry Research 61 (2022) 3233–3253.

[52] National Institute of Standards and Technology (NIST), Thermophysical Properties of Fluid Systems, `https://webbook.nist.gov/chemistry/fluid/`, 2023. [last accessed March 21, 2023].

[53] O. Kunz, W. Wagner, The GERG-2008 Wide-Range Equation of State for Natural Gases and Other Mixtures: An Expansion of GERG-2004, Journal of Chemical & Engineering Data 57 (2012) 3032–3091.

[54] M. R. Tek, Underground storage of natural gas: theory and practice, 171, Springer Science & Business Media, 1989.

[55] C. K. Ho, S. W. Webb (Eds.), Gas transport in porous media, number v. 20 in Theory and applications of transport in porous media, Springer, Dordrecht, 2006. OCLC: 65766881.

[56] B. H. Kueper, E. O. Frind, An overview of immiscible fingering in porous media, Journal of Contaminant Hydrology 2 (1988) 95–110.

[57] Y. Sanchez-Vicente, T. C. Drage, M. Poliakoff, J. Ke, M. W. George, Densities of the carbon dioxide+hydrogen, a system of relevance to carbon capture and storage, International Journal of Greenhouse Gas Control 13 (2013) 78–86.

[58] C. Wilke, A viscosity equation for gas mixtures, The journal of chemical physics 18 (1950) 517–519.

[59] B. E. Poling, J. M. Prausnitz, J. P. O'Connell, The properties of gases and liquids, 5th ed ed., McGraw-Hill, New York, 2001.

[60] F. Herning, L. Zipperer, Calculation of the viscosity of technical gas mixtures from the viscosity of the individual gases, Gas u. Wasserfach 79 (1936) 69.

[61] B. Khosravi, B. Betken, J. P. Jakobsen, S. W. Løvseth, R. Span, Viscosity measurements of CO_2-rich; CO_2+ N_2 and CO_2+ H_2 mixtures in gas or supercritical phase at temperatures between 273 and 473 K and pressures up to 8.7 MPa, Fluid Phase Equilibria 560 (2022) 113519.

[62] J. C. Giddings, S. L. Seager, Method for the rapid determination of diffusion coefficients. theory and application, Industrial & Engineering Chemistry Fundamentals 1 (1962) 277–283.

[63] E. B. G. Castillo, Relative Permeability Hysteresis in Porous Media (2020).

[64] R. Massoudi, A. D. King, Effect of pressure on the surface tension of water. Adsorption of low molecular weight gases on water at 25.deg., The Journal of Physical Chemistry 78 (1974) 2262–2266.

[65] C. Duchateau, D. Broseta, A simple method for determining brine–gas interfacial tensions, Advances in Water Resources 42 (2012) 30–36.

[66] B. Pan, X. Yin, S. Iglauer, Rock-fluid interfacial tension at subsurface conditions: Implications for H_2, $CO_2$and natural gas geo-storage, International Journal of Hydrogen Energy 46 (2021) 25578–25585.

[67] M. Ali, N. K. Jha, A. Al-Yaseri, Y. Zhang, S. Iglauer, M. Sarmadivaleh, Hydrogen wettability of quartz substrates exposed to organic acids; Implications for hydrogen geo-storage in sandstone reservoirs, Journal of Petroleum Science and Engineering 207 (2021) 109081.

[68] Y. F. Chow, G. C. Maitland, J. M. Trusler, Interfacial tensions of (H_2O + H_2) and (H_2O + CO_2+ H_2) systems at temperatures of (298–448) K and pressures up to 45 MPa, Fluid Phase Equilibria 475 (2018) 37–44.

[69] M. Hosseini, J. Fahimpour, M. Ali, A. Keshavarz, S. Iglauer, H_2-brine interfacial tension as a function of salinity, temperature, and pressure; implications for hydrogen geo-storage, Journal of Petroleum Science and Engineering 213 (2022) 110441.

[70] L. Hashemi, M. Boon, W. Glerum, R. Farajzadeh, H. Hajibeygi, A comparative study for H 2 –CH 4 mixture wettability in sandstone porous rocks relevant to underground hydrogen storage, Advances in Water Resources 163 (2022) 104165.

[71] W. Van Rooijen, L. Hashemi, M. Boon, R. Farajzadeh, H. Hajibeygi, Microfluidics-based analysis of dynamic contact angles relevant for underground hydrogen storage, Advances in Water Resources 164 (2022) 104221.

[72] H. Esfandyari, M. Hosseini, M. Ali, S. Iglauer, M. Haghighi, A. Keshavarz, Assessment of the interfacial properties of various mineral/hydrogen/water systems, Journal of Energy Storage 60 (2023) 106637.

[73] S. Iglauer, M. Ali, A. Keshavarz, Hydrogen Wettability of Sandstone Reservoirs: Implications for Hydrogen Geo-Storage, Geophysical Research Letters 48 (2021).

[74] L. Hashemi, W. Glerum, R. Farajzadeh, H. Hajibeygi, Contact angle measurement for hydrogen/brine/sandstone system using captive-bubble method relevant for underground hydrogen storage, Advances in Water Resources 154 (2021) 103964.

[75] A. Al-Yaseri, N. Yekeen, M. Mahmoud, A. Kakati, Q. Xie, A. Giwelli, Thermodynamic characterization of H_2-brine-shale wettability: Implications for hydrogen storage at subsurface, International Journal of Hydrogen Energy 47 (2022) 22510–22521.

[76] S. Higgs, Y. Da Wang, C. Sun, J. Ennis-King, S. J. Jackson, R. T. Armstrong, P. Mostaghimi, In-situ hydrogen wettability characterisation for underground hydrogen storage, International Journal of Hydrogen Energy 47 (2022) 13062–13075.

[77] Z. D. Isfehani, A. Sheidaie, M. Hosseini, J. Fahimpour, S. Iglauer, A. Keshavarz, Interfacial tensions of (brine + H_2 + CO_2) systems at gas geo-storage conditions, Journal of Molecular Liquids 374 (2023) 121279.

[78] M. Hosseini, M. Ali, J. Fahimpour, A. Keshavarz, S. Iglauer, Assessment of rock-hydrogen and rock-water interfacial tension in shale, evaporite and basaltic rocks, Journal of Natural Gas Science and Engineering 106 (2022) 104743.

[79] M. Hosseini, M. Ali, J. Fahimpour, A. Keshavarz, S. Iglauer, Calcite–Fluid Interfacial Tension: H_2 and CO_2Geological Storage in Carbonates, Energy & Fuels (2023). Publisher: American Chemical Society.

[80] M. Hosseini, J. Fahimpour, M. Ali, A. Keshavarz, S. Iglauer, Hydrogen wettability of carbonate formations: Implications for hydrogen geo-storage, Journal of Colloid and Interface Science 614 (2022) 256–266.

[81] M. Hosseini, M. Ali, J. Fahimpour, A. Keshavarz, S. Iglauer, Basalt-H_2-brine wettability at geo-storage conditions: Implication for hydrogen storage in basaltic formations, Journal of Energy Storage 52 (2022) 104745.

[82] P. Chiquet, J.-L. Daridon, D. Broseta, S. Thibeau, CO_2/water interfacial tensions under pressure and temperature conditions of CO_2geological storage, Energy Conversion and Management 48 (2007) 736–744.

[83] M. Naylor, M. Wilkinson, R. Haszeldine, Calculation of CO_2 column heights in depleted gas fields from known pre-production gas column heights, Marine and Petroleum Geology 28 (2011) 1083–1093.

[84] L. Paterson, The implications of fingering in underground hydrogen storage, International journal of hydrogen energy 8 (1983) 53–59.

[85] R. Chuoke, P. van Meurs, C. van der Poel, The Instability of Slow, Immiscible, Viscous Liquid-Liquid Displacements in Permeable Media, Transactions of the AIME 216 (1959) 188–194.

[86] J. Dumore, Stability considerations in downward miscible displacements, Society of Petroleum Engineers Journal 4 (1964) 356–362.

[87] J. Millat, J. Dymond, C. N. de Castro, W. Wakeham, Transport properties of fluids, Cambridge University Press Cambridge, 1996.

[88] M. L. Huber, E. W. Lemmon, I. H. Bell, M. O. McLinden, The nist refprop database for highly accurate properties of industrially important fluids, Industrial & Engineering Chemistry Research 61 (2022) 15449–15472.

[89] J. C. Chichester, M. L. Huber, Documentation and Assessment of Transport Property Model for Mixtures Implemented in NIST REFPROP (Version 8.0), US Department of Commerce, Technology Administration, National Institute of Standards and Technology, 2008.

[90] O. Fandiño, J. M. Trusler, D. Vega-Maza, Phase behavior of (CO_2+H_2) and (CO_2+N_2) at temperatures between (218.15 and 303.15)K at pressures up to 15MPa, International Journal of Greenhouse Gas Control 36 (2015) 78–92.

[91] M. A. Christie, High-Resolution Simulation of Unstable Flows in Porous Media, SPE Reservoir Engineering 4 (1989) 297–303.

[92] R. X. Suzuki, F. W. Quah, T. Ban, M. Mishra, Y. Nagatsu, Experimental study of miscible viscous fingering with different effective interfacial tension, AIP Advances 10 (2020) 115219.

[93] M. W. Legatski, D. L. Katz, Dispersion Coefficients for Gases Flowing in Consolidated Porous Media, Society of Petroleum Engineers Journal 7 (1967) 43–53.

[94] T. C. Flowers, J. R. Hunt, Viscous and gravitational contributions to mixing during vertical brine transport in water-saturated porous media, Water resources research 43 (2007).

[95] A. Alkindi, Y. Al-Wahaibi, B. Bijeljic, A. Muggeridge, Investigation of longitudinal and transverse dispersion in stable displacements with a high viscosity and density contrast between the fluids, Journal of Contaminant Hydrology 120-121 (2011) 170–183.

[96] J. D. Van der Waals, Over de Continuiteit van den Gas-en Vloeistoftoestand, volume 1, Sijthoff, 1873.

[97] E. C. Carlson, Don't gamble with physical properties for simulations, Chemical engineering progress 92 (1996) 35–46.

[98] P. Carden, L. Paterson, Physical, chemical and energy aspects of underground hydrogen storage, International Journal of Hydrogen Energy 4 (1979) 559–569.

[99] Y. Sanchez-Vicente, T. C. Drage, M. Poliakoff, J. Ke, M. W. George, Densities of the carbon dioxide+hydrogen, a system of relevance to carbon capture and storage, International Journal of Greenhouse Gas Control 13 (2013) 78–86.

[100] G. Soave, Equilibrium constants from a modified Redlich-Kwong equation of state, Chemical Engineering Science 27 (1972) 1197–1203.

[101] D.-Y. Peng, D. B. Robinson, A New Two-Constant Equation of State, Industrial & Engineering Chemistry Fundamentals 15 (1976) 59–64.

[102] R. Smith, H. Inomata, C. Peters, Equations of State and Formulations for Mixtures, in: Supercritical Fluid Science and Technology, volume 4, Elsevier, 2013, pp. 333–480. URL: https://linkinghub.elsevier.com/retrieve/pii/B9780444522153000064. doi:10.1016/B978-0-444-52215-3.00006-4.

[103] A. Péneloux, E. Rauzy, R. Fréze, A consistent correction for Redlich-Kwong-Soave volumes, Fluid Phase Equilibria 8 (1982) 7–23.

[104] C. H. Twu, H.-S. Chan, Rigorously Universal Methodology of Volume Translation for Cubic Equations of State, Industrial & Engineering Chemistry Research 48 (2009) 5901–5906.

[105] R. Privat, J.-N. Jaubert, Y. Le Guennec, Incorporation of a volume translation in an equation of state for fluid mixtures: which combining rule? which effect on properties of mixing?, Fluid Phase Equilibria 427 (2016) 414–420.

[106] O. Kunz, E. G. R. Group (Eds.), The GERG-2004 wide-range equation of state for natural gases and other mixtures, number 557 in Fortschritt-Berichte VDI Reihe 6, Energietechnik, als ms. gedr ed., VDI-Verl, Düsseldorf, 2007.

[107] A. Aasen, M. Hammer, S. Lasala, J.-N. Jaubert, O. Wilhelmsen, Accurate quantum-corrected cubic equations of state for helium, neon, hydrogen, deuterium and their mixtures, Fluid Phase Equilibria 524 (2020) 112790.

[108] L. F. Baladão, R. P. Soares, P. R. B. Fernandes, Comparison of the GERG-2008 and Peng-Robinson Equations of State for Natural Gas Mixtures 8 (2018) 10.

[109] R. Beckmüller, M. Thol, I. H. Bell, E. W. Lemmon, R. Span, New Equations of State for Binary Hydrogen Mixtures Containing Methane, Nitrogen, Carbon Monoxide, and Carbon Dioxide, Journal of Physical and Chemical Reference Data 50 (2021) 013102.

[110] Compass - charms, https://charms.gitlabpages.inria.fr/ComPASS/index.html, 2021.

[111] L. Beaude, K. Brenner, S. Lopez, R. Masson, F. Smai, Non-isothermal Compositional Two-Phase Darcy Flow: Formulation and Outflow Boundary Condition, in: C. Cancès, P. Omnes (Eds.), Finite Volumes for Complex Applications VIII - Hyperbolic, Elliptic and Parabolic Problems, Springer Proceedings in Mathematics & Statistics, Springer International Publishing, Cham, 2017, pp. 317–325. doi:10.1007/978-3-319-57394-6_34.

[112] L. Beaude, K. Brenner, S. Lopez, M. Roland, F. Smaï, Non-isothermal compositional liquid gas darcy flow: formulation, soil-atmosphere boundary condition and application to high-energy geothermal simulations, Computational Geosciences 23 (2019).

[113] E. Dalissier, C. Guichard, P. Havé, R. Masson, C. Yang, ComPASS : a tool for distributed parallel finite volume discretizations on general unstructured polyhedral meshes, ESAIM: Proceedings 43 (2013) 147–163.

[114] F. Xing, R. Masson, S. Lopez, Parallel numerical modeling of hybrid-dimensional compositional non-isothermal Darcy flows in fractured porous media, Journal of Computational Physics 345 (2017) 637–664.

[115] A. Armandine Les Landes, D. Castanon Quiroz, L. Jeannin, S. Lopez, M. Roland, Two-phase geothermal model with fracture network and multi-branch wells, The SMAI Journal of computational mathematics 9 (2023) 121–149.

[116] N. Birgle, M. Roland, T. Laurent, A domain decomposition method to couple nonisothermal compositional gas liquid Darcy and free gas flows, 2017.

[117] N. Birgle, R. Masson, L. Trenty, A nonlinear domain decomposition method to couple compositional gas liquid Darcy and free gas flows, in: C. Cancès, P. Omnes (Eds.), FVCA: International Conference on Finite Volumes for Complex Applications VIII, Finite Volumes for Complex Applications VIII - Hyperbolic, Elliptic and Parabolic Problems, Springer, Lille, France, 2017. URL: https://hal.science/hal-01541149. doi:10.1007/978-3-319-57397-7.

[118] K. Coats, J. Richardson, Calculation of Water Displacement by Gas in Development of Aquifer Storage, Society of Petroleum Engineers Journal 7 (1967) 105–112.

[119] A. Lauser, C. Hager, R. Helmig, B. Wohlmuth, A new approach for phase transitions in miscible multi-phase flow in porous media, Advances in Water Resources 34 (2011) 957–966.

[120] O. Angelini, C. Chavant, E. Chénier, R. Eymard, S. Granet, Finite volume approximation of a diffusion–dissolution model and application to nuclear waste storage, Mathematics and Computers in Simulation 81 (2011) 2001–2017.

[121] R. Neumann, P. Bastian, O. Ippisch, Modeling and Simulation of Two-Phase Two-Component Flow with Disappearing Nonwetting Phase, Computational Geosciences 17 (2013) 139–149. ArXiv:1209.4752 [physics].

[122] A. Abadpour, M. Panfilov, Method of negative saturations for modeling two-phase compositional flow with oversaturated zones, Transport in Porous Media 79 (2009) 197–214. Received: September 2, 2008; Accepted: November 10, 2008; Published: December 9, 2008.

[123] R. Masson, L. Trenty, Y. Zhang, Fomulations of two phase liquid gas compositional Darcy flows with phase transitions, International Journal on Finite Volumes 11 (2014) 34.

[124] I. B. Gharbia, E. Flauraud, Study of compositional multiphase flow formulation using complementarity conditions, Oil & Gas Science and Technology – Revue d'IFP Energies nouvelles 74 (2019) 43.

[125] I. B. Gharbia, J. Jaffré, Gas phase appearance and disappearance as a problem with complementarity constraints, 2014. URL: `http://arxiv.org/abs/1111.3808`, arXiv:1111.3808 [physics].

[126] R. Eymard, C. Guichard, R. Herbin, R. Masson, Vertex-centred discretization of multiphase compositional Darcy flows on general meshes, Computational Geosciences 16 (2012) 987–1005.

[127] G.-i. Kaminishi, T. Toriumi, Vapor-Liquid Phase Equilibrium in the CO_2-112, C O2-N_2 and CO_2-02 Systems, The Journal of the Society of Chemical Industry, Japan 69 (1966) 175–178.

[128] J. O. Spano, C. K. Heck, P. L. Barrick, Liquid-vapor equilibria of the hydrogen-carbon dioxide system, Journal of Chemical & Engineering Data 13 (1968) 168–171.

[129] W. B. Streett, A. Heintz, P. Clancy, D. Chokappa, Phase Equilibria in Hydrogen Binary Mixtures From 63 to 280 K and Pressures to 6000 Bars, MRS Proceedings 22 (1983) 105.

[130] K. Bezanehtak, G. B. Combes, F. Dehghani, N. R. Foster, D. L. Tomasko, Vapor–liquid equilibrium for binary systems of carbon dioxide + methanol, hydrogen + methanol, and hydrogen + carbon dioxide at high pressures, Journal of Chemical & Engineering Data 47 (2002) 161–168.

[131] O. Fandiño, J. M. Trusler, D. Vega-Maza, Phase behavior of (CO_2+H_2) and (CO_2+N_2) at temperatures between (218.15 and 303.15)K at pressures up to 15MPa, International Journal of Greenhouse Gas Control 36 (2015) 78–92.

[132] M. Yorizane, S. Yoshimura, H. Masuoka, Vapor liquid equilibrium at high pressure: N_2-CO_2, H_2-CO_2 system, Chemical engineering 34 (1970) 953–957,a1.

[133] P. Cath, C. Crommelin, H. K. Onnes, Isothermals of di-atomic substances and their binary mixtures. xix. a preliminary determination of the critical point of hydrogen, in: KNAW, Proceedings, volume 20, 1918, pp. 178–184.

[134] G. Morrison, Effect of water on the critical points of carbon dioxide and ethane, The Journal of Physical Chemistry 85 (1981) 759–761.

[135] M. A. Ben Souissi, R. Kleinrahm, X. Yang, M. Richter, Vapor-phase (p, ρ, t, x) behavior and virial coefficients for the binary mixture (0.05 hydrogen + 0.95 carbon dioxide) over the temperature range from (273.15 to 323.15 k) with pressures up to 6 mpa, Journal of Chemical & Engineering Data 62 (2017) 2973–2981.

[136] C. CMG, Cmg-gem technical manual, Computer Modelling Group.[Google Scholar] (2017).

[137] J. Simon, A. Ferriz, L. Correas, HyUnder – Hydrogen Underground Storage at Large Scale: Case Study Spain, Energy Procedia 73 (2015) 136–144.

[138] M. D. Aminu, S. A. Nabavi, C. A. Rochelle, V. Manovic, A review of developments in carbon dioxide storage, Applied Energy 208 (2017) 1389–1419.

[139] D. Vernet, Stockages souterrains de gaz et conservation des nappes aquiffères, La Houille Blanche 57 (1971) 737–750.

[140] H. Alnes, O. Eiken, S. Nooner, G. Sasagawa, T. Stenvold, M. Zumberge, Results from sleipner gravity monitoring: Updated density and temperature distribution of the CO_2 plume, Energy Procedia 4 (2011) 5504–5511.

[141] Hydrogen Storage In European Subsurface | HyStorIES Project | Fact Sheet | H2020, 2020. URL: `https://cordis.europa.eu/project/id/101007176`.

[142] A. Sainz-Garcia, E. Abarca, V. Rubi, F. Grandia, Assessment of feasible strategies for seasonal underground hydrogen storage in a saline aquifer, International Journal of Hydrogen Energy 42 (2017) 16657–16666.

[143] W. T. Pfeiffer, S. A. al Hagrey, D. Köhn, W. Rabbel, S. Bauer, Porous media hydrogen storage at a synthetic, heterogeneous field site: numerical simulation of storage operation and geophysical monitoring, Environmental Earth Sciences 75 (2016) 1177.

[144] B. Hagemann, M. Rasoulzadeh, M. Panfilov, L. Ganzer, V. Reitenbach, Mathematical modeling of unstable transport in underground hydrogen storage, Environmental Earth Sciences 73 (2015) 6891–6898.

[145] K. Luboń, R. Tarkowski, Numerical simulation of hydrogen injection and withdrawal to and from a deep aquifer in NW Poland, International Journal of Hydrogen Energy 45 (2020) 2068–2083.

[146] D. S. Mahdi, E. A. Al-Khdheeawi, Y. Yuan, Y. Zhang, S. Iglauer, Hydrogen underground storage efficiency in a heterogeneous sandstone reservoir, Advances in Geo-Energy Research 5 (2021) 437–443.

[147] N. Heinemann, J. Scafidi, G. Pickup, E. Thaysen, A. Hassanpouryouzband, M. Wilkinson, A. Satterley, M. Booth, K. Edlmann, R. Haszeldine, Hydrogen storage in saline aquifers: The role of cushion gas for injection and production, International Journal of Hydrogen Energy 46 (2021) 39284–39296.

[148] B. Hagemann, M. Rasoulzadeh, M. Panfilov, L. Ganzer, V. Reitenbach, Hydrogenization of underground storage of natural gas, Computational Geosciences 20 (2016) 595–606.

[149] J. Scafidi, M. Wilkinson, S. M. V. Gilfillan, N. Heinemann, R. S. Haszeldine, A quantitative assessment of the hydrogen storage capacity of the UK continental shelf, International Journal of Hydrogen Energy 46 (2021) 8629–8639.

[150] CMGL-GEM, GEM software, `https://www.cmgl.ca/gem`, 2023.

[151] E. M. Thaysen, I. B. Butler, A. Hassanpouryouzband, D. Freitas, F. Alvarez-Borges, S. Krevor, N. Heinemann, R. Atwood, K. Edlmann, Pore-scale imaging of hydrogen displacement and trapping in porous media, International Journal of Hydrogen Energy 48 (2023) 3091–3106.

[152] B. Pan, K. Liu, B. Ren, M. Zhang, Y. Ju, J. Gu, X. Zhang, C. R. Clarkson, K. Edlmann, W. Zhu, S. Iglauer, Impacts of relative permeability hysteresis, wettability, and injection/withdrawal schemes on underground hydrogen storage in saline aquifers, Fuel 333 (2023) 126516.

[153] R. Juanes, E. J. Spiteri, F. M. Orr Jr., M. J. Blunt, Impact of relative permeability hysteresis on geological CO_2 storage, Water Resources Research 42 (2006).

[154] S. Chabab, P. Théveneau, C. Coquelet, J. Corvisier, P. Paricaud, Measurements and predictive models of high-pressure H_2 solubility in brine (H_2O+NaCl) for underground hydrogen storage application, International Journal of Hydrogen Energy 45 (2020) 32206–32220.

[155] M. D. Lucia, P. Pilz, A. Liebscher, M. Kühn, Measurements of H_2 Solubility in Saline Solutions under Reservoir Conditions: Preliminary Results from Project H2STORE, Energy Procedia 76 (2015) 487–494.

[156] G. Wang, G. Pickup, K. Sorbie, E. Mackay, Numerical modelling of H_2 storage with cushion gas of CO_2in subsurface porous media: Filter effects of CO_2solubility, International Journal of Hydrogen Energy 47 (2022) 28956–28968.

[157] R. Sander, Compilation of Henry's law constants, version 3.99, preprint, Gases/Laboratory Studies/Troposphere/Chemistry (chemical composition and reactions), 2014. URL: `https://acp.copernicus.org/preprints/14/29615/2014/acpd-14-29615-2014.pdf`. doi:`10.5194/acpd-14-29615-2014`.

[158] H. de Moegen, H. Giouse, Long-Term Study of Cushion Gas Replacement by Inert Gas, in: Proceedings of the 64th Annual Technical Conference and Exhibition of the Society of Petroleum Engineers, San Antonio, TX, 1989, p. 12.

[159] L. W. Gelhar, C. Welty, K. R. Rehfeldt, A critical review of data on field-scale dispersion in aquifers, Water Resources Research 28 (1992) 1955–1974. _eprint: https://onlinelibrary.wiley.com/doi/pdf/10.1029/92WR00607.

[160] P. M. Sigmund, Prediction of molecular diffusion at reservoir conditions. ii. estimating the effects of molecular diffusion and convective mixing in multicomponent systems, J. Can. Pet. Technol.;(Canada) 15 (1976).

[161] S. R. Lekkala, Impact of injecting inert cushion gas into a gas storage reservoir, West Virginia University, 2009.

[162] E. R. Okoroafor, S. D. Saltzer, A. R. Kovscek, Toward underground hydrogen storage in porous media: Reservoir engineering insights, International Journal of Hydrogen Energy 47 (2022) 33781–33802.

[163] M. Zamehrian, B. Sedaee, Underground hydrogen storage in a partially depleted gas condensate reservoir: Influence of cushion gas, Journal of Petroleum Science and Engineering 212 (2022) 110304.

[164] A. V. Milkov, Molecular hydrogen in surface and subsurface natural gases: Abundance, origins and ideas for deliberate exploration, Earth-Science Reviews 230 (2022) 104063.

[165] E. Frery, L. Langhi, M. Maison, I. Moretti, Natural hydrogen seeps identified in the north perth basin, western australia, International Journal of Hydrogen Energy 46 (2021) 31158–31173.

[166] M. Leila, K. Loiseau, I. Moretti, Controls on generation and accumulation of blended gases (ch4/h2/he) in the neoproterozoic amadeus basin, australia, Marine and Petroleum Geology 140 (2022) 105643.

[167] V. Zgonnik, The occurrence and geoscience of natural hydrogen: A comprehensive review, Earth-Science Reviews 203 (2020) 103140.

[168] A. Prinzhofer, C. S. T. Cissé, A. B. Diallo, Discovery of a large accumulation of natural hydrogen in bourakebougou (mali), International Journal of Hydrogen Energy 43 (2018) 19315–19326.

[169] D. Briere, T. Jerzykiewicz, On generating a geological model for hydrogen gas in the southern taoudeni megabasin (bourakebougou area, mali), in: International Conference and Exhibition, Barcelona, Spain, 3-6 April 2016, Society of Exploration Geophysicists and American Association of Petroleum . . . , 2016, pp. 342–342.

[170] J. F. Ely, H. Hanley, Prediction of transport properties. 1. viscosity of fluids and mixtures, Industrial & Engineering Chemistry Fundamentals 20 (1981) 323–332.

[171] A. Predvoditelev, Some invariant quantities in the heat-conduction and viscosity theory, Zh. Fiz. Khim. 22 (1948) 339–348.

[172] G. Galliéro, C. Boned, A. Baylaucq, Molecular dynamics study of the lennard- jones fluid viscosity: application to real fluids, Industrial & engineering chemistry research 44 (2005) 6963–6972.

[173] R. S. Brokaw, Predicting transport properties of dilute gases, Industrial & Engineering Chemistry Process Design and Development 8 (1969) 240–253.

[174] M. L. Michelsen, J. M. Mollerup, Thermodynamic models: fundamentals & computational aspects, 2. ed ed., Tie-Line Publications, Holte, 2007.